



Molecular design and synthesis of asymmetrically extended molecules optimized for the process of annihilation upconversion

Dissertation

zur Erlangung des Grades eines

„Doktor rerum naturalium (Dr. rer. nat.)“

des Fachbereichs 09:

Chemie, Pharmazie, Geographie und Geowissenschaften,

der Johannes Gutenberg-Universität, Mainz

vorgelegt von

Ernesta Heinrich

Mainz, 2019

This thesis was carried out from May 2016 until March 2019 in the department of [REDACTED]
[REDACTED] in the group of [REDACTED] at the Max Planck Institute
for Polymer Research, Mainz.

Dean: [REDACTED]

Vice-dean: [REDACTED]

First reviewer: [REDACTED]

Second reviewer: [REDACTED]

Date of oral examination:

Declaration

I hereby declare that I wrote the dissertation submitted without any unauthorized external assistance and used only sources acknowledged in this work. All textual passages which are appropriate verbatim or paraphrased from published and unpublished texts, as well as all information obtained from oral sources, are duly indicated and listed in accordance with bibliographical rules. In carrying out this research, I complied with the rules of standard scientific practice as formulated in the statutes of Johannes Gutenberg-University Mainz to insure standard scientific practice.

Date, place

(Ernesta Heinrich)

Acknowledgements

First of all, I would like to thank [REDACTED] for the opportunity to perform my PhD thesis in her group at the Max Planck Institute for Polymer Research and therefore being able to have such an outstanding scientific and interpersonal experience.

Second, my gratitude goes to [REDACTED] for entrusting me with a captivating research topic and his continuous support and motivation.

Additionally, I thank [REDACTED] and [REDACTED] [REDACTED] for reading my thesis and agreeing to being my examiners at the PhD defence.

Furthermore, I would like to thank the people, who supported me along the way: [REDACTED]
[REDACTED]
[REDACTED].

Additionally, [REDACTED] deserves my deep gratitude for helping me tackle the synthesis and [REDACTED] and [REDACTED] for countless measurements.

The AG [REDACTED] lunch group needs to be thanked as well for their support and friendliness.

All of AK [REDACTED], AK [REDACTED] and the many nice people from the MPI-P shall be thanked for a warm and helpful working environment.

I would also like to give thanks to the PhD Committee for bringing much fun to the game.

Needless to say, my friends, who encouraged me through rough patches, deserve my gratitude.

In particular I have to thank my parents for the sacrifices they made, my partner for taking the good and the bad and my daughter for showing me what matters.

In summary it was a once in a lifetime experience that sadly needs to end and will be remembered and cherished forever, thank you!

This work was performed under the European Union's Horizon 2020 Research and Innovation Program under Grant agreement No. 732794—project HYPOSENS.

List of abbreviations and acronyms

¹ H-NMR	proton nuclear magnetic resonance
br	broad
BODIPY	boron-dipyrromethene
d	doublet
dF	delayed fluorescence
DB-BODIPY	3,5-bis(ethoxycarbonyl)-1,2,6,7-dibenzo-8-(3,5-di- <i>tert</i> -butylphenyl) BODIPY
DCM	dichloromethane
DDQ	2,3-dichloro-5,6-dicyano-1,4-benzoquinone
dPh	delayed phosphorescence
DPh-BODIPY 3,5-diphenyl-8-(3,5-di- <i>tert</i> -butylphenyl) BODIPY	
IR	infrared
ISC	intersystem crossing
HOMO	highest occupied molecular orbital
K	constant
ln	natural logarithm
LUMO	lowest unoccupied molecular orbital
m	multiplet
MALDI-TOF	matrix-assisted laser desorption/ionization - time of flight
MPh-MB-BODIPY	3-phenyl-5-ethoxycarbonyl-6:7-benzo-8-(3,5-di- <i>tert</i> -butylphenyl) BODIPY
p	para

Pd-B ₄ N ₀	palladium-tetrabenzoporphyrin
Pd-B ₃ N ₁	palladium-mononaphthotribenzoporphyrin
Pd-B ₂ N ₂	palladium-dinaphthodibenzoporphyrin
Pd-B ₁ N ₃	palladium-trinaphthomonobenzoporphyrin
Pd-B ₀ N ₄	palladium-tetranaphthoporphyrin
Pd-BNP	palladium-benzoahtoporphyrin
Pd-N ₄ A ₀	palladium-tetranaphthoporphyrin
Pd-N ₃ A ₁	palladium-monoanthratrinaphthoporphyrin
Pd-N ₂ A ₂	palladium-dianthrakinaphthoporphyrin
Pd-N ₁ A ₃	palladium-trianthramononaphthoporphyrin
Pd-N ₀ A ₄	palladium-tetraanthraporphyrin
Pd-TBP	palladium-tetrabenzoporphyrin
Pd-TNP	palladium-tetranaphthoporphyrin
R	gas constant
rF	residual phosphorescence
s	singlet
S _n	singlet state <i>n</i>
t	triplet
T	temperature
T _n	triplet state <i>n</i>
TDI	terrylenediimide
TLC	thin layer chromatography
TTA	triplet-triplet annihilation

TTA-UC	triplet-triplet annihilation upconversion
TTT	triplet-triplet transfer
UC	upconversion
UV	ultra-violet
UV-Vis	ultraviolet-visible
w	weak
WAT	white adipose tissue
ΔG	change in Gibbs free energy
ΔH	change in enthalpy
ΔS	change in entropy
λ	wavelength

Abstract: Molecular design and synthesis of asymmetrically extended molecules optimized for the process of annihilation upconversion

Organic materials possessing delocalized π -electrons are able to absorb certain wavelengths of the sunlight spectrum. The resulting intensive colour of these materials explains their historic use as dyes. In recent years though, organic dyes have left this straightforward application and entered various modern fields like photovoltaics and biomedicine. Likewise, their ability to interact with certain wavelengths of sunlight is utilized. Especially the use of a photophysical process called triplet-triplet annihilation upconversion has proven to be fruitful. Here a two-dye system undergoes absorption of a photon by one dye, intersystem crossing, triplet-triplet transfer to the second dye species and triplet-triplet annihilation upconversion, ultimately resulting in an emitted photon of higher energy than the one initially absorbed. Since the energetic levels of the involved dye species need to be precisely matching for the photophysical process to take place and they depend on the structure of the involved molecules, those need to be custom tailored.

This thesis describes dyes for three different upconversion applications. The mixed porphyrin chapter presents the preparation of mixed benzo-naphtho and naphtho-antra porphyrin families, which result in a broad absorption spectrum in the entire deep-red spectral range of the sun irradiation with the aim of increasing the yield of organic solar harvesting devices. The mixed emitter chapter focuses on the preparation of asymmetrical benzo-fused BODIPY molecules as an adequate emitter for the previously discussed mixed porphyrins. This combination of sensitizer and emitter dye enables an all-optical temperature sensing within the biological tissue. Therefore, the penetration and emanation of light is ensured by alteration of the dye structure to be able to use the TTA-UC as a sensing tool within the narrow optical tissue transparency window. The evolution of the minimally invasive sensing within biological tissue idea is found in the last chapter. In order to maximize the penetration depth and hence give rise to biomedical applications, it is necessary to develop a molecule with absorption in the IR-region. This can be achieved by the preparation of a fused porphyrin molecule as a sensitizer dye.

In summary, this thesis investigates the molecular design strategies and synthetic challenges for the preparation of novel organic dyes with defined photophysical characteristics.

Zusammenfassung: Molekulare Gestaltung und Synthese von asymmetrisch erweiterten Molekülen, optimiert für den Prozess der Annihilation-Aufkonversion

Organische Substanzen besitzen delokalisierte π -Elektronen, wodurch sie diskrete Wellenlängen des Sonnenlichtspektrums absorbieren können. Die daraus resultierende intensive Färbung dieser Materialien erklärt den historischen Nutzen als Färbemittel. In jüngster Zeit wurde diese offensichtliche Anwendung ausgedehnt in neue moderne Felder wie die Photovoltaik und der Biomedizin. Auch hier wird die Fähigkeit der Interaktion mit bestimmten Wellenlängen des Sonnenlichts ausgenutzt. Besonders der photophysikalische Prozess der Triplett-Triplett-Annihilations-Aufkonversion hat sich als erfolgreich herausgestellt. Dabei wird in einem zwei Farbstoffsystem von einem ersten Farbstoff ein Photon absorbiert, welches über Intersystemcrossing, Triplett-Triplett-Transfer zu einer zweiten Farbstoffspezies übertragen wird, welche wiederum Triplett-Triplett-Annihilation-Aufkonversion durchführen mit dem Resultat, dass das emittierte Photon eine höhere Energie aufweist als das initial absorbierte. Da zum Funktionieren des photophysikalischen Prozesses die Energilevels der beteiligten Farbstoffe genau zusammenpassen müssen und diese von der Struktur der beteiligten Moleküle abhängen, müssen diese maßgeschneidert werden.

Diese Arbeit beschreibt Farbstoffe für drei verschiedene Anwendungen des Aufkonversionsprozesses. Das Kapitel der gemischten Porphyrine zeigt die Herstellung von gemischten Benzo-Naphto- und Naphtho-Antha-Porphyrin-Familien, welche ein breites Absorptionsspektrum im gesamten tiefroten Bereich der Sonnenstrahlung aufweisen mit dem Ziel, die Ausbeute organischer Solarzellen zu erhöhen. Das Kapitel der gemischten Emittoren konzentriert sich auf die Synthese von asymmetrisch Benzo-fusionierten BODIPY-Molekülen als passende Emitter für die zuvor diskutierten gemischten Porphyrine. Diese Kombination von Chromophoren ermöglicht die Messung der Temperatur innerhalb biologischen Gewebes mittels rein optischer Verfahren. Dabei wird das Eindringen und wieder Heraustreten des Lichtes durch die Optimierung der Farbstoffstruktur ermöglicht, so dass die TTA-UC nun als ein Detektor innerhalb des engen optischen Gewebefensters fungiert. Die Weiterentwicklung dieser minimal invasiven Detektionsidee innerhalb biologischen Gewebes ist im letzten Kapitel zu finden. Zur Maximierung der Eindringtiefe und den damit interessanten biomedizinischen

Anwendungen ist ein Molekül mit Absorption im IR-Bereich notwendig. Dies kann durch die Synthese eines fusionierten Porphyrins erreicht werden.

Zusammenfassend untersucht diese Arbeit die molekulare Gestaltungsstrategien und synthetischen Herausforderungen für die Herstellung neuartiger Farbstoffe mit definierten photophysikalischen Charakteristika.

Table of contents

Declaration.....	IV
Acknowledgements	V
List of abbreviations and acronyms	VII
Abstract.....	X
Zusammenfassung.....	XII
Table of contents	XIV
1 Introduction.....	1
2 Theoretical background and state of the art.....	3
2.1 Photophysics.....	3
2.2 Triplet-triplet annihilation upconversion (TTA-UC)	5
2.3 Oxygen.....	7
2.4 Solar cells.....	8
2.5 Hyposens.....	10
2.5.1 Oxygen and temperature measurement.....	12
2.5.2 Tissue transparency window	14
2.6 Experimental setup	16
2.7 Chromophores for TTA-UC	18
2.7.1 Requirements.....	18
2.7.2 Sensitizer dyes.....	18
2.7.3 Emitter dyes.....	20
2.8 Chromophore design.....	21
2.8.1 Porphyrin syntheses.....	21
2.8.2 Three-dimensional shape.....	24
2.8.3 Influence of metalation.....	26
2.8.4 Solubility and aggregation.....	29
2.8.5 Redshift of triplet levels.....	30

3	Motivation.....	34
4	Results and discussion.....	36
4.1	Mixed porphyrin	36
4.1.1	Syntheses of precursors	36
4.1.2	Mixed benzo-naphtho porphyrin family.....	48
4.1.3	Mixed naphtho- anthra porphyrin family	51
4.1.4	Application.....	53
4.2	Mixed emitter	57
4.2.1	DPh-BODIPY and MPh-MB-BODIPY	57
4.2.2	DB-BODIPY	62
4.2.3	Application.....	65
4.3	Fused porphyrin	70
4.3.1	Original reaction scheme	70
4.3.2	Second reaction scheme	72
4.3.3	Third reaction scheme.....	75
4.3.4	Fourth reaction scheme.....	80
4.3.5	Fifth reaction scheme	84
5	Experimental section.....	98
5.1	Instruments	98
5.2	Chemicals and other materials.....	98
5.3	Preparation of samples for temperature measurements.....	99
5.4	Syntheses.....	100
5.4.1	Mixed porphyrin.....	100
5.4.2	Mixed emitter	117
5.4.3	Fused porphyrin.....	123
6	Summary.....	132
7	Appendix	XVII
7.1.1	List of tables	XVII

7.1.2 List of figures.....	XVII
7.1.3 List of publications and other work.....	XXIV
7.1.4 Curriculum vitae.....	XXV
7.1.5 Bibliography	XXVII

1 Introduction

Organic dyes such as indigo have been known for many centuries as strong colorants. They absorb certain wavelengths of the sunlight and reflect other resulting in a characteristic colour. In recent years their application has been extended into the field of photonics.^{1,2} Here one major field of interest is the development of solar harvesting devices in order to solve the problem of dependability on the limited fossil fuel recourses. They have been shrinking dramatically and the prognosis is, that they will be used up by the end of the 21th century.³ Therefore, renewable energy is the only way to maintain our current standard of life. In 1953, the first silicon based solar cell was developed. Since then there was a rapid further development. Due to the high production cost, the research has focused since the 1980s on organic semiconductor materials.^{4,5} Clear advantages next to the reduced production cost are the thinner shape and flexibility. So far, the usable light has been in the region of roughly 400 nm to 750 nm, depending on the type of solar cell, limiting the utilized light to only a small region of the electromagnetic spectrum of the sun. New developments focus on extending the absorption spectrum of the photovoltaic device into the IR-A-region. This proves to be challenging since such long electromagnetic waves are not energetic enough to be used by standard solar cells. Possible solutions range from perovskite/silicon tandem cells⁶ over thermoelectric generators (TEG)⁷ and concentrated photovoltaic (CPV) solar cells. This results in drastic changes to the characteristics of the photovoltaic devices architecture or its photosensitive material.⁸ A long-forgotten process, yet currently rising to a new fame, called TTA-UC, could prove to be a simple and powerful fix to maximize the absorption range of the photosensitive material while keeping the integrity of already existing solar devices. Hereby a sensitizer dye is excited with a certain lower energy light. It transfers this energy to a second dye, which ultimately emits light of an energy higher than initially absorbed.^{9,10}

A key factor for the TTA-UC process to take place are the precisely matching triplet energy levels of the sensitizer and emitter dye species. They are closely linked to their molecular structure. Therefore, careful design of the custom-tailored dyes is crucial. Additional requirements are high triplet-triplet transfer (TTT) rate, highly different ISC-coefficients for the sensitizer and emitter dyes, correctly situated triplet energy levels of the emitter molecule, photostability and solubility, just to name a few.¹¹ Accordingly, in this thesis it is shown, that the preparation of a suitable dye family absorbing noncoherent light in the deep-red-region was successful. The broad absorption spectrum of the sensitizer

dyes from the mixed Pd-metallated benzo-naphtho and naphtho-antra porphyrin family ensured a maximized harvesting of the so far unused deep-red-region energy. Through TTA-UC this energy could be upconverted to wavelengths usable by already known solar harvesting systems.¹²

Fascinatingly, the TTA-UC chromophores are not limited to solar applications. Since the structure of the chromophores is closely linked to the specific wavelengths of the absorbed photons, it is possible to adjust the TTA-UC dye couple to absorb and emit photons within a certain range of the electromagnetic spectrum. This is of particular interest since the human tissue possesses a narrow transparency window, which allows entering and emanation of luminescence without reabsorption by other chromophores of the living cells such as for example melanin, oxygenated hemoglobin, bilirubin and water or scattering by other cells like white adipose tissue (WAT).^{13,14} Since the luminescence signal is strongly dependent on the temperature of the environment, sensing of the local temperature is possible. In case of biological tissue, sensing of the local temperature of a living cell can be performed. Encapsulation of the Pd-metallated benzo-naphtho porphyrin family and emitter from the mixed benzo-BODIPY family into a natural wax matrix with sensitivity to the surrounding temperature ensures the integrity of the system, protection against oxygen and overall biocompatibility. The achieved detectable change in temperature is 200 mK and is centered around the physiologically relevant temperature of 36 °C. Hence a minimally invasive, biocompatible temperature sensing system for biological tissue is achieved.¹²

This biomedical application is of particular interest for breast cancer patients. So far, the golden standard to determine the cancer stage and hence the treatment and life expectancy is the sentinel lymph node biopsy (SLNB). The European Hyposens project¹⁵ focusses on replacing the biopsy with all its risks, costs and limitations by developing an organic dye dependent, photonic device, designed to recognize metastases in the sentinel lymph nodes in a minimally invasive, all optical way. Here the cells local temperature^{16,17} and oxygen¹⁸ levels, which are characteristic parameters for the evaluation of its health,^{19,20} are measured. Local hyperthermia and hypoxia are strong indicators for the development of cancerous cells. To ensure a high penetration depth and subject the tissue to the least amount of damage, while ensuring all luminescence is situated within the tissue transparency window, the sensitizer molecule should depict absorption in the IR-region. This was achieved by the successful preparation of a fused Palladium-phenyl-anthracene porphyrin species.

2 Theoretical background and state of the art

2.1 Photophysics

According to the atomic orbital model used to describe the structure of an atom or molecule, the valence electrons possess a distinct energy. The lowest energy level or ground state is called S_0 (S for singlet) as shown in Figure 2.1. It consists of many vibrational states with according energies. After a valence electron absorbs a photon of corresponding energy, it transitions to a higher energy level; the first being the excited state S_1 . While the electrons transition to a different energetic level, the nucleus remains in position, since this absorption process only takes 10^{-15} s. But not all vibronic transitions are equally likely to occur. The Franck-Condon principle states, that absorptions or emissions between two energy levels with similar wave functions are favoured. Figure 2.1 being a visual representation of this principle defines that wave functions, which can be connected by a strictly vertical line, represent most probable transitions.²¹

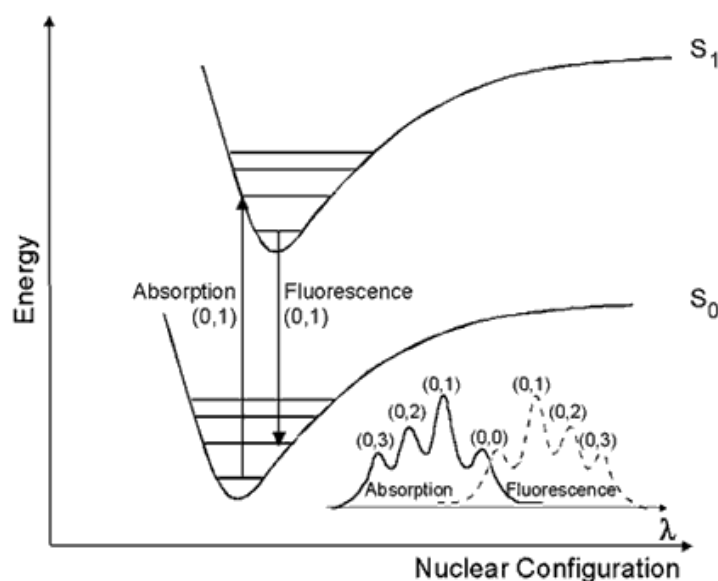


Figure 2.1: Transition between energy levels of a molecule demonstrating the Franck-Condon principle.²²

From an excited energy level there are various processes which lead to emission of the absorbed photon and return to the ground state. Elaborating on the previous Figure 2.1 illustrating the Franck-Condon principle Alexander Jablonski described in his 1933 proposed diagram the possible electronic states of valence electrons of a dissolved molecule and their transitions, which is displayed in Figure 2.2.²¹

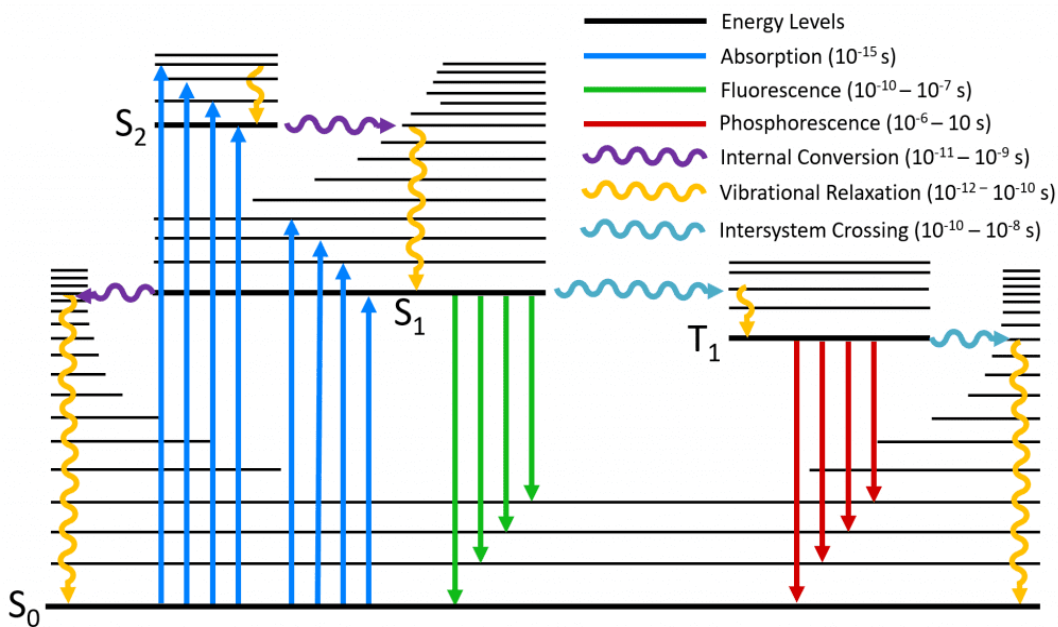


Figure 2.2: Jablonski diagram depicting possible transitions between energy levels of the valence electrons of a molecule in solution.²³

The vibrational energy levels of the ground state and the excited states are depicted as horizontal lines. Absorption (green vertical lines) of light enables electrons from the ground S_0 level to be elevated to excited states S_1 , S_2 etc. Descend from higher excited level to the first excited level is achieved through loss of energy via a non-radiative process called internal conversion (broken black line). Within a level the electron can relax to its lowest vibrational energy level through dissipation of energy from the molecule to its surroundings, which is referred to as vibrational relaxation (dotted black line). From the S_1 level the electron can transition to its ground level by two different emission processes, fluorescence (blue line) and phosphorescence (red line). First is the direct emission of energy, second a two-step process. Here the non-radiative mechanism of intersystem crossing (thick black line) enables the electron to reach a third kind of level, the triplet

level T_1 located energetically lower than the S_1 level. Emission of energy through phosphorescence leads to return of the electron to its ground level.²¹

Absorption and emission can be monitored via UV-Vis spectroscopy. Comparison of these two obtained spectra either presents an emission signal red-shifted, which is referred to as Stokes shift, or blues-shifted, then named anti-Stokes shift, in regard to the absorption signal (Figure 2.3).²¹

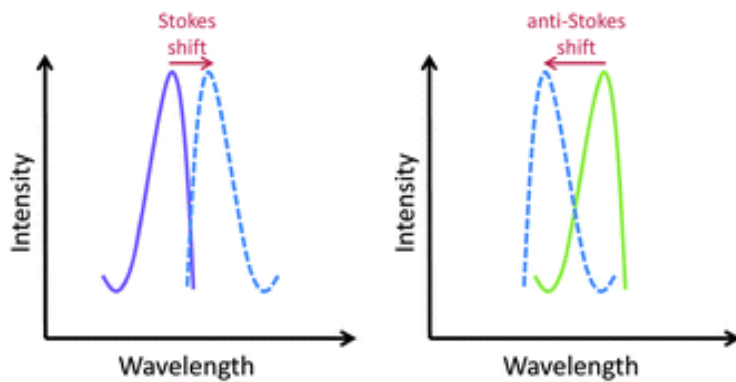


Figure 2.3: Visual representation of red-shifted emission signal (left, broken line) and blue-shifted emission signal (right, broken line).²⁴

2.2 Triplet-triplet annihilation upconversion (TTA-UC)

Triplet-triplet annihilation upconversion (TTA - UC) is the only upconversion method that has been experimentally demonstrated to operate with non-coherent low intensity illumination such as moderate concentrated sunlight.^{25,26} Such low-energy threshold allows for the development of several unique applications in material science²⁷⁻²⁹, solar cell devices,^{30,31} solar fuels,³² bioimaging^{33,34} and extension of the infrared limit of oxygenic photosynthesis.³⁵ The TTA – UC process takes place in multi-chromophore systems consisting of energetically optimized pairs of sensitizer (transition metal chelates and macrocycles) and emitter molecules (polycyclic aromatic hydrocarbons or BODIPYs): shortly, photon energy absorbed by the Q-band of a sensitizer (Figure 2.4) is stored in its triplet state, formed via the process of intersystem crossing (ISC). Further, this energy is transferred to an emitter triplet state in a process of triplet-triplet energy transfer (TTT). Next, the excited triplet states of two emitter molecules undergo triplet-triplet annihilation (TTA), in which one emitter molecule returns back to its singlet ground state and the other

molecule gains the energy of both triplet states and is excited to a higher energy singlet state. As the singlet state emitter decays radiatively back to the ground state, a fluorescence photon is emitted which is strongly blue-shifted compared to the excitation photons.¹²

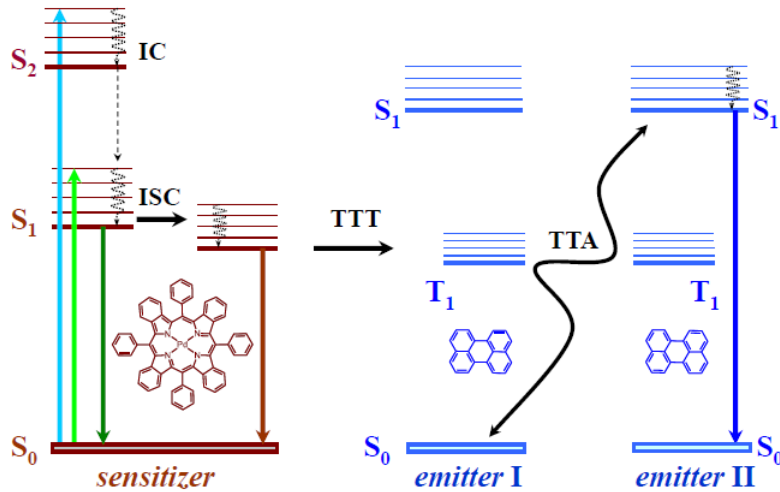


Figure 2.4: Simplified energetic scheme of the TTA – UC process in multicomponent organic system. Upper – general structures of the sensitizer ensemble, right – structure of the emitter (rubrene).¹²

The quantum yield (QY_{TTA-UC}) of the TTA – UC process is certainly of decisive importance, when further applications in solar energy harvesting devices are planned. It has to be pointed out, that a classical term (such as quantum yield) is attributed to a complex system like the TTA – UC process. In our study we use the term quantum yield in a classical meaning: the “absorption” of the UC-media will be determined by the Q-band absorption of the used sensitizer, and the “emission” will be attributed to the UC-fluorescence of the emitter species: $QY_{TTA-UC} = N_{\text{emitted}}^{\text{photons}} / N_{\text{absorbed}}^{\text{photons}}$. In soft matter matrix the TTA-process is diffusion controlled, demonstrating essential dependences on the material and environmental parameters such as degree of overlapping of the interacting energy states, matrix temperature, matrix viscosity and presence of molecular oxygen.¹²

Simultaneously, if the energy overlap between the triplet manifolds of the emitter and sensitizer molecules is not optimal or if the rotational diffusion of the interacting sensitizer/emitter triplet states is not high enough, the sensitizer triplet state will not be

completely depopulated and therefore residual sensitizer phosphorescence (brown arrow, Figure 2.4, called shortly rPh) will be observed as well.³⁶⁻³⁸

2.3 Oxygen

Naturally occurring oxygens ground state is the triplet state T_0 (Figure 2.5). Hence oxygen is able to interact with other molecules with energy in the T_1 level.

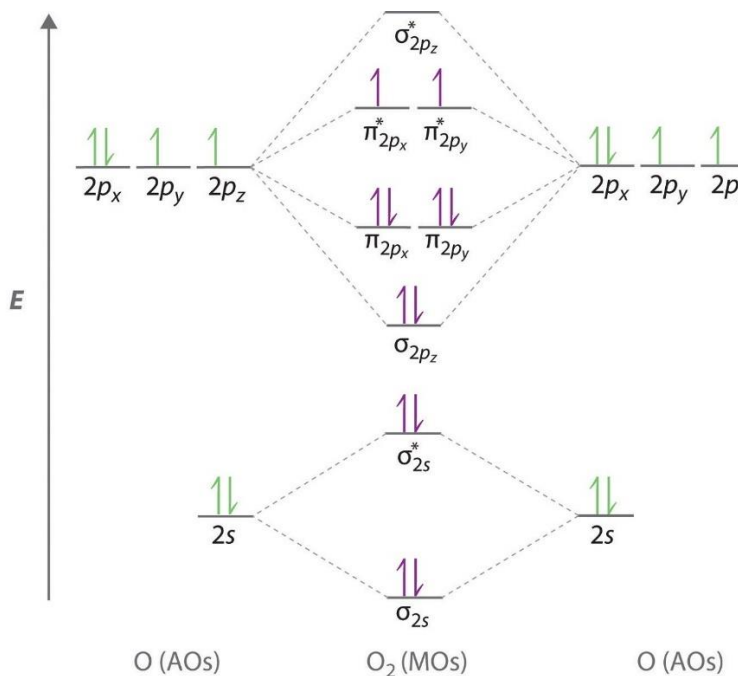


Figure 2.5: Molecular orbital of oxygen in its ground level, the triplet state.³⁹

This explains, why, in the presence of molecular oxygen, the energy stored in the excited states of the triplet ensembles, is being actively dissipated competing with emissive (phosphorescence) or non-emissive (triplet to triplet) energy transfer processes. Here the process of energy transfer between the organic molecules triplet state and ground state of molecular oxygen leads to generation of singlet oxygen (Figure 2.6).¹² Singlet oxygen is a highly reactive species, causing oxidation of the photoactive molecules, followed by further loss of efficiency. In fact, even very small oxygen concentrations on the level of 2-10 ppm could affect the TTA – UC efficiency substantially.^{12,21,40}

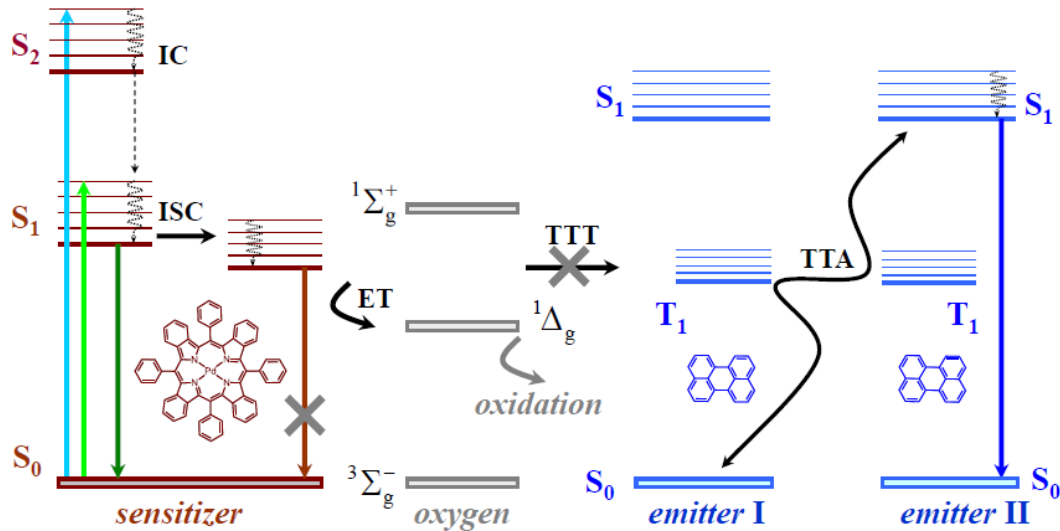


Figure 2.6: Mechanism of quenching of the TTA-UC process due to the presence of oxygen, which competes with the emitter molecules for the energy transfer from the sensitizer, leading to excitation of oxygen from its triplet ground state to its singlet excited state.⁴¹

Therefore, to fully exploit the TTA – UC process in different applications, the development of an effective protection strategy against quenching by molecular oxygen and protection against the subsequent production of highly reactive singlet oxygen is essential.^{12,41,42} The various defence mechanisms developed can be assigned to one of the two general approaches: passive or active protection methods. Passive protection methods focus on decreasing the oxygen permeability of the sample by for example encapsulation into polymer films⁴³ or micro- and nanocarriers,⁴⁴ which might be coated with an additional protective layer⁴⁵ or incorporation into supramolecular complexes⁴⁶ or dendrimers⁴⁷. Active protection methods are based on application of oxygen scavenging species as for example protective solvents^{48,49} or chromophore molecules with imbedded protection moieties^{50,21}.

2.4 Solar cells

Since the invention of the first solar cell by Chapin, Fuller and Pearson in 1954, it has been one of the key technologies for the future realization of a sustainable energy production worldwide.^{51,52} By now many different types of solar cells exist, ranging from

the first generation of crystalline silicon solar cells over the second generation of thin-film solar cells to the current third generation of organic solar cells.^{53,54}

Crystalline silicon (c-Si) solar cells are the most common ones and show the highest efficiency. The actual value varies a lot depending if it is a research or market manufactured solar cell, if it is a solar panel or a single solar cell, etc. Commercially produced monocrystalline solar panels have an average efficiency of 16%. Their simplified setup contains two semiconducting silicon layers, an electron rich one referred to as the n-type layer and a hole rich one called the p-type layer. As the sunlight penetrates the solar cell, certain wavelengths are able to excite the electrons from the valence band to the conduction band in the n-type layer, which results in their dissipation to the p-type layer. An electric current is generated. The big disadvantage of this type of solar cell are the too high production costs and the limited silicon resources.⁵⁵⁻⁵⁷

Therefore, much effort has been put in the development of organic solar cells (OPV). Here the semiconducting layer is made from organic materials. This active layer once again contains donor and acceptor structures (Figure 2.7). Upon exposure to sunlight, excitons are formed in the active layer, the charges dissipate to the electrodes and a current is generated. The use of organic materials results in much lower production costs and enhanced applicability but has the downside of shorter lifetime and lower efficiency.^{58,59}

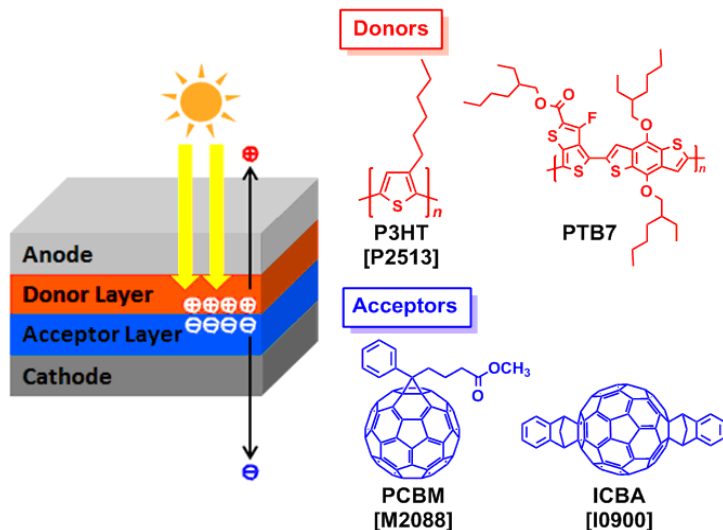


Figure 2.7: Simplified organic solar cell and possible donor and acceptor materials.⁶⁰

2.5 Hyposens

The European Hyposens project (No. 732794) has the aim to develop a minimally-invasive tool for the detection of breast cancer metastases via measurement of the cell's temperature and oxygen levels simultaneously and independently, replacing the sentinel lymph node biopsy. Energetically optimized UC-couple, encapsulated and taken up by the cells, are being excited within the tissue-transparency window and emit a response light that is highly connected to the oxygen and temperature levels present in the cell (Figure 2.8).¹⁵

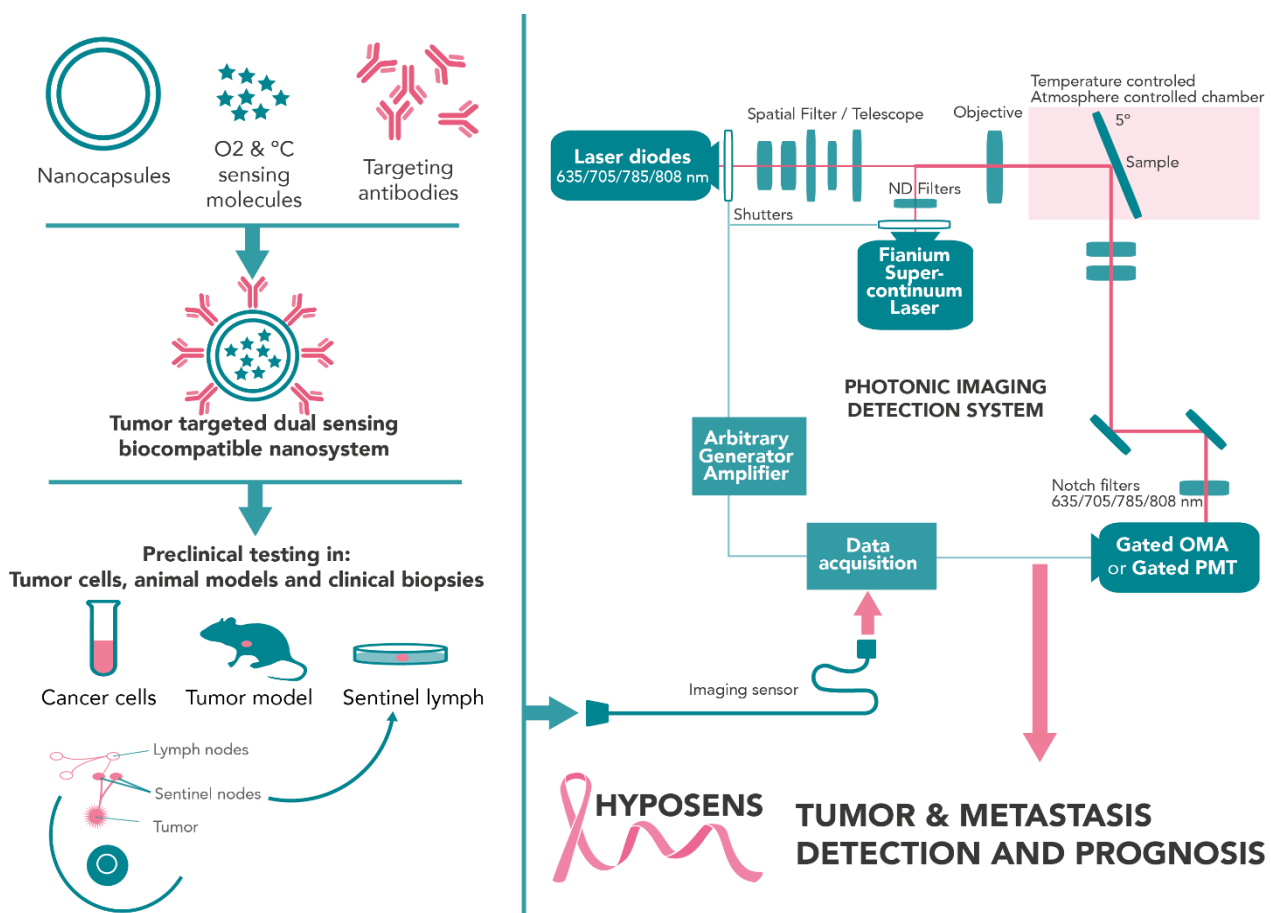


Figure 2.8: Methodology of the European Hyposens project. Formation of nanocapsules with oxygen and temperature sensing molecules and coating with targeting antibodies. Subsequent preclinical testing in tumour cells, animal models and clinical biopsies. Detection of optical signal containing information about temperature and oxygen concentration via photonic imaging detection system.¹⁵

In such a manner the oxygen and temperature locally in a cell can be measured minimally-invasively and simultaneously. Table 1.1 depicts the partial pressure of oxygen for normal and tumorous tissue for certain cancer types as an example of the tumour induced hypoxia.⁶¹

Table 1.1: Partial pressure of oxygen for normal tissue and for certain types of tumours. Reprint by permission from British Institute of Radiology: *BJR*, 2014, **87** (1035), 20130676 – 1-12, Copyright (2019).

Tumour type	n	Median tumour pO ₂	Median % oxygen	n	Median normal tissue pO ₂	Median % oxygen
Brain (6)	104	13.0	1.7	104	26.0	3.4
Head and neck cancer (13)	592	10.0	1.3		ND	5.9
	30	12.2	1.6	14	40.0	5.3
	23	14.7	1.9	30	43.8	5.8
	65	14.6	1.9	65	51.2	6.7
	6	14.3	1.9		ND	5.6
Lung cancer	20	16.6	2.2		42.8	5.6
Breast cancer (10)	212	10.0	1.3	212	52.0	6.8
Cervical cancer (12)	730	9.0	1.2			
				48	42.0	5.5
Liver	4	6.0	0.8	4	30.0	3.9
Pancreatic cancer	7	2.7	0.4	7	51.6	6.8
	1	2.0	0.3			
Prostate cancer	59	2.4	0.3	59	30.0	3.9
	55	4.5	0.6		ND	
	10	9.4	1.2	2	26.2	3.4

2.5.1 Oxygen and temperature measurement

For the oxygen and temperature measurement the organic dyes are encapsulated in a matrix consisting of natural waxes/oils and scavenger molecules, which ensures the ability to tune the temperature sensitivity range towards the biologically relevant temperature window (centred at $T = 36\text{ }^{\circ}\text{C}$) and allows a defined level of oxygen penetration into the capsule interior.^{41,62,63}

Altogether three different organic dyes are used, one sensitizer and one emitter dye for the temperature measurement and one sensitizer dye for the oxygen concentration measurement (Figure 2.9).

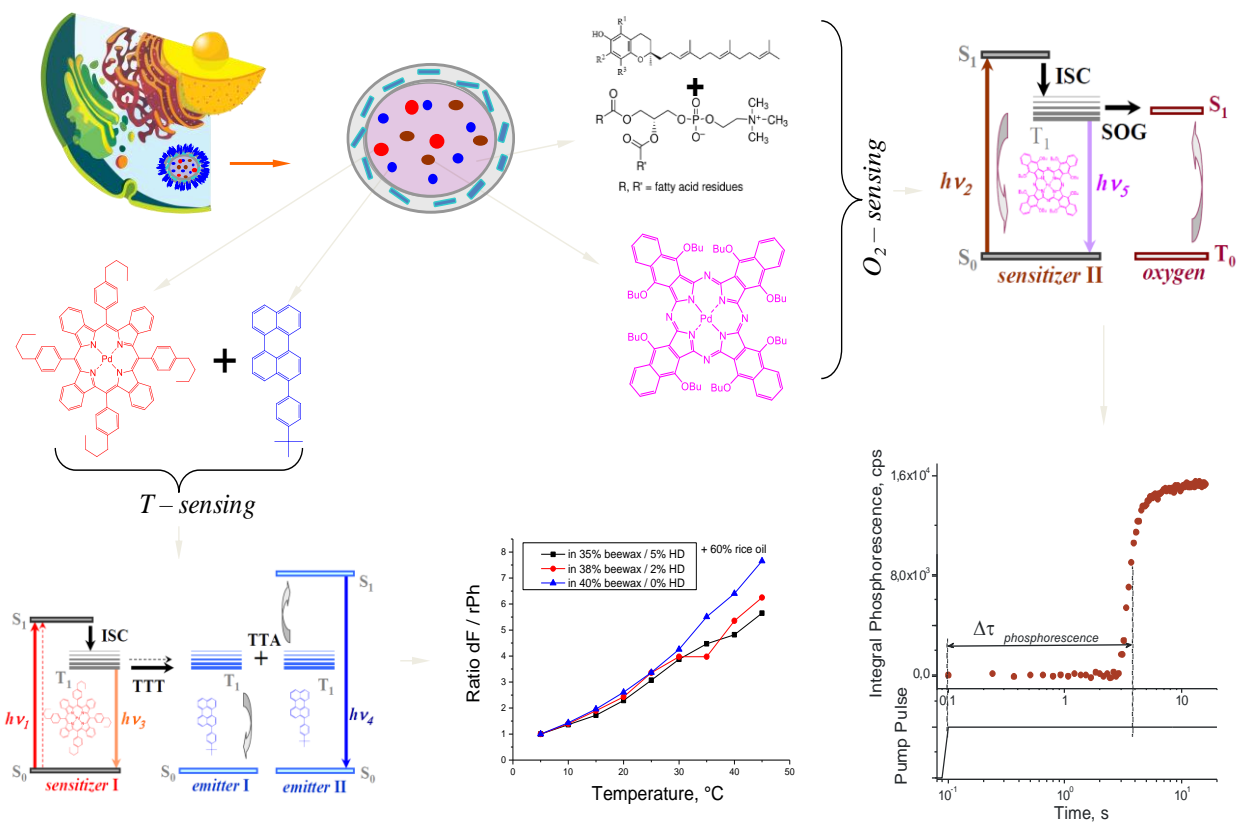


Figure 2.9: Overview of composition of capsules for temperature and oxygen concentration measurement via TTA-UC.⁶⁴

Since, due to the composition of the capsule, oxygen was able to penetrate and reach equilibrium, excitation ($\lambda_{\text{exc}} = 660 \text{ nm}$) of the oxygen sensing dye, a phthalocyanine-derivative, leads to quenching of its triplet states by oxygen in its triplet ground state forming singlet oxygen (Figure 2.9, top right). Hence, after a certain amount of time, all triplet oxygen present in the illuminated area have been transformed into singlet oxygen and chemically bound by the organophosphate matrix with pronounced singlet oxygen scavenging properties within a couple, hundred milliseconds. Now the excitation with the 660 nm laser allows the detection of the phosphorescence signal of the sensitizer dye since the triplet levels are not any more depopulated through energy transfer from the sensitizer dye by the triplet oxygen (Figure 2.9, bottom right). The time until the detection of the phosphorescence signal can ultimately give the initial triplet oxygen concentration through calibration. Once the irradiated spot is free of triplet oxygen through generation of singlet oxygen and its immobilizing via scavengers, the temperature-sensing can be performed. Therefore, the organic dyes, a porphyrin derivative as the sensitizer and a perylene derivative as the emitter are subjected to the classical TTA-UC process (Figure 2.9, left middle and bottom) with an excitation wavelength of 635 nm. The levels of the residual phosphorescence and delayed fluorescence signal are highly dependent on the environment's temperature. From the luminescence signal it is possible to obtain a ratiometric curve, which ensures significant independence of the data obtained of parameters such as excitation intensity instabilities, local molecular concentration fluctuations and field-of-view variations (Figure 2.9, bottom middle).⁶⁵ Since the 'cleaning' from triplet oxygen is very fast, the measurements are performed practically simultaneous.

For simultaneous measurement, it is crucial to avoid interference between the sensing dyes. Hence the absorption and emission spectra need to avoid overlap. This is ensured by careful selection of the utilized sensitizer dyes and excitation wavelengths. Figure 2.10 shows the absorption spectra of the dye employed for oxygen sensing, a phthalocyanine (PdPcOPh), with a maximum at 687 nm and its phosphorescence signal at 1040 nm and the dye used for temperature sensing, a porphyrin derivative (PdTBP) with an absorption maximum at 629 nm and its phosphorescence at 800 nm. Hence, the 635 nm laser is only able to excite the phthalocyanine derivative. The corresponding triplet phosphorescence at 1040 nm is not energetic enough to undergo TTT with the perylene based emitter for temperature sensing. Only the temperature sensing dyes triplet phosphorescence at 800 nm is energetic enough to populate the emitters triplet levels. As a result, the temperature and oxygen measurements are performed independently.

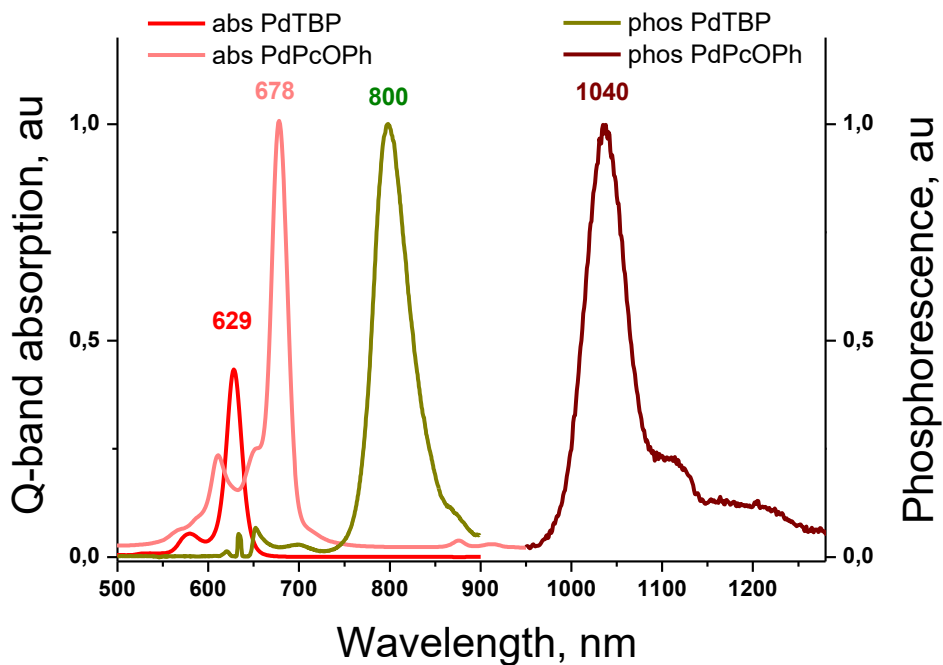


Figure 2.10: Q-band sensitizer absorption: PdTBP (red line); PdPcOPh (light red line); sensitization phosphorescence: PdTBP (green line); PdPcOPh (brown line).⁶⁴

2.5.2 Tissue transparency window

Straightforward *in vivo* application of the measurement described in the previous section is not possible due to absorbing and scattering abilities of the human tissue, namely the oxygenated hemoglobin in the human blood, the skin and fat tissue (Figure 2.11). Nonetheless there are three tissue transparency windows (here only two are shown), that allow photons from certain wavelength ranges to enter and leave the cells with minimal optical losses (absorption and scattering). The first tissue transparency window ranges from roughly 650 to 950 nm, the second from 1000 to 1350 nm and the third from 1500 -1700 nm.⁶⁶⁻⁶⁸

Therefore the targeted optical sensing materials must fulfil a chain of very specific requirements: (1) the excitation intensity must be comparable with the intensity of the sun, since such light intensity accompanies the living organisms during their evolution and they are accommodated to it; (2) the excitation wavelength must coincide optimally with the transparency window of the different components of the human skin in order to ensure maximum penetration depth of the sensing light; (3) the emission wavelengths of the

optical signals must match optimally the optical transparency window of the studied object; (4) even though trapped within a certain wavelength range, there should be as little overlap of the luminescence and excitation signals as possible to prevent reabsorption.

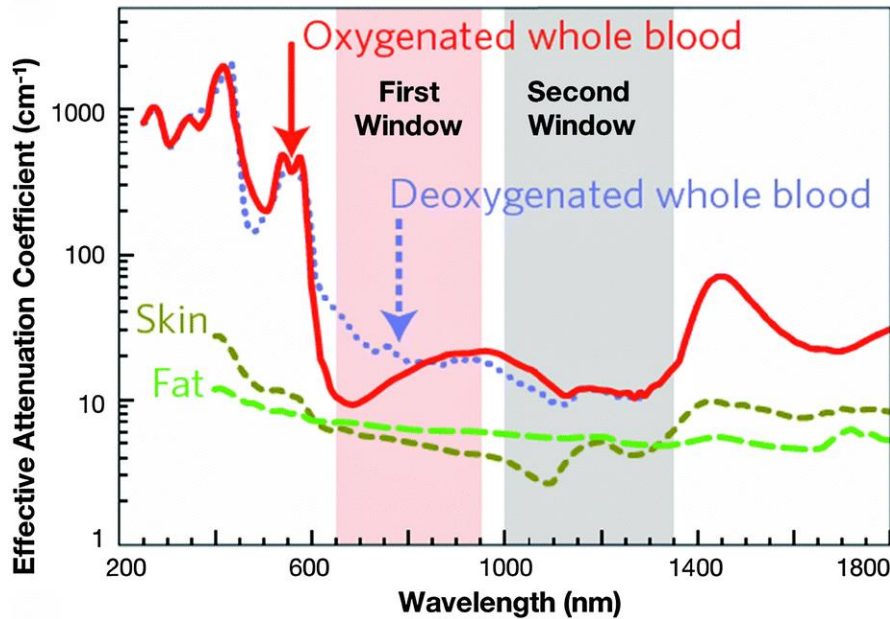


Figure 2.11: Effective attenuation coefficient of oxygenated whole blood, skin and fat versus the wavelength displaying the ranges of lower attenuation being called first and second (third one not shown) tissue transparency window. Reprinted by permission from Macmillan Publishers Ltd: *Nature Natotechnol.* 2009, **4**, 710-711, Copyright (2019).

All these requirements predetermine a new, non-orthodox optimization strategy for the process of TTA-UC: up to now, all synthetic efforts³⁶⁻³⁸ were directed towards as possible high anti-stokes shift of the UC-delayed fluorescence signal. In this respect, in order to fit the complete TTA-UC spectrum into the restricted human skin transparency window, it is necessary to minimize the anti-stokes shift. As seen in Figure 2.12, the UC-fluorescence signal with the emission central wavelength at $\lambda < 600$ nm (HbO_2 -absorption) is strongly absorbed. Even if such UC-signal is efficiently generated into the studied tissue, a tiny part of this signal is able to escape out of the tissue. Simultaneously, the residual sensitizer phosphorescence signal faces the same problem, if the central emission wavelength is higher than $\lambda > 850$ nm (WAT-absorption, Figure 2.12).

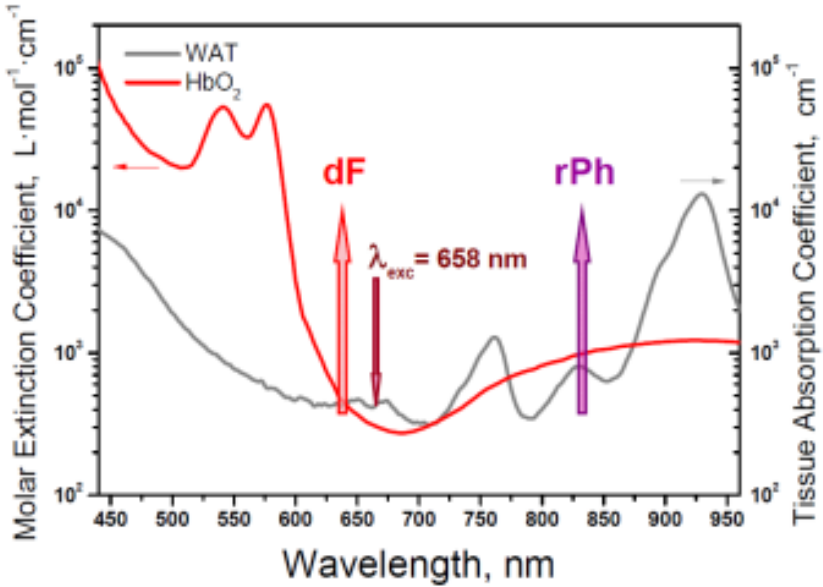


Figure 2.12: Molar extinction coefficient for different breast tissue components¹²⁵ as follows: – oxygenated haemoglobin (HbO_2 , red line, in water) and purified white adipose tissue (WAT, grey line) compared with the emission spectral range of the signals of delayed emitter fluorescence (dF) and residual sensitizer phosphorescence (rPh) excited in upconversion regime, using deep-red excitation light with extremely low excitation intensity of 1 mW cm^{-2} .

2.6 Experimental setup

A basic scheme of the experimental setup for TTA-UC measurements is shown in Figure 2.13. Here, the supercontinuum laser emits a beam that is reflected by a removable reflecting mirror and passes through a 4-f monochromator, which is based on a Brewster prism with high dispersion. After the selection of the wavelength for the pump emission, the beam passes a spatial filter, an attenuator, a beam splitting cube and after vertical beam spreading and focusing via use of an achromatic lens, the beam reaches the sample, which is in a horizontal position to minimize the effect of solvent convection.

Depending on the specific characterization of the TTA-UC systems, the experimental setup needs to be optimized accordingly. For example, for the application of the organic dyes in the photovoltaic and biomedical field the setup with laser intensities close to the sun (AM 1.5) are needed.

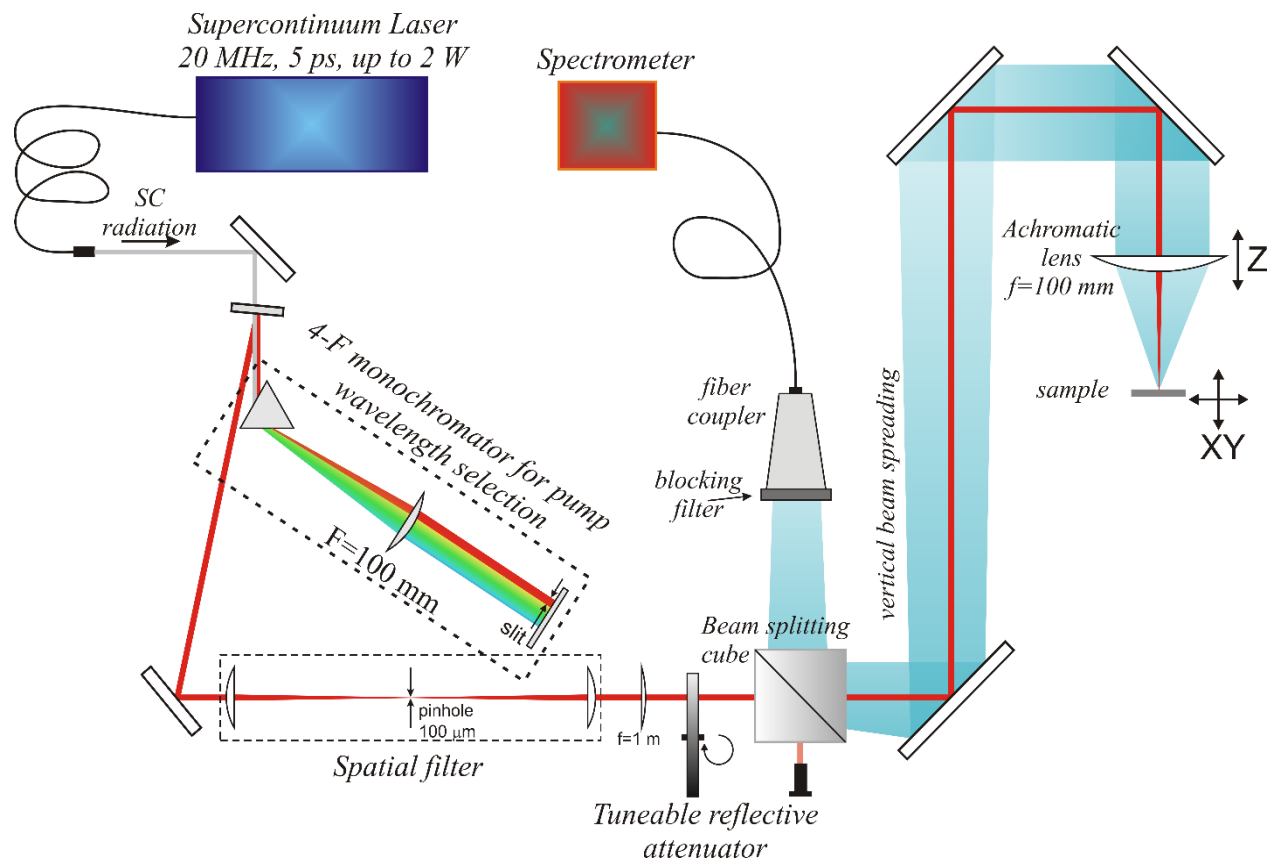


Figure 2.13: Experimental setup for measurement of the TTA - UC quantum yield.¹²

2.7 Chromophores for TTA-UC

2.7.1 Requirements

In order to achieve high TTA-UC quantum yield results, the sensitizer and emitter molecules must fulfil a couple of requirements. First, a maximum population of the sensitizer dye in its triplet state is needed, which is ensured by a high ISC rate, which itself is strongly dependent on the central metal ion. With this demand fulfilled, a high quantum yield of the sensitizer's phosphorescence is likely. Second, a matching emitter dye with its triplet levels on a very similar energetic level to the sensitizers needs to exist or potentially be prepared. This will result in a high TTT rate. Third, the absorption wavelengths of the sensitizer and the emission wavelengths of the emitter molecules should avoid overlap. Otherwise reabsorption and loss of efficiency of the TTA-UC process occur. Hence, the absorption spectrum should depict only very few band-like absorption areas. Depending on the application field, additional requirements such as a certain solubility and low toxicity arise.

2.7.2 Sensitizer dyes

For the process of TTA-UC, certain organic chromophores are more suitable than others. Literature states the use of metalated porphyrins⁶⁹ and phthalocyanines⁷⁰, ruthenium (II)-⁷¹, platinum-⁷² and iridium (III)⁷³ complexes as sensitizer dyes (Figure 2.14).

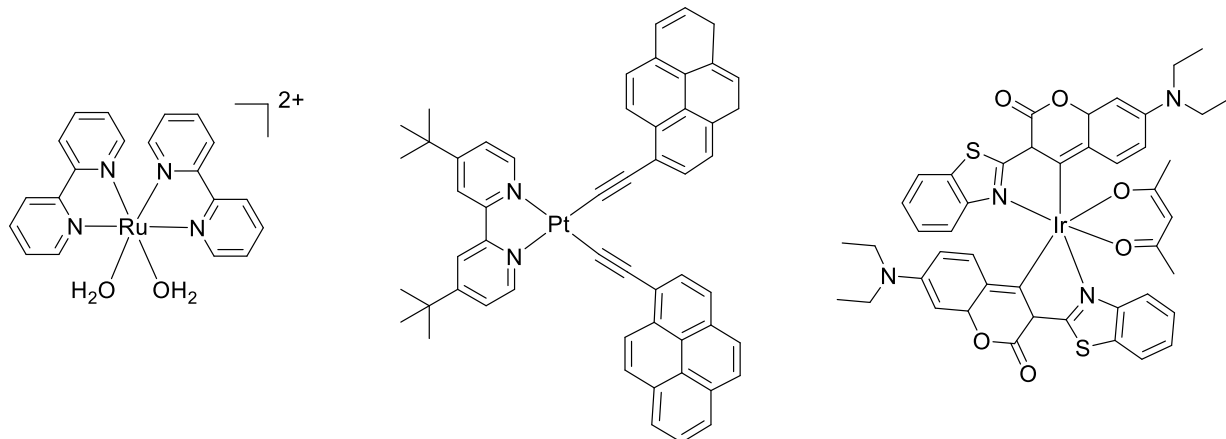


Figure 2.14: Ruthenium (II), platinum- and iridium (III) complex derivatives as TTTA-UC sensitizers.

A crucial drawback of ruthenium (II)-, platinum and iridium (III) complexes is the position of the phosphorescence signal regarding the absorption signal. A significant overlap results in reabsorption and therefore in very low quantum yield of the TTA-UC process.

Porphyrins and phthalocyanines with a metal ion inside (Figure 2.15) on the other hand depict two narrow absorption maxima, the Soret-band, located around 430 nm and the Q-band with a more flexible position (Figure 2.16).

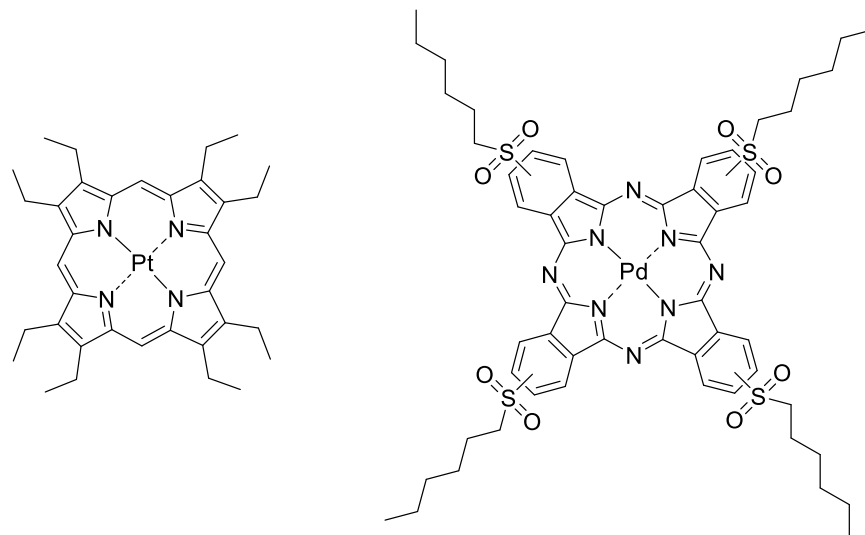


Figure 2.15: Porphyrin and phthalocyanine derivatives as TTA-UC sensitizers.

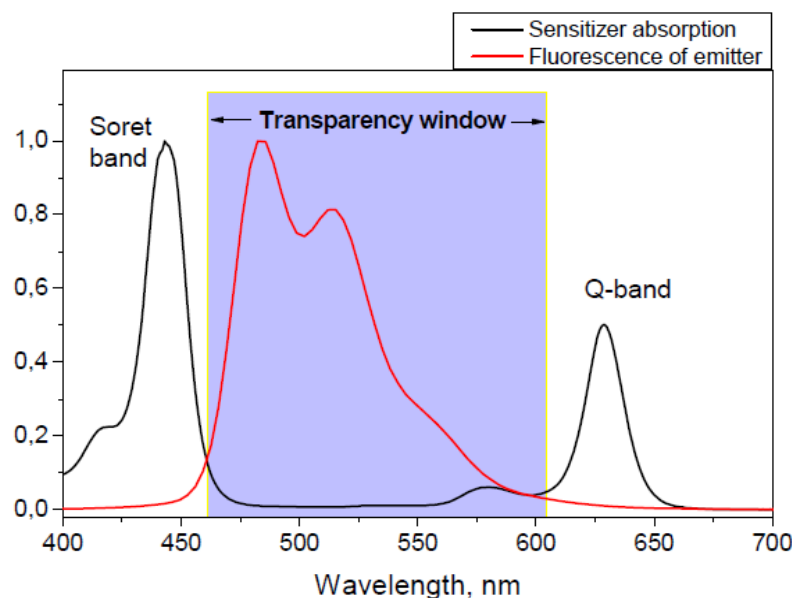


Figure 2.16: Absorption spectrum of a porphyrin sensitizer dye (black line) and delayed fluorescence signal of an emitter dye (red) within the transparency window.⁷⁴

The Soret-band shows the wavelengths necessary to excite electrons from the ground state S_0 to the second excited state S_2 . This energy is connected to the porphyrin core structure and stays fairly the same regardless on the modification of the β - and *meso*-positions. The position of the Q-band, which marks the energy needed for the excitation from the S_0 to the first excited state S_1 , is influenced by the overall structure of the chromophore. Hence a clever design of the porphyrin structure leads to absorption in the desired region. The delayed fluorescence signal of the emitter can be positioned in the area between Soret- and Q-band, which is called the transparency window. The hereby avoided overlap and reabsorption of the TTA-UC signals results in a high quantum yield.

Taking this into account as well as the fact that metalation with palladium or platinum ensures high ISC rates, it is comprehensible why scientific research up to now mainly focused on porphyrins and the very similar phthalocyanines, as sensitizer dye candidates.

2.7.3 Emitter dyes

Emitters used for TTA-UC need to match the triplet levels of the sensitizer dye, should possess a high delayed fluorescence quantum yield and avoid overlap with any absorption signals of the particular TTA-UC pair. In literature mainly polycyclic aromatic heterocarbons are found as for example perylene⁷⁵, rubrene⁷⁶ and BODIPY⁷⁷ (Figure 2.17). Perylene shows a fluorescence signal ranging from 430 - 530 nm. It matches well with sensitizer triplet levels around 900 - 1100 nm. Rubrenes fluorescence signal is located around 530 – 650 nm, making it a good emitter for sensitizers with triplet levels around 1100 -1300 nm. BODIPY shows emission around 500 – 600 nm. Structural modifications to these emitter dyes also alter the absorption and emission spectra. Hence a tuning of the photophysical characteristics to match the triplet levels of the sensitizer dye and avoid overlap with absorption signals is possible.

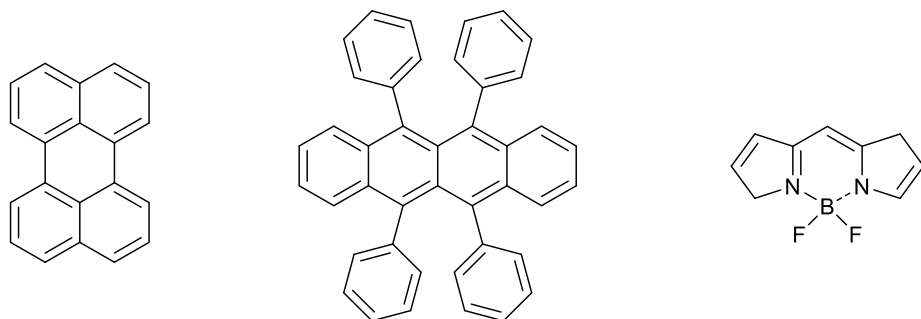


Figure 2.17: TTA-UC emitter dyes: perylene, rubrene and BODIPY as unsubstituted core structures (from left to right).

2.8 Chromophore design

2.8.1 Porphyrin syntheses

The first synthesis of a porphyrin was performed in 1935 by Paul Rothenmund with the preparation of tetraphenylporphyrin.⁷⁸ Therefore, he heated four equivalents of pyrrole and aldehyde each, catalysed by hydrochloric acid at 150 °C for 24 h with subsequent oxidation forming a *meso*-substituted porphyrin derivative (Figure 2.18).

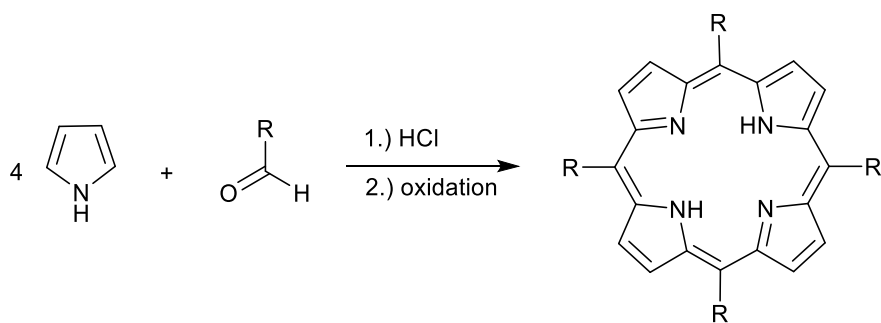


Figure 2.18: Rothenmund reaction using four equivalents of pyrrole and aldehyde to form *meso*-substituted porphyrin.

The use of such harsh reaction conditions resulted in a yield of roughly 5% and limited the variety of utilizable benzaldehydes. In 1964, Alan Adler and Frederick Longo were able to increase the yield up to 20% by using milder reaction conditions, heating at

141 °C for 30 min and using propionic acid as the Lewis acid. Purification was difficult though due to high levels of tarry residues and the batch-to-batch reproducibility displayed a huge variation.⁷⁹ Only in 1986, Jonathan Lindsey was able to introduce a reaction procedure with a yield of up to 40%.⁸⁰ The mild reaction conditions, stirring at room temperature for 2 h, broadened the scope of applicable benzaldehydes tremendously. The reason for this major improvement lies in the realization that the reaction mechanism steps are in thermodynamic equilibrium until the final oxidation step is performed (Figure 2.19).

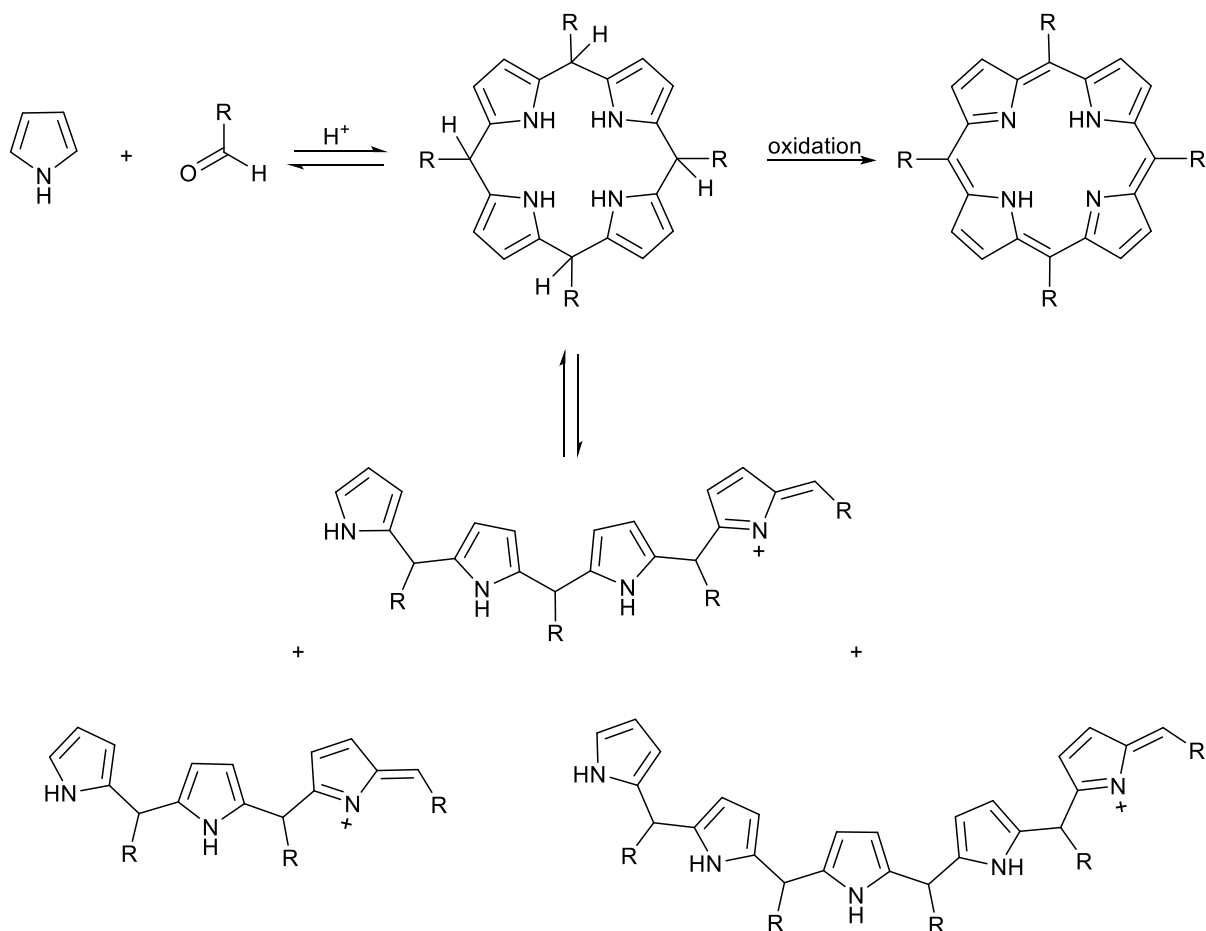


Figure 2.19: Lindsey condensation with pyrrole and benzaldehyde reaching equilibrium, where cyclic tetraphenylporphyrinogen is thermodynamically favoured over linear polypyrrylmethanes and irreversible oxidation step of cyclic porphyrinogen to porphyrin.

This equilibrium distribution of cyclic tetraphenylporphyrinogen and linear polypyrrylmethanes is amongst others highly dependent on the concentration of the reactants. The highest porphyrin yield was found at equimolar pyrrole and benzaldehyde

concentration of $10^{-2} \frac{\text{mol}}{\text{L}}$. Dilution as well as concentration lead to reduced yield and increased tarry side products. Dilution shifts the oligomer distribution towards shorter, whereas concentration shifts it towards longer polypyrrylmethanes. Additionally, the presence of water causes a shift in the equilibrium towards polypyrrylmethanes, hence reducing the yield significantly.

Besides modification of the porphyrin core in *meso*-position, modification in β -position is possible by addition of alkyl⁸¹ or aryl⁸² moieties (Figure 2.20). This can be either done before or after the Lindsey-condensation.

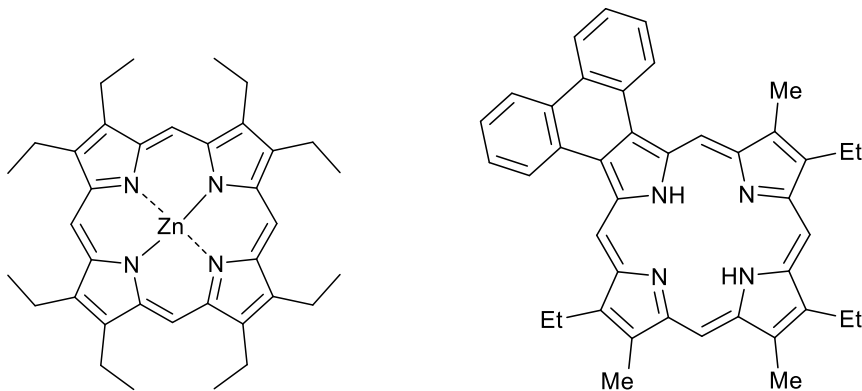


Figure 2.20: Modification of the porphyrin core in β -position in the case of octaethylporphyrin (left) and phenanthroporphyrin (right).

Finikova et al reported the synthesis of tetraaryltranaphtho[2,3]porphyrins via precursor assembly of the corresponding benzo[f]isoindole derivatives.⁸³ Here a cyclic system is transformed into a vinyl sulfone, which ultimately forms a pyrrole moiety (Figure 2.21). This design idea can be employed also for many other cyclic systems and has the advantage of substituent introduction to the cyclic system prior to the porphyrin assembly via Lindsey-condensation.

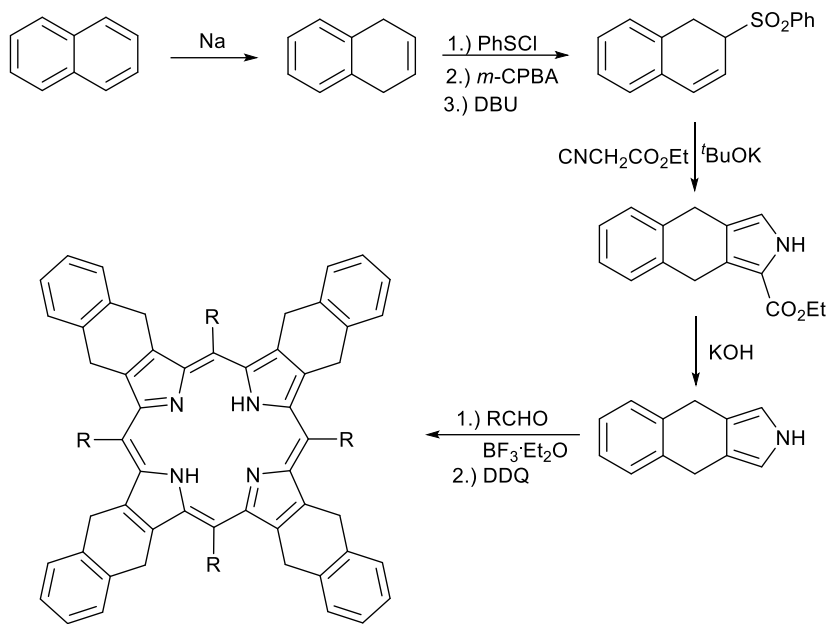


Figure 2.21: In β -position modified porphyrin via Lindsey-condensation of predesigned units.

2.8.2 Three-dimensional shape

The 3D shape of the porphyrin monomer is of high interest since it influences the reactivity, photophysical characteristics and aggregation tendencies.

The porphyrin core can either show a planer or distorted shape. The distortion can be in various ways ranging from a dome like structure over saddled and waved to ruffled and other not so frequently occurring shapes and mixtures of the different shapes (Figure 2.22).⁸⁴

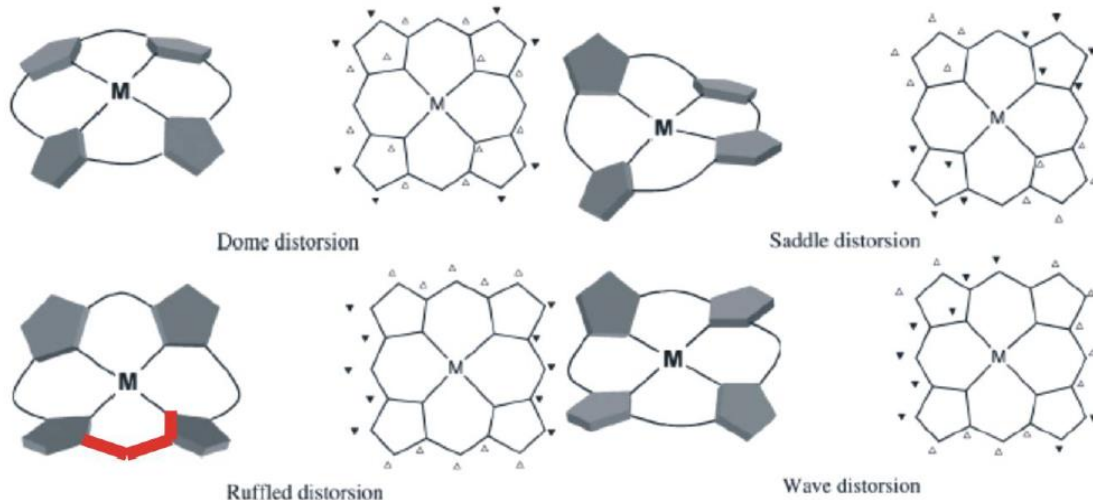


Figure 2.22: Common distorted 3D shapes of the porphyrin core. Reprinted by permission from Science Direct: *Microchemical Journal*, 2013, **107**, 47-62, Copyright (2019).

The unsubstituted porphyrin core is of planar shape and aromatic character. Introduction of aryl-substituents in *meso*-position of β -substituted porphyrins results in distortion due to steric repulsion and relief of the steric strain. Actually, two opposing forces, one trying to preserve the planarity and aromaticity of the system and another one trying to bring the *meso*-aryl-group into conjugation with the porphyrin core system determine the final shape.⁸⁵ Interestingly, even distorted porphyrins still display a significant ring current.

This distortion results in altered reactivity. So has the group of Takano reported that the oxygen affinity of the haemoglobins heme group, which is a porphyrin derivative, in red blood cells changes its affinity to oxygen upon the degree of distortion of its originally planar shape.⁸⁶ Looking at the structure of the heme group (Figure 2.23), it becomes obvious why the planar shape is better suited for the binding of the oxygen molecule. A for example ruffled distortion sterically hinders the two partners to statistically meet and hence reduces the effectivity of the oxygen binding.

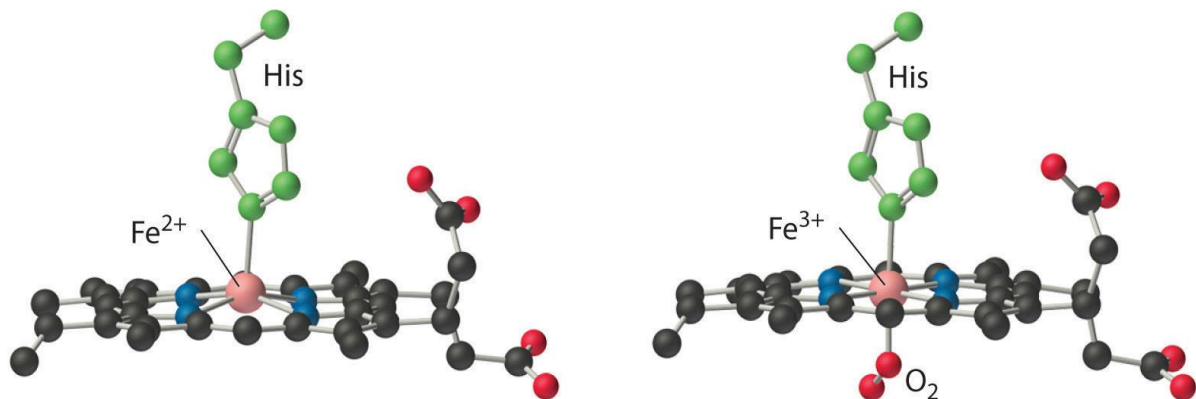


Figure 2.23: Binding (right) and release (left) of oxygen on the heme group of haemoglobin in the red blood cells designed for oxygen transportation in the mammal body.⁸⁷

Change of the chemical reactivity upon distortion can also be demonstrated with nonenzymatic porphyrins. Compared to planar porphyrins as a reference, the bend versions display an increased basicity, faster metalation rate and were easier to oxidize. Additionally, certain reactions decreased due to steric difficulties to access the porphyrin cavity. Consequently, the distortion of the porphyrin core influences the photophysical characteristics of the molecule. Medforth and coworkers could demonstrate that with increased distortion the absorption and emission spectra are bathochromically shifted.⁸⁸ Additionally, the signals increase accordingly in width,⁸⁵ the quantum yields and lifetime of the fluorescence signal decreases as a result of accelerated non-radiative decay processes⁸⁹.

2.8.3 Influence of metalation

The central metal ion is chelated by the porphyrin core through coordinative bonds. The strength of this complex can be illustrated by its equilibrium constant K linked to the Gibbs free energy by: $\Delta G = -RT(\ln K) = \Delta H - \Delta S$. Therefore, the complexation strength is dependent on the temperature as well as the enthalpy and entropy.

But other factors play an even more important role, such as the size limitation for metal ions of the porphyrin core. The distance between two nitrogen atoms of a planar

free-base porphyrin without substitution is roughly 2.6 Å. Depending on the size of the metal ion, certain metals fit better into the porphyrins core than others (Figure 2.24).

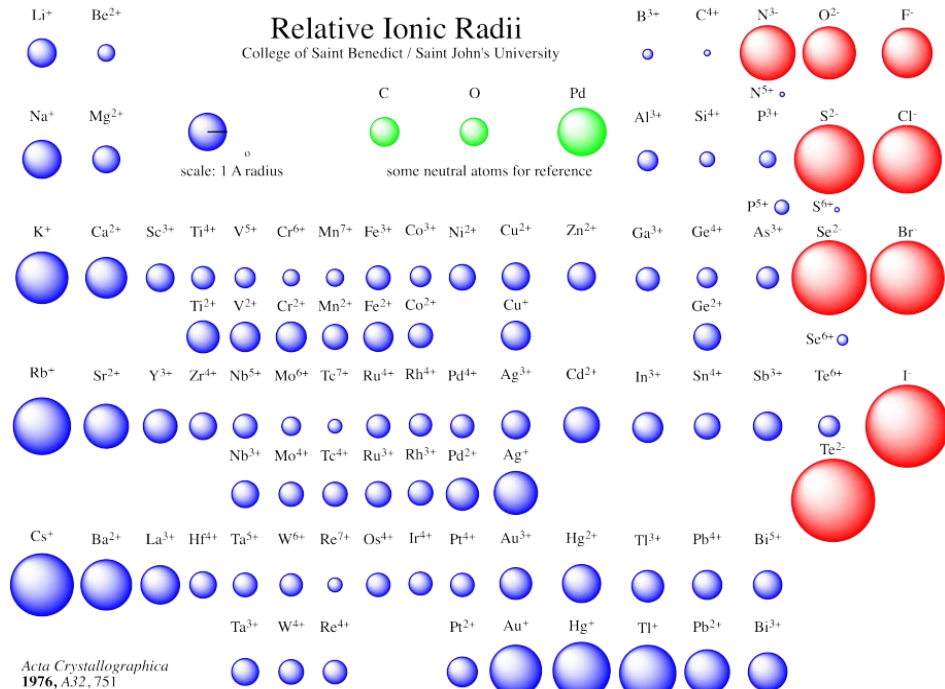
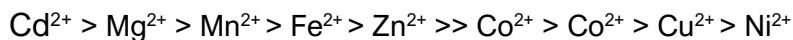


Figure 2.24: Relative ionic radii of the elements.¹²⁶

Binding of too small metal ions occur but result in shortened M-N bonds and a ruffled deformation. This is for example the case for Ni²⁺ and Cr³⁺ complexes, which lead to contraction of the coordination cavity and a therefore saddle or ruffled distortion shape. Contrary, complexes with large metal ions like Pb²⁺, form dome shaped metalloporphyrins, since these ions don't fit into the cavity of the porphyrin core and hence coordinate in a less stable way above the pyrrolic nitrogens. Also, complexes with metal ions in the porphyrin plane, but with ionic bonding like Zn²⁺ or Mg²⁺ are as well more easily to be exchanged.⁸⁴

Even if the stability of the metalloporphyrin complexes depend on a variety of factors (solvent effects etc.), a general trend for different metal ions was proposed by Hambright derived from acid solvolysis reactions ranging from weakest to highest:



This correlates with laboratory findings where porphyrins with Zn^{2+} in its core are easily demetalated by small amounts of acid at room temperature. On the other hand, Ni^{2+} porphyrins are very stable and can hardly be demetalated even under harsh reaction conditions. If the porphyrin structure prior to metalation is already distorted, similar principles apply. Therefore, a smaller cavity of a distorted porphyrin favours binding of smaller metal ions and results in increased lability when binding bigger metal ions. Hence, even if the conjugation of the porphyrin core seeks a planar shape, peripheral substituents and the size of the bound metal determine the final shape through balancing steric strains and relief thereof.⁹⁰

Due to the changes in reactivity of porphyrins based on changes in the 3D shape as a result of de- or metalation or metal-exchange, this needs to be considered during the design of the synthetic route. Hence, synthetic procedures in literature state metalation with Ni^{2+} early on during the syntheses. Since Ni^{2+} forms one of the most stable complexes, it prevents the unwanted metalation of heavy metal ions, used as catalysts, and ensures ease of reaction and following workup. On the downside, the stability of this metalloporphyrin is high and demetalation challenging. Therefore, Zn^{2+} has often been employed as a placeholder and later on been exchanged with the final metal ion.

Since the type of metal ion also affects the shape of the porphyrin and leads to significant distortion, the photophysical character is accordingly affected. Taking the corresponding free-base as reference, a planar porphyrin being out-of-plane distorted upon binding of a metal ion displays a bathochromically shifted absorption spectrum. A nonplanar porphyrin that is in-plane distorted upon binding of a metal ion shows a hypsochromically shifted absorption spectrum. Demetalation and protonation of the free-base follows the same principles. In the case of protonation of a planar free-base porphyrin, the resulting dication's cavity is now more crowded and therefore reliefs the strain by out-of-plane distortion, often of the saddle type, which is visible by a redshifted absorption.⁹¹

Porphyrin distortion result in decreased fluorescence yields and shorter lifetimes of the lowest excited state due to faster intersystem crossing and internal conversion rates. This is of particular interest for the utilization of the TTA-UC process. Therefore, the ISC rate should be high to ensure a densely populated triplet state of the sensitizer dye. Porphyrins coordinating Pd^{2+} or Pt^{2+} ions fulfil this requirement. Given the high oxidation potential of Pt-porphyrins, TTA-UC porphyrins are usually metalated with Pd^{2+} ions.

2.8.4 Solubility and aggregation

Upon increased size of a macrocycle, the system becomes more prone to poor solubility and aggregation. An attempt to circumvent the solubility problem is by introduction of peripheral long hydrocarbons or bulky groups to increase the solubility in organic solvents. The aggregation phenomenon stems from π - π -stacking forming either J-aggregates or H-aggregates.⁹² The single members of the H-aggregates are face to face aligned, like stacked plates, the ones of the J-aggregates are edge to edge aligned, like shifted plates (Figure 2.25).

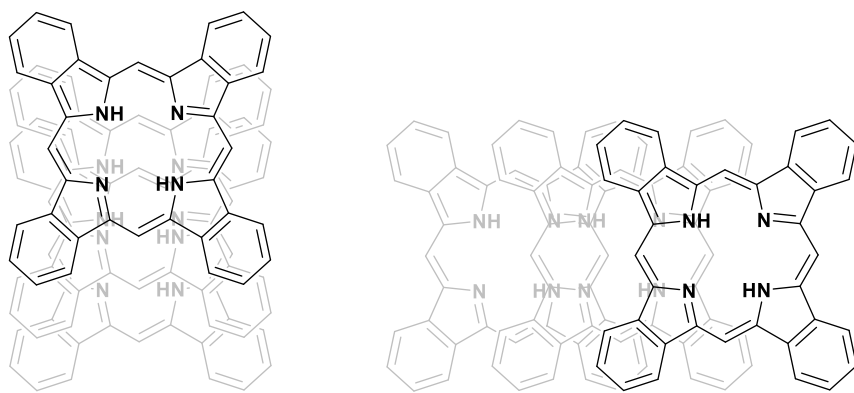


Figure 2.25: Exemplary tetrabenzoporphyrin in H-aggregation (left) and in J-aggregation (right).

This reversible self-assembly is driven by π - π dispersive interactions between polarizable groups and depends highly on the concentration and temperature.⁹³ Since these clusters of dye molecules are highly ordered, the absorption and emission band are very narrow and shifted in regard to the not aggregated species. J-aggregates are bathochromically shifted, H-aggregates hypsochromically. Planar porphyrins are prone to form H-aggregates. Distorted porphyrins are likely to show J-type aggregation.⁹⁴ The assembly for these three-dimensional structures lead to partial quenching of the phosphorescence signal potentially attribute to solubility issues.

2.8.5 Redshift of triplet levels

The influence of the porphyrin's structure on its photophysical characteristics can be used to fine tune the absorption and emission signals of dyes when taking advantage of the TTA-UC process. The need for chromophores absorbing in the NIR or IR region for photovoltaic or biomedical purposes gave rise to a new family of organic chromophores.

The challenging question is how to alter already very well working porphyrin dyes, so the absorption and emission lies in the desired NIR or even IR region. In the previous chapters some principles have already been introduced. Metalation with Pd^{2+} is the predefined metal ion as the TTA-UC process requires a high ISC rate to generate a highly populated triplet level. Substitution in *meso*-position ensures not only solubility, but also results in distortion of the porphyrin molecule, which manifests in a redshift of the absorption and emission signals.

Cheprakov and Filatov could show that free-base porphyrin displays an increased redshift upon increased extension of the π -system.^{35,85} Here, addition of the benzo-group in β -position manifests in a shift of the Q-band maximum by 100 nm without loss of intensity, seen relatively to the Soret-band, actually, even an increase thereof. On the other hand, the Soret band shifts in much smaller degree, only by about 25 nm (Figure 2.26). This arising optical window is of particular interest for applications with TTA-UC processes, since the delayed fluorescence signal can fit without reabsorption of the generated signal. These changes of the photophysical characteristics are once more attributed to the steric repulsion between annealed benzo groups and the substituents in *meso*-position. X-ray measurements revealed saddle type distortion, while the nitrogen atoms in the cavity and the four *meso*-carbons lie in a plane. Hence, the aromaticity of the system is preserved and the Soret-band absorption changes only slightly (maximal 40 nm). The Q-bands then again show a drastic bathochromic shift which has been reported for linearly fused acenes.

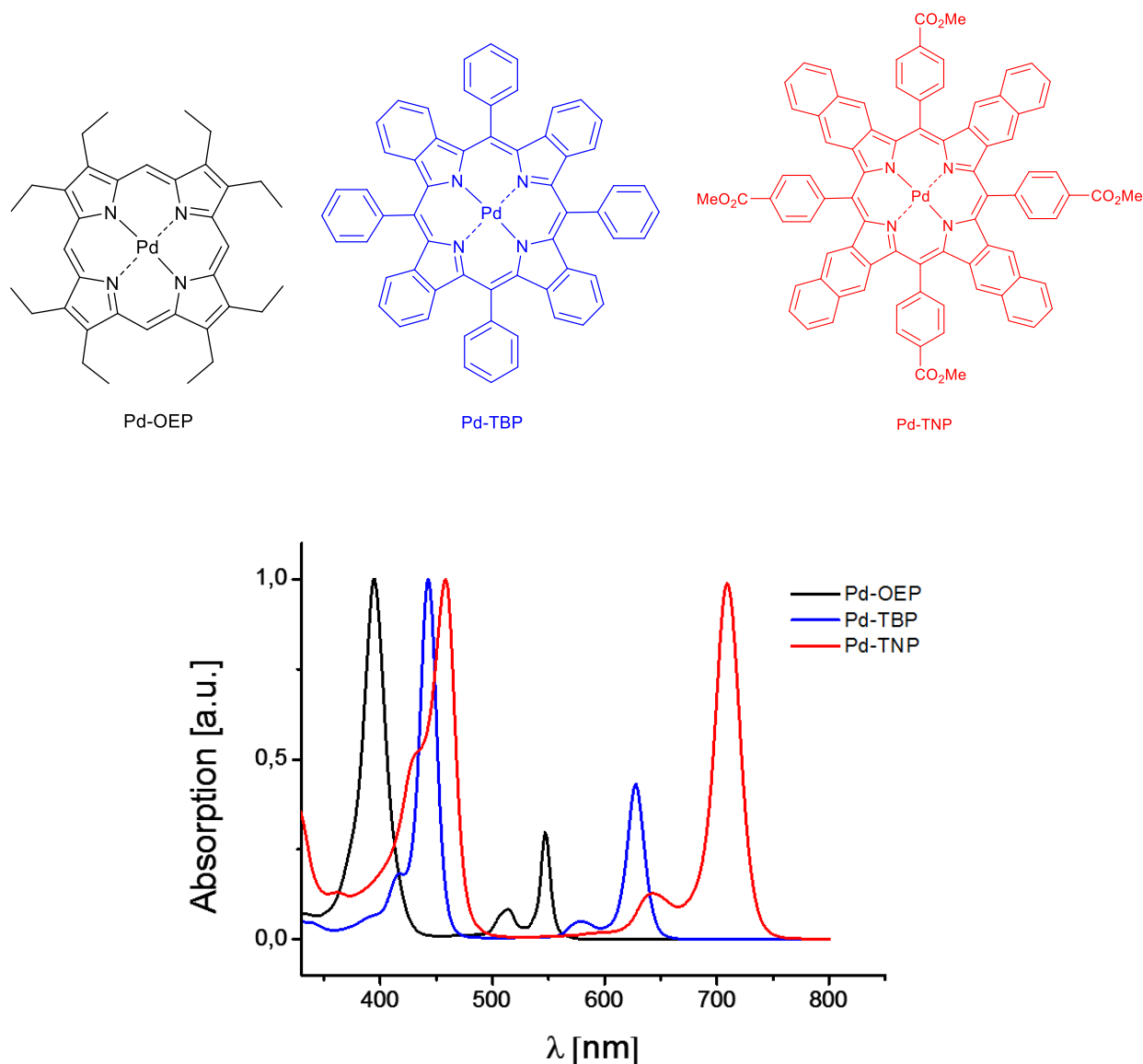


Figure 2.26: Absorption spectra of palladium-octaethylporphyrin (Pd-OEP, black), palladium-tetrabenzoporphyrin (Pd-TBP, blue) and palladium-tetranaphthophorphyrin (Pd-TNP, red).

In order to understand this behaviour, a closer inspection of the energetic levels is necessary. Figure 2.27 shows the HOMO and LUMO levels of alkenes with increased conjugation. It becomes obvious that with increased conjugation, the energy levels split accordingly and the HOMO LUMO gap shrinks. Hence the energy needed to excite the electrons from the ground state to the first excited state decreases, shifting the absorption signal bathochromically. Thus, extension of the conjugated π -system results in red shift of the absorption and emission wavelengths.⁹⁵

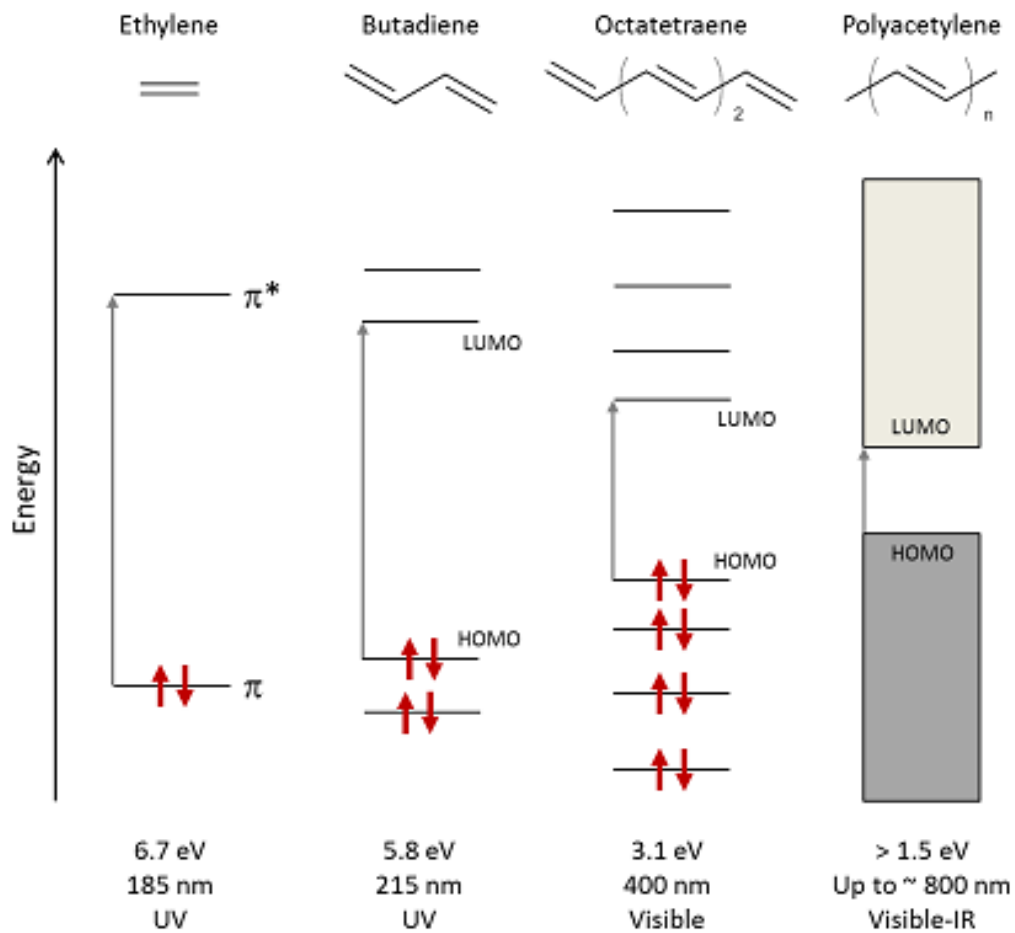


Figure 2.27: HOMO and LUMO levels of alkenes with increasing conjugation length.⁹⁵

This linear extension is limited though. Cheprakov and Filatov found anthracene moieties with covalently bound oxygen. Here depopulation of the triplet level of the porphyrin through triplet oxygen resulted in singlet oxygen species. These are very reactive and undergo a [4+2] Diels-Alder reaction forming four endoperoxide bridges and altering the photophysical characteristics of the tetraanthraporphyrin.³⁵

Expansion of the conjugated π -system can also be achieved through fusion of meso-substituents to the core porphyrin structure. The group of Osuka et al. reported azulene-fused porphyrins.⁹⁶ As expected the absorption signals are bathochromically shifted corresponding with the amount of azulene molecules annealed (Figure 2.28). The width of the absorption maxima depends on the type fused of molecule. In the case of azulene the signal is quite broad, whereas in the case of fused anthracene moieties the signals are sharper and additionally more intensive. On the downside such large fused

systems are synthetically difficult to achieve due to low solubility and problematic fusion under harsh conditions.^{97,98}

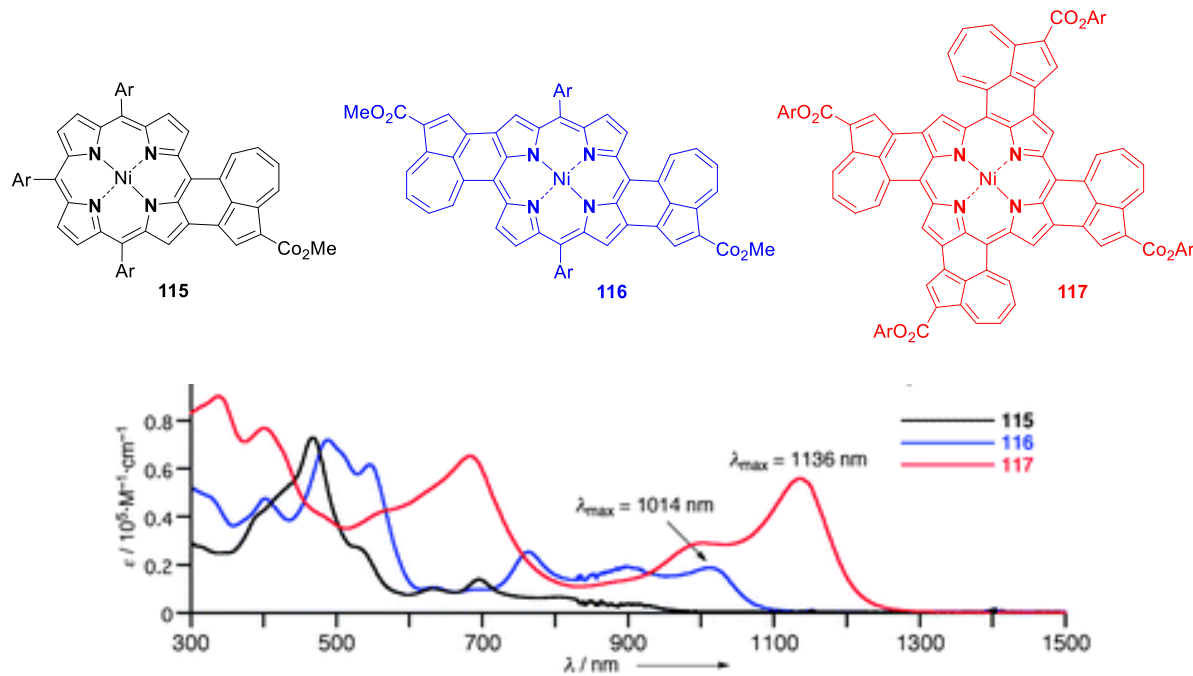


Figure 2.28: Nickel-porphyrin with one, two or four azulene moieties fused resulting in red-shifted absorption spectrum (modified picture).⁹⁷

3 Motivation

Solar energy storage and conversion is a key technology for the future realization of a sustainable energy production worldwide. Unfortunately, solar cells can only harvest wavelengths in the visible region. Attempts to maximize the utilizable electromagnetic range into the deep-red and IR-region have been unsuccessful since these energies are too low to initiate an electric current within the solar cell.^{51,52} Here, traditional solar cells with the addition of custom tailored organic dyes combined with the TTA-UC process, could be a clever solution. By absorbing photons from the deep-red region and upconverting them to the visible region, the area of utilized wavelengths is broadened, while commercially available solar harvesting devices stay in their particular operating characteristics unchanged. In order to maximize the newly utilized deep-red spectral range, the sensitizer dye should depict a broad absorption area. This can be achieved by stepwise extension of the conjugated π -system by annulation, resulting in slight bathochromic shifts of the Q-band absorption maximum. Therefore, the goal is the design and syntheses of organic dyes applicable in a TTA-UC process, showing a broad absorption range in the deep-red sunlight region.¹² Accompanying, this asks for the creation of matching emitters. Precise overlap of the triplet levels of the chromophore pair will ensure best chances for the maximized quantum yield of the TTA-UC process. Here fine tuning of the photophysical characteristics of the emitter dye can be done by a mixed pyrrole condensation strategy, previously known for porphyrins⁹⁹ with benzo-annulation on a pyrrole ring.

Besides sustainable energy production the modern society faces other challenges, such as the rising number of cancer related deaths. Alone in 2011, the World Health Organization reported that approximately 508 000 women died due to breast cancer.¹⁰⁰ Therefore it is crucial to determine the patient's cancer stage and approximate the survival chances or as a part of a check-up after cancer remission. Up to now the sentinel lymph node biopsy (SLNB) is performed for detection of possible lymph node metastases. This is not only a surgical procedure with all its risk, but also not extensively repeatable. Here the European Hyposens projects aims to develop a nano-confined photonic system which minimally invasive detects the oxygen concentration and temperature of cells. These are important markers for the health of cells and their potential mutation into cancerous cells.⁶¹ For this diagnostic tool, organic dyes play once again a crucial role, since their luminescence is highly dependent on environmental factors. Employing the TTA-UC

method the dyes luminescence give insight to the oxygen and temperature levels within cells, simultaneously and independently. Therefore, to the standard TTA-UC parameters for the design of chromophores, additional criteria arise. For instance, all materials need to be biocompatible, the excitation wavelength for the sensitizer dye, its residual phosphorescence and delayed fluorescence from the emitter dye need to fit within the tissue transparency window and a sufficient penetration depth needs to be ensured.⁶⁸ This ultimately leads to the design idea of a Pd-metallated porphyrin-based dye as the sensitizer, which absorbs in the near IR-region, providing maximum penetration depth, least amount of photophysical damage and pin pointing all absorption and emission signals within the tissue transparency window. The necessary IR-absorption of the sensitizer should be achieved by enlargement of the conjugated π -system resulting in a bathochromic shift via fusion of phenyl-anthracene moieties attached to two *meso*-positions of the porphyrin core. The solubility is ensured by attaching 3,5-di-*tert*-butylphenyl moieties to the remaining two *meso*-positions. Accompanying, emitter molecules used for subcutaneous sensing need to be designed so their delayed fluorescence is located within the tissue transparency window.

4 Results and discussion

4.1 Mixed porphyrin

In order to maximize the utilizable sunlight spectrum of traditional solar cells while keeping their existing operating characteristics, the implementation of organic dyes able to be used for the TTA-UC process is desired. Therefore, the following chapter focusses on the preparation of these organic dyes, which possess a characteristic broad absorption in the deep-red region. This is achieved by the synthesis of precursor molecules via the stepwise annulation method and their assembly yielding a mixed benzo-naphtho and naphtho-antra porphyrin family. The measurement of luminescence spectra were performed by [REDACTED]. The work presented in this chapter has been published in the Journal of Photonics for Energy, Volume 8 (2), pages 022002-1 – 022002-14, 6 November 2017, Copyright (2019).

4.1.1 Syntheses of precursors

The synthesis of mixed porphyrins is based on assembly of buildings blocks, benzo- **B**, naphtho- **N** and anthra- **A** isoindole (Figure 4.1).

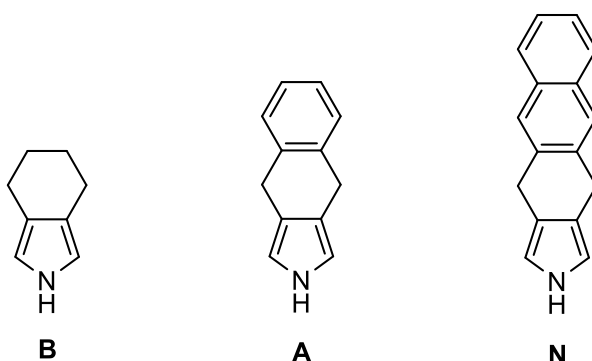


Figure 4.1: Benzo- **B**, naphtho- **N** and anthra-isoindole **A** building blocks as precursors for mixed porphyrins.

4.1.1.1 Benzo-building block

The preparation of the benzo-building block is depicted in Figure 4.2. First cyclohexane **1** and methylformate were introduced within 10 min to a solution of sodium in methanol. After stirring over night at room temperature, 2-formylcyclohexanone sodium salt **2** could be precipitated by adding diethyl ether in 62% yield.

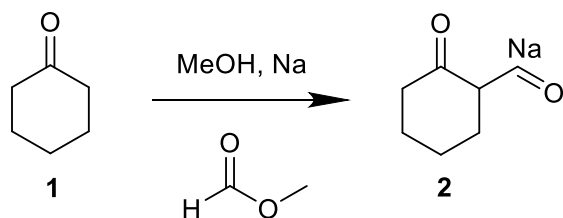


Figure 4.2: Synthesis of 2-formylcyclohexanone sodium salt **2** from cyclohexanone **1**.

Consecutively, the sodium salt **2** was dissolved in ethanol, glycine-ethyl-ester-hydrochloride introduced to the solution and the reaction was stirred at room temperature overnight. Evaporation of the solvent under reduced pressure resulted in the enamin ethyl-((2-oxocyclohexylidene)methyl)glycinate **3** in 70% yield (Figure 4.3).

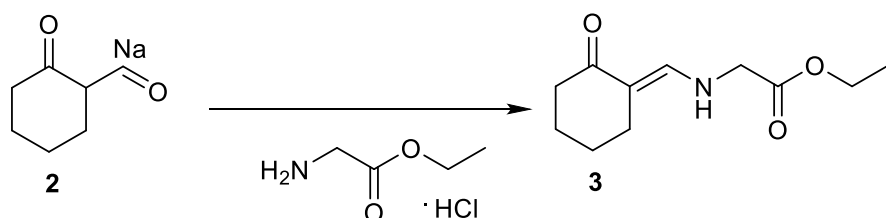


Figure 4.3: Synthesis of the enamin ethyl-((2-oxocyclohexylidene)methyl)glycinate **3** from 2-formylcyclohexanone sodium salt **2**.

Following, ethyl-((2-oxocyclohexylidene)methyl)glycinate **3** was added to a solution of sodium in ethanol and the reaction mixture was heated at 40 °C for 5 h. Extraction with DCM, evaporation of the organic phase under vacuum and recrystallization gave the enamin ethyl-4,5,6,7-tetrahydro-2*H*-isoindole-1-carboxylate **4** in 30% yield (Figure 4.4).

The introduction of the ethyl-ester group is important, since it protects the isoindole from unwanted oxidation during longer storage time by suppressing the occurrence of the hydroperoxide derivative.

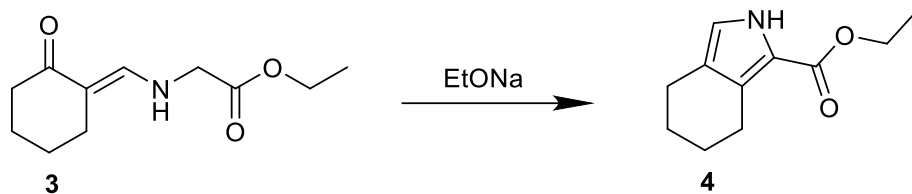


Figure 4.4: Synthesis of ethyl-ester-protected 4,5,6,7-tetrahydro-2H-isoindole **4** from ethyl-((2-oxocyclohexylidene)methyl)glycinate **3**.

The $^1\text{H-NMR}$ spectrum shows the matching signals for ethyl-4,5,6,7-tetrahydro-2H-isoindole-1-carboxylate **4** (Figure 4.5). Here the secondary amine group's proton can be found around 8.87 ppm as a broad signal. The protective group's proton signals are located from 1.77 until 1.29 ppm.

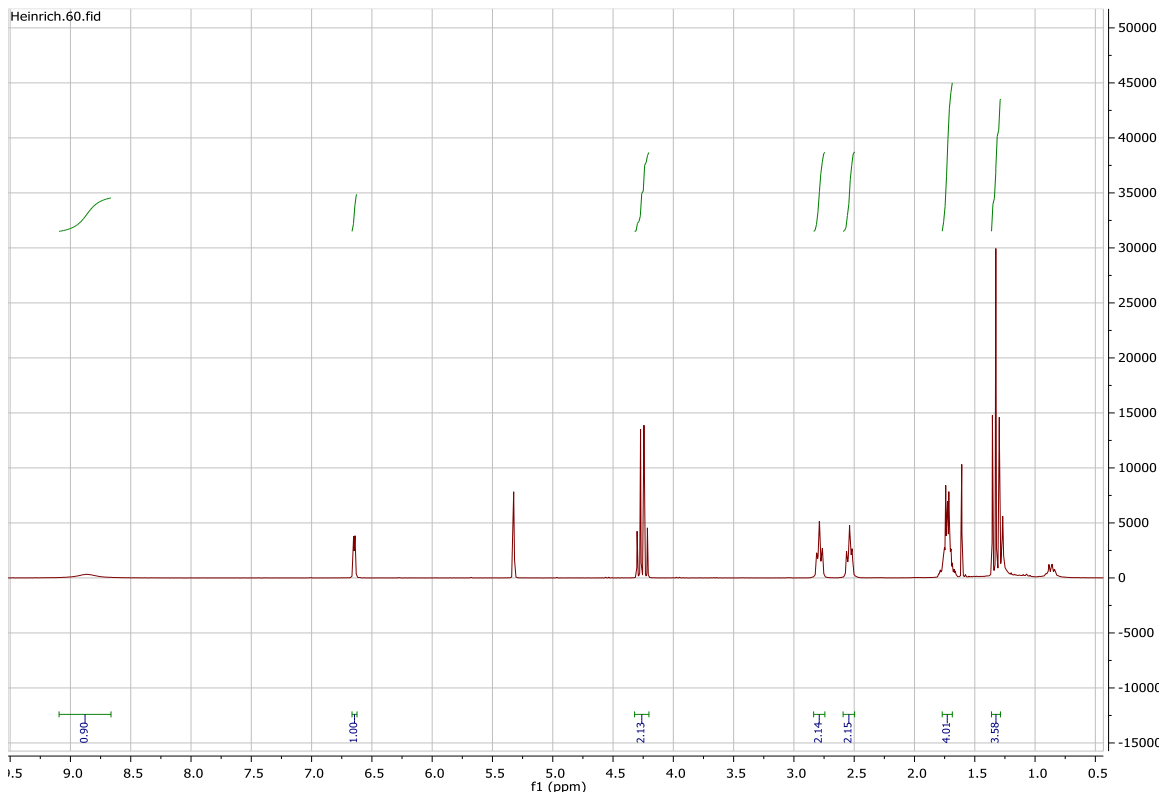


Figure 4.5: $^1\text{H-NMR}$ spectrum of ethyl-4,5,6,7-tetrahydro-2H-isoindole-1-carboxylate **4**.

Before further use ethyl-4,5,6,7-tetrahydro-2H-isoindole-1-carboxylate **4** must be decarboxylated by boiling in ethylenglykol with potassiumhydroxide for 1 h under inert atmosphere. Washing with water, evaporation of the organic solvent and flash chromatography gave 4,5,6,7-tetrahydro-2H-isoindole **B** in 67 % yield (Figure 4.6).

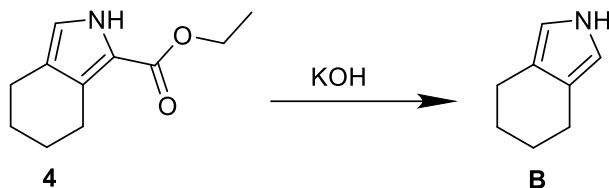


Figure 4.6: Decarboxylation of ethyl-4,5,6,7-tetrahydro-2H-isoindole-1-carboxylate **4** yielding 4,5,6,7-tetrahydro-2H-isoindole **B**.

4.1.1.2 Naphtho-building block

The starting material for the naphtho-building block was naphthalene **5**. It was hydrogenated by stirring in a solution of sodium lumps dissolved in ethanol and subsequent extraction with DCM. Liquid 1,4-dihydronaphthalene **6** was obtained in 80% yield (Figure 4.7).

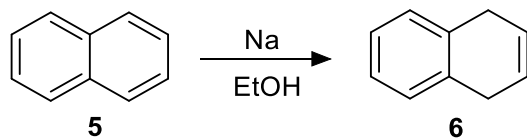


Figure 4.7: Hydration of naphthalene **5** forming 1,4-dihydronaphthalene **6**.

Phenylsulfenylchloride **8**, necessary for the next step, was freshly prepared by chlorination of thiophenol **7** with N-chlorosuccinimide (NCS) in DCM under argon atmosphere within 30 min (Figure 4.8) and immediate utilization.

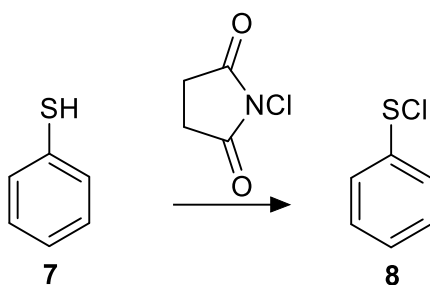


Figure 4.8: Preparation of phenylsulfenylchloride **8** from thiophenol **7** with NCS.

The resulting phenylsulfenylchloride **8** was added slowly to 1,4-dihydronaphthalene **6** in DCM and stirred for 30 min yielding 90% (3-chloro-1,2,3,4-tetrahydronaphthalen-2-yl)(phenyl)sulfane **9** (Figure 4.9).

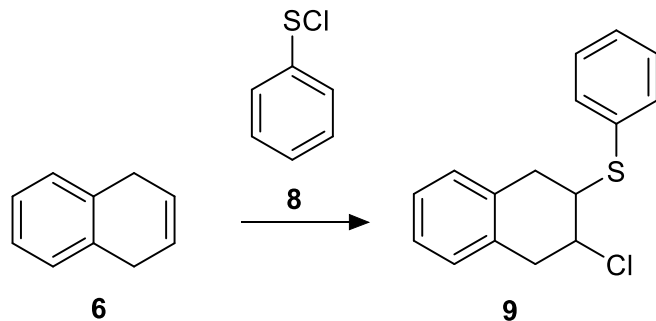


Figure 4.9: Addition of phenylsulfenylchloride **8** to 1,4-dihydronaphthalene **6** forming (3-chloro-1,2,3,4-tetrahydronaphthalen-2-yl)(phenyl)sulfane **9**.

The oxidation of the sulfan **9** leading to a sulfone **10** was performed by dissolving (3-chloro-1,2,3,4-tetrahydronaphthalen-2-yl)(phenyl)sulfane **9** in THF, cooling the solution down to 0 °C and adding an oxone in water solution. Afterwards the mixture was allowed to stir at room temperature for two days. Afterwards extraction with DCM and evaporation

of the solvent under vacuum and recrystallization gave yellowish 2-chloro-3-(phenylsulfonyl)-1,2,3,4-tetrahydronaphthalene **10** in 57% yield (Figure 4.10).

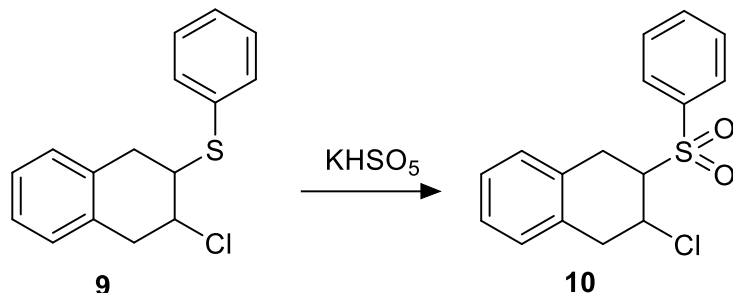


Figure 4.10: Oxidation of (3-chloro-1,2,3,4-tetrahydronaphthalen-2-yl)(phenyl)sulfane **9** to 2-chloro-3-(phenylsulfonyl)-1,2,3,4-tetrahydronaphthalene **10**.

In order to eliminate the chlorine-group 2-chloro-3-(phenylsulfonyl)-1,2,3,4-tetrahydro-naphthalene **10** was dissolved in DCM, 1,8-diazabicyclo[5.4.0]undec-7-ene (DBU) was added and the reaction mixture stirred for 30 min resulting in 2-(phenylsulfonyl)-1,2-dihydro-naphthalene **11** in 56% yield after recrystallization from ethanol (Figure 4.11).

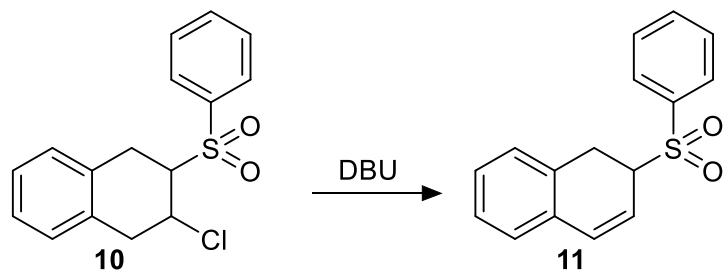


Figure 4.11: Elimination of chlorine from 2-chloro-3-(phenylsulfonyl)-1,2,3,4-tetrahydro-naphthalene **10** to form 2-(phenylsulfonyl)-1,2-dihydronaphthalene **11**.

The pyrrole forming Barton-Zard-reaction was performed by adding *t*-butyl-cyanoacetate to *tert*-butoxide in THF and 2-(phenylsulfonyl)-1,2-dihydronaphthalene **11**, followed by 2 h of stirring. Washing and evaporation of the solvent and recrystallization from ethanol gave the *t*-butyl ester protected 4,9-dihydro-2*H*-benzo[*A*]isoindole **12** in 43% yield (Figure 4.12).

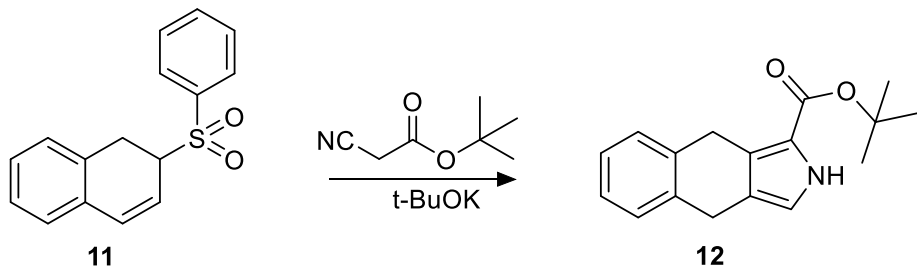


Figure 4.12: Barton-Zard-reaction of 2-(phenylsulfonyl)-1,2-dihydro-naphthalene **11** with t-butyl-cyanoacetate forming t-butyl-4,9-dihydro-2H-benzo[*f*]isoindole-1-carboxylate **12**.

The $^1\text{H-NMR}$ spectrum shows the matching signals t-butyl-4,9-dihydro-2H-benzo[*f*]isoindole-1-carboxylate **12** (Figure 4.13). Here the secondary amine group proton can be found around 9.12 ppm as a broad signal. The protective group's proton signals are located around 1.29 ppm.

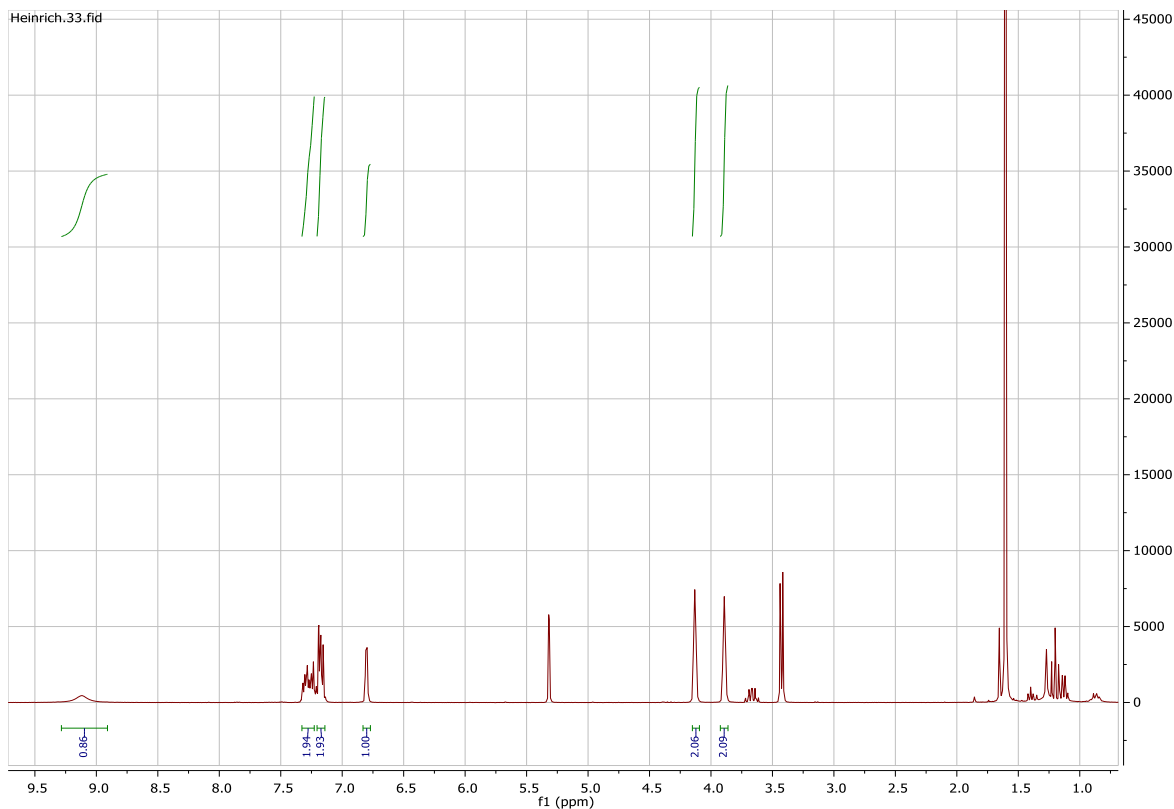


Figure 4.13: $^1\text{H-NMR}$ spectrum of t-butyl 4,9-dihydro-2H-benzo[*f*]isoindole-1-carboxylate **12**.

Here again, before further use the protected naphtho-building block must be decarboxylated by boiling in ethylenglykol with potassiumhydroxide for 1 h under inert atmosphere giving 4,9-dihydro-2*H*-benzo[*J*]isoindole **N** in 67% yield after flash chromatography (Figure 4.14).

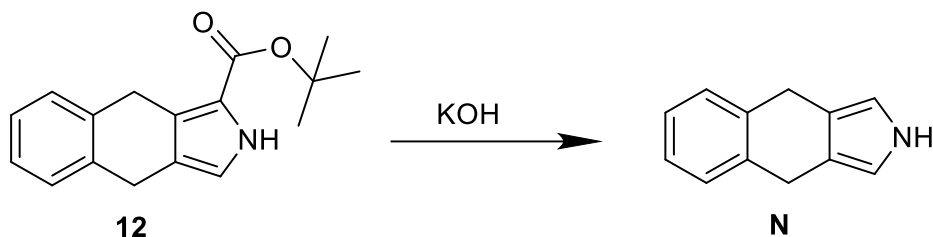


Figure 4.14: Deprotection of *t*-butyl 4,9-dihydro-2*H*-benzo[*J*]isoindole-1-carboxylate **12** forming the naphto- building block 4,9-dihydro-2*H*-benzo[*J*]isoindole **N**.

4.1.1.3 Anthra-building block

The starting material for the anthra-building block is 1,2-dibromobenzene **13**, which reacts with furan **14** in THF in a [2+4] type Diels-Alder-reaction at -50 °C under argon atmosphere with carefully added n-BuLi in hexane. After stirring for 30 min, the mixture was allowed to reach room temperature and the solvents were evaporated under reduced pressure affording 4-dihydro-1,4-epoxynaphthalene **15** in 86% yield (Figure 4.15).

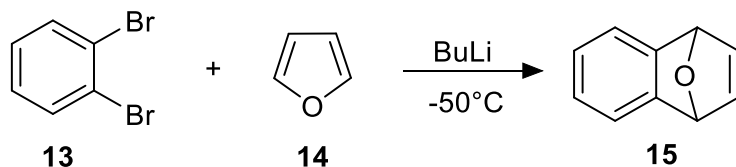


Figure 4.15: Diels-Alder-reaction of 1,2-dibromobenzene **13** and furan **14** forming 1,4-dihydro-1,4-epoxynaphthalene **15**.

A following [2+2] type Diels-Alder-reaction of 1,4-dihydro-1,4-epoxynaphthalene **15** and 3-sulfolene **16** was performed in a high-pressure glass flask at 120 °C in the presence of NaHCO₃ and pyridine resulting in 1,4,4a,9,9a,10-hexahydro-9-10-epoxyanthracene **17**

in 48% yield after filtration, evaporation of the solvent and flash chromatography with DCM (Figure 4.16).

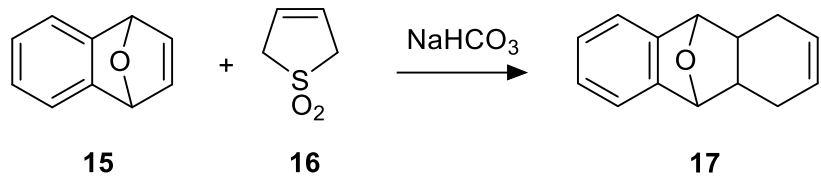


Figure 4.16: Diels-Alder-reaction of 1,4-dihydro-1,4-epoxynaphthalene **15** and 3-sulfolene **16** forming 1,4,4a,9,9a,10-hexahydro-9-10-epoxyanthracene **17**.

The subsequent dehydration of 1,4,4a,9,9a,10-hexahydro-9-10-epoxyanthracene **17** was achieved by refluxing the ethanol dissolved solution overnight in the presence of concentrated hydrochloric acid. The recrystallized crude mixture afforded 56% 1,4-dihydroanthracene **18** (Figure 4.17).

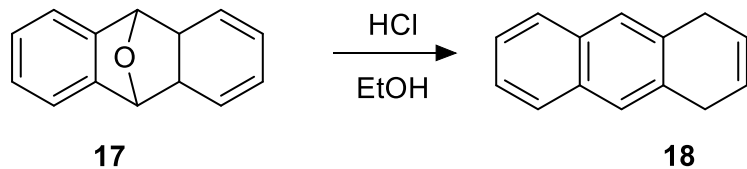


Figure 4.17: Synthesis of 1,4-dihydroanthracene **18** from 1,4,4a,9,9a,10-hexahydro-9-10-epoxyanthracene **17**.

Subsequently, 1,4-dihydroanthracene **18** was transformed into (3-chloro-1,2,3,4-tetrahydroanthracene-2-yl)(phenyl)sulfane **19** through reaction with freshly prepared phenylsulfenylchloride **8**, which was prepared as described for the naphto-building block (Figure 4.18).

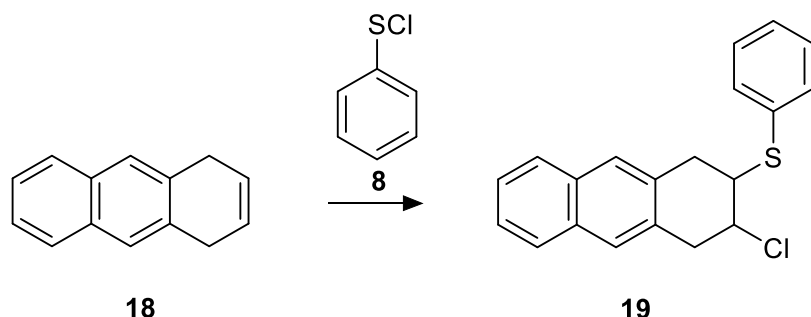


Figure 4.18: Addition of phenylsulfenylchloride **8** to 1,4-dihydroanthracene **18** forming (3-chloro-1,2,3,4-tetrahydroanthracene-2-yl)(phenyl)sulfane **19**.

Accordingly, sulfan **19** in THF reacted with oxone in water within two days of stirring, resulting in the sulfon 2-chloro-3-(phenylsulfonyl)-1,2,3,4-tetrahydroanthracene **20** in 55% yield after recrystallization from ethanol (Figure 4.19).

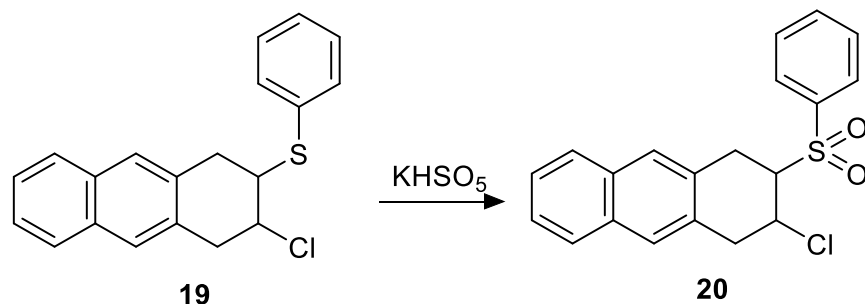


Figure 4.19: Oxidation of (3-chloro-1,2,3,4-tetrahydroanthracene-2-yl)(phenyl)sulfane **19** to 2-chloro-3-(phenylsulfonyl)-1,2,3,4-tetrahydroanthracene **20**.

The elimination of the chlorine group was performed via stirring of 2-chloro-3-(phenylsulfonyl)-1,2,3,4-tetrahy-droanthracene **20** in DCM after addition of DBU for 30 min. Recrystallization from ethanol gave 2-(phenylsulfonyl)-1,2-dihydroanthracene **21** in 72% yield (Figure 4.20).

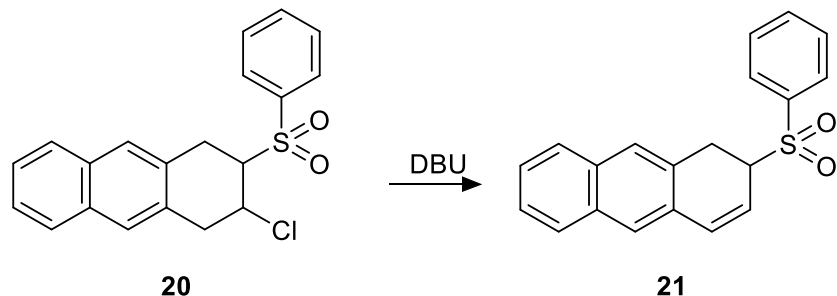


Figure 4.20: Elimination of chlorine from 2-chloro-3-(phenylsulfonyl)-1,2,3,4-tetrahydroanthracene **20** to form 2-(phenylsulfonyl)-1,2-dihydroanthracene **21**.

The last step yielding ethyl 4,11-dihydro-2*H*-naphtho[2,3-*J*]isoindole-1-carboxylate **21** is once more the Barton-Zard-Reaction. Hereby, the 2-(phenylsulfonyl)-1,2-dihydroanthracene **21** is stirred with ethyl-2-cyanoacetate for 2 h under basic conditions (Figure 4.21). The product ethyl 4,11-dihydro-2*H*-naphtho[*J*]isoindole-1-carboxylate **22** (53% yield after recrystallization from ethanol) is characterised by the ¹H-NMR spectrum shown in Figure 4.22. Here the secondary amine group's proton can be found around at 8.22 ppm as a broad signal. The protective group's proton signals are located at around 1.20 to 1.10 ppm.

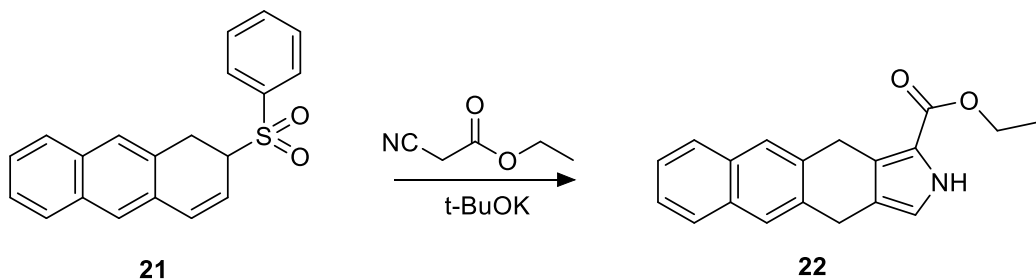


Figure 4.21: Barton-Zard-reaction of 2-(phenylsulfonyl)-1,2-dihydroanthracene **21** with ethyl-2-cyanoacetate forming ethyl 4,11-dihydro-2*H*-naphtho[2,3-*J*]isoindole-1-carboxylate **22**.

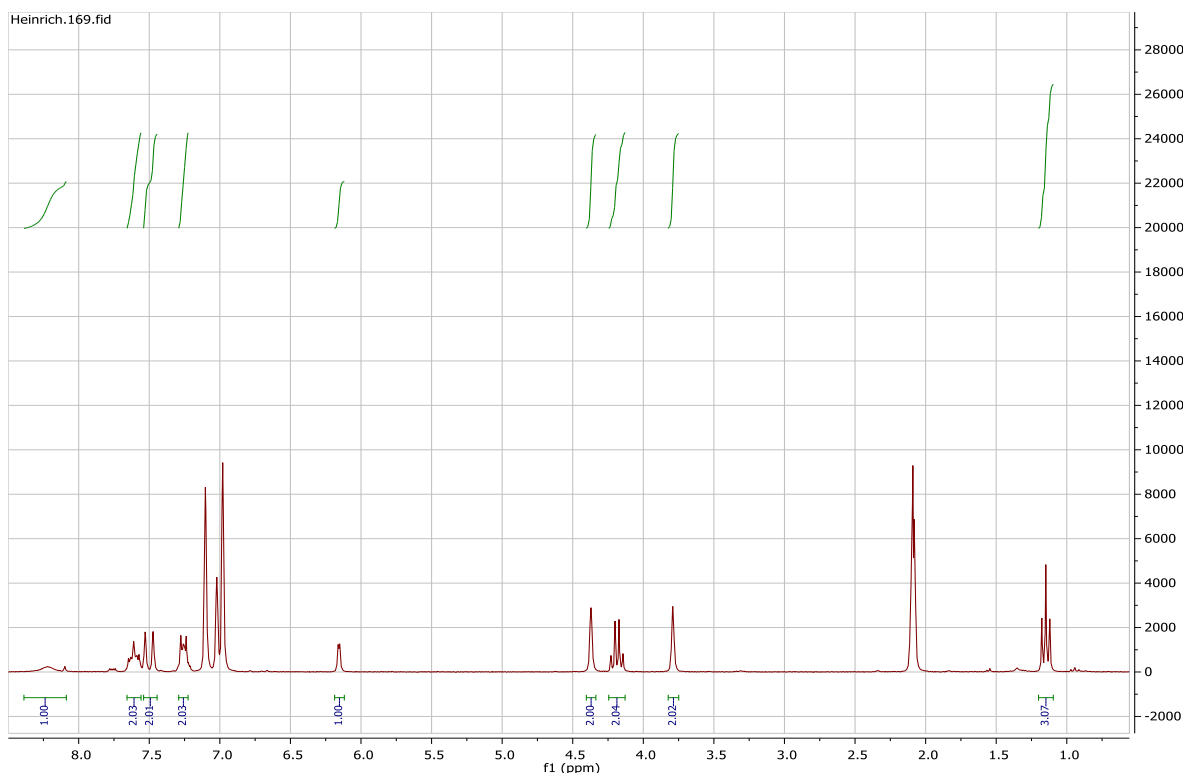


Figure 4.22: ¹H-NMR spectrum of ethyl 4,11-dihydro-2H-naphtho[1,2-f]isoindole-1-carboxylate **22**.

Here again, before further use, the protected anthra-building block must be decarboxylated by boiling in ethylenglykol with potassiumhydroxide for 1 h under inert atmosphere. Cooling down to room temperature, washing with water, concentration of the organic layer until beginning precipitation and flash chromatography yielded 61% 4,11-dihydro-2H-naphtho[2,3-f]isoindole **A** (Figure 4.23).

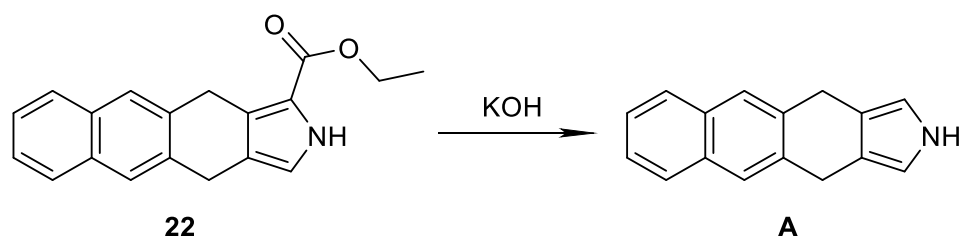


Figure 4.23: Deprotection of ethyl 4,11-dihydro-2H-naphtho[1,2-f]isoindole-1-carboxylate **22** forming the anthra- building block 4,11-dihydro-2H-naphtho[2,3-f]isoindole **A**.

4.1.2 Mixed benzo-naphtho porphyrin family

The isolation of the individual porphyrins with fixed number of benzo- and naphtho-mieties from the mixture can be achieved by two routes. First is the isolation of free-base porphyrins by chromatography and the metal insertion into the individual substances. Second is the metal insertion into the porphyrins mixture and subsequent separation of the metalloporphyrins. Using the first route, only the negligible amount of the target compounds could be isolated after several subsequent chromatographic separations. The second approach shows that the Pd-porphyrins move on the TLC plate and on the column as a single zone and cannot be separated. However, the mixture of Pd-porphyrins could be isolated in a high yield, showing a sharp Soret band and Q-bands forming a broad absorption band between 620 and 790 nm.

In order to prepare a mixed benzo-naphtho porphyrin family, the two precursor species, 4,5,6,7-tetrahydro-2*H*-isoindole **B** and 4,9-dihydro-2*H*-benzo[*f*]isoindole **N** and an aldehyde, 4-butylbenzaldehyde **23**, underwent a Lindsey-condensation. Therefore the starting material was dissolved in DCM and stirred for 10 min at room temperature under nitrogen atmosphere. After addition of the catalyst $\text{BF}_3\cdot\text{Et}_2\text{O}$, the mixture was stirred for 1 h, then DDQ was added and stirred for another hour. Regular workup through silica gel chromatography yielded the mixed benzo-naphtho porphyrin family **24**.

Following the assembly of the basic porphyrin structure metalation with Pd^{2+} was performed by refluxing the porphyrin family **24** with bis(benzonitrile)palladium(II)chloride and triethylamine in benzonitrile for 1 h under nitrogen atmosphere. The progress of the reaction was checked via TLC. After completion, the crude mixture was filtered and purified by silica gel chromatography yielding the mixed benzo-naphtho porphyrin family **25**.

Subsequently, the mixed porphyrin **25** was aromatized by refluxing for roughly 30 min with DDQ in THF. After complete aromatization, the mixture was worked up, the solvent evaporated under reduced vacuum, purified by silica gel chromatography and characterized by FD-mass spectroscopy (Figure. 4.24).

Results and discussion: Mixed porphyrin

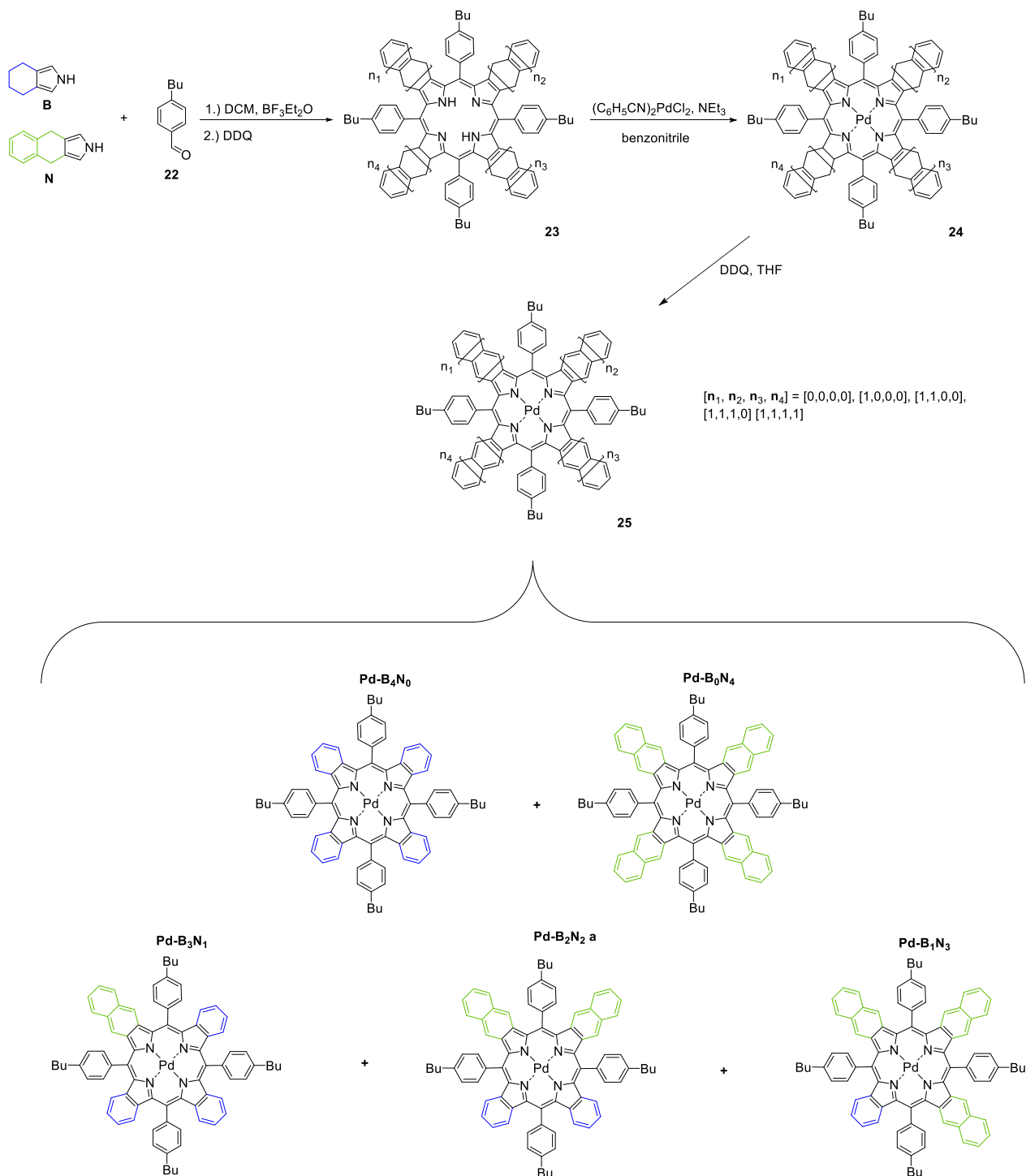


Figure 4.24: Synthetic route for obtaining the mixed benzo-naphtho porphyrin family **25**.

The mixed benzo- naphtho porphyrins **25** with varying amounts of the two precursor molecules could be isolated by HPLC. The superimposed absorption spectra of the following composition can be seen in Figure 4.27: 20% Pd-B₄N₀, 36% Pd-B₃N₁, 29% Pd-B₂N₂, 12% Pd-B₁N₃, 3% Pd-B₀N₄. Since a broad absorption is desired, isolation of the different fractions is counterproductive. The characteristic absorption area of the mixed benzo- naphtho porphyrin family is shown in Figure 4.25.

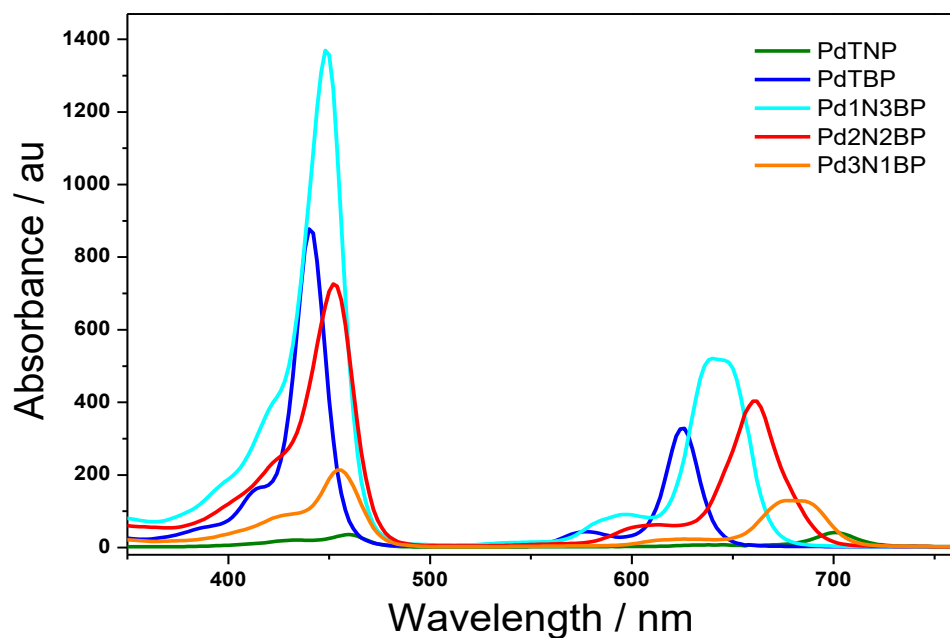


Figure 4.25: Absorption spectra of individual HPLC fractions of the mixed benzo- naphtho porphyrin family **25**.

4.1.3 Mixed naphtho- anthra porphyrin family

The procedure for the mixed naphtho- anthra porphyrin family is similar to the one described in the previous chapter. First the porphyrin core structure from the naphto- and anthra- precursors and an aldehyde are assembled via Lindsey-condensation. Therefore, a mixture of 4,9-dihydro-2H-benzo[*f*]isoindole **N**, 4,11-dihydro-2H-naphtho[2,3-*f*]isoindole **A** and 3,5-di-*tert*-butylbenzaldehyde **26** in DCM was stirred for 10 min at room temperature under nitrogen, followed by addition of the catalyst $\text{BF}_3\text{Et}_2\text{O}$ and stirring for 1 h. Subsequently DDQ was added and stirred for another hour and purified by silica gel chromatography yielding mixed naphtho- anthra porphyrin family **27**.

Second the insertion of Pd^{2+} into the core was performed by refluxing porphyrin mixture **27**, bis(benzonitrile)palladium(II)chloride and trimethylamine in benzonitrile for 1 h under nitrogen atmosphere, followed by filtration and silica gel chromatography giving metalated mixed porphyrin family **28**.

The final step, the aromatization of the mixed porphyrin **28** was carried out by refluxing with DDQ for around 30 min (Figure 4.26), followed by standard silica gel chromatography assisted purification resulting in final mixed naphto- anthra porphyrin family **29**. The characterisation with FD-Mass can be seen in Figure 4.27.

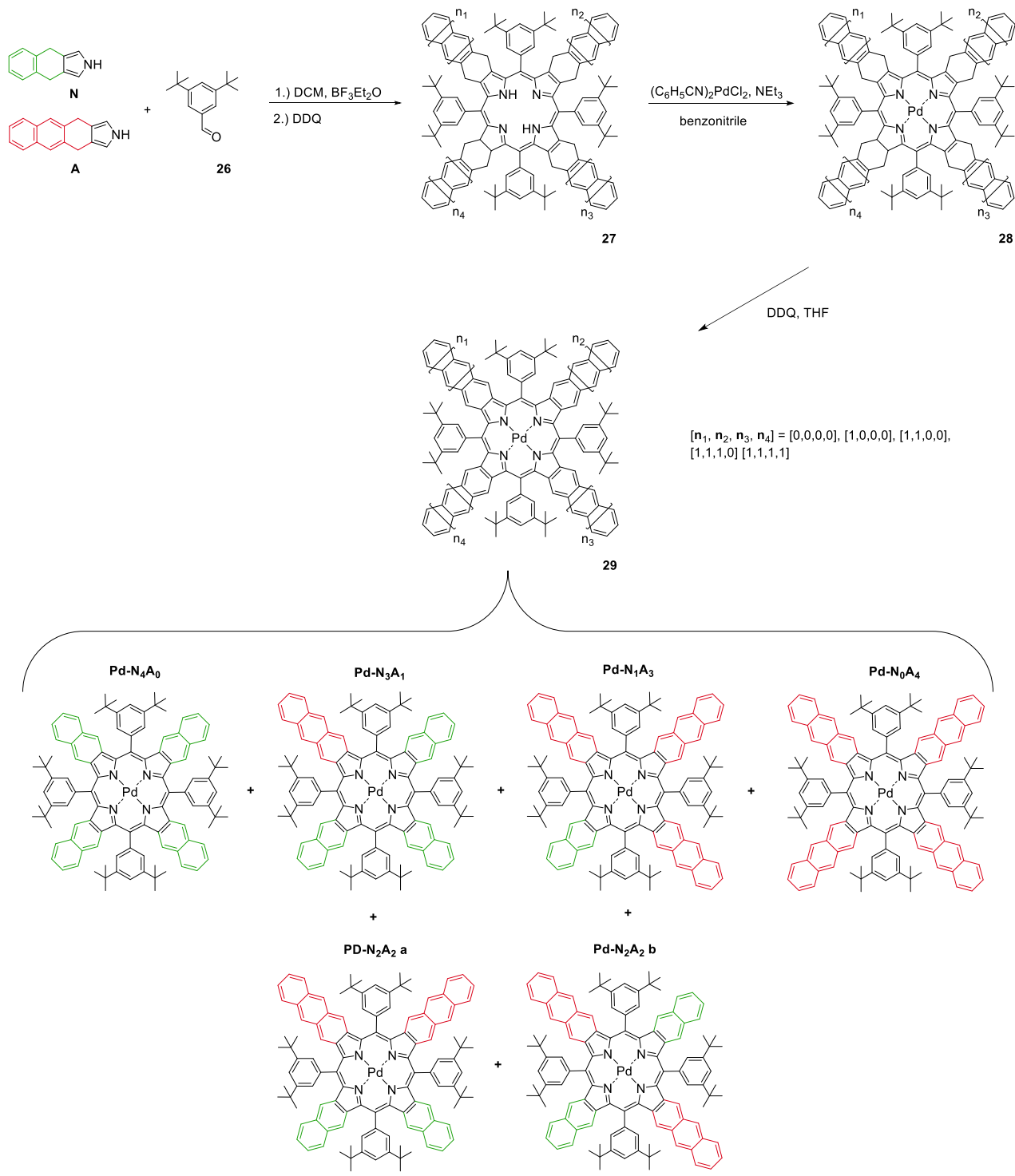


Figure 4.26: Synthetic route for obtaining the mixed naphtho-antra porphyrin family 29.

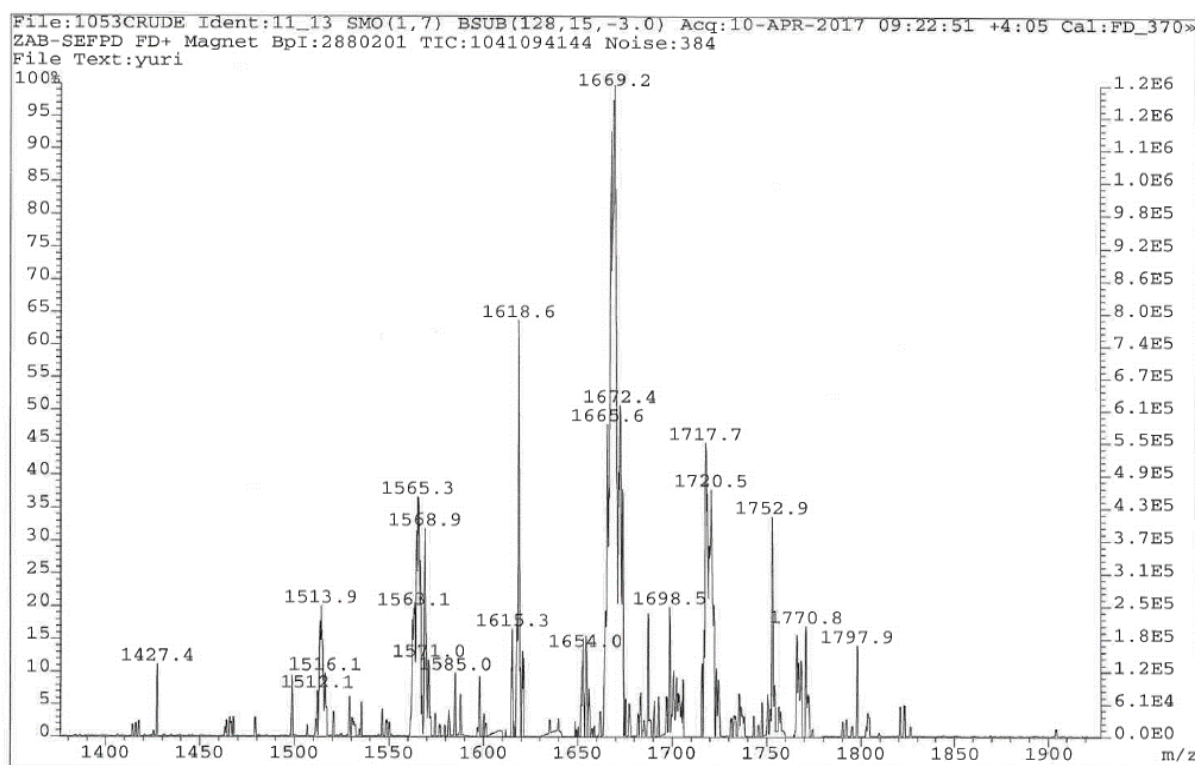


Figure 4.27: MS spectra of the mixed naphtho-antra porphyrin family **29** in toluene.

4.1.4 Application

The absorption spectra of the synthesized sensitizer families – the mixed benzo-naphtho porphyrin family **25** and mixed naphtho-antra porphyrin family **29** are shown in Figure 4.28 a and 4.28 b respectively. Variances of the absorption maxima and shape of the graph are possible since they dependent on the precise composition of the mixed porphyrin family. In the case of the mixed benzo-naphtho porphyrin family depicted in Figure 4.3 (a) the following composition was present: 20% Pd-B₄N₀, 36% Pd-B₃N₁, 29% Pd-B₂N₂, 12% Pd-B₁N₃, 3% Pd-B₀N₄.

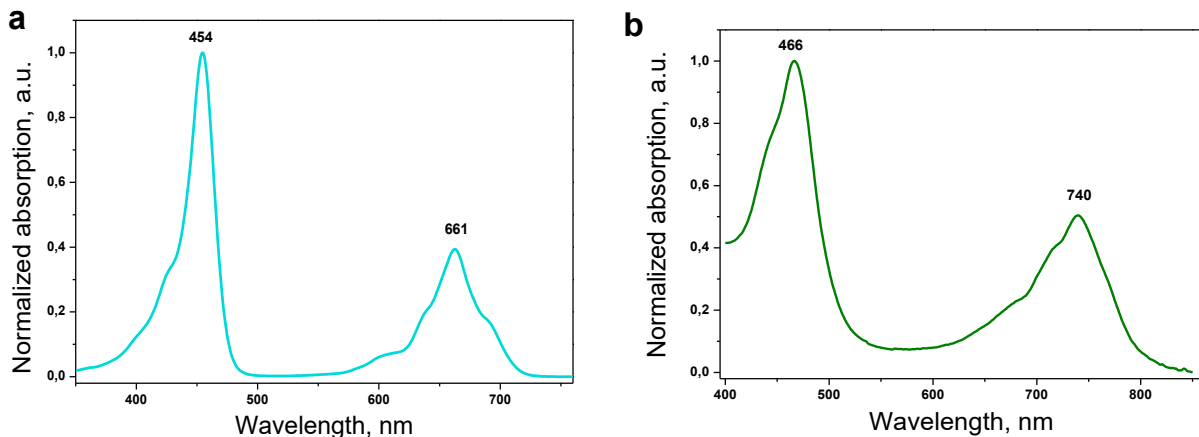


Figure 4.28: Normalized absorption spectra of (a) - mixed benzo-naphtho porphyrin family 25 and (b) - mixed naphtho-antra porphyrin family 29, both measured in toluene. These measurements were performed by [REDACTED].

For characterization of the TTA-UC systems, an experimental setup emulating sunlight excitation with low degree of concentration was used. The supercontinuum laser source (SC400-2-PP, Fianium Ltd.) delivers *quasi*-monochromatic light with mean power up to 2 W and 20 MHz repetition rate at intensity comparable with 1 \div 100 Suns (AM1.5). This light source can produce excitation spectrum with a freely chosen bandwidth. Thus, the Q-band absorption spectrum of each sensitizer can be covered completely, Figure 4.29 a. This is achieved via a 4-F monochromator and a retro-reflector equipped with mechanical optical slit for precise selection of the excitation wavelength. The spatial distribution of the excitation beam is Gaussian; TEM₀₀ mode, beam waist \sim 1300 μ m. The beam waist is controlled by Slit Scanning Beam Profiler (BP104-VIS, Thorlabs Inc.). The emission spectra were registered by Optical Multichannel Analyzer (Hamamatsu Inc.). The excitation laser wavelengths were effectively suppressed (more than 10⁵ times) by using a custom-made super broad notch-filter (ZET690/140nf, AHF Analyzentechnik GmbH): in Figure 4.29 b the filter transmission is shown. In a standard procedure, the solutions of UC active compounds are filled into an optical glass tube prepared and sealed in a nitrogen-filled glove box using dry organic solvents.

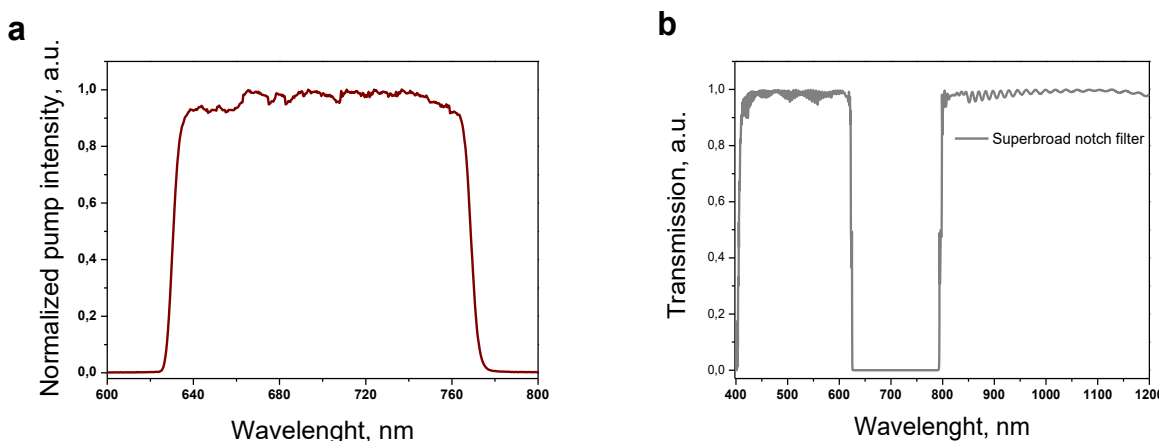


Figure 4.29: Excitation spectrum – (a); Transmission spectrum of the broadband notch filter – (b)
The measurements were performed by [REDACTED].

In Figure 4.30 the absorption spectrum of a sensitizer ensemble composed from a benzo-naphtho porphyrin family **25** and naphtho-antra porphyrin family **29** is shown. The Q-band absorption covers the entire deep-red region of the terrestrial sun irradiation. The spectral width of the excitation spectrum (defined at FWHM) is more than $\Delta\lambda \sim 142$ nm. This allows harvesting the complete sunlight energy of the deep-red region and transferring it via the TTA-UC in visible light, assessable for further use through any type of energy storage technology.

The fluorescence spectrum of the emitter molecule (rubrene) working effectively with every single sensitizer from the benzo-naphtho porphyrin family **25** and naphtho-antra porphyrin family **29** is shown in Figure 4.30 as well. It is important to notice, that emitter fluorescence spectrum matches well with the transparency window of the sensitizer ensemble, thus no parasitic reabsorption of the generated UC-emission was observed. The extremely broad excitation spectrum of the sensitizer ensemble combined with the energetically well-situated transparency window explains the observed high overall TTA – UC quantum yield – on the level of 0.04 (following the classical definition) measured at total excitation intensity of 100 mWcm^{-2} , obtained by super broad excitation spectrum (shown in Figure 4.29 a). At sunlight concentration of 11 times (AM1.5) the observed TTA – UC yield was 0.038. The UC-samples were prepared and sealed in a nitrogen-filled glove-box at oxygen level less than 2 ppm; solvent – dry hexadecane.

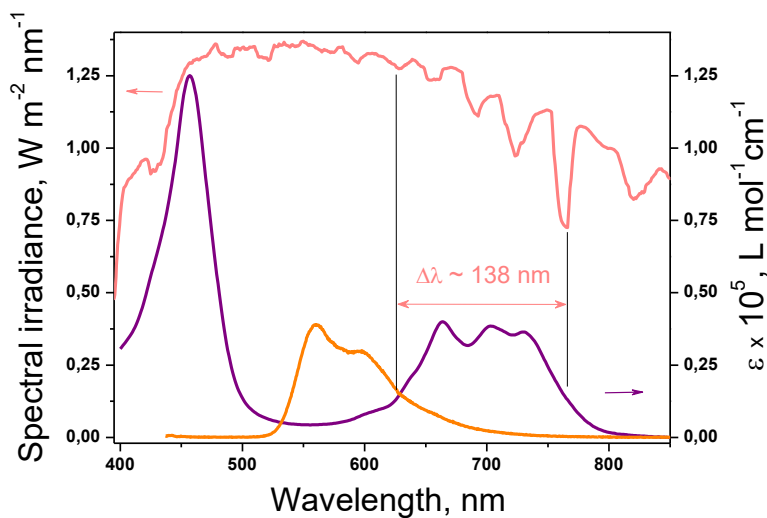


Figure 4.30: Molar extinction of a sensitizer blend composed of mixed benzo-naphtho porphyrin family **25** and mixed naphtho-antra porphyrin family **29** in molar ratio 1:2, total molar concentration 1×10^{-5} M (the violet line); Sun spectral irradiance (pink line), AM 1.5; Fluorescence spectrum of the emitter – rubrene (orange line); For simplicity, the emitter fluorescence spectrum is normalized regarding the Q-band absorption of the sensitizer ensemble. The measurements were performed by [REDACTED].

This extremely broad excitation spectrum allows solving another technological problem, limiting the sunlight-based energy storage technologies: UC-devices application should require as low as possible sunlight concentration and allow application of nanoimaging optical devices, such as solar concentrators based on Fresnel lenses or 2D polymer micro lens arrays. Even very low sunlight concentration ratio (less than 10 times) obtained by Fresnel-Köhler flat optical design¹⁰⁵ lenses, aspheric lenses created on a flat polymer substrate, polymer microlens arrays obtained by ink-jet printing technique¹⁰⁶ or microlens arrays based on polymer network liquid crystal¹⁰⁷, allows the effective transformation of the deep-red sunlight spectral range via the studied process of TTA – UC in visible light.¹²

4.2 Mixed emitter

Given that precise overlap of the triplet levels of the chromophore is necessary to ensure maximized quantum yield of the utilized TTA-UC process and the strong connection between structure and optical properties, the need for custom tailored emitter dyes is immanent. This chapter focusses on the syntheses of mixed benzo-BODIPY emitter chromophores, which enable in combination with Pd-metallated benzo-naphtho porphyrin sensitizer dyes, application in biological tissue, specifically minimally invasive temperature sensing. In a similar fashion to the preparation of the mixed porphyrin families, a mixed pyrrole condensation strategy has been applied. (The measurement of luminescence spectra were performed by [REDACTED].)

4.2.1 DPh-BODIPY and MPh-MB-BODIPY

Modification of BODIPY dyes via π -extension is a known method to shift their absorption bathochromically¹⁰⁸. Introduction of a phenyl ring is a common way to make monofunctional dyes, whereas a substitution of pyrrole with aryl groups at the alpha position shifts the absorption significantly^{109,110}. Another way is the benzoannulation¹¹¹, similar to porphyrins and perylene dyes^{112,113}. For the double annulation, the same synthetic precursors as for the tetrabenzoporphyrins can be used. Recently, monobenzo-BODIPY was prepared by a reaction with tetrahydroisoindole with formylpyrrole¹¹⁴.

As known for the preparation of porphyrins, the acid catalysed Lindsey condensation can be performed between one equivalent of aldehyde and two equivalents of an α -substituted pyrrole in order to suppress the formation of higher condensates and yielding the BODIPY core structure. Using two different pyrrole derivatives, ethyl-4,5,6,7-tetrahydro-2H-isoindole-1-carboxylate **4** and 2-phenylpyrrole **30** together with 3,5-di(*tert*-butyl)benzaldehyde **26**, dissolved in DCM and trifluoroacetic acid (TFA) as a catalyst, the mixture was stirred at room temperature overnight in darkness. After allowing to reach equilibrium of the different condensates dry 2,3-dichloro-5,6-dicyano-1,4-benzoquinone (DDQ) was added and the stirring was continued for 2 h. After adding a couple drops of triethylamine, the mixture was washed and the solvent removed under vacuum (Figure 4.31).

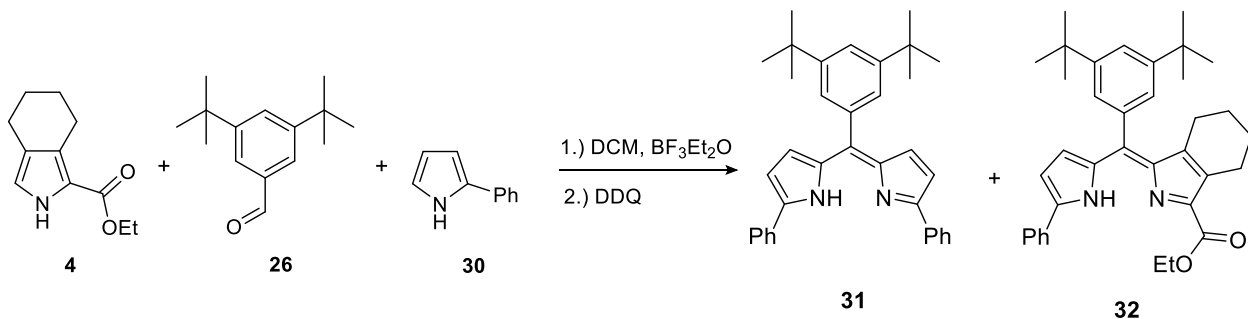


Figure 4.31: TFA mediated condensation of ethyl-4,5,6,7-tetrahydro-2H-isoindole-1-carboxylate **4**, 2-phenylpyrrole **30** and 3,5-di(tert-butyl)benzaldehyde **26** with additional aromatization with DDQ forming dipyrromethenes **31** and **32**.

For the subsequent modification of the core, *N,N*-diisopropylethylamine (DIEA) and CH_2Cl_2 were added under argon atmosphere and the solution was stirred at room temperature for 10 min. $\text{BF}_3\text{-OEt}_2$ was added and stirring was continued for 2 h. After washing with a 5% NaHCO_3 solution, the solvent was once again removed under vacuum (Figure 4.32) and the aromatization step continued without separation of the products.

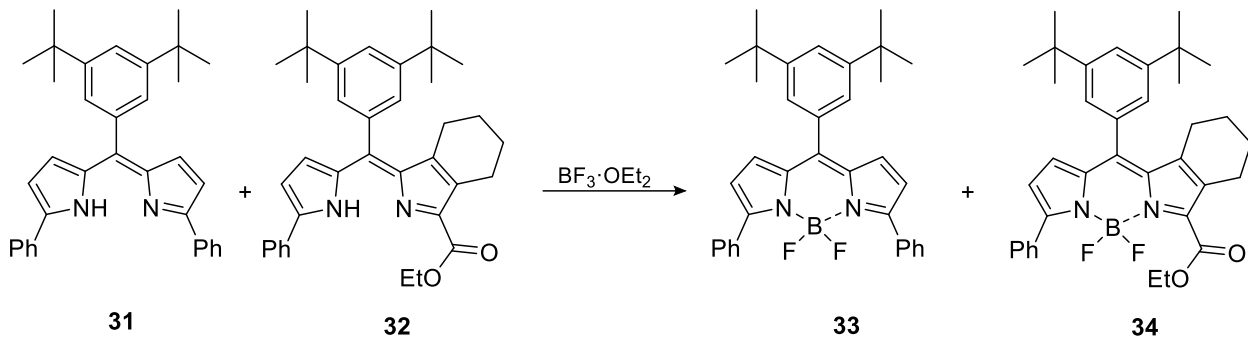


Figure 4.32: Chelation reaction of dipyrromethenes **31** and **32** with $\text{BF}_3\text{-OEt}_2$ yielding DPh-BODIPY **33** and the non-oxidized MPh-MB-BODIPY **34**.

Aromatization of molecule **34** was undertaken by dissolving the crude mixture in toluene and 1,4-dioxane, stirring for 5 min, adding DDQ and heating at 110 °C for 15 h (Figure 4.33).

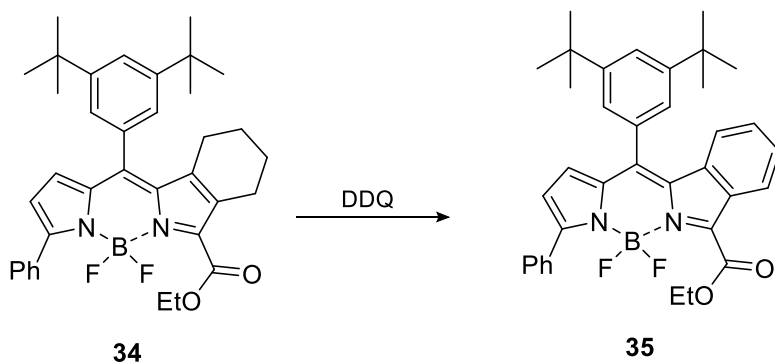


Figure 4.33: Aromatization of non-oxidized MPh-MB-BODIPY **34** with DDQ yielding MPh-MB-BODIPY **35**.

Once cooled down, the solvents were removed in vacuum and silica gel chromatography afforded DPh-BODIPY **33** as a first red fraction with yellow fluorescence, which was evaporated and recrystallized from CH_2Cl_2 /methanol to afford dark red crystals after drying under vacuum with 39% yield. The second fraction, violet with red fluorescence, was evaporated, dissolved in cyclohexane and freeze-dried for 24 h, to afford MPh-MB-BODIPY **35** as a violet powder with 23% yield. No evidence for the formation of 3,5-bis(ethoxycarbonyl)-1,2,6,7-dibenzo-8-(3,5-di-*tert*-butylphenyl)BODIPY (DB-BODIPY) **38** or its non-oxidized precursors **37** were found.

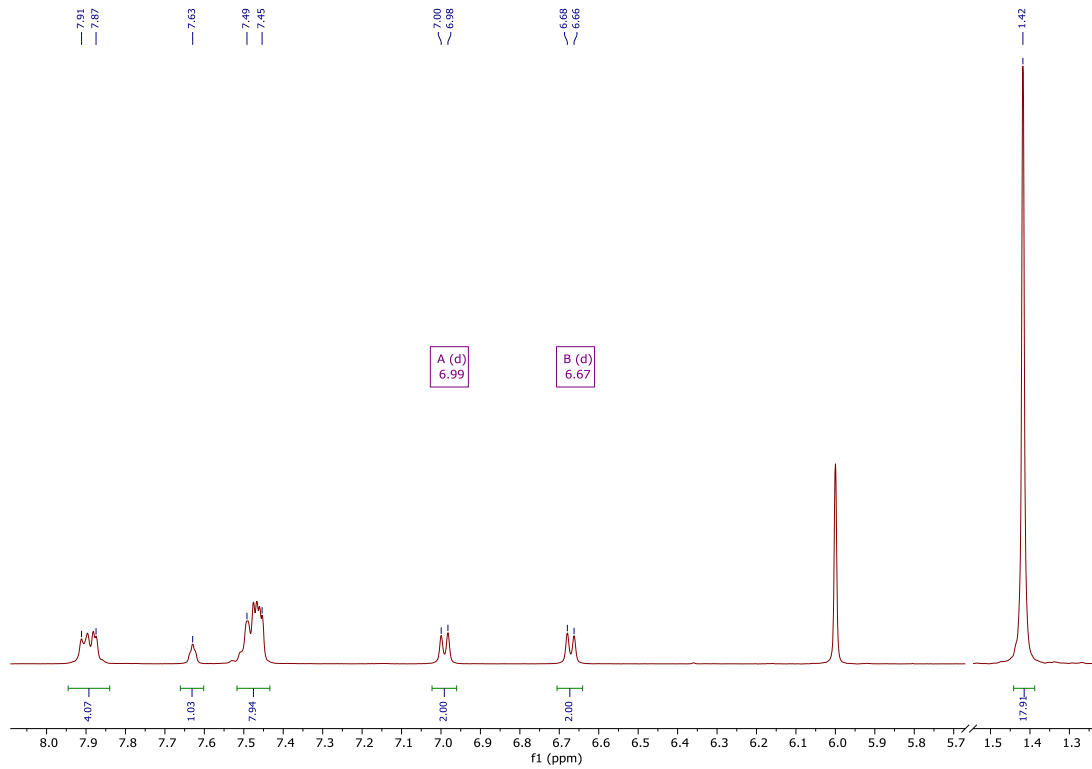


Figure 4.34: ^1H -NMR spectrum of DPh-BODIPY **33** and MPh-MB-BODIPY **35** in $\text{C}_2\text{D}_2\text{Cl}_4$.

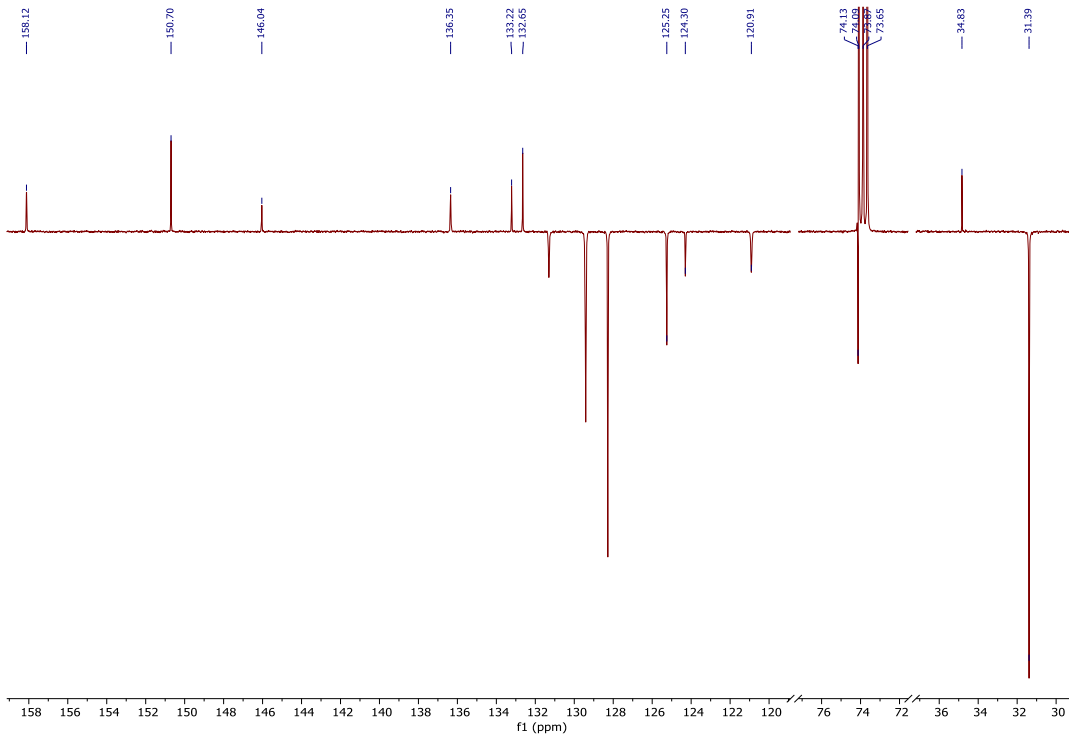


Figure 4.35: ^{13}C -NMR spectrum of DPh-BODIPY **33** and MPh-MB-BODIPY **35** in $\text{C}_2\text{D}_2\text{Cl}_4$.

Results and discussion: Mixed emitter

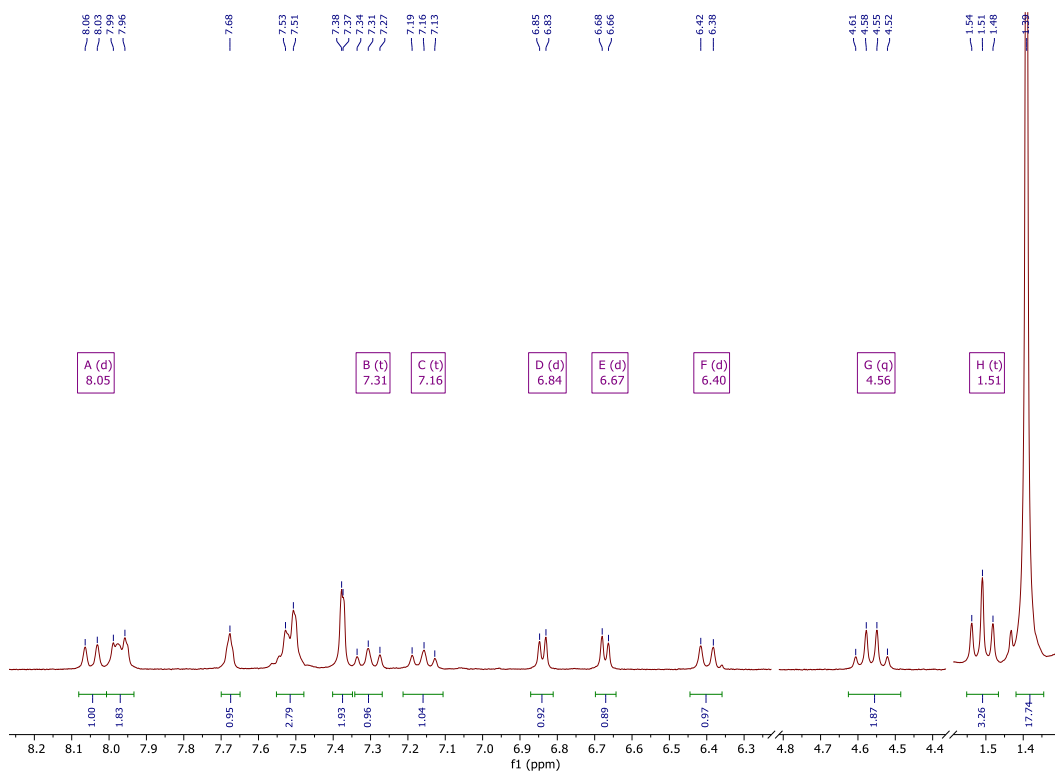


Figure 4.36: ^1H -NMR spectrum of MPh-MB-BODIPY **35** in $\text{C}_2\text{D}_2\text{Cl}_4$.

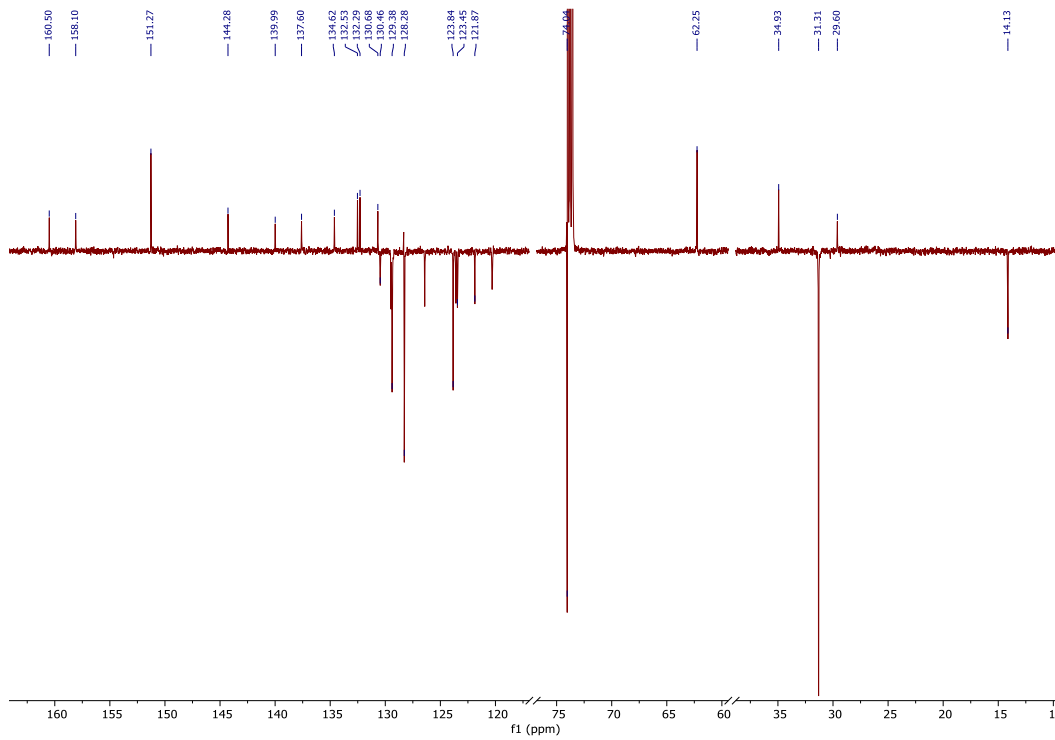


Figure 4.37: ^{13}C -NMR spectra of MPh-MB-BODIPY **35** in $\text{C}_2\text{D}_2\text{Cl}_4$.

4.2.2 DB-BODIPY

Similar to the previously described synthesis of DPh-BODIPY **33**, DB-BODIPY **38** was prepared. 3,5-Di(*tert*-butyl)benzaldehyde **26** and 2 equivalents of ethyl-4,5,6,7-tetrahydro-2H-isoindole-1-carboxylate **4** were dissolved in 100 mL of CH₂Cl₂ under argon atmosphere. Three drops of trifluoroacetic acid (TFA) were added, and the solution was stirred at room temperature overnight in the darkness. DDQ was added and stirring was continued for 2 h. Triethylamine was added, the mixture washed and the solvents evaporated in vacuum (Figure 4.38).

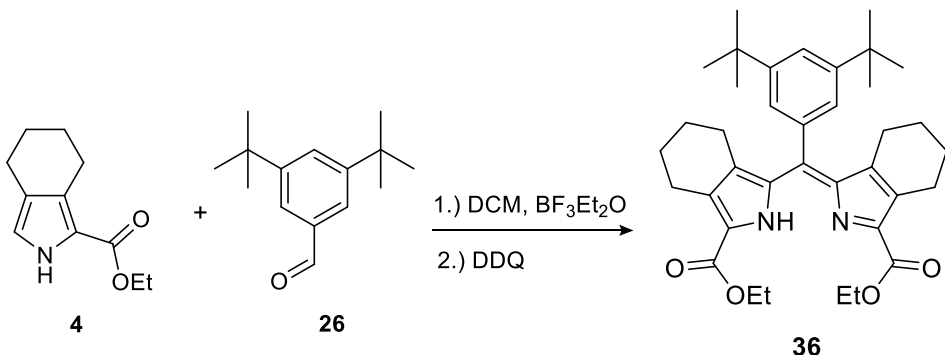


Figure 4.38: TFA mediated condensation of ethyl-4,5,6,7-tetrahydro-2H-isoindole-1-carboxylate **4** and 3,5-di(*tert*-butyl)benzaldehyde **26** and subsequent aromatization with DDQ forming dipyrromethene **36**.

Without purification DIEA and CH₂Cl₂ were added to the crude mixture under an argon atmosphere and the solution was stirred at room temperature for 10 min. BF₃·OEt₂ was added and the stirring was continued for 4 h. The reaction mixture was washed with 5% NaHCO₃ solution, washed with water and evaporated until dryness (Figure 4.39).

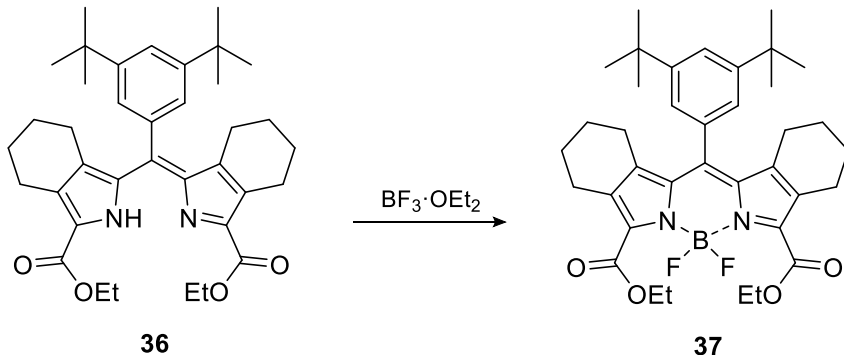


Figure 4.39: Chelation reaction of dipyrromethene **36** with $\text{BF}_3\cdot\text{OEt}_2$ yielding non-oxidized DB-BODIPY **37**.

Following, toluene and 1,4-dioxane were added to the crude reaction mixture, the solution was stirred for 5 min, DDQ was added and stirred at 110 °C for 15 h. The solution was cooled down, washed with aqueous sodium sulfite. The organic layers were separated, dried over anhydrous sodium sulfate, and evaporated to dryness. Column chromatography with silica gel afforded blue fraction, which was evaporated, dissolved in cyclohexane and freeze-dried for 24 h to afford a blue powder of DB-BODIPY **38** in 37% yield (Figure 4.40).

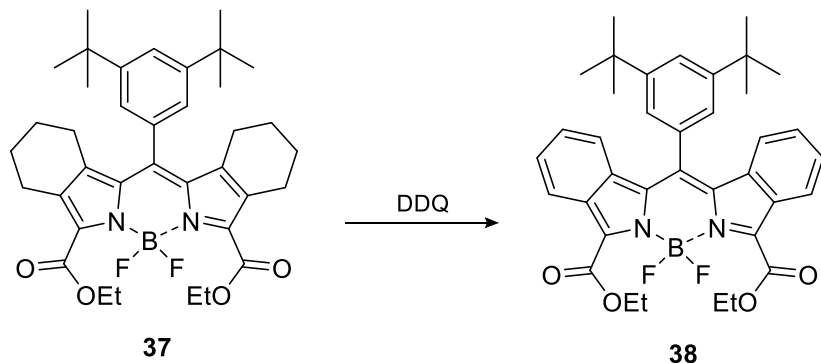


Figure 4.40: Aromatization of non-oxidized DB-BODIPY **37** with DDQ yielding DB-BODIPY **38**.

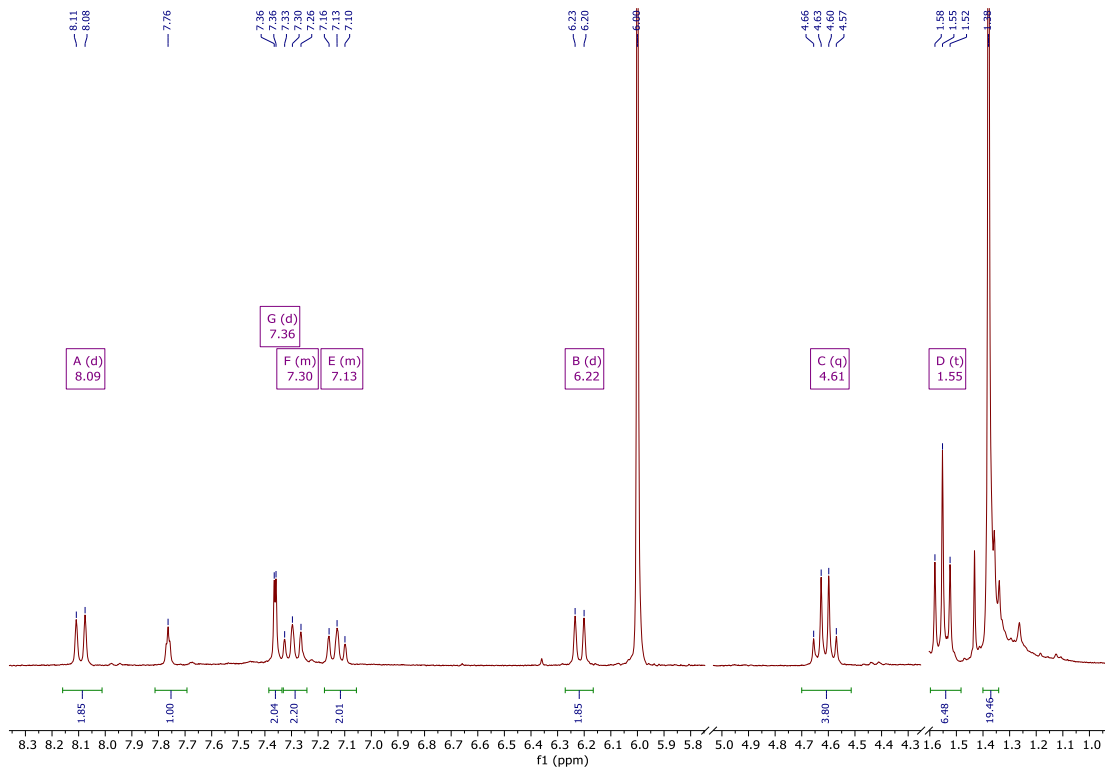


Figure 4.41: ^1H -NMR spectrum of DB-BODIPY **38** in $\text{C}_2\text{D}_2\text{Cl}_4$.

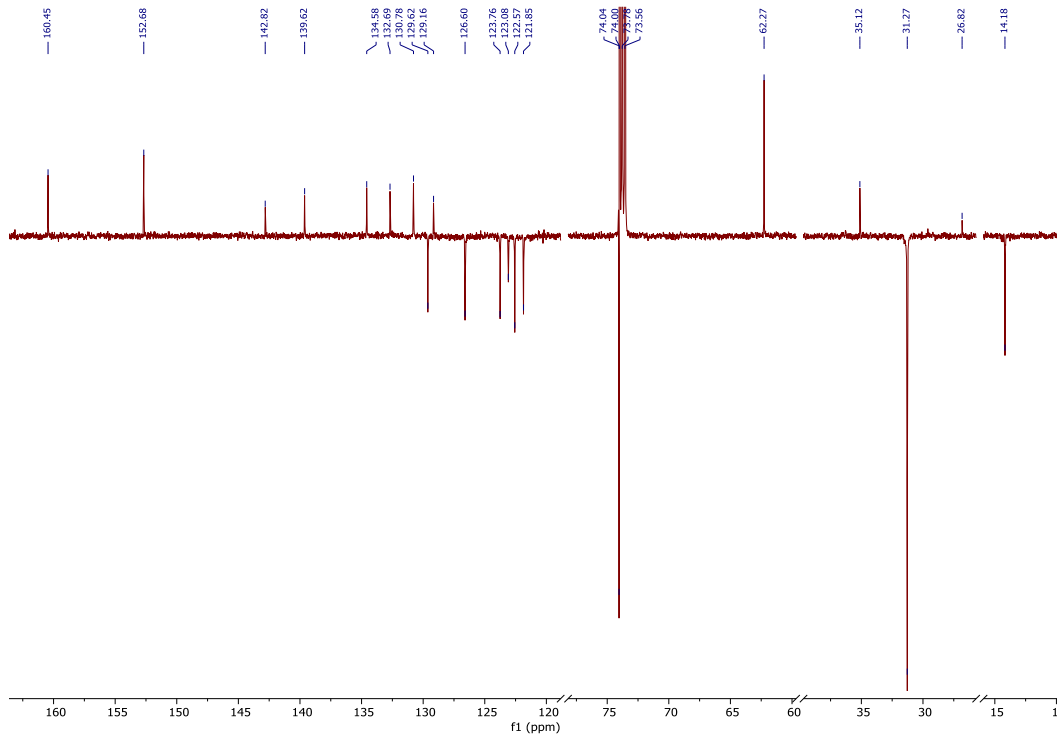


Figure 4.42: ^{13}C -NMR spectrum of DB-BODIPY **38** in $\text{C}_2\text{D}_2\text{Cl}_4$.

4.2.3 Application

The obtained three BODIPY dyes are strongly coloured solids; their solutions show a ranging from deep-red to blue colours. Strong fluorescence of first two dyes was visible even by the naked eye. Absorption spectra revealed that every annulation step shifts the absorption bathochromically by 40-45 nm; at the same time molar absorptivity is growing as well, due to enlargement of the π -system. All dyes show bright fluorescence, with quantum yields of 0.56-0.74 and a Stokes shift of 608-1033 cm⁻¹ (see Table 4.1).

Table 4.1: Spectral properties of the different BODIPYs in toluene at room temperature.

^aFluorescence quantum yields for all BODIPYs ($\lambda_{\text{exc}} = 560$ nm) were calculated using Lumogen Red as a standard ($\Phi_f = 0.96$ in chloroform). The measurements were performed by [REDACTED]

	Absorbance λ_{max} [nm]	ϵ [M ⁻¹ cm ⁻¹]	Emission λ_{max} [nm]	Φ_f ^[a]	Stokes shift [cm ⁻¹]
DPh-BODIPY 33	557	30600	591	0.68	1033
MPh-MB-BODIPY 35	597	52650	630	0.74	877
DB-BODIPY 38	641	67100	667	0.56	608

The normalized absorption and fluorescence spectra of the asymmetric BODIPY, together with the normalized absorption spectrum of the family of mixed benzo-naphtho porphyrins **25** are shown in Figure 4.43. As expected,¹¹⁵ the studied BODIPYs demonstrate efficient TTA-UC when the UC-couples are combined, as shown in Table 4.2.

Here, the UC-system with the smallest anti-stokes shift is the system obtained by the mixed-condensation strategy, both for the sensitizer and for the emitter molecules. Despite this advantage, there are three other optical parameters derived from the tissue transparency windows and Table 4.2 making the UC dye-couple PdBNP **25**/ MPh-MB-BODIPY **35** an optimal system for under-cutaneous sensing applications: (1) comparing the absorption coefficients of the HbO₂ for the specific excitation wavelengths $\lambda = 635$ nm (the UC-couple PdTBP / DPh-BODIPY **33**) and $\lambda = 658$ nm (the UC-couple PdBNP **25**/ MPh-MB-BODIPY **35**), there is a more than a 1.5 times higher absorption for the shorter excitation wavelength; (2) the crucial advantage of the asymmetrical UC-couple is the fact,

that the emission generated inside the tissue will be more than 5.3 times less absorbed, than the signal of the UC dye-couple PdTBP / DPh-BODIPY **33**; (3) regarding the absorption coefficient for the residual phosphorescence signal, the asymmetrical UC dye-couple reveals more than 7.5 times lower optical losses, than it is observed for the strongly red-shifted UC dye-couple PdTNP / DB-BODIPY **38**.

Table 4.2: TTA – UC parameters for different UC-couples, in toluene at room temperature, glove-box conditions. The measurements were performed by [REDACTED].

Sensitizer	Emitter	Excitation	dF	rPh	Anti-Stokes shift [cm^{-1}]
		[nm]	λ_{max} [nm]	λ_{max} [nm]	
PdTBP	DPh-BODIPY 33	635	591	795	1170 (0.145 eV)
PdBNP 25	MPh-MB-BODIPY 35	658	630	850	677 (0.084 eV)
PdTNP	DB-BODIPY 38	705	667	900	806 (0.100 eV)

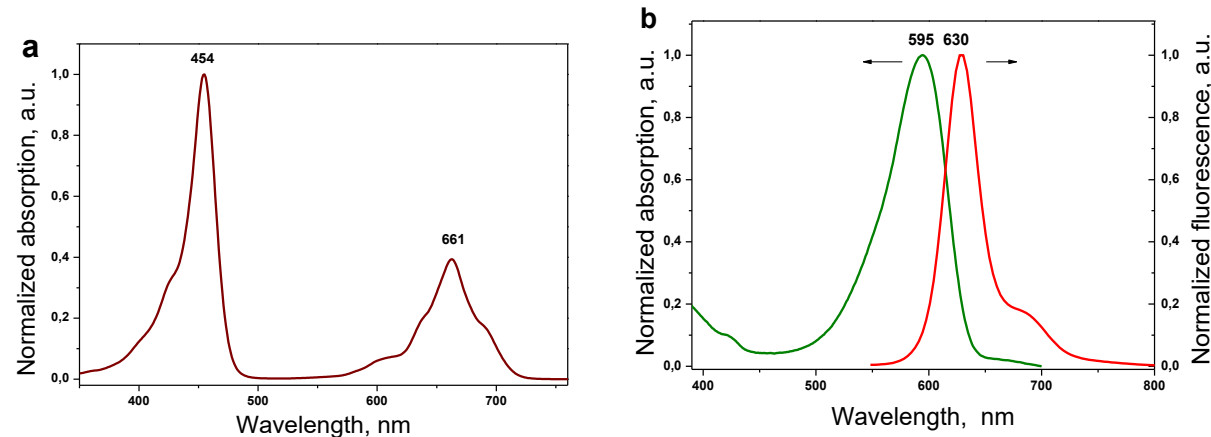


Figure 4.43: (a) – Normalized absorption spectrum of the mixed palladium benzo-naphtho porphyrin family (PdBNP) **25**; (b) – Normalized absorption (the green curve) and fluorescence (the red curve) of MPh-MB-BODIPY **35** in toluene. The measurements were performed by [REDACTED].

Summarizing the data presented in (1), (2) and (3), one can conclude that the registered dF or rPh signals for the UC dye-couple PdBNP **25**/ MPh-MB-BODIPY **35** collected after the sequential processes – excitation (tissue penetration), TTA-UC, i.e.

generation of delayed fluorescence and residual phosphorescence, emanation of optical signal (escape from the tissue) – are more than 8 times higher, keeping all other experimental conditions the same (namely, excitation photon flux, TTA-UC quantum yield, dye concentrations, oxygen content, sample temperature, etc.) constant.

In presence of molecular oxygen, dissolved in the wax/oil sample, singlet oxygen is generated continuously during the optical excitation. The phytochemical compounds of the vegetable oils (for example, tocopherol, tocotrienol and γ -oryzanol) demonstrate a remarkable ability to bind chemically all present amounts of singlet oxygen. Since the oxygen permeation rate through the samples surface is much lower than the rate of chemical binding of singlet oxygen across the optically assessed spot, already after a short initial period (around 4 s in this case, see Figure 4.44), the entire oxygen content is consumed. This fact is manifested by the actually stationary intensity of the signals of dF and rPh, as demonstrated in Figure 4.44.

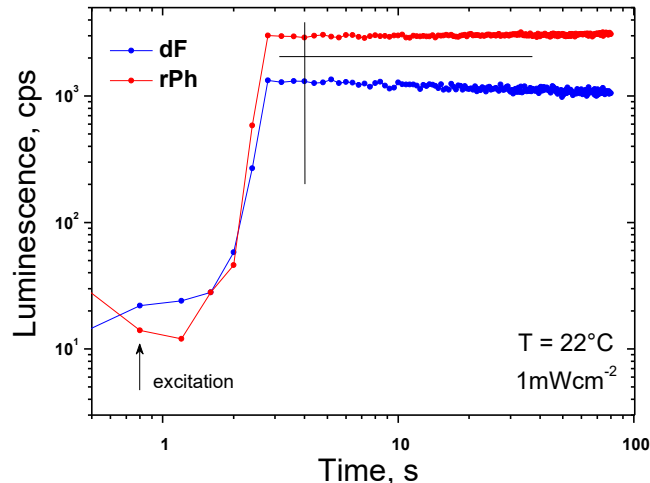


Figure 4.44: Temporal evolution of the signals of dF and rPh at sample temperature of $T = 22\text{ }^\circ\text{C}$. The excitation intensity is kept constant at 1 mW cm^{-2} for all measurements; *cw* – diode laser at $\lambda_{exc} = 658\text{ nm}$; air saturated environment; excitation spot diameter $d = 1.8 \times 10^{-3}\text{ m}$; sample thickness $b = 4 \times 10^{-4}\text{ m}$. Material composition, as follows, $1 \times 10^{-5}\text{ M PdBNP 14/ 2} \times 10^{-4}\text{ M MPh-MB-BODIPY 35/ 40 wt.\% carnauba wax / 30 wt.\% squalene oil / 30 wt.\% peanut oil}$. The black lines are a guide for the eye. The measurements were performed by [REDACTED].

This remarkable stability of the signals of dF and rPh even in an oxygen saturated environment allows one to study the temperature dependence of the TTA-UC process. In Figure 4.45 a the luminescence spectra of the studied material composition are

demonstrated for two boundary temperature values, namely 18 °C and 42 °C. As expected, a significant decrease of the residual sensitizer phosphorescence, accompanied with a well observable increase of the emitter delayed fluorescence with increasing sample temperature was detected. The data presented in Figure 4.45 a is summarized in Figure 4.45 b, where the dependence of the dF and rPh signals for a stepwise increase of the sample temperature is reported.

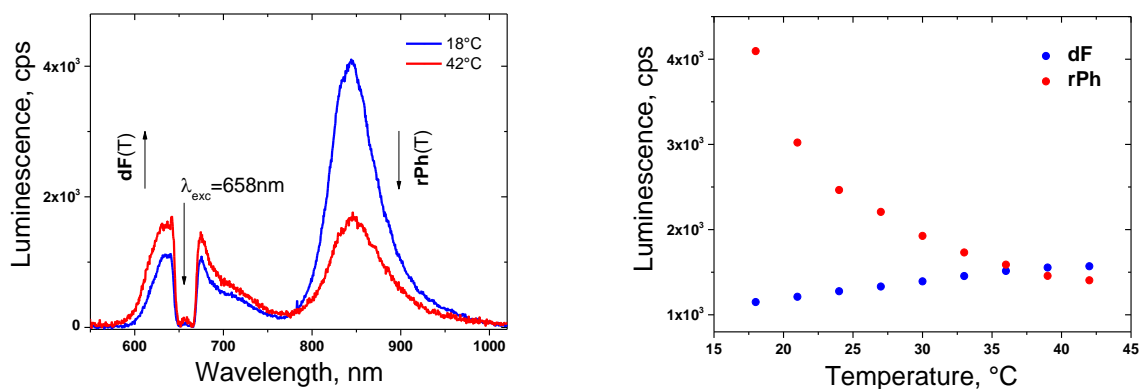


Figure 4.45: (a) – Luminescence spectra of the UC-systems for different sample temperatures; (b) – Temperature dependence of the signals of dF (at $\lambda_{\text{max}} = 630$ nm, the blue dots) and rPh (at $\lambda_{\text{max}} = 850$ nm, the red dots) on the sample temperature. Experimental conditions for all measurements: material composition, as follows, 1×10^{-5} M PdBNP **25** / 2×10^{-4} M MPh-MB-BODIPY **35** / 40 wt.% carnauba wax / wt.30 % squalene / 30 wt.% peanut oil. The spectra are obtained at the $t = 4$ s after starting the optical excitation. The excitation intensity is kept constant, at 1 mW cm^{-2} for all measurements; *cw* – diode laser at $\lambda_{\text{exc}} = 658$ nm; air saturated environment. The measurements were performed by [REDACTED].

As shown in Figure 4.45 b, the signals of dF and rPh have comparable intensity. Additionally, the dF signal increases monotonically with increasing sample temperature; simultaneously the rPh signal decreases monotonically with increasing sample temperature. Thus, it allows to achieve a non-ambiguous calibration curve, shown in Figure 4.46. From this figure it is evident, that this biocompatible material composition, (1×10^{-5} M PdBNP **25** / 2×10^{-4} M MPh-MB-BODIPY **35** / 40 wt.% carnauba wax / 30 wt.% squalene oil / 30 wt.% peanut oil) demonstrates a high temperature sensitivity since the ratio dF / rPh is changed more than 4 times within the physiologically relevant temperature window of interest $\Delta = \sim 18$ °C - 42 °C.

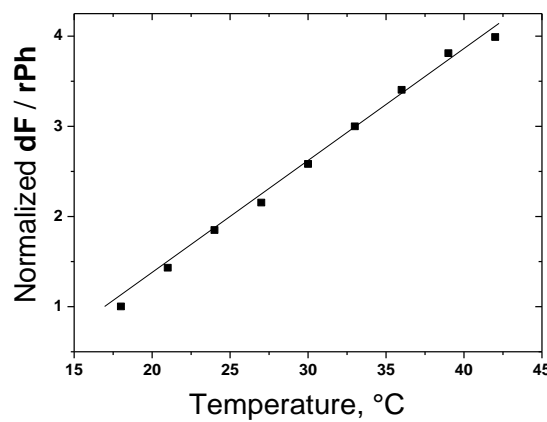


Figure 4.46: Temperature calibration curve - ratiometric response. Normalized ratio of the signals of dF / rPh as a function of the sample temperature, demonstrated in Figure 4.45 b.

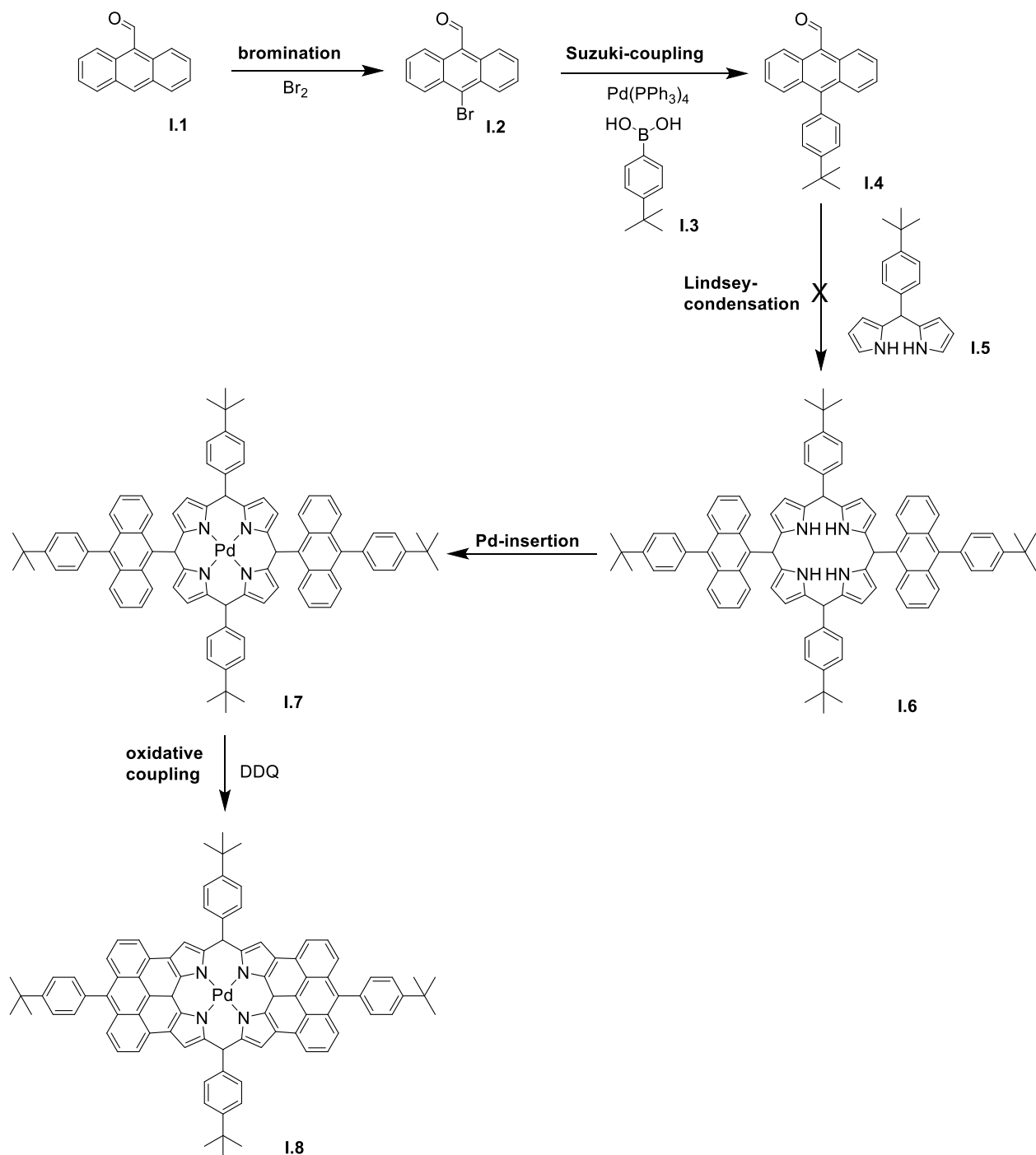
4.3 Fused porphyrin

As a replacement for the sentinel lymph node biopsy for the diagnosis of breast cancer metastases the European Hyposens project aims to develop a nano-confined photonic system which minimally invasive detects the oxygen concentration and temperature of cells. Hence, carefully finetuned TTA-UC chromophores with absorption and luminescence wavelengths within the tissue transparency window are necessary. The preparation of a Pd-metallated porphyrin-based sensitizer dye with absorption in the IR-region and maintained solubility is the main focus of this chapter.

4.3.1 Original reaction scheme

The original plan for the synthesis of the double fused Pd-phenyl-anthracene-porphyrin **I.8** is depicted in Figure 4.47.

First, 9-anthracene-carboxaldehyde **I.1** was successfully brominated. The subsequent Suzuki-coupling gave 10-(4-*tert*-butyl)-phenyl-9-anthracenecarboxylic acid **1.4** in 88% yield. The subsequent Lindsey-condensation failed. The reason might be sterical hindrance.

**Figure 4.47:** Original synthetic plan.

4.3.2 Second reaction scheme

In order to decrease the sterical hindrance preventing the Lindsey-condensation to take place, the synthetic route was modified in a way that the addition of the bulky phenyl-anthracene groups was performed after the preparation of the porphyrin core structure similar to literature procedure from Nicola Davis et al. (Figure 4.52).^{98,116} The first step was a Lindsey-condensation, where 1 equivalent of 2,2'-dipyrromethane **II.1** and 3,5-di-*tert*-butyl-benzaldehyde **II.2** was dissolved in DCM under nitrogen atmosphere. The catalyst boron trifluoride diethyl etherate was added and the mixture was stirred for 2 h at room temperature. Subsequently DDQ was introduced into the reaction flask and the resulting mixture was stirred overnight. Column chromatography with silica resulted in raspberry coloured 5,15-bis(3,5-di-*tert*-butylphenyl)porphyrin **II.3** crystals in 56 % yield (Figure 4.48).

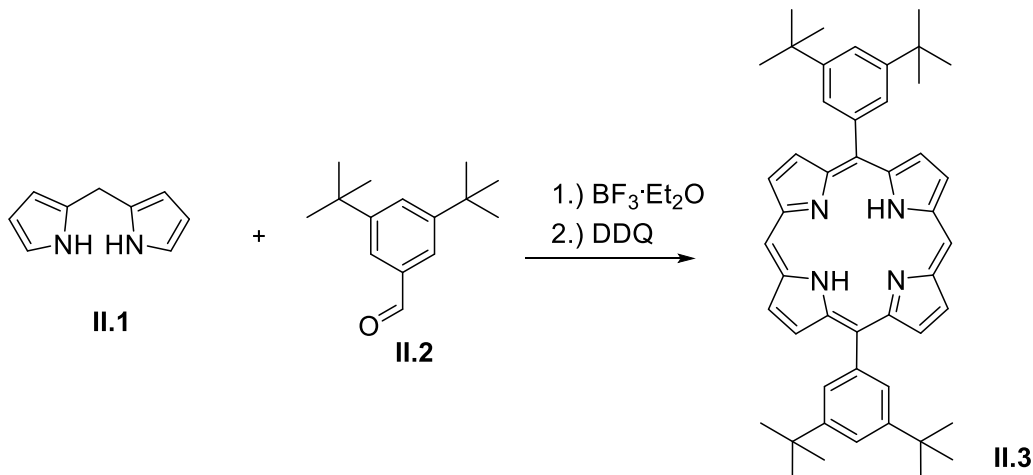


Figure 4.48: Lindsey-Condensation of 2,2'-dipyrromethane **II.1** with 3,5-di-*tert*-butylbenzaldehyde **II.2** yielding 5,15-bis(3,5-di-*tert*-butylphenyl)porphyrin **II.3**.

The $^1\text{H-NMR}$ spectrum in Figure 4.49 shows the matching signals for 5,15-bis(3,5-di-*tert*-butylphenyl)porphyrin **II.3** as described in literature. The H_{meso} signal can be found at 10.35 ppm as a singulett equivalent to 2 protons. The MALDI-TOF spectrum displays a weight matching the calculated weight for porphyrin **II.3** (Figure 4.50).

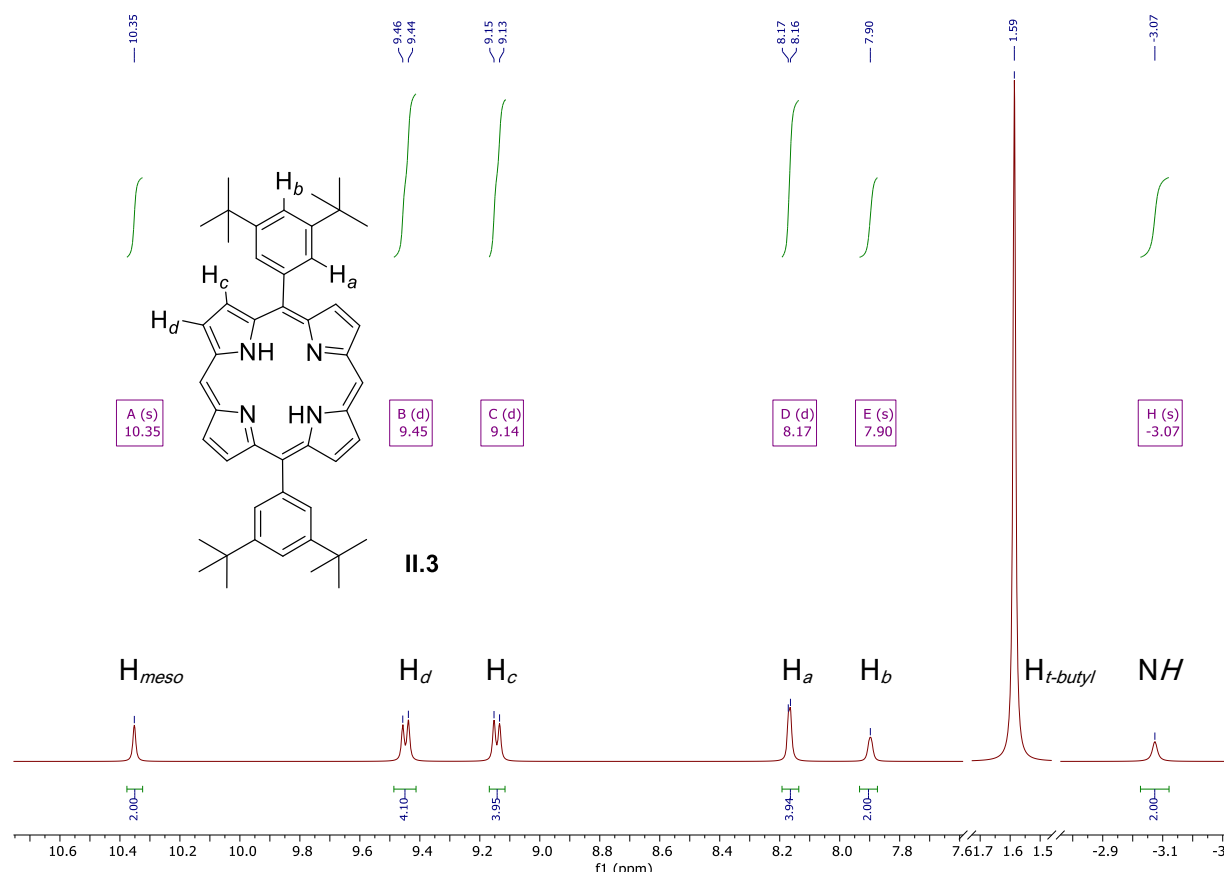


Figure 4.49: ^1H -NMR spectrum of 5,15-bis(3,5-di-*tert*-butylphenyl)porphyrin II.3.

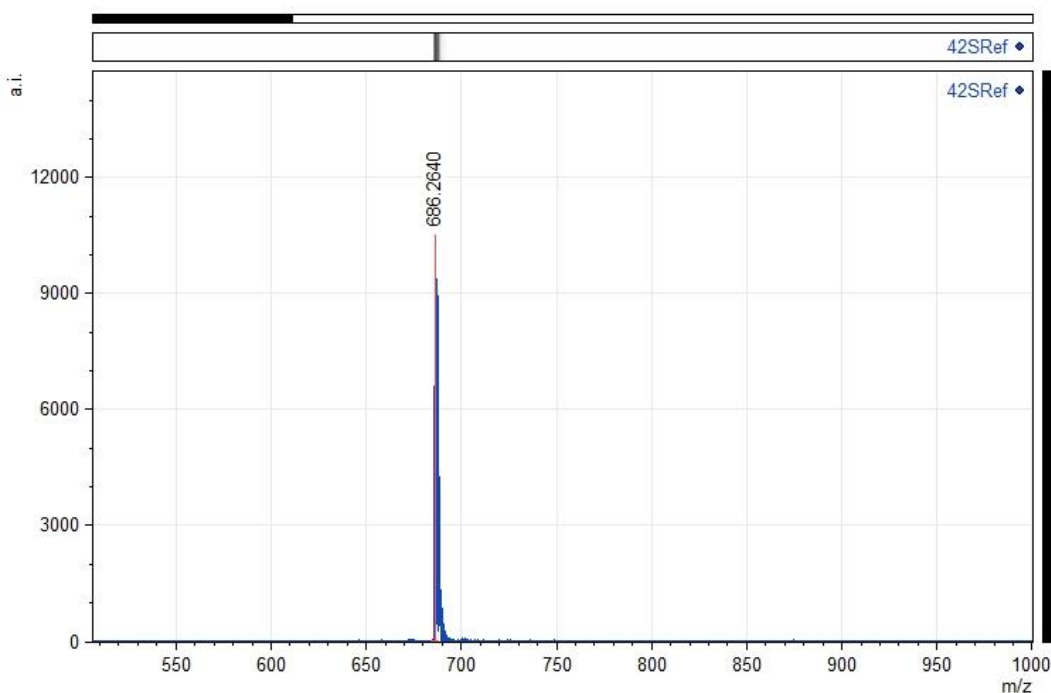


Figure 4.50: MALDI-TOF spectrum of 5,15-bis(3,5-di-*tert*-butylphenyl)porphyrin II.3.

The absorption spectrum of 5,15-bis(3,5-di-*tert*-butylphenyl)porphyrin **II.3** is shown in Figure 6.51. The characteristic high absorption of the Soret-band compared to the Q-band is evident. The absorbed wavelengths belong to the energetically high region of the electromagnetic spectrum.

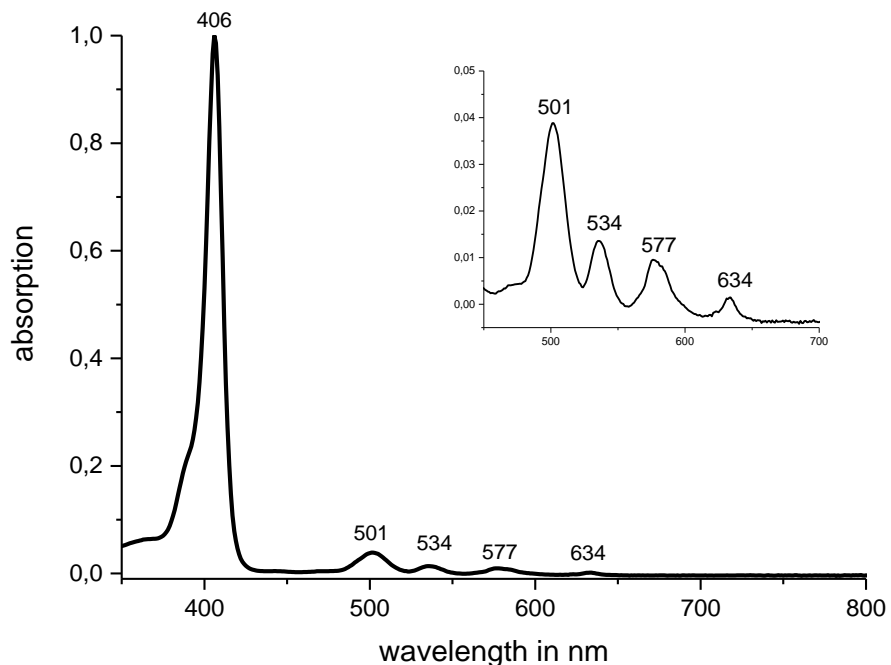


Figure 4.51: Normalized UV-Vis spectrum of 5,15-bis(3,5-di-*tert*-butylphenyl)porphyrin **II.3**. The inset shows scaled-up Q-bands.

With the utilization of the sterically smaller reactants, the Lindsey-condensation was successful. The subsequent insertion of Zinc could be performed in 72% yield. Bromination, though, led to undesired overhalogenation, which proved to be inseparable with standard chromatographic techniques (Figure 4.52).

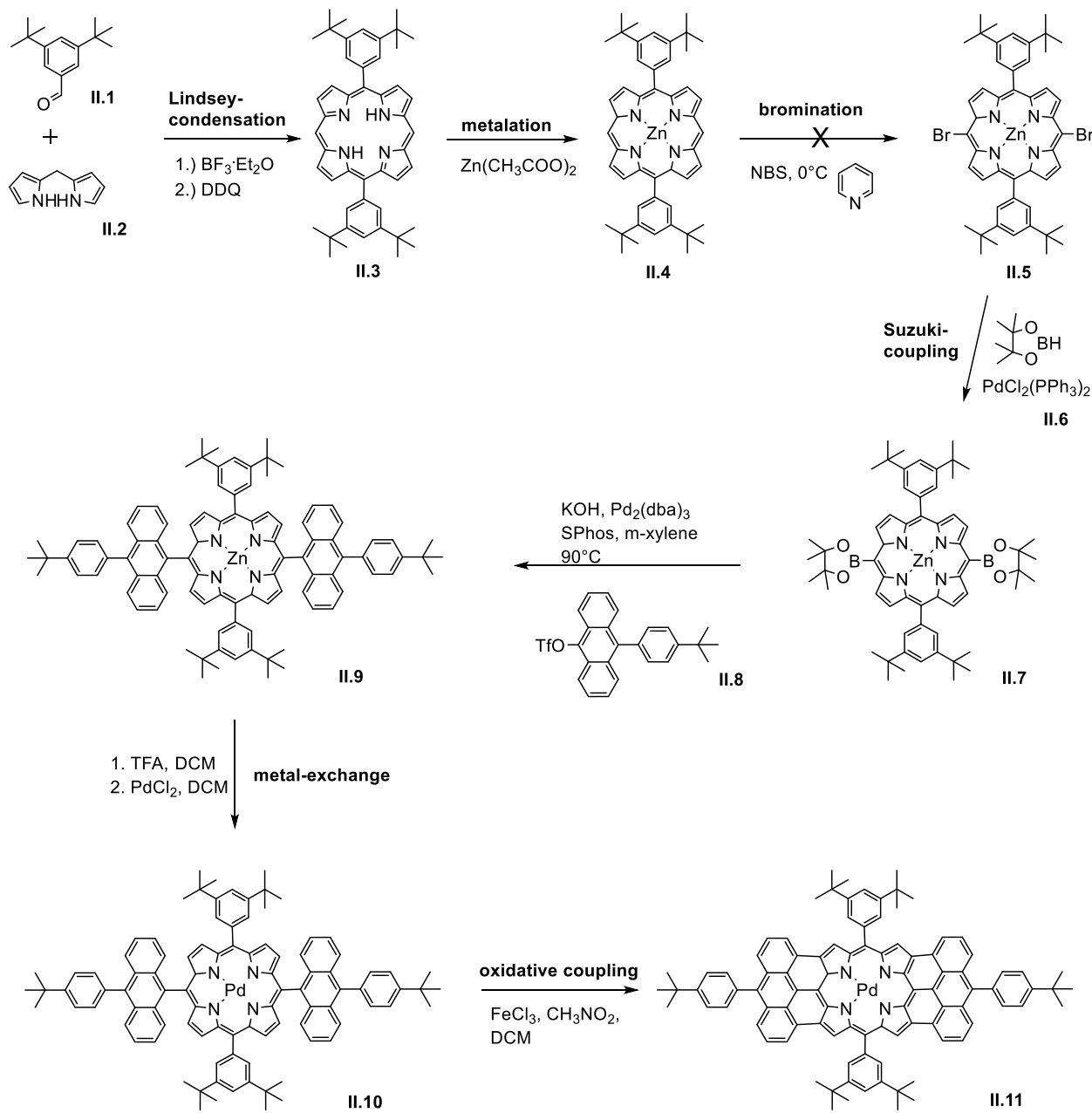


Figure 4.52: Second synthetic plan, first modification.

4.3.3 Third reaction scheme

Hence, the reverse order, first bromination of the porphyrin free-base, then Zn-insertion was attempted (Figure 4.53). The successfully prepared product of the Lindsey-condensation from the second reaction scheme, 5,15-bis(3,5-di-*tert*-butylphenyl)porphyrin II.3 was dissolved in chloroform, pyridine was added and the

reaction mixture cooled down to 0 °C. Afterwards NBS was added dropwise and the reaction progress monitored by TLC. At completion the reaction was quenched by addition of acetone. The solvents were removed under reduced pressure, the crude product washed with methanol and then recrystallized from chloroform-methanol (1:1). Purple crystals of 5,15-dibromo-10,20-bis(3,5-di-*tert*-butylphenyl)porphyrin **III.4** were achieved in 75% yield.

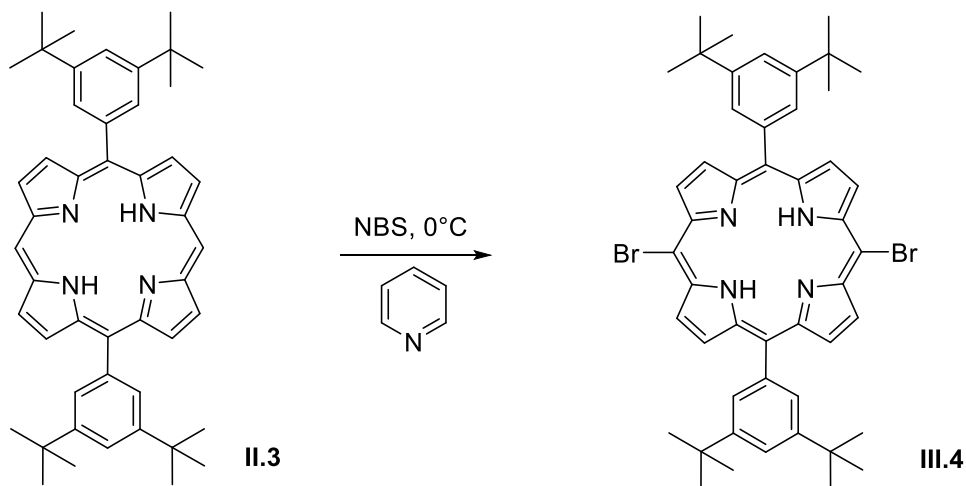


Figure 4.53: Bromination of 5,15-bis(3,5-di-*tert*-butylphenyl)porphyrin **II.3** with NBS yielding 5,15-dibromo-10,20-bis(3,5-di-*tert*-butylphenyl)porphyrin **III.4**.

The $^1\text{H-NMR}$ spectrum in Figure 4.54 shows the matching signals 5,15-dibromo-10,20-bis(3,5-di-*tert*-butylphenyl)porphyrin **III.4** as described in literature. The H_{meso} signal is no longer detectable. The MALDI-TOF spectrum displays a weight matching the calculated weight for porphyrin **III.4** (Figure 4.55).

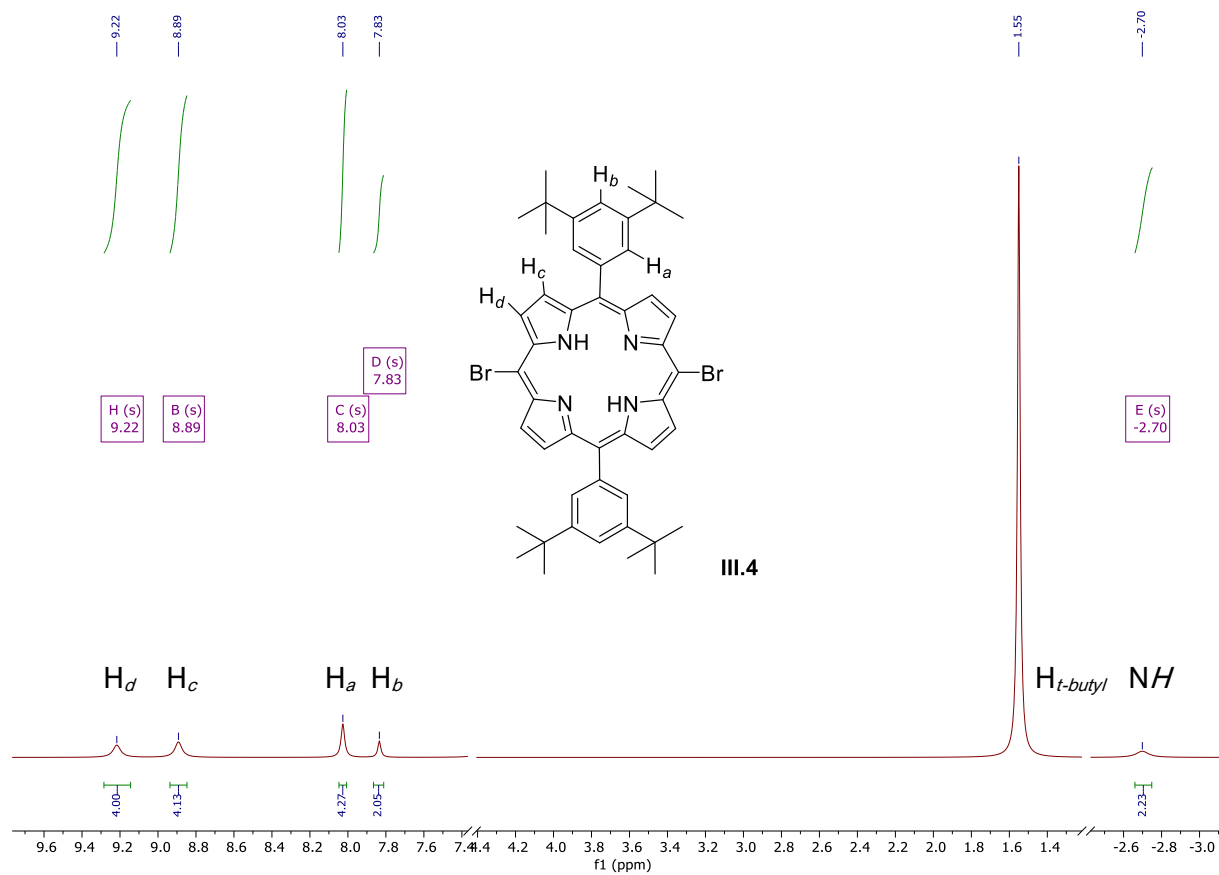


Figure 4.54: ¹H-NMR spectrum of 5,15-dibromo-10,20-bis(3,5-di-*tert*-butylphenyl)porphyrin III.4.

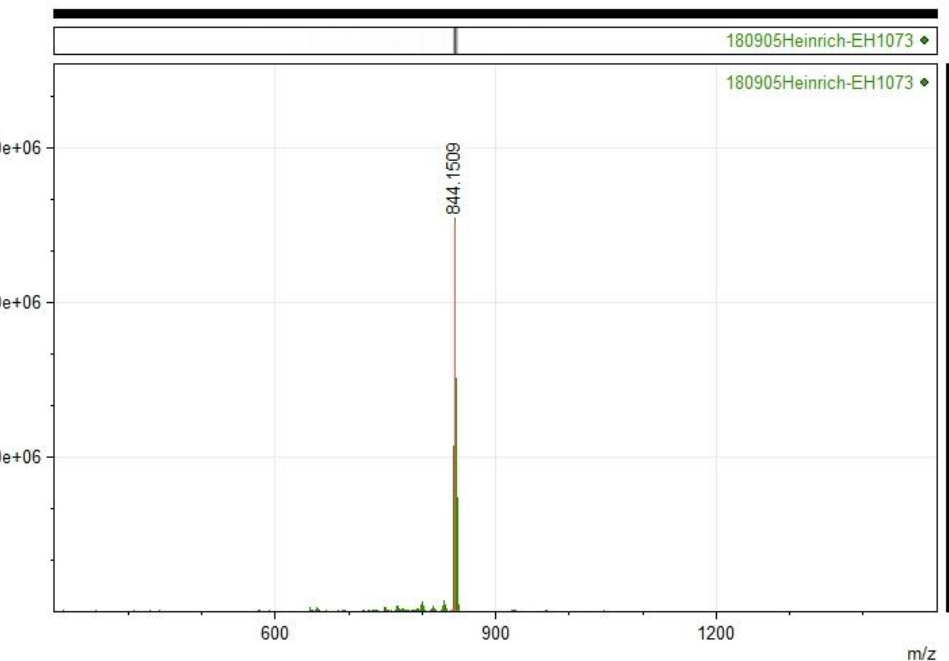


Figure 4.55: MALDI-TOF spectrum of 5,15-dibromo-10,20-bis(3,5-di-*tert*-butylphenyl)porphyrin III.4.

As shown in Figure 4.56 the bromination of 5,15-bis(3,5-di-*tert*-butylphenyl)porphyrin **II.3** resulted in no significant alteration to the absorption spectrum.

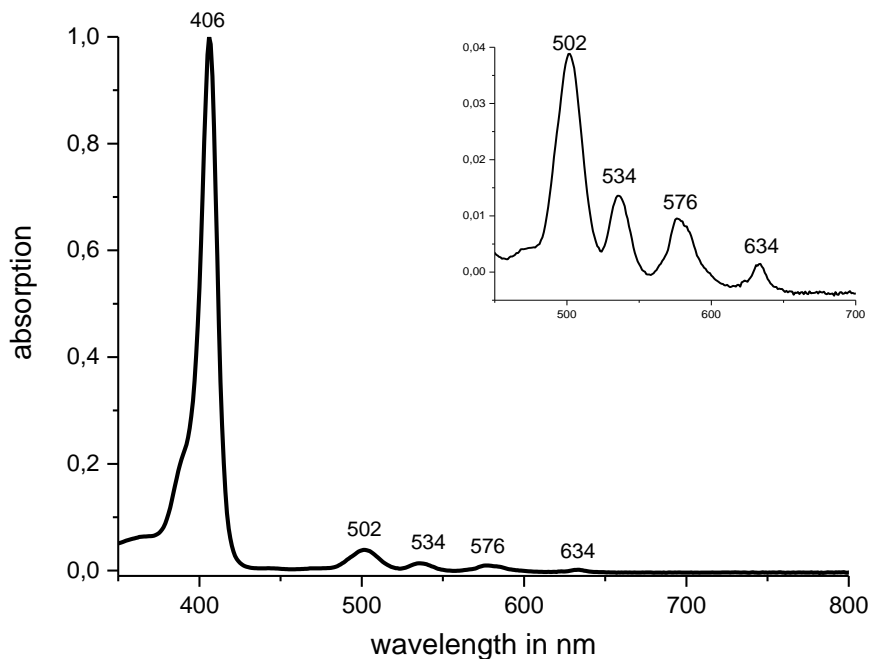


Figure 4.56: Normalized UV-Vis spectrum of 5,15-dibromo-10,20-bis(3,5-di-*tert*-butylphenyl)porphyrin **III.4**. The inset shows scaled-up Q-bands.

The changes to the synthetic route, resulted in the circumvention of undesired bromination and impossible separation (Figure 4.57). The subsequent Zn-insertion was successful affording porphyrin **III.5** in 79% yield. Following Suzuki-coupling attempts were ineffective and led to destruction of the starting molecule.

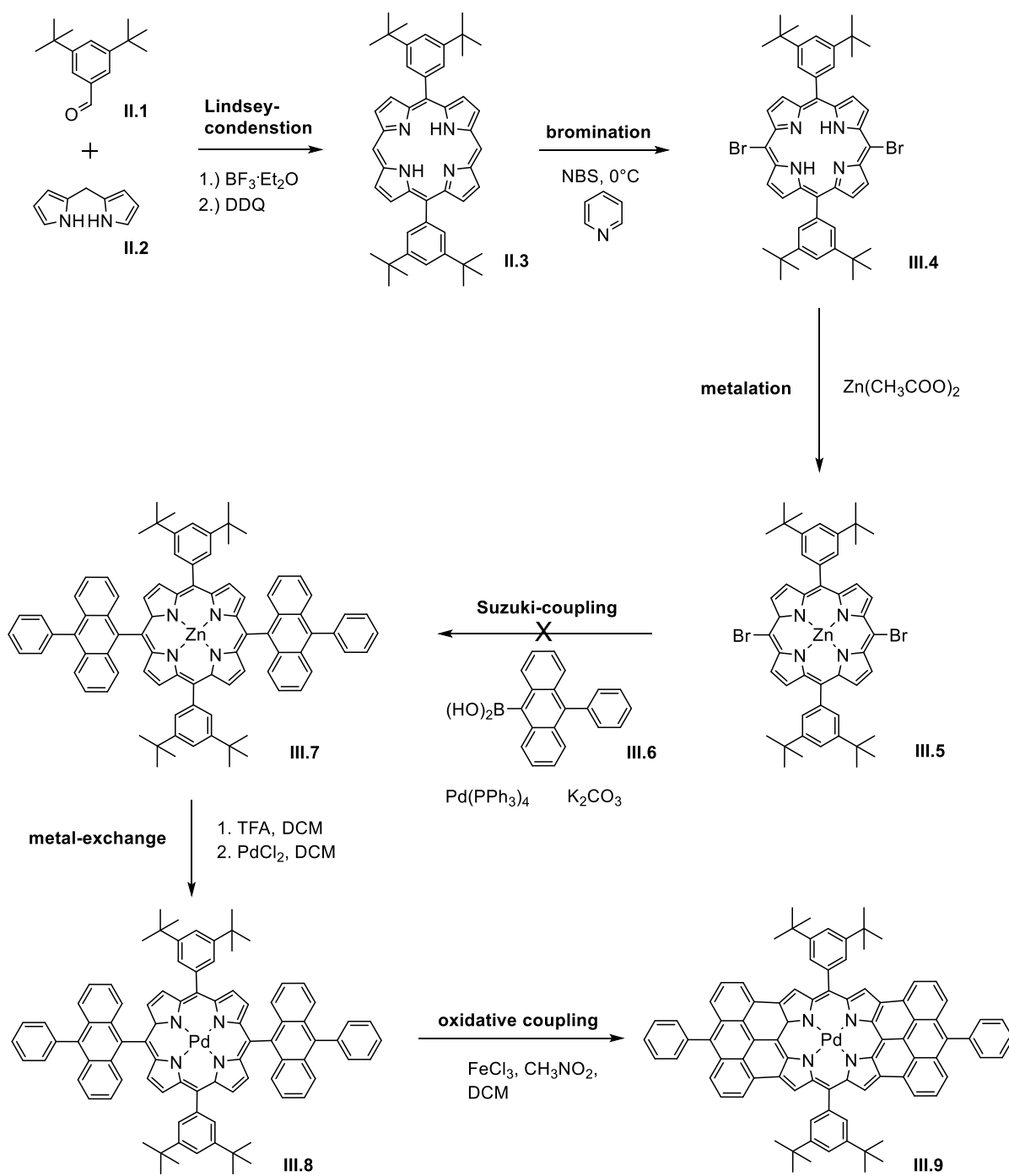


Figure 4.57: Third synthetic plan.

4.3.4 Fourth reaction scheme

In order to circumvent the problem, an alternative path was chosen, a reverse Suzuki-coupling, where the 10-phenyl-anthracene moiety possesses the bromo-group. Therefore, the porphyrin **III.4** was subjected to a Suzuki-Miyaura-Borylation and only then the Suzuki-coupling was performed.

4,4,5,5-Tetramethyl-1,3,2-dioxaborolane, Et₃N and 1,2-dichloroethan were added to 5,15-dibromo-10,20-bis(3,5-di-*tert*-butylphenyl)porphyrin **III.4** and PdCl₂(PPh₃)₂. Much care was taken to minimize the amount of oxygen present by replacing it nitrogen via purging and degassing and bubbling of the solution with nitrogen. Subsequently the mixture was heated at 90 °C overnight. Silica gel chromatography and following evaporation resulted in purple crystals of 5,15-bis(3,5-di-*tert*-butylphenyl)-10,20-bis(4,4,5,5-tetramethyl-1,3,2-dioxaborolan-2-yl)porphyrin **IV.5** in 52% yield (Figure 4.58).

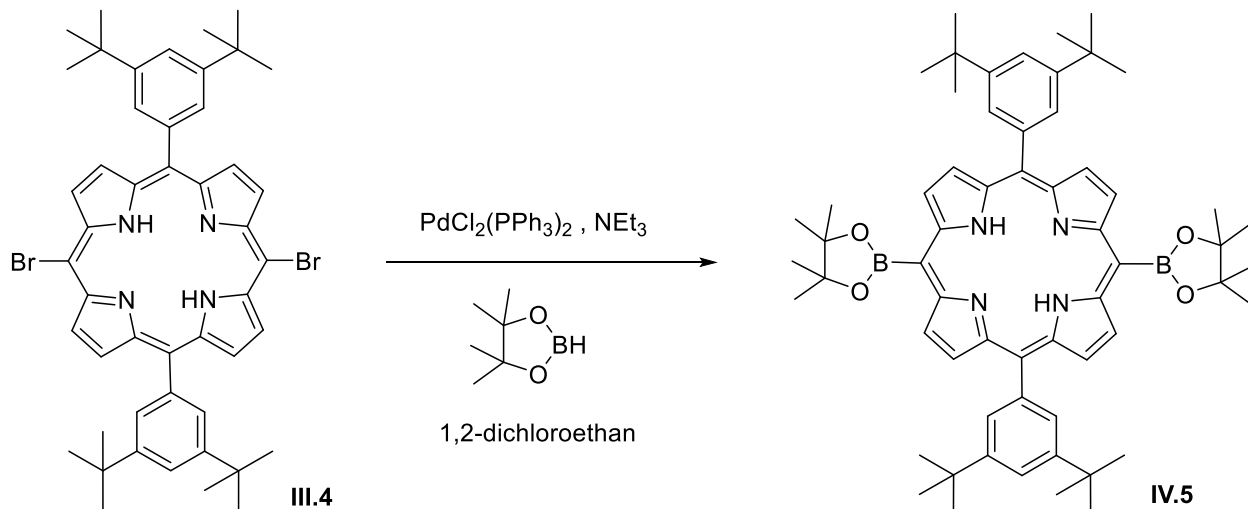


Figure 4.58: Miyaura-borylation of 5,15-dibromo-10,20-bis(3,5-di-*tert*-butylphenyl)porphyrin **III.4** with 4,4,5,5-tetramethyl-1,3,2-dioxaborolane forming 5,15-bis(3,5-di-*tert*-butylphenyl)-10,20-bis(4,4,5,5-tetramethyl-1,3,2-dioxaborolan-2-yl)porphyrin **IV.5**.

The ¹H-NMR spectrum in Figure 4.59 shows the matching signals 5,15-bis(3,5-di-*tert*-butylphenyl)-10,20-bis(4,4,5,5-tetramethyl-1,3,2-dioxaborolan-2-yl)porphyrin **IV.5** as described in literature. The H_{Bpin} signal is located at 1.84 ppm. The MALDI-TOF spectrum displays a weight matching the calculated weight for porphyrin **IV.5** (Figure 4.60).

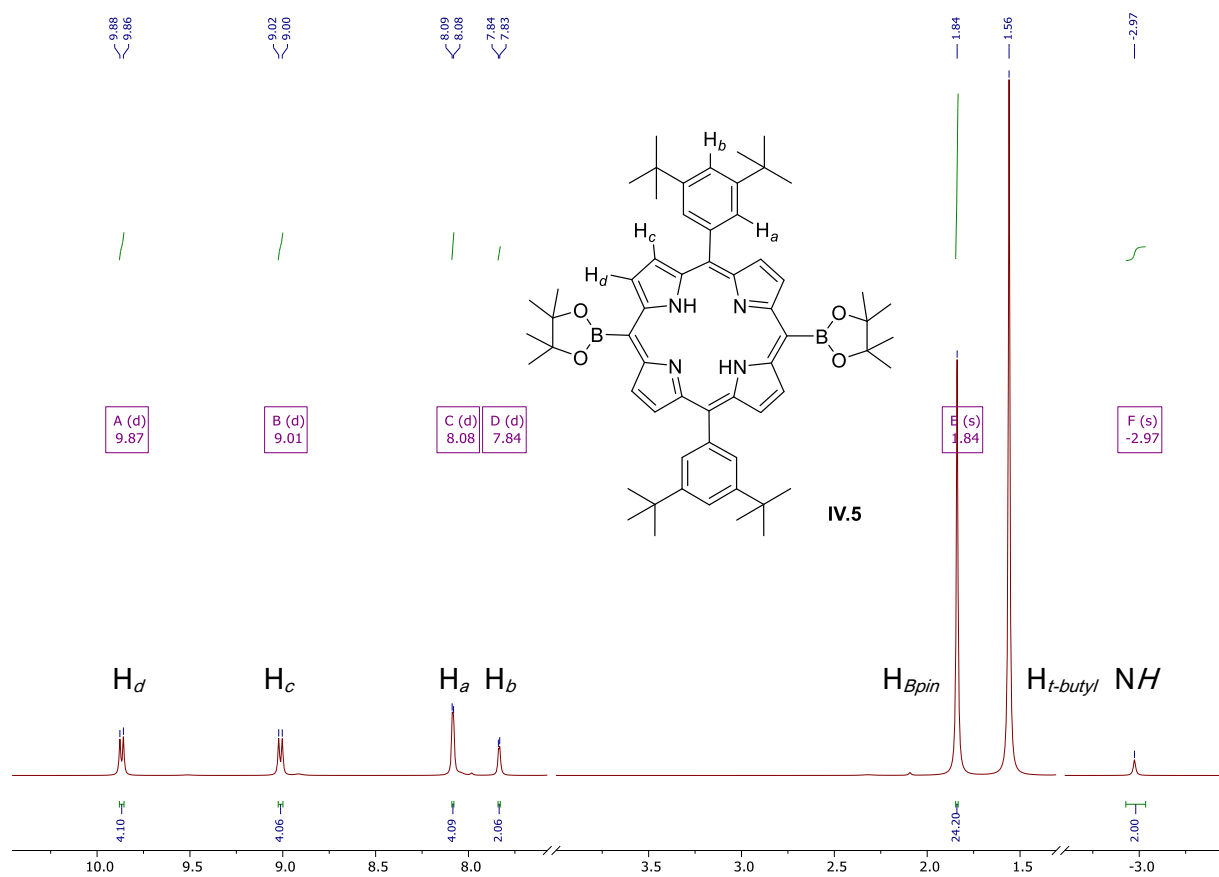


Figure 4.59: ^1H -NMR spectrum of 5,15-bis(3,5-di-*tert*-butylphenyl)-10,20-bis(4,4,5,5-tetramethyl-1,3,2-dioxaborolan-2-yl)porphyrin **IV.5**.

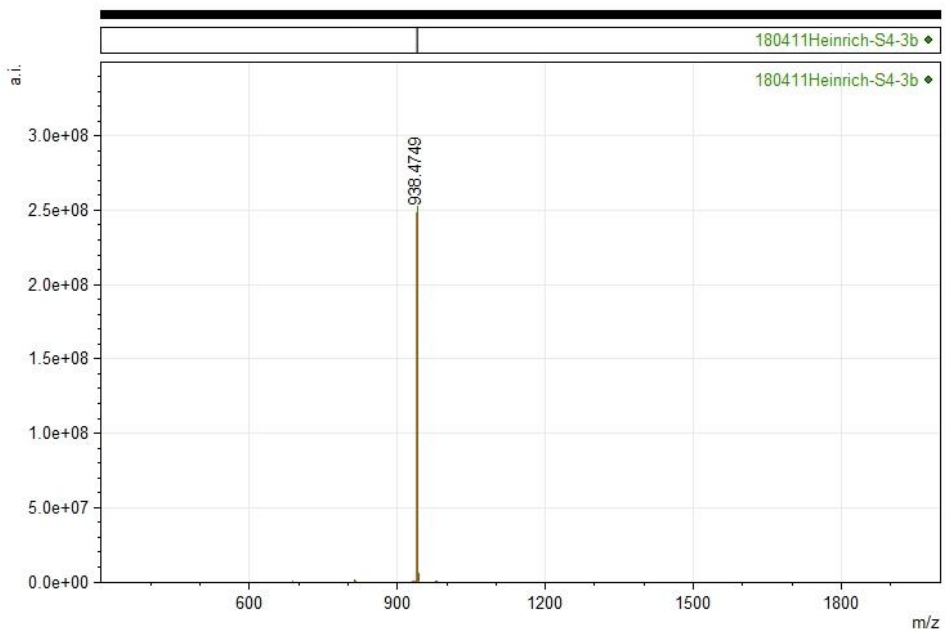


Figure 4.60: MALDI-TOF spectrum of 5,15-bis(3,5-di-*tert*-butylphenyl)-10,20-bis(4,4,5,5-tetramethyl-1,3,2-dioxaborolan-2-yl)porphyrin **IV.5**.

Figure 4.61 displays only a slight red-shift of the absorbed wavelengths upon exchange of the bromine groups with Bpin moieties.

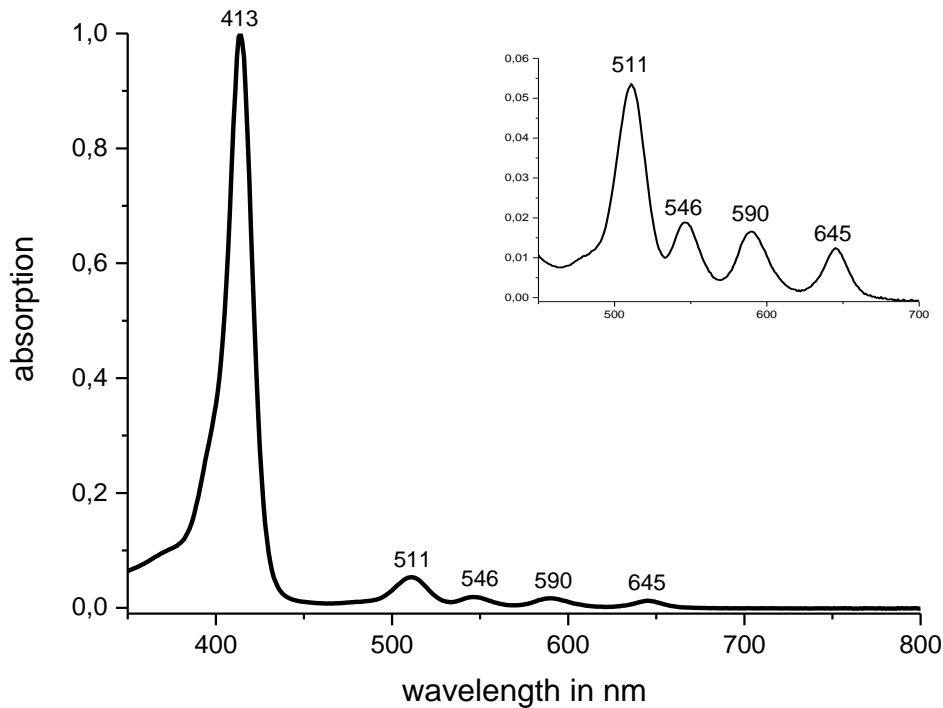


Figure 4.61: Normalized UV-Vis spectrum of 5,15-bis(3,5-di-*tert*-butylphenyl)-10,20-bis(4,4,5,5-tetramethyl-1,3,2-dioxaborolan-2-yl)porphyrin **IV.5**. The inset shows scaled-up Q-bands.

Synthesis of porphyrin **IV.5** was successful, but the following Suzuki-coupling failed (Figure 4.62).

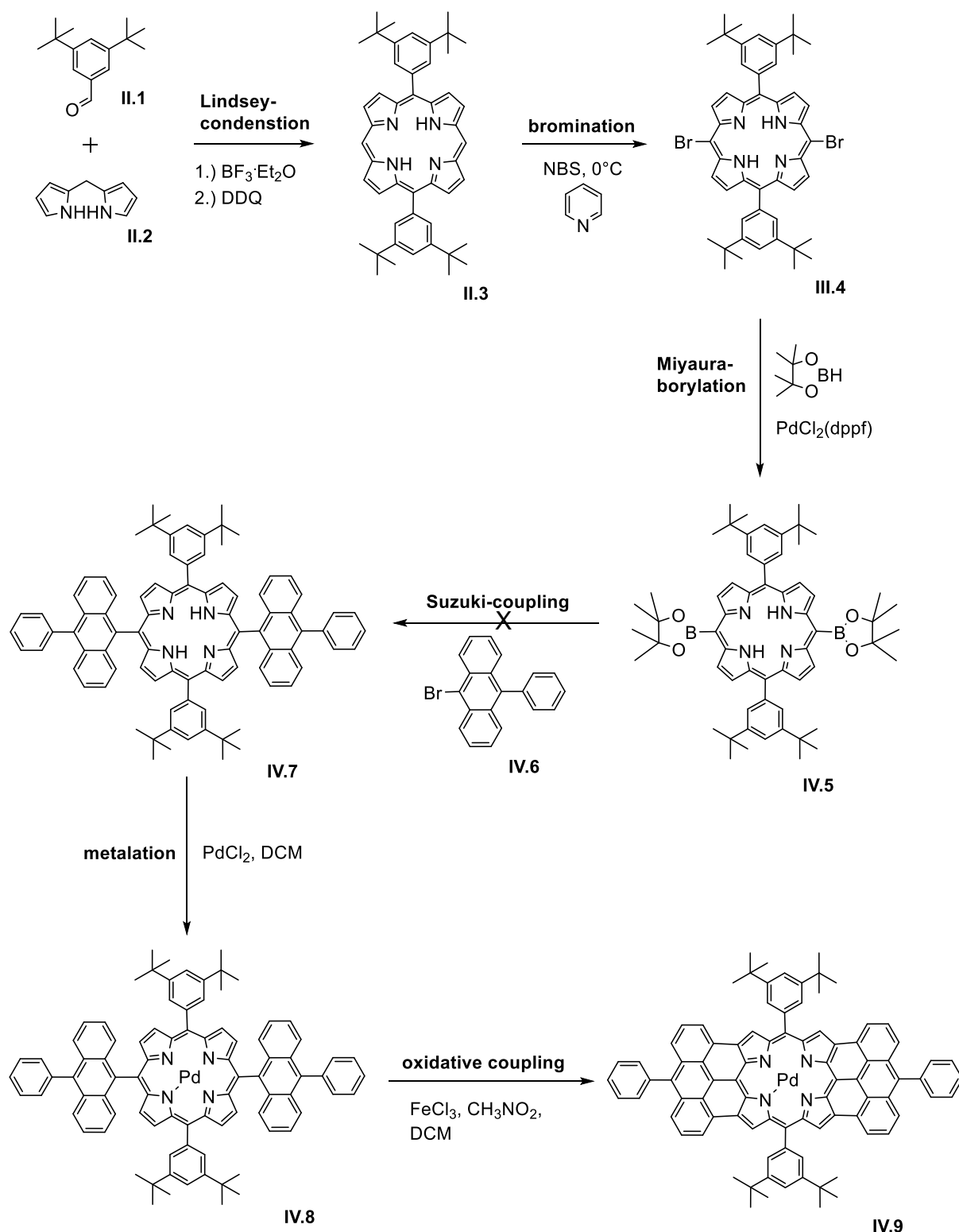


Figure 4.62: Fourth synthetic plan.

4.3.5 Fifth reaction scheme

Since the reactivity of the porphyrin is strongly correlated with the 3D structure and potential metalation, Zn^{2+} was introduced to porphyrin **IV.5** prior to the Suzuki-coupling.

5,15-bis(3,5-di-*tert*-butylphenyl)-10,20-bis(4,4,5,5-tetramethyl-1,3,2-dioxaborolan-2-yl)porphyrin **IV.5** and $Zn(CH_3COO)_2$ were dissolved in a mixture of DCM and methanol. The solution was refluxed for 2 h, filtered through a silica gel pad and evaporated until dryness resulting in a raspberry coloured solid [5,15-bis(3,5-di-*tert*-butylphenyl)-10,20-bis(4,4,5,5-tetramethyl-1,3,2-dioxaborolan-2-yl)porphyrinato]zinc(II) **V.6** in 64% yield (Figure 4.63).

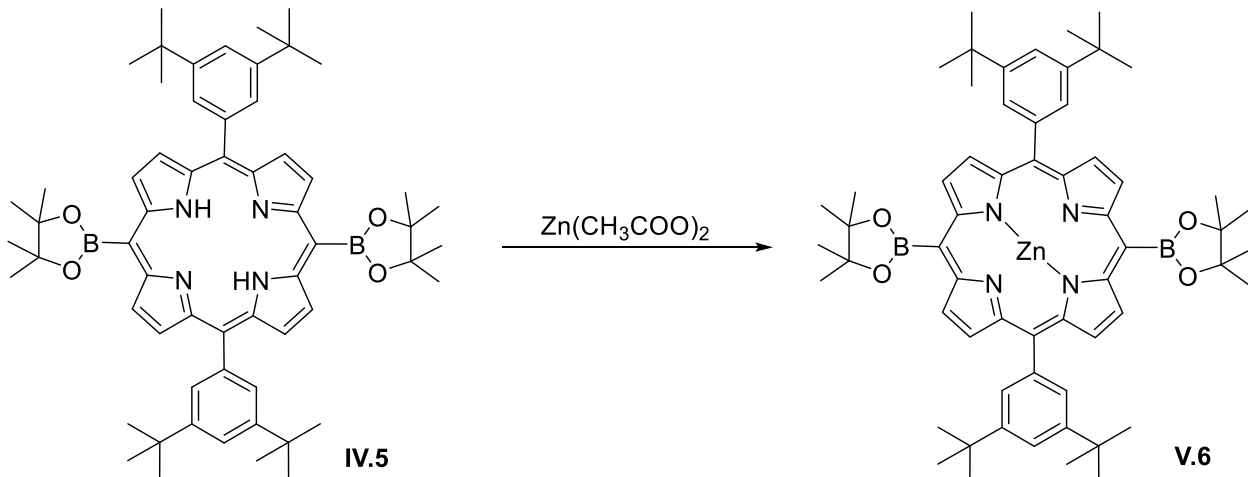


Figure 4.63: Metalation of 5,15-bis(3,5-di-*tert*-butylphenyl)-10,20-bis(4,4,5,5-tetramethyl-1,3,2-dioxaborolan-2-yl)porphyrin **IV.5** with zinc acetate yielding [5,15-bis(3,5-di-*tert*-butylphenyl)-10,20-bis(4,4,5,5-tetramethyl-1,3,2-dioxaborolan-2-yl)porphyrinato]zinc(II) **V.6**.

The 1H -NMR spectrum in Figure 4.64 shows the matching signals of [5,15-bis(3,5-di-*tert*-butylphenyl)-10,20-bis(4,4,5,5-tetramethyl-1,3,2-dioxaborolan-2-yl)porphyrinato]zinc(II) **V.6** as described in literature. The NH signal previously visible around -3 ppm is not detectable any longer, suggesting the successful metallation with Zn^{2+} . The MALDI-TOF spectrum displays a weight matching the calculated weight for porphyrin **V.6** (Figure 4.62).

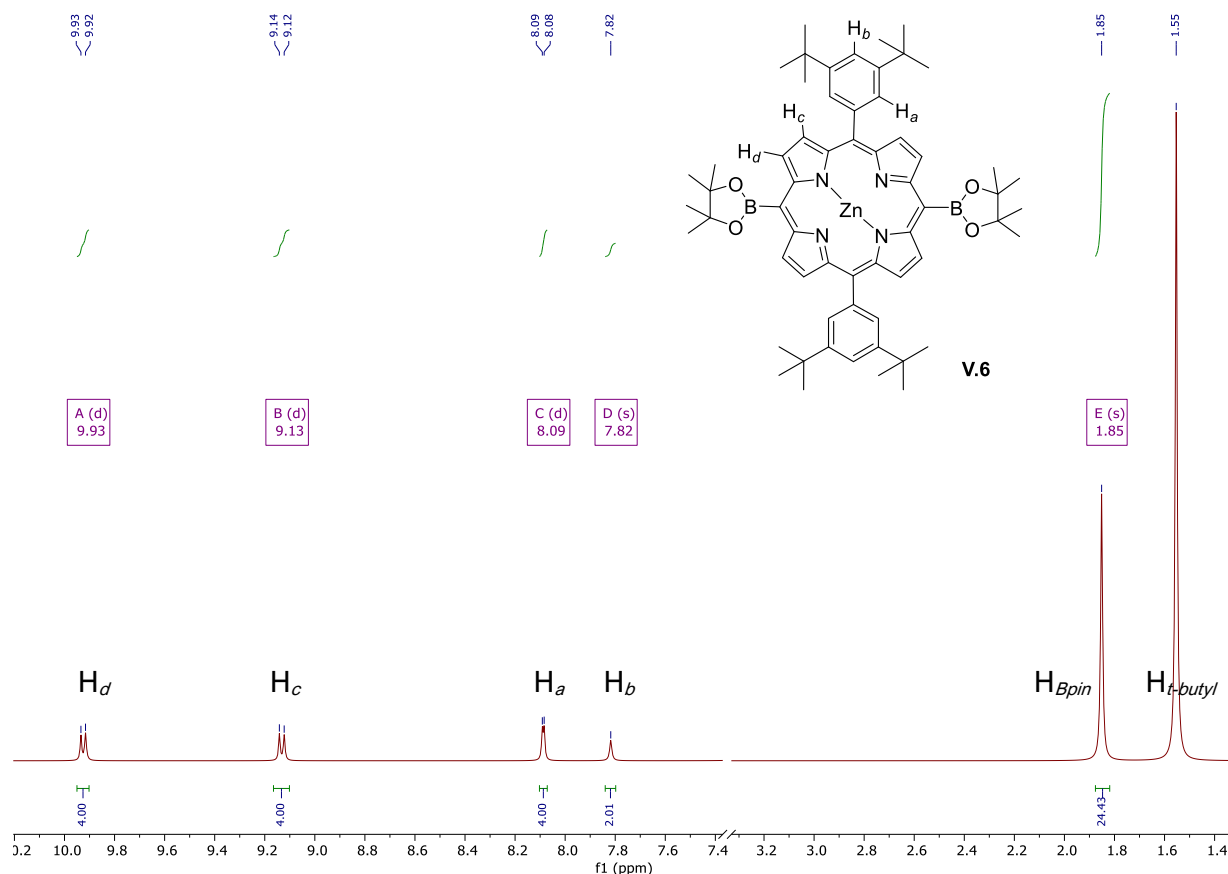


Figure 4.64: ¹H-NMR spectrum of [5,15-bis(3,5-di-*tert*-butylphenyl)-10,20-bis(4,4,5,5-tetramethyl-1,3,2-dioxaborolan-2-yl)porphyrinato]zinc(II) **V.6**.

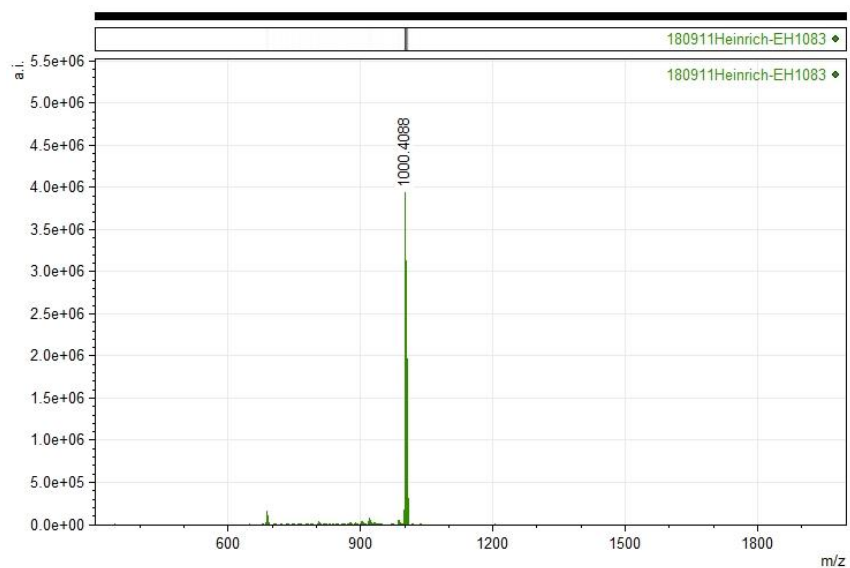


Figure 4.65: MALDI-TOF spectrum of [5,15-bis(3,5-di-*tert*-butylphenyl)-10,20-bis(4,4,5,5-tetramethyl-1,3,2-dioxaborolan-2-yl)porphyrinato]zinc(II) **V.6**.

Figure 4.66 clearly shows the effect of Zn-insertion into 5,15-bis(3,5-di-*tert*-butylphenyl)-10,20-bis(4,4,5,5-tetramethyl-1,3,2-dioxaborolan-2-yl)porphyrin **IV.5**. While the Soret-band remains mostly stoic, the Q-band decreases in the intensity of the peaks.

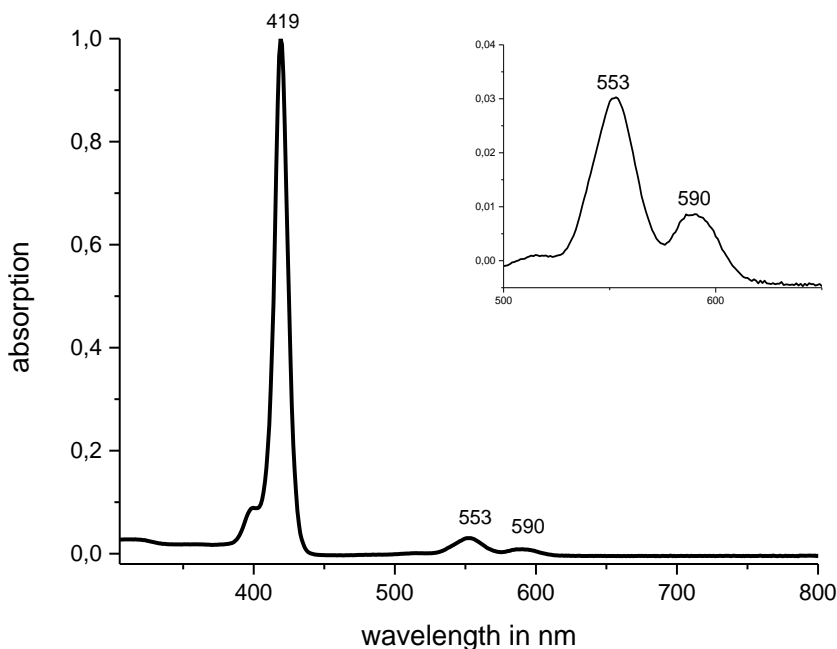


Figure 4.66: Normalized UV-Vis spectrum of [5,15-bis(3,5-di-*tert*-butylphenyl)-10,20-bis(4,4,5,5-tetramethyl-1,3,2-dioxaborolan-2-yl)porphyrinato]zinc(II) **V.6**. The inset shows scaled-up Q-bands.

For the following Suzuki-coupling the metalated porphyrin [5,15-bis(3,5-di-*tert*-butylphenyl)-10,20-bis(4,4,5,5-tetramethyl-1,3,2-dioxaborolan-2-yl)porphyrinato]zinc(II) **V.6**, 9-bromo-10-phenanthracene, potassium hydroxide, 2-dicyclohexylphosphino-2',6'-dimethoxybiphenyl and tris(dibenzylideneacetone)dipalladium(0) were dried under vacuum for 6h. Afterwards dry m-xylol was added. The reaction mixture was freeze-thaw degassed and subsequently purged with nitrogen. The solution was stirred for 5 h at 90 °C. Filtration through a silica plug and recrystallization gave a purple-reddish solid of porphyrin **V.7** in 65% yield (Figure 4.67).

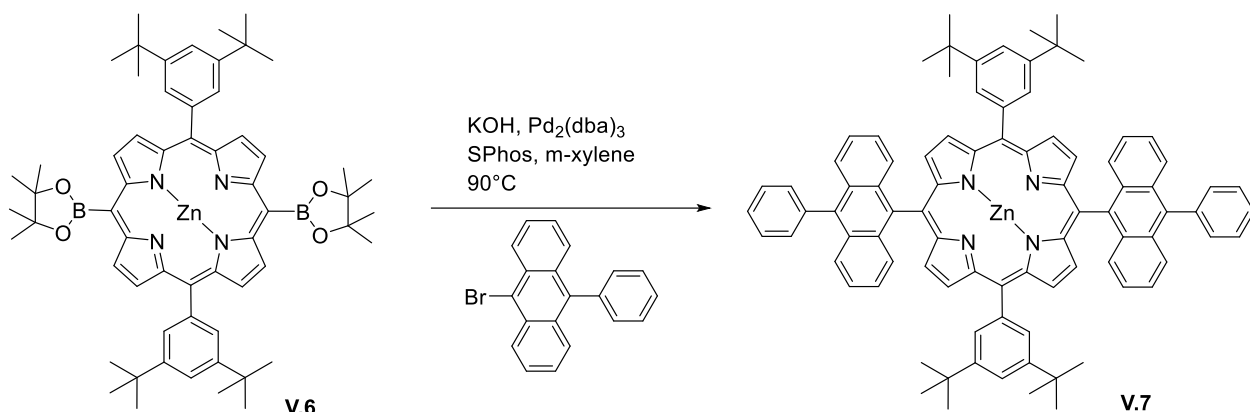


Figure 4.67: Suzuki coupling of [5,15-bis(3,5-di-*tert*-butylphenyl)-10,20-bis(4,4,5,5-tetramethyl-1,3,2-dioxaborolan-2-yl)porphyrinato]zinc(II) **V.6** with 9-Bromo-10-phenylanthracene yielding porphyrin **V.7**.

The ¹H-NMR spectrum in Figure 4.68 shows the signals of porphyrin **V.7**. Due to the increase in aromatic H signals, it is no longer possible to precisely match the protons to the NMR-signals. The MALDI-TOF spectrum displays a weight matching the calculated weight for porphyrin **V.7** (Figure 4.69).

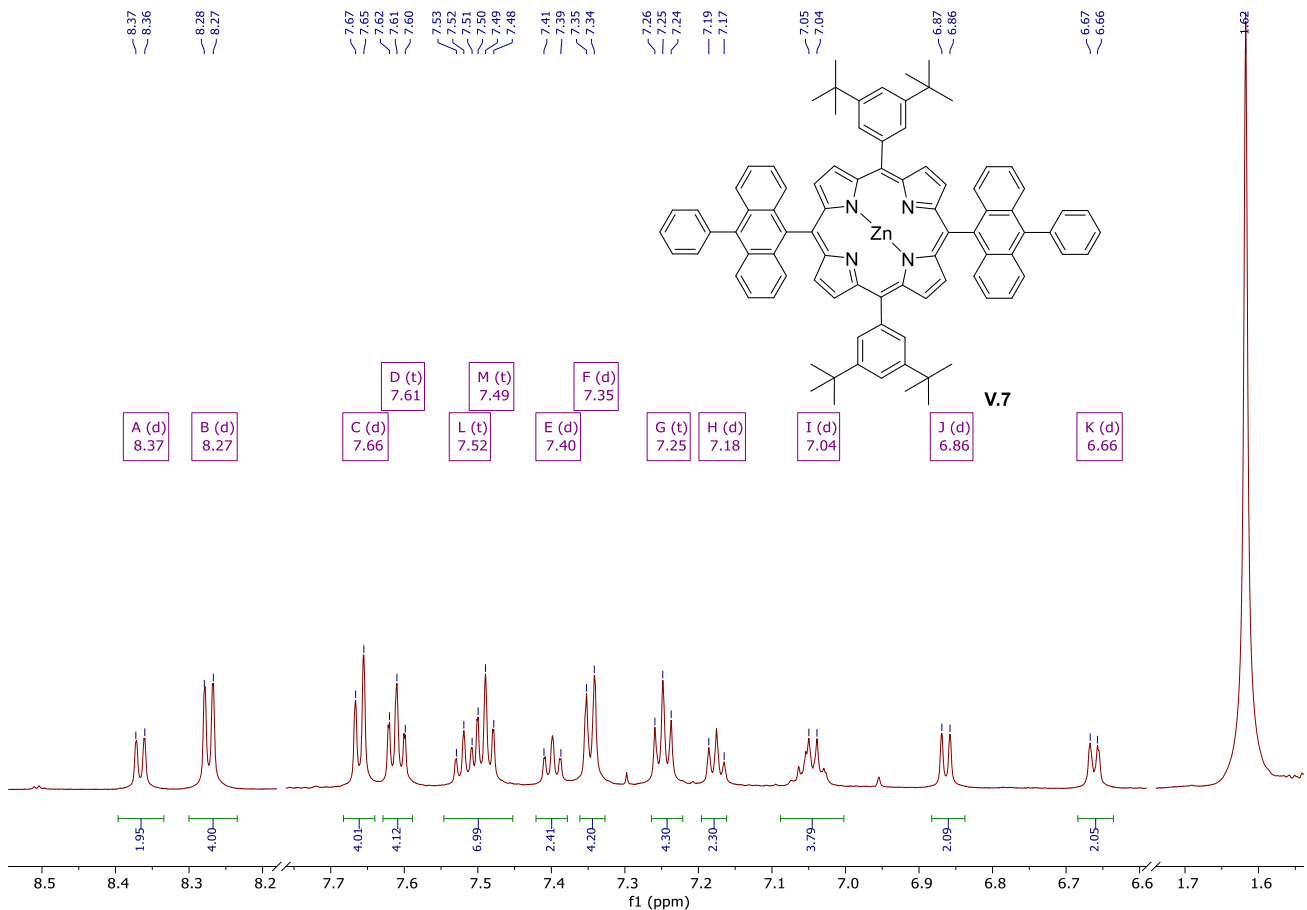


Figure 4.68: ¹H-NMR spectrum of porphyrin V.7.

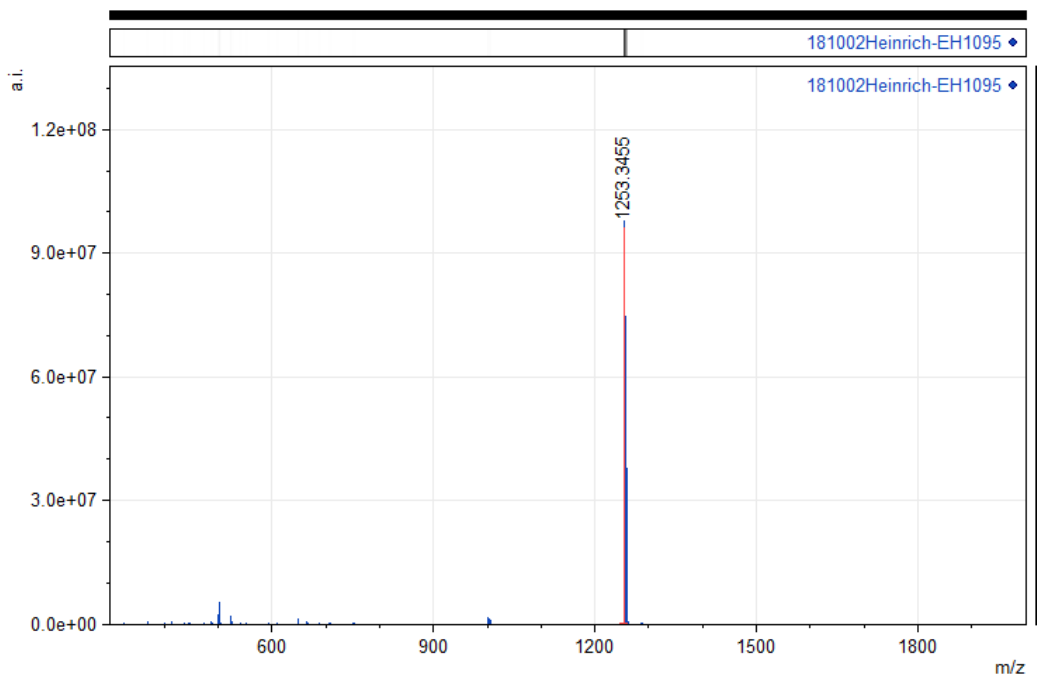


Figure 4.69: MALDI-TOF spectrum of porphyrin V.7.

Upon increase of the aromatic system via addition of phenyl-anthracene-groups the Soret-band and Q-band absorption is slightly redshifted (Figure 4.70).

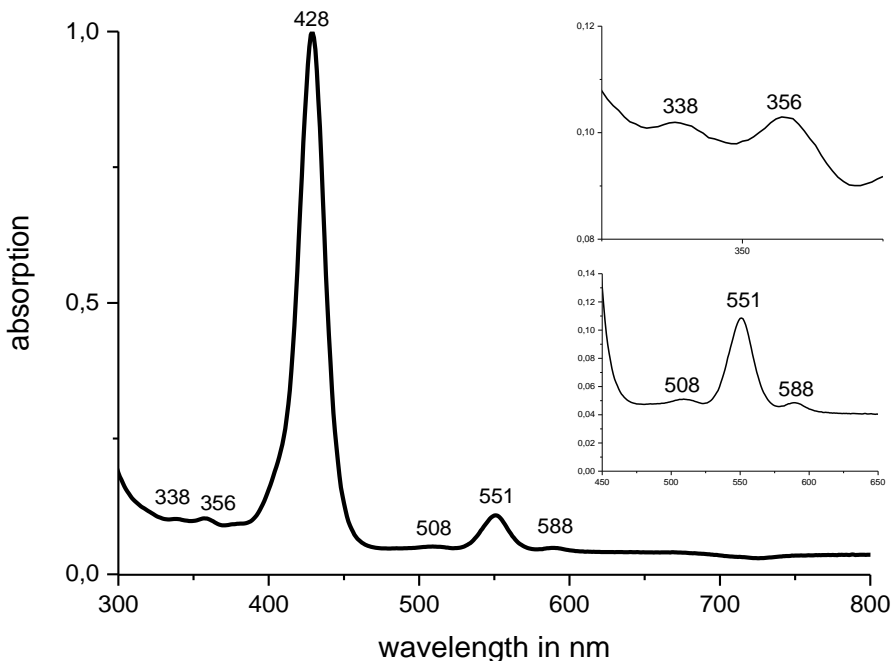


Figure 4.70: Normalized UV-Vis spectrum of porphyrin **V.7**. The inset shows scaled-up Q-bands.

The successful Suzuki-coupling underlined the importance of a molecules 3D structure for its reactivity. The resulting fifth reaction scheme is depicted in Figure 4.71.

The following metal-exchange from zinc to palladium could be performed directly without prior demetalation with TFA or alternatively, in the traditional way of demetalation and insertion of the new metal species, yielding porphyrin **V.8**.

Porphyrin **V.7** and $\text{PdCl}_2(\text{PhCN})_2$ were dissolved in benzonitrile and refluxed under nitrogen flow at 140 °C. Once the reaction was completed, the solvent was evaporated under reduced pressure. Flash chromatography and precipitation by addition of methanol resulted in orange crystals of porphyrin **V.8** in 70% yield (Figure 4.72).

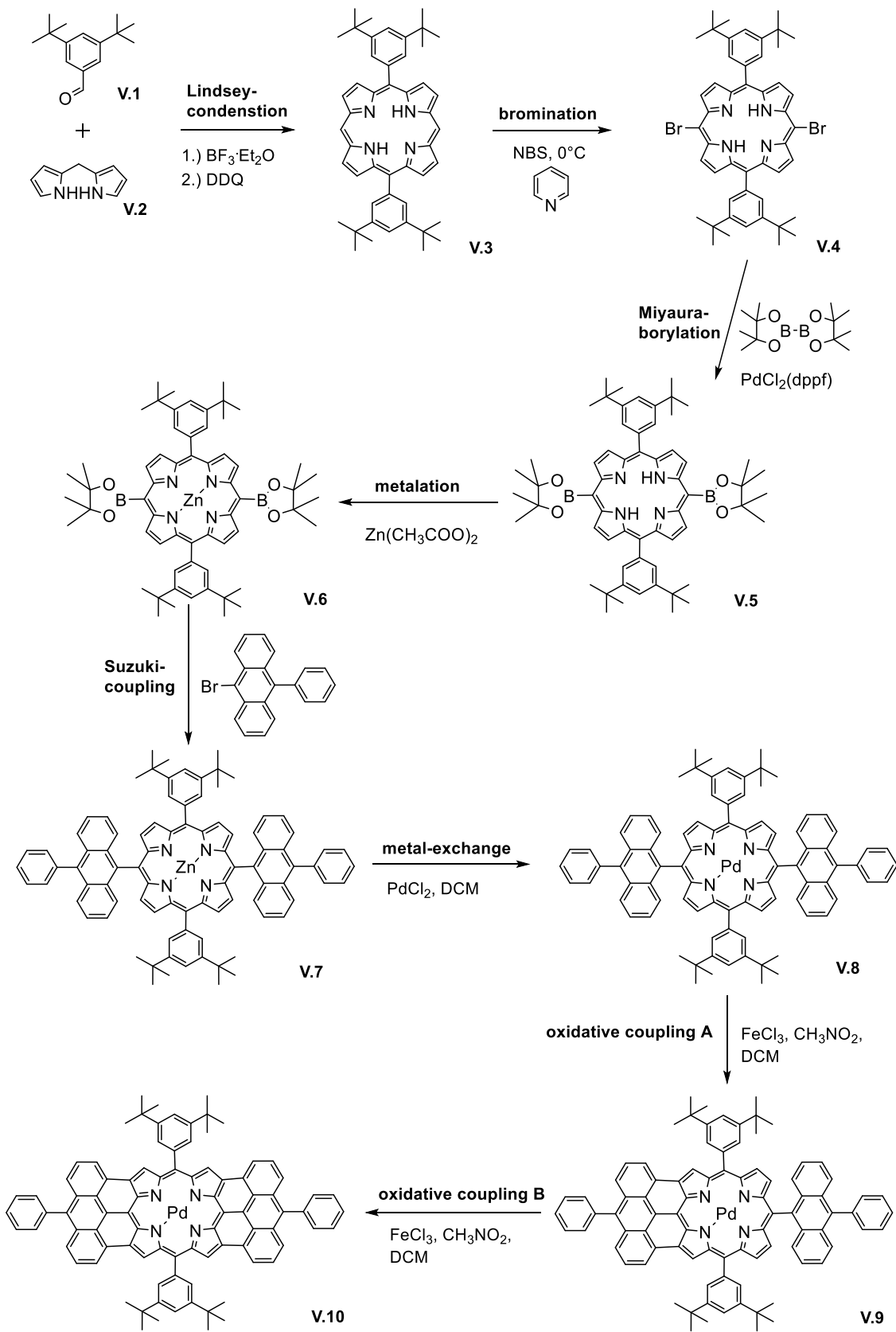


Figure 4.71: Fifth synthetic plan, fourth modification.

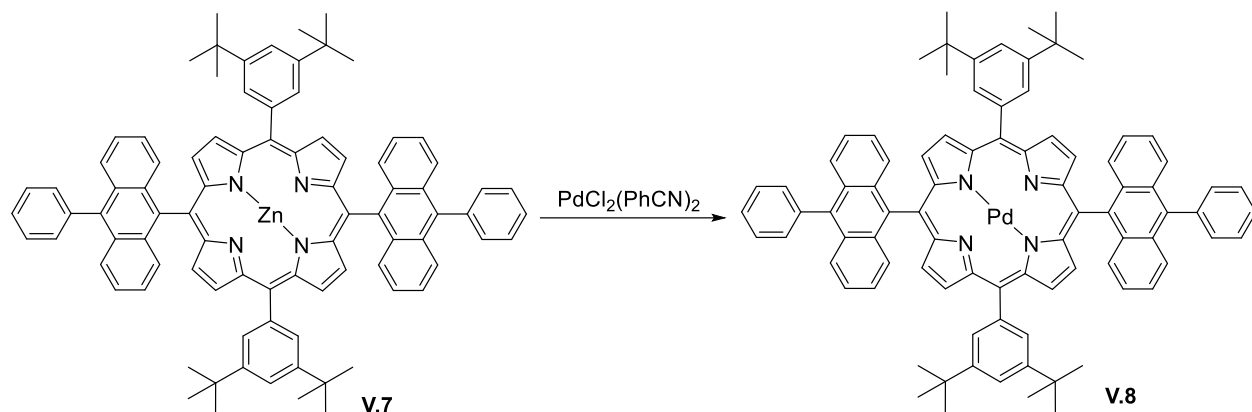


Figure 4.72: Metal-exchange of the zinc core in porphyrin **V.7** with bis(benzonitrile)palladium(II) chloride forming porphyrin **V.8**, now with a palladium core.

The MALDI-TOF spectrum displays a weight matching the calculated weight for porphyrin **V.7** (Figure 4.73).

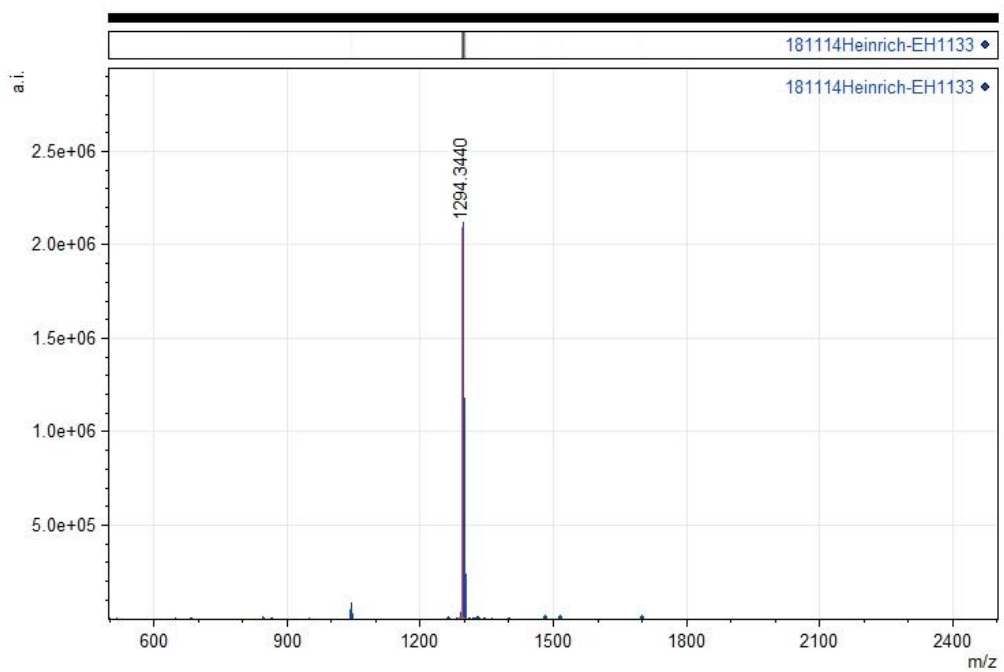


Figure 4.73: MALDI-TOF spectrum of porphyrin **V.8**.

Figure 4.74 shows that change of the metal ion from Zn^{2+} to Pd^{2+} almost didn't exhibit any effect at all.

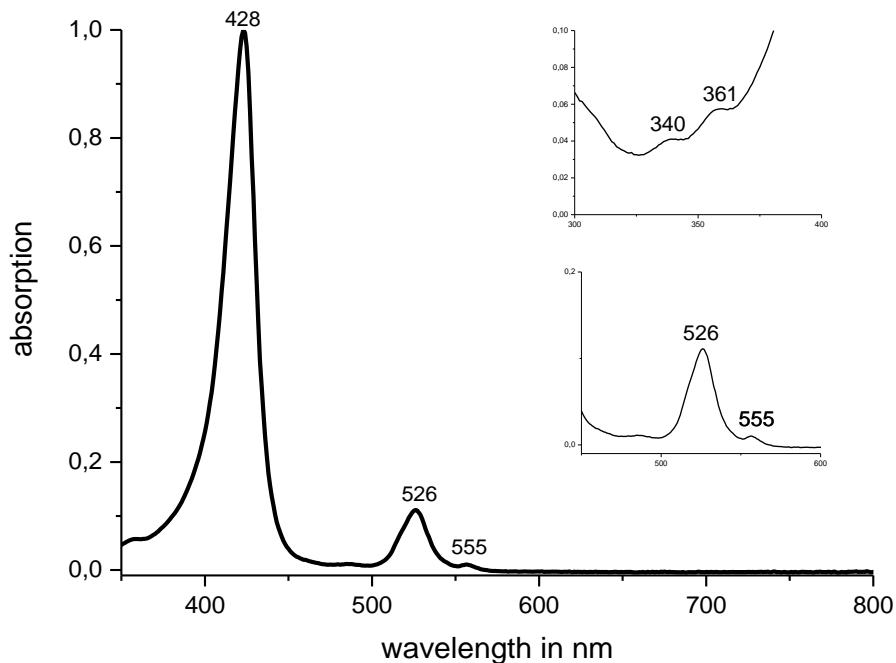


Figure 4.74: Normalized UV-Vis spectrum of porphyrin V.8. The inset shows scaled-up Q-bands.

One sided fusion was performed afterwards with iron(III) chloride as the oxidising agent. In detail, porphyrin V.8 was dissolved in dry DCM and the mixture was bubbled for 30 min with nitrogen. Here the presence of water had to be strictly avoided and work under inert conditions was obligatory. Iron(III) chloride, dissolved in nitromethane was added dropwise. The solution was stirred at room temperature and monitored by TLC. At completion, the solvents were evaporated under reduced pressure. Chromatography through silica resulted in a reddish brown porphyrin V.9. Chlorination with one additional chlorine-atom as a side reaction could not be avoided. The one time fused porphyrin V.9 could be nonetheless prepared as the main component in 57% yield (Figure 4.75). Separation of main and side product with neither possible by preparative chromatography nor by crystallization.

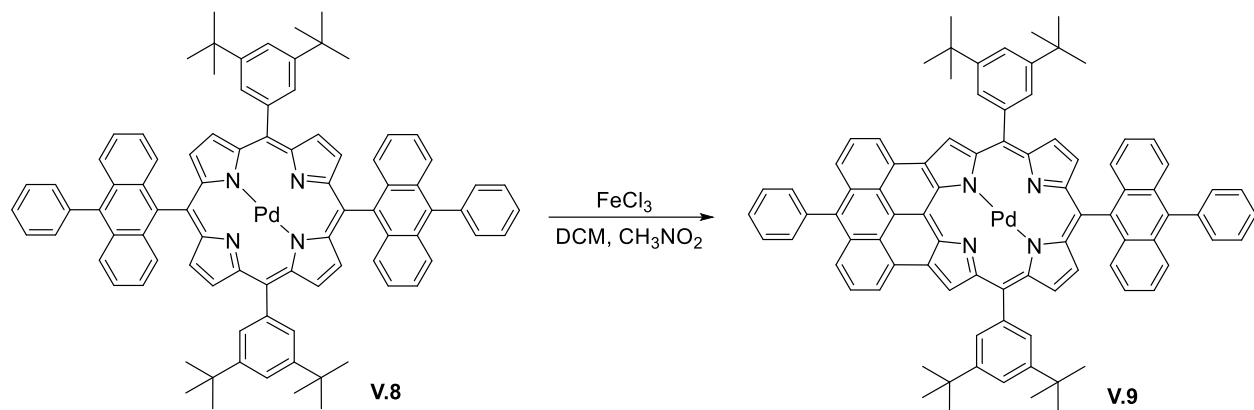


Figure 4.75: Cyclodehydrogenation reaction of porphyrin **V.8** with iron(III) chloride yielding on one side fused porphyrin **V.9**.

The MALDI-TOF spectrum displays a weight matching the calculated weight for porphyrin **V.9** as well as a one time chlorinated derivative (Figure 4.76).

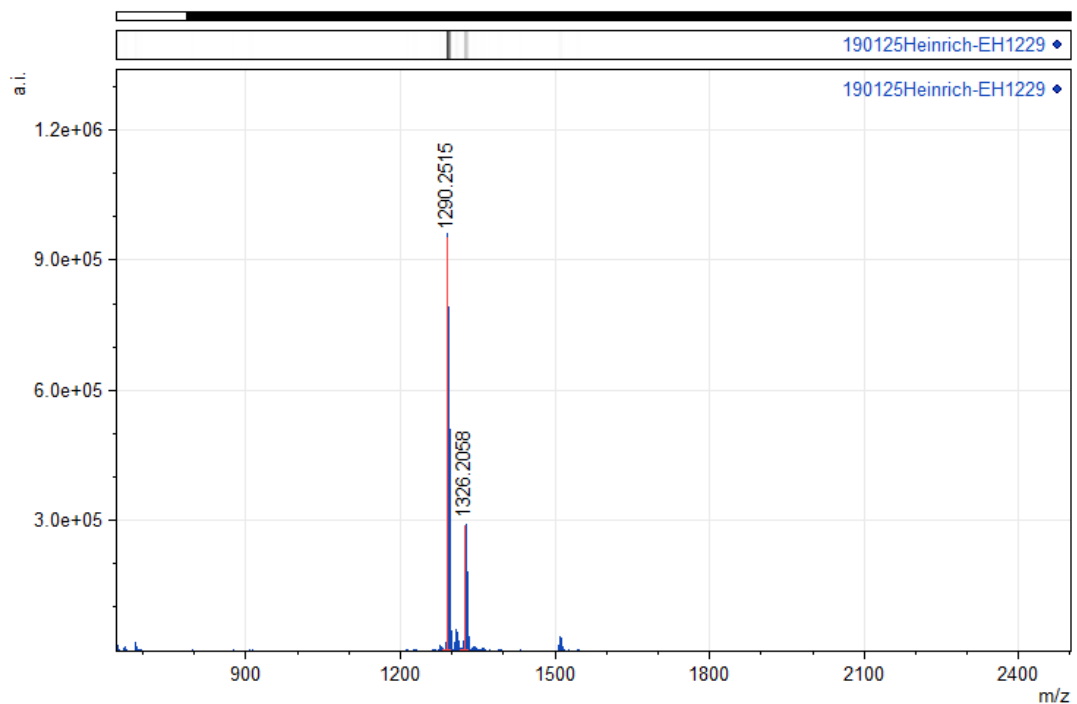


Figure 4.76: MALDI-TOF spectrum of porphyrin **V.9**. One time chlorinated derivative of porphyrin **V.9** is also visible at 1326.21. Separation proved impossible due to similar R_f values.

The biggest impact on the absorption spectrum of all the structural modification can be seen in Figure 4.77. Once the introduced aromatic system of phenyl-anthracene is able to conjugate with the aromatic system of the porphyrin core structure after oxidative coupling on one side, the effect is dramatic. The Soret-band signal has increased from only one peak centred around 400 nm to roughly 5 peaks in the area between 300 to 600 nm. Additionally the Q-band signals have been dramatically red-shifted from around 500 nm to now 740 and 820 nm.

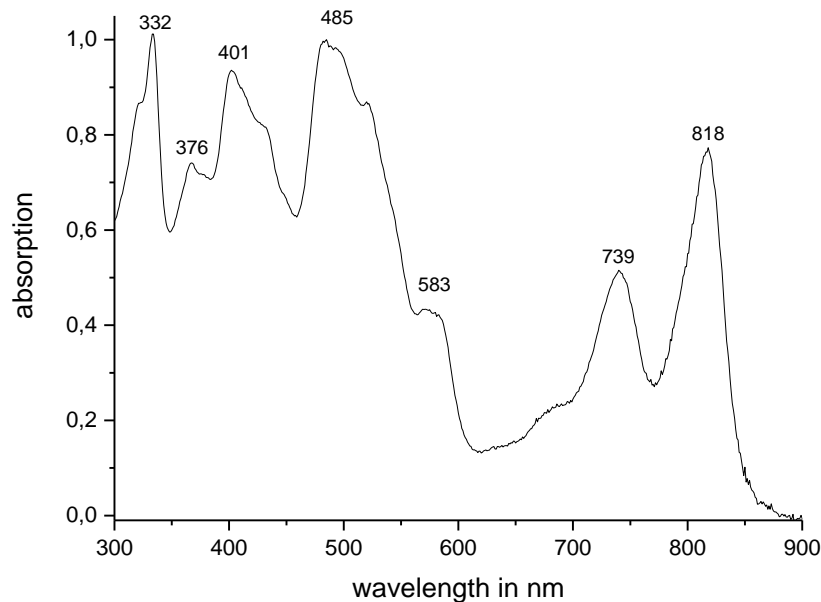


Figure 4.77: Normalized UV-Vis spectrum of porphyrin **V.9**.

The second fusion and final step of the syntheses was performed in a similar fashion as the previous. Porphyrin **V.9** and scandium(III) triflate were dissolved in dry DCM. The mixture was bubbled for 30 min with nitrogen. Iron(III) chloride dissolved in nitromethane was added dropwise. The solution was stirred at room temperature and monitored by TLC. After filtration through a silica plug the porphyrin **V.10**, a purple solid, was achieved in 32% yield (Figure 4.78).

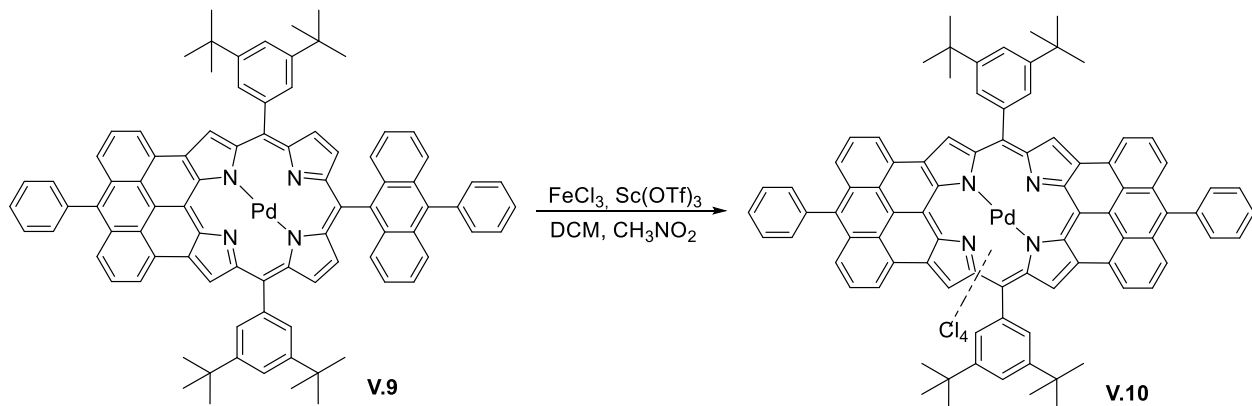


Figure 4.78: Cyclodehydrogenation reaction of porphyrin **V.9** with iron(III) chloride yielding fully fused porphyrin **V.10**.

This time the already before occurring chlorination side reaction dominated. Use of silver triflate as a chloride scavenger was without noticeable effect. The attempted second fusion was successful, but the product showed a mass corresponding to four added chloro-groups. Literature¹¹⁶⁻¹¹⁸ also states, that chlorination is an unavoidable side reaction and purification highly complicated due to very close R_f values and solubility issues. The alternative fusion with DDQ^{118,119} was unsuccessful and led to degradation of the starting material.

The four times chlorinated fully fused porphyrin showed an increased solubility, which is an enormous advantage given the very poor solubility and extreme stacking tendency of higher molecular porphyrins, which usually leads to aggregation and therefore almost total loss of desired material.^{116,120} Therefore, if the photophysical characteristics are fulfilled, the two times fused porphyrin with four chlorine-groups could be considered as an alternative sensitizer with the additional benefit of increased solubility, reduced aggregation tendency and potentially increased photostability.¹²¹

The MALDI-TOF spectrum displays a weight matching the calculated weight for porphyrin **V.10** as well as a the porphyrin species with 1 to 5 additional chlorine atoms (Figure 4.79).

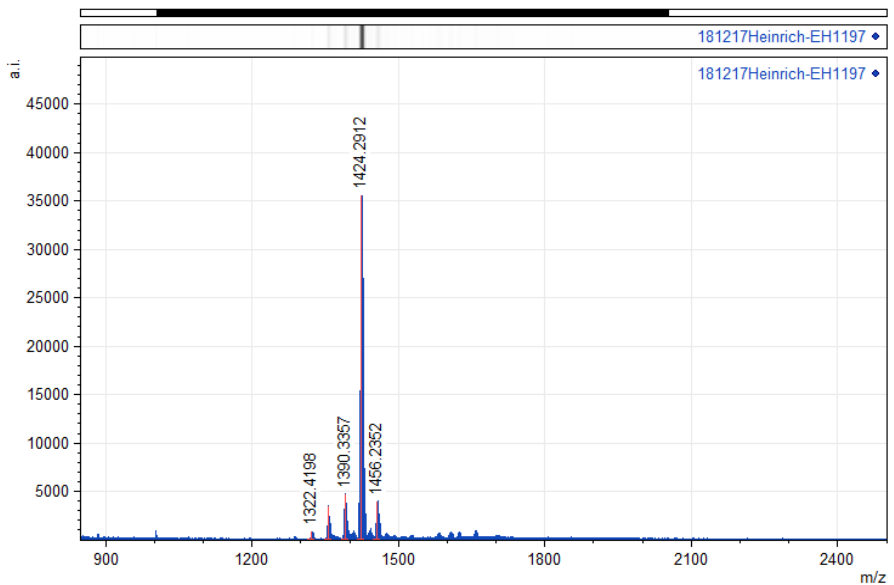


Figure 4.79: MALDI-TOF spectrum of porphyrin **V.10**. Derivatives of porphyrin **V.10** with 1,2,3 and 5 chlorines are also detected, but impossible to separate due to similar R_f values.

The UV-Vis spectrum of the chlorinated, fused porphyrin is shown in Figure 4.80. Once again the second enlargement of the aromatic system via oxidative coupling had a profound influence on the absorption spectrum. The Soret-band shows a decreased absorption intensity, resulting in one main peak at 532 nm. The Q-band absorption is even further red-shifted with a maximum at 934 nm.

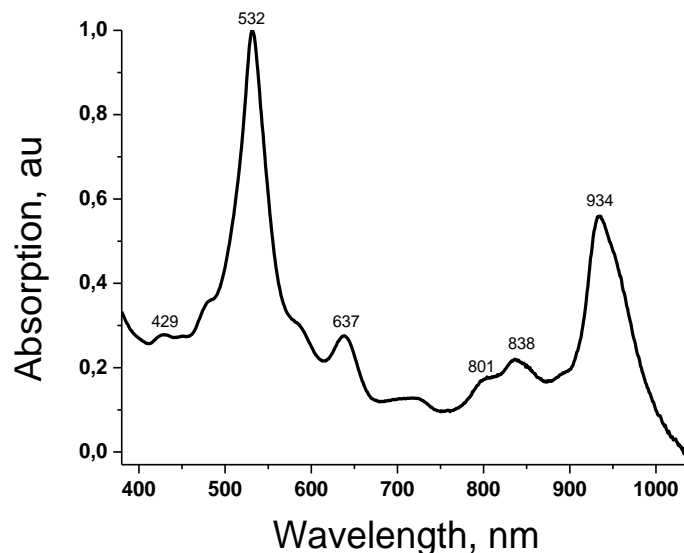


Figure 4.80: Normalized UV-Vis spectrum of porphyrin **V.10**.

For comparison, the maximum of the Q-band absorption of porphyrin **II.3** 501 nm and of the unfused porphyrin **V.8** is at 526 nm (Figure 4.81). Already a one-sided fusion leads to a Q-band absorption maximum at 818 nm, which is 292 nm. The second fusion reaction shifts the maximum by another 116 nm to the value of 934 nm, which is well in the IR-A-region. Hence, the design strategy of enlargement of the conjugated π -system via fusion proved successful.

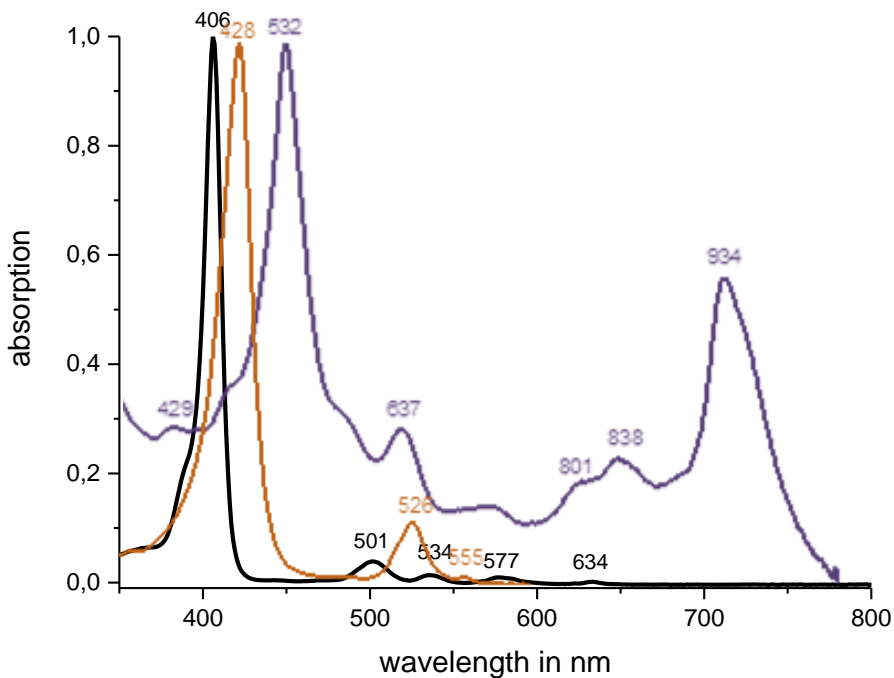


Figure 4.81: Normalized UV-Vis spectrum of porphyrin **II.3** (black line), porphyrin **V.8** (orange line) and porphyrin **V.10** (purple line).

This red-shift of the Q-band absorption ensures maximum penetration depth in human tissue, the least amount of photophysical damage and potentially the fitting of all TTA-UC signals into the tissue transparency window. The residual phosphorescence signal shows a maximum at 1400 nm (not shown). A matching dye for the TTA-UC measurement could be a TDI derivative¹²² (measurements pending).

5 Experimental section

5.1 Instruments

- NMR spectra: ¹H-NMR and ¹³C-NMR spectra were recorded using the liquid state spectrometer Bruker Avance 250, Bruker AC300 NMR and Bruker Avance 500 at 298 K. Thereby the solvent proton or the carbon signal served as an internal standard.
- Mass spectra: MALDI-TOF measurements were performed on a Bruker Reflex III with Dithranol as a matrix and an Advion Expression L spectrometer.
- Absorption spectra: A PerkinElmer Lambda 25 UV/Vis spectrometer obtained the electronic absorption spectra.
- Emission- and phosphorescence lifetime spectra: A home-built spectrometer was used for excitation and irradiation of samples.²⁷ Fluorescence spectra were recorded on a Spex Fluorolog 3 spectrometer. Fluorescence quantum yields were determined by the relative method using Lumogen Red as a reference¹²³.

5.2 Chemicals and other materials

The solvents and reagents were either prepared in the laboratory according to previously described procedure or purchased commercially from Sigma-Aldrich, Acros or Roth and used as obtained. Cyclohexanone, naphthalene and 1,2-dibromobenzene were commercially bought. 3,5-di(*tert*-butyl)benzaldehyde (TCI Chemicals), DDQ, carnauba wax, squalene, peanut oil (Acros), Triethylamine (Roth), DIPEA (Roth), boron trifluoride etherate (Merck), anhydrous dichloromethane (Aldrich) and 2-phenylpyrrole (Chempur) were used as received. Deuterated solvents used for ¹H-NMR spectroscopy were bought from Deutero GmbH. Dry DCM was acquired by distillation of a CaH₂ mix. The silica powder necessary for preparative column chromatography with the particle size of 0.063 – 0.200 mm was purchased from Marchery-Nagel.

5.3 Preparation of samples for temperature measurements

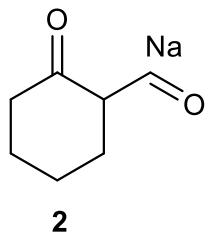
Vitrotubes (0.4 x 8 x 50 mm) were divided on two parts of 25 mm length, and one size was sealed using two component epoxy glue. Stock solutions of BODIPY dyes (10^{-3} M) and Pd-porphyrins (10^{-4} M) in toluene were prepared in advance. 100 μ L of porphyrin solution and 200 μ L of BODIPY solution were placed in 10 mL round-bottom flask and the solvent was evaporated to dryness under vacuum. 300 mg of peanut oil and 300 mg of squalene were added and the mixture was placed into ultrasonic bath at elevated temperatures (50-100 °C) to get a clear solution. Carnauba wax (400 mg) was added and a mixture was heated and homogenized in ultrasound bath until a clear solution was formed. Hot solution was injected into the preheated sealed vitrotube using a hot syringe. After cooling to room temperature the solution was solidified and formed a wax layer of a defined thickness inside a tube. The temperature of the sample during UC measurements was controlled using a thermostat and a Peltier element.

5.4 Syntheses

The characterization of the chemical substances was carried out via $^1\text{H-NMR}$ -, UV/Vis-, and MALDI-TOF spectroscopy.

5.4.1 Mixed porphyrin

5.4.1.1 2-Formylcyclohexanone sodium salt **2**



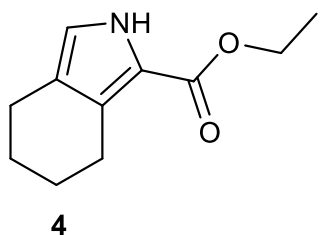
11.5 g (0.5 mol) of sodium lumps were dissolved in 150 mL of methanol. Cyclohexanone **1** (49.0 g; 0.5 mol) and methylformate (30 g; 0.5 mol) were added during 10 min. The reaction was stirred at room temperature overnight. 100 mL diethyl ether were added, the precipitate filtered and dried. The resulting 2-formylcyclohexanone sodium salt **2** was obtained as a white powder with 62% yield (45.88 g; 0.31 mol). The product was subjected to synthesis without further analysis.

5.4.1.2 Ethyl-(E)-((2-oxocyclohexylidene)methyl)glycinate **3**



2-Formyl-cyclohexanone-sodium salt **2** (40.0 g, 0.27 mol) was dissolved in ethanol (300 mL), glycine-ethyl-ester-hydrochloride (37.69 g, 0.27 mol) was added and the reaction stirred overnight at room temperature. The solvent was evaporated under reduced pressure resulting in 70% (39.88 g; 0.19 mol) of ethyl-((2-oxocyclohexylidene)methyl)glycinate **3** as a white solid. The product was subjected to synthesis without further analysis.

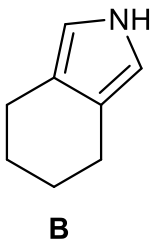
5.4.1.3 Ethyl-4,5,6,7-tetrahydro-2*H*-isoindole-1-carboxylate **4**



Sodium lumps (2.3 g, 0.10 mol) were dissolved in 200 mL ethanol, 20 g (0.10 mol) ethyl-((2-oxocyclohexylidene)methyl)glycinate **3** were added and the resulting solution was heated for 5 h at 40 °C. Afterwards the reaction mixture was allowed to cool down to room temperature. The product was extracted with DCM, which was further on evaporated in vacuum. Recrystallization from a mix 1:1 mix of ethanol and DCM yielded 30% (5.79 g, 0.03 mol) white crystalline ethyl-4,5,6,7-tetrahydro-2*H*-isoindole-1-carboxylate **4**.

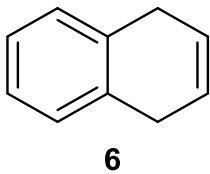
¹H-NMR (300 MHz, CD₂Cl₂): δ (ppm) 8.87 (br, s, 1H), 6.65 (d, 1H), 4.26 (q, 2H), 2.84–2.74 (m, 2H), 2.59–2.50 (m, 2H), 1.77–1.69 (m, 4H), 1.36 -1.29 (t, 3H).

5.4.1.4 4,5,6,7-Tetrahydro-2*H*-isoindole **B**



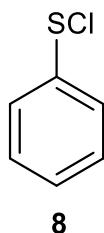
Ethyl-4,5,6,7-tetrahydro-2*H*-isoindole-1-carboxylate **4** (3.0 g, 0.02 mol) and 3 pieces of potassiumhydroxide were dissolved in 30 mL of ethylenglykol and refluxed for 60 min under nitrogen atmosphere. After cooling down to room temperature, the reaction mixture was poured into water, the organic layer separated, washed with water, dried over sodiumsulfate and concentrated through distillation in vacuum. Flash chromatography yielded 4,5,6,7-tetrahydro-2*H*-isoindole **B** (1.26 g, 0.01 mol, 67%).

5.4.1.5 1,4-Dihydronaphthalene **6**



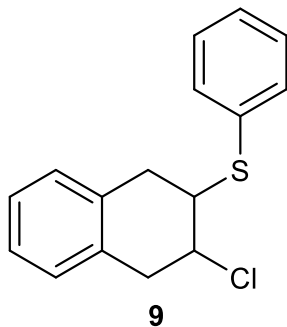
50.00 g (0.39 mol) Naphthalene **5** was dissolved in 500 mL ethanol. 50.00 g (2.00 mol) sodium was added within 20 min. Water was added and the solution was extracted with DCM. After the solvent was evaporated under reduced pressure 40.61 g (0.31 mol, 80 % yield) of liquid 1,4-dihydronaphthalene **6** was obtained. The product was subjected to synthesis without further analysis.

5.4.1.6 Phenylsulfenylchloride **8**



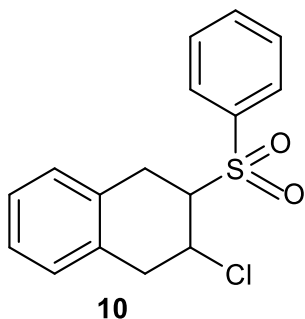
NCS (41.1 g, 0.31 mol) was dissolved in 200 mL DCM in a flask with argon atmosphere. After completed addition of 33.91 g (0.31 mol) thiophenol **7**, the mixture was stirred for additional 30min. Subsequently the resulting phenylsulfenylchloride **8** was utilized without further analysis for the reaction with 1,4-dihydronaphthalene **6**.

5.4.1.7 (3-Chloro-1,2,3,4-tetrahydronaphthalen-2-yl)- (phenyl)sulfane **9**



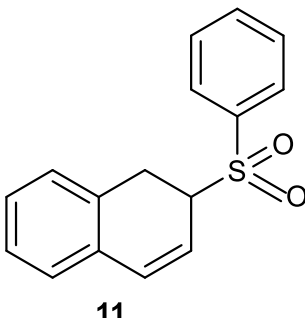
1,4-Dihydronaphthalene **6** (40.60 g, 0.31 mol) was mixed with 200 mL DCM in a flask under argon atmosphere. Phenylsulfenylchloride **8** was added slowly and the resulting mixture stirred for an 30 min. The solvent was evaporated under reduced pressure, leaving crude (3-chloro-1,2,3,4-tetrahydronaphthalen-2-yl)(phenyl)sulfane **9**.

5.4.1.8 2-Chloro-3-(phenylsulfonyl)-1,2,3,4-tetrahydronaphthalene **10**



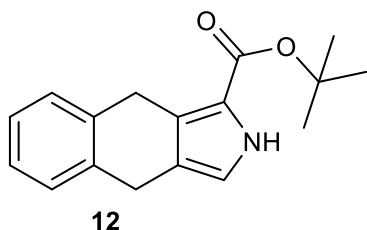
76.95 g (0.28 mol) of (3-chloro-1,2,3,4-tetrahydronaphthalen-2-yl)(phenyl)sulfane **9** were dissolved in 200 mL THF and cooled with an ice bath. Oxone (85.23 g, 0.56 mol) dissolved in 200 mL water was added. The mixture was allowed to stir at room temperature for two days. Thereafter it was diluted with 500 mL water and extracted with DCM. The solvent was evaporated and the crude product recrystallized from ethanol. This resulted in 49.02 g (0.16 mol, 57% yield) of yellowish 2-chloro-3-(phenylsulfonyl)-1,2,3,4-tetrahydronaphthalene **10**.

5.4.1.9 2-(Phenylsulfonyl)-1,2-dihydronaphthalene **11**



2-Chloro-3-(phenylsulfonyl)-1,2,3,4-tetrahy-dro-naphthalene **10** (49.02 g, 0.16 mol) was dissolved in DCM and DBU (25.10 g, 0.16 mol) were added. The reaction mixture was stirred for 30 min. The mixture was washed with water, dried and the solved evaporated under reduced pressure. Recrystallization from ethanol yielded 24.31 g (0.09 mol, 56%) 2-(phenylsulfonyl)-1,2-dihydro-naphthalene **11**.

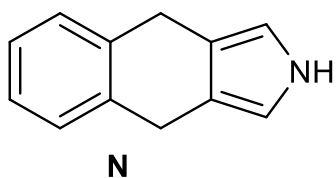
5.4.1.10 t-Butyl 4,9-dihydro-2*H*-benzo[*J*]isoindole-1-carboxylate **12**



Into a flask with potassium *tert*-butoxide (4.49 g, 0.04 mol) dissolved in 20 mL THF, t-butyl-cyanoacetate (5.65 g, 0.04 mol) was added. 2-(Phenylsulfonyl)-1,2-dihydro-naphthalene **11** (11.19 g, 0.04 mol) was added under argon atmosphere and stirred for 2 h. The solvent was evaporated, the crude product washed with water and extracted with DCM. After evaporation to dryness, recrystallization from ethanol resulted in the t-butyl ester protected 4,9-dihydro-2*H*-benzo[*J*]isoindole **12** with 43% yield (4.85 g, 0.02 mol).

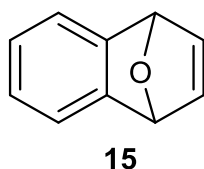
¹H-NMR (300 MHz, CD₂Cl₂): δ (ppm) 9.12 (br, 1H), 7.33-7.23 (d, 2H), 7.20-7.14 (d, 2H), 6.80 (s, 1H), 4.15-4.10 (d, 2H), 3.92-3.86 (d, 2H), 1.61 (s, 3H).

5.4.1.11 4,9-Dihydro-2*H*-benzo[*J*]isoindole **N**



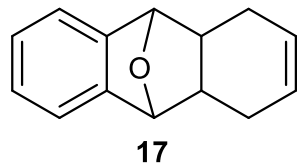
t-Butyl 4,9-dihydro-2*H*-benzo[f]isoindole-1-carboxylate **12** (4.83 g, 0.02 mol) and 3 pieces of potassiumhydroxide were dissolved in 30 mL of ethylenglykol and refluxed for 60 min under nitrogen atmosphere. After cooling down to room temperature, the reaction mixture was poured into water, the organic layer separated, washed with water, dried over sodiumsulfate and concentrated through distillation in vacuum. Flash chromatography yielded 4,9-dihydro-2*H*-benzo[f]isoindole **N** (1.26 g, 0.01 mol, 67%).

5.4.1.12 1,4-Dihydro-1,4-epoxynaphthalene **15**



1,2-Dibromobenzene **13** (60.00 g, 0.25 mol) and furan **14** (17.00 g, 0.25 mol) were dissolved in 500 mL THF. The reaction mixture was cooled to -50 °C under argon atmosphere. n-BuLi (16.00 g, 0.25 mol) in hexane was added slowly. The mixture was stirred for additional 30 min at -50 °C. Subsequently 10 mL water was added and after the mixture reached room temperature, the solvent was evaporated under reduced pressure. This resulted in 31.12 g (0.22 mol, 86% yield) of 1,4-dihydro-1,4-epoxynaphthalene **15**.

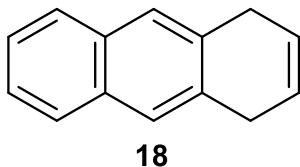
5.4.1.13 1,4,4a,9,9a,10-Hexahydro-9-10-epoxyanthracene **17**



1,4-Dihydro-1,4-epoxynaphthalene **15** (30.96 g, 0.22 mol) and 3-sulfolene **16** (25.37 g, 0.22 mol), NaHCO₃ (0.76 g, 0.009 mol) and 15 mL pyridine were added to a high-pressure

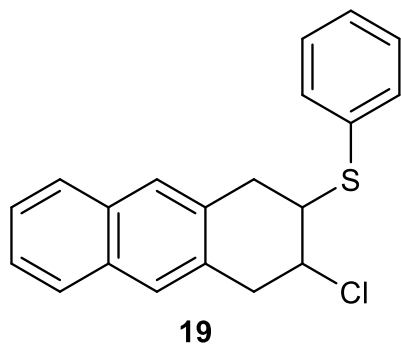
glass flask and heated 18 h at 120 °C. Upon completion, the mixture was filtered and the solvent evaporated under reduced pressure. Flash chromatography with DCM as the eluent resulted in a beige powder of 1,4,4a,9,9a,10-hexahydro-9-10-epoxyanthracene **17** with 48% yield (20.31 g, 0.10 mol).

5.4.1.14 1,4-Dihydroanthracene **18**



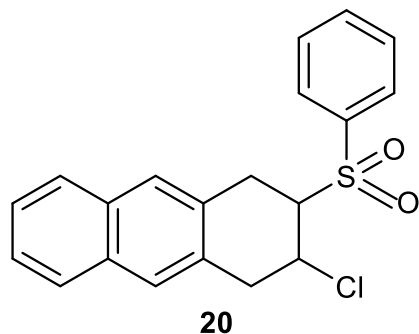
1,4,4a,9,9a,10-Hexahydro-9-10-epoxyanthracene **17** (20.31 g, 0.10 mol) was dissolved in 400 mL ethanol in a flask under argon atmosphere. 20 mL concentrated hydrochloric acid was added and the reaction mixture was refluxed overnight. The solvent was evaporated under reduced pressure and the crude product was recrystallized from ethanol, resulting in 56% (10.44 g, 0.06 mol) of 1,4-dihydroanthracene **18**.

5.4.1.15 (3-Chloro-1,2,3,4-tetrahydroanthracene-2-yl)- (phenyl)sulfane **19**



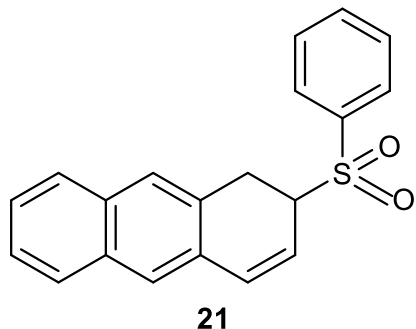
NCS (7.41 g, 0.06 mol) was dissolved in 50 mL DCM in a flask with argon atmosphere. After completed addition of 6.11 g (0.06 mol) thiophenol, the mixture was stirred for additional 30 min. Subsequently 1,4-dihydroanthracene **18** (10.20 g, 0.06 mol) was mixed with 50 mL DCM in a flask with argon atmosphere. Phenylsulfenylchloride **8** was added slowly and the resulting mixture stirred for an additional 30 min. The solvent was evaporated under reduced pressure, leaving 17.81 g (0.05 mol, 91% yield) (3-chloro-1,2,3,4-tetrahydroanthracene-2-yl)(phenyl)sulfane **19**.

5.4.1.16 2-Chloro-3-(phenylsulfonyl)-1,2,3,4-tetrahydroanthracene **20**



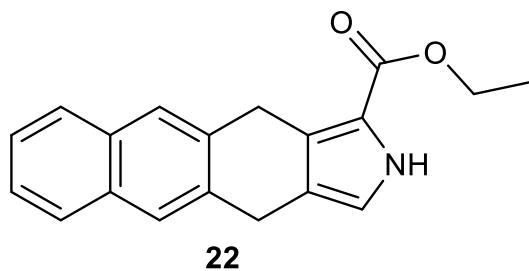
17.72 g (0.05 mol) of 3-chloro-1,2,3,4-tetrahydroanthracene-2-yl)(phenyl)sulfane **19** was dissolved in 50 mL THF and cooled with an ice bath. Oxone (16.74 g, 0.11 mol), dissolved in 30 mL water, was added. The mixture was allowed to stir at room temperature for two days. Thereafter it was diluted with 30 mL water and extracted with DCM. The solvent was evaporated and the crude product recrystallized from ethanol. This resulted in 10.71 g (0.03 mol, 55% yield) of yellowish 2-chloro-3-(phenylsulfonyl)-1,2,3,4-tetrahydroanthracene **20**.

5.4.1.17 2-(Phenylsulfonyl)-1,2-dihydroanthracene **21**



2-Chloro-3-(phenylsulfonyl)-1,2,3,4-tetrahydronaphthalene **20** (10.65 g, 0.03 mol) was dissolved in DCM and DBU (4.57 g, 0.03 mol) were added. The reaction mixture was stirred for 30 min. The mixture was washed with water, dried and the solution evaporated under reduced pressure. Recrystallization from ethanol yielded 6.41 g (0.02 mol, 72%) 2-(phenylsulfonyl)-1,2-dihydro-anthracene **21**.

5.4.1.18 Ethyl 4,11-dihydro-2*H*-naphtho[2,3-*f*]isoindole-1-carboxylate **22**

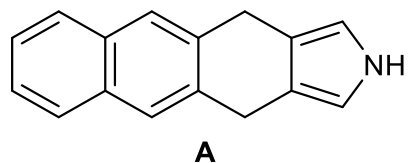


Into a flask with potassium *tert*-butoxide (1.27 g, 0.01 mol) dissolved in 20 mL THF, ethyl 2-cyanoacetate (1.28 g, 0.01 mol) was added. 2-(Phenylsulfonyl)-1,2-dihydroanthracene **21** (3.63 g, 0.01 mol) was added under argon atmosphere and stirred for 2 h. The solvent was evaporated, the crude product washed with water and extracted with DCM. After

evaporation to dryness, recrystallization from ethanol resulted in ethyl 4,11-dihydro-2*H*-naphtho[2,3-*J*]isoindole-1-carboxylate **22** with 53% yield (1.75 g, 0.006 mol).

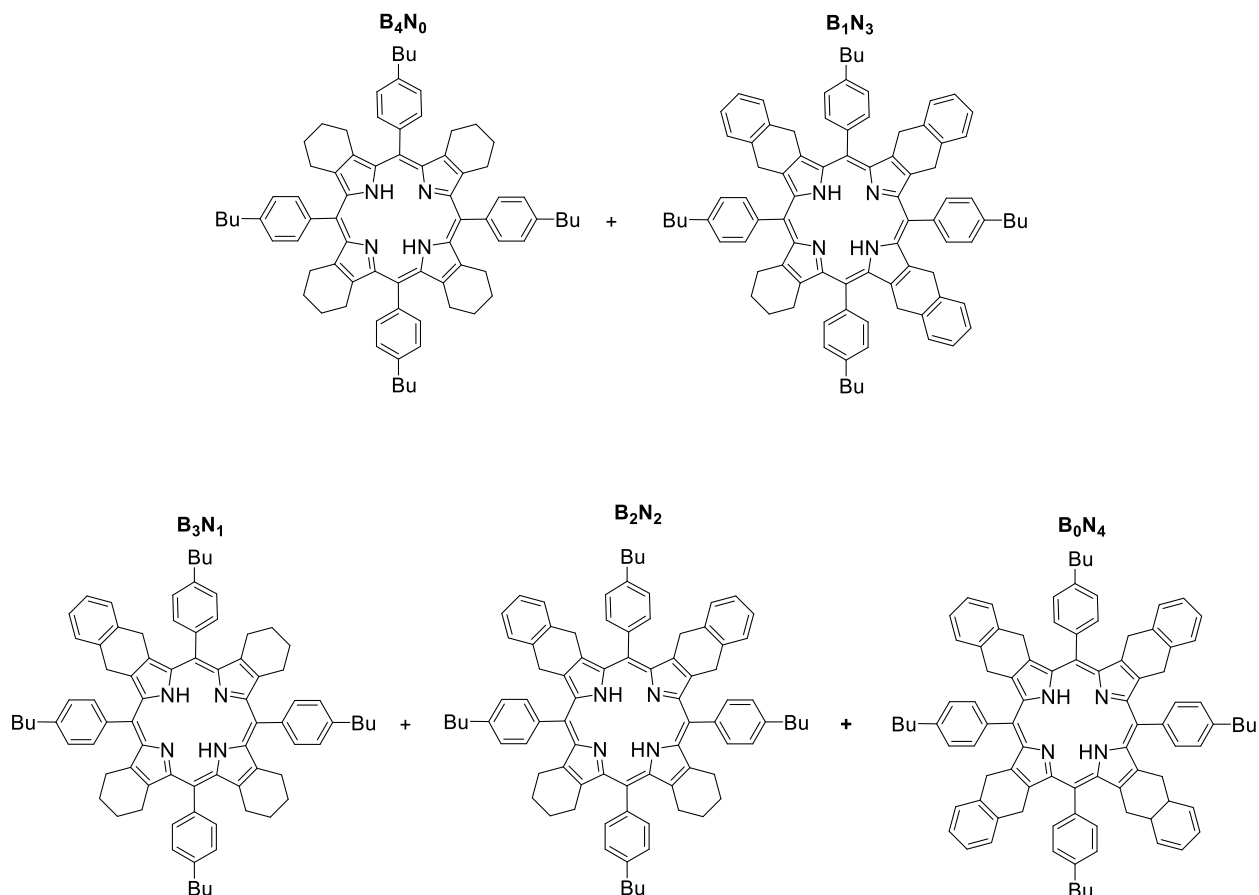
¹H-NMR (300 MHz, d-toluol): δ (ppm) 8.22 (br, 1H), 7.66-7.56 (m, 2H), 7.54-7.45 (d, 2H), 7.29-7.23 (d, 2H), 6.16 (s, 2H), 4.37 (s, 2H), 4.15-4.13 (dd, 2H), 3.79 (s, 2H), 1.20-1.10 (t, 3H).

5.4.1.19 4,11-Dihydro-2*H*-naphtho[2,3-*J*]isoindole **A**



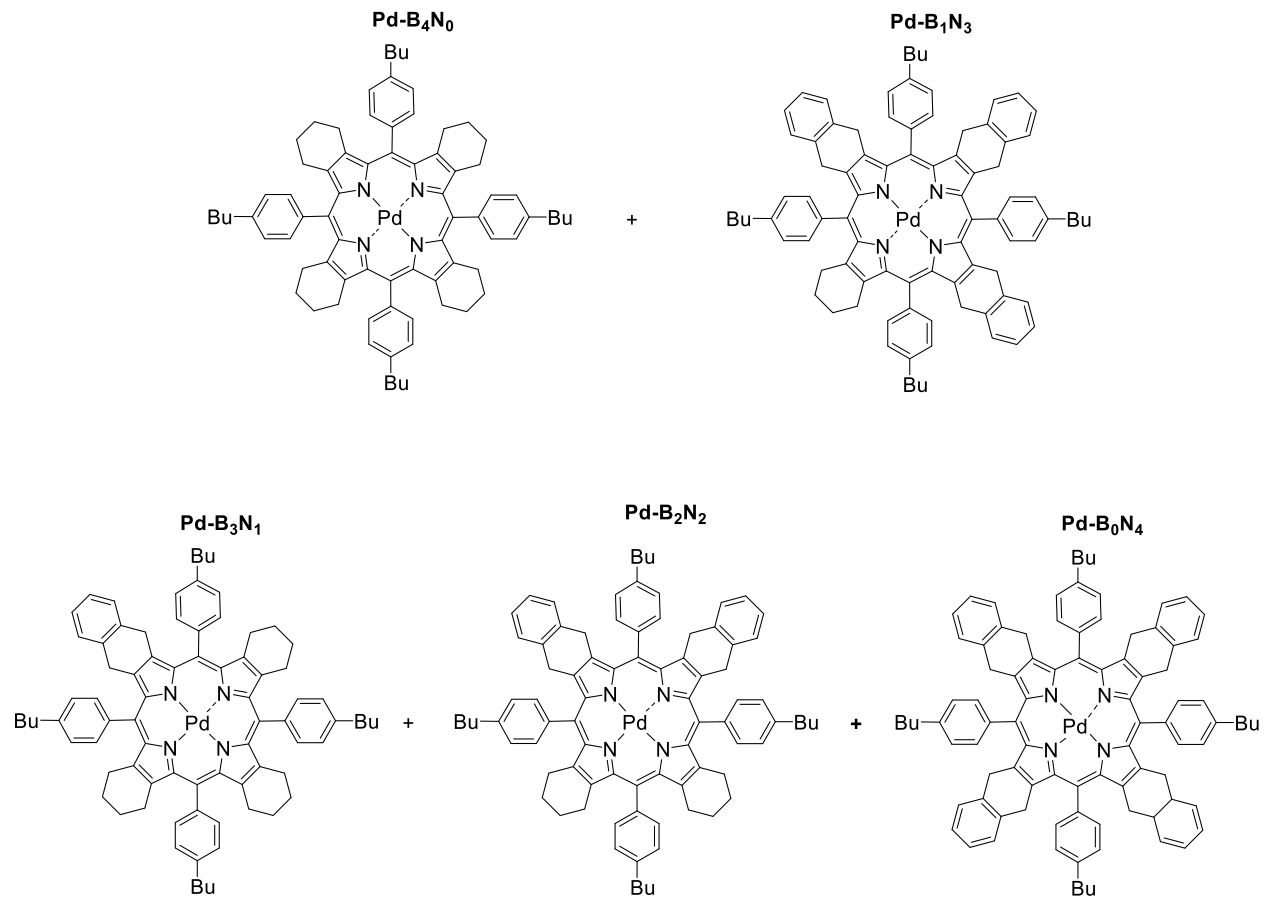
Ethyl 4,11-dihydro-2*H*-naphtho[2,3-*J*]isoindole-1-carboxylate **22** (1.39 g, 0.005 mol) and 3 pieces of potassiumhydroxide were dissolved in 30 mL of ethylenglykol and refluxed for 60 min under nitrogen atmosphere. After cooling down to room temperature, the reaction mixture was poured into water, the organic layer separated, washed with water, dried over sodiumsulfate and concentrated through distillation in vacuum. Flash chromatography yielded 4,11-dihydro-2*H*-naphtho[2,3-*J*]isoindole **A** (669 mg, mol, 61%).

5.4.1.20 Mixed benzo-naphtho porphyrin family **23**



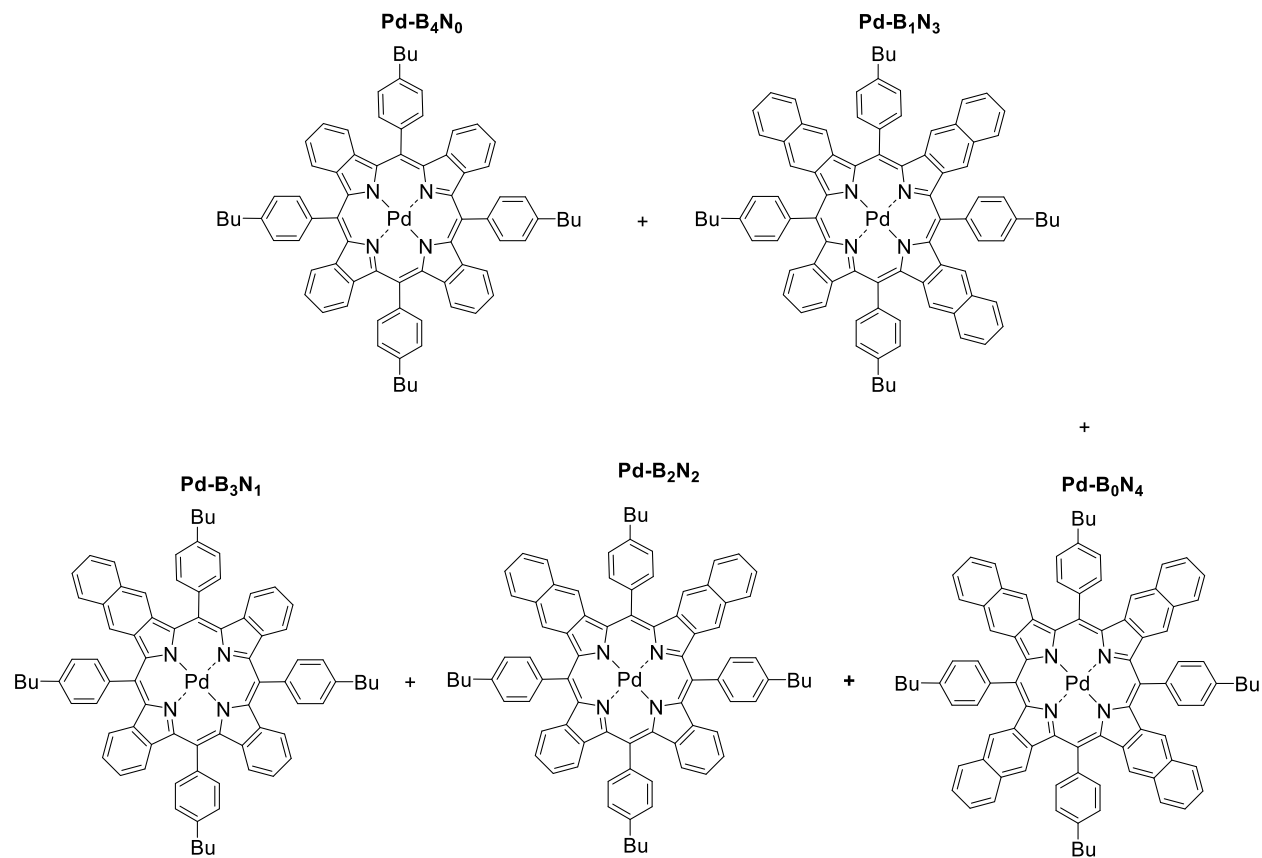
A mixture of 4,5,6,7-tetrahydro-2*H*-isoindole **B** (0.143 g, 1.18 mmol), 4,9-dihydro-2*H*-benzo[*f*]isoindole **N** (0.200 g, 1.18 mmol) and 4-butylbenzaldehyde **22** (0.383 g, 2.36 mmol) in 200 mL of CH₂Cl₂, which was freshly distilled from CaH₂, was stirred for 10 min at room temperature under nitrogen. After addition of the catalyst BF₃Et₂O (0.033 g, 0.236 mmol) the mixture was stirred for 1 h. Following the addition of DDQ (0.268 g, 1.18 mmol), it was stirred once again for 1 h. Afterwards the mixture was washed with aqueous Na₂SO₃, dried over Na₂SO₄ and the solvent evaporated in vacuum. The crude product was purified on a silica gel column (eluent CH₂Cl₂) resulting in 0.755 g of the mixed benzo-naphtho porphyrin family **23**.

5.4.1.21 Metalated mixed benzo-naphtho porphyrin family **24**



The mixture of porphyrin **23** (0.500 g), bis(benzonitrile)palladium(II)chloride (0.120 g, 0.31 mmol) and trimethylamine (0.222 g, 2.50 mmol) in benzonitrile (30 mL) was refluxed for 1 h under nitrogen atmosphere. After completed metal-insertion, the reaction mixture was allowed to cool down to room temperature. The solvent was evaporated in vacuum. The remaining Pd black was separated from the crude product via dissolving in CH₂Cl₂ and filtration through a thin layer of celite. Purification was carried out by chromatography on silica gel using CH₂Cl₂ as an eluent yielding 0.398 g of mixed benzo-naphtho porphyrin family **24**.

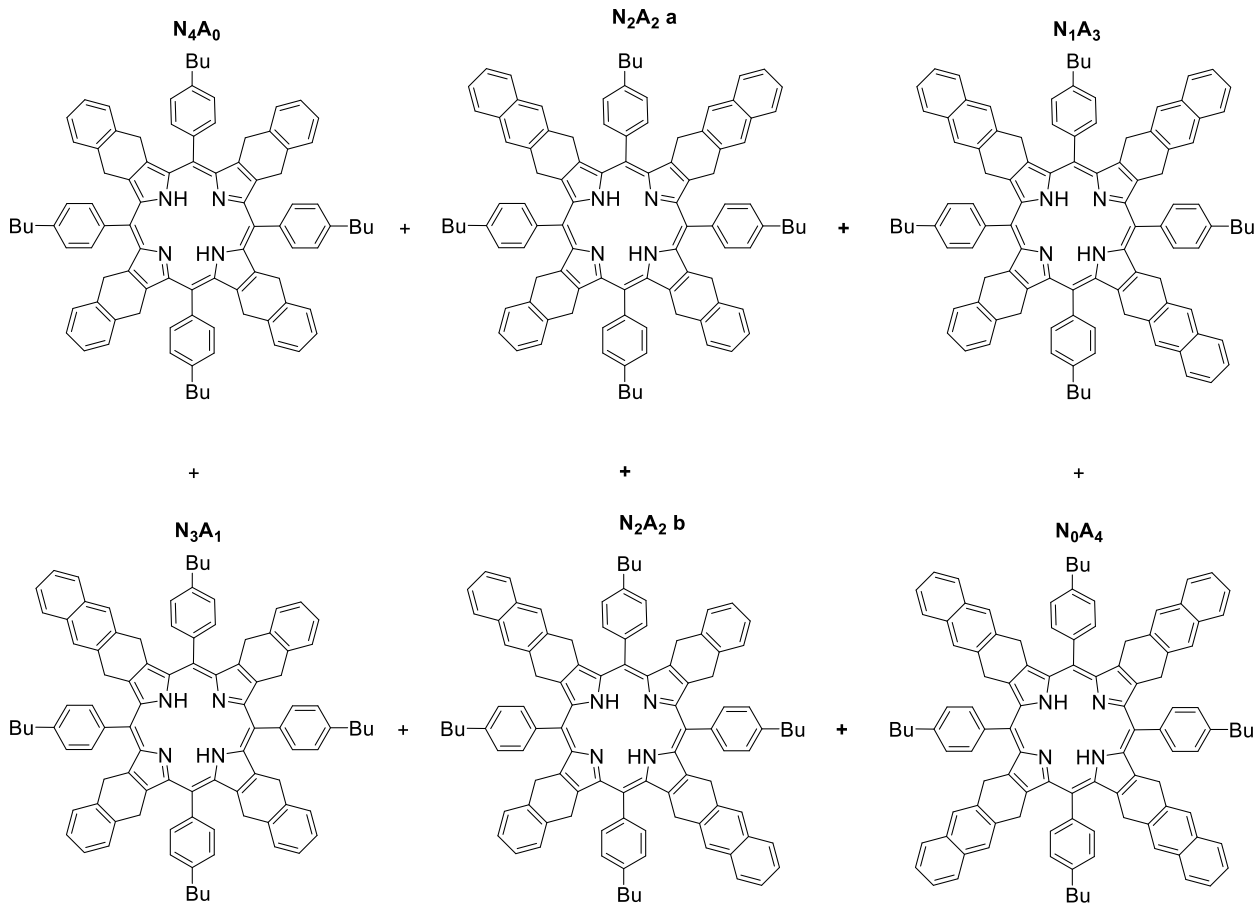
5.4.1.22 Aromatized mixed benzo-naphtho porphyrin family **25**



A mixture of the mixed porphyrin family **24** (0.200 g) and DDQ (0.215 g, 0.94 mmol) in THF was refluxed for 20-40 min. After complete aromatization, the mixture was allowed to cool down to room temperature. The volume of the solvent was increased and the mixture was washed with a 10% aqueous solution of Na₂SO₃, followed by brine and dried over Na₂SO₄. The solved was evaporated in vacuum and the crude product was purified on a silica gel column (eluent: CH₂Cl₂) yielding 0.160 g of the mixed benzo-naphtho porphyrin family **25** with the following composition: PdTBP – 20%, Pd1N3BP – 36%, Pd2N2BP – 29%, Pd3N1BP – 12%, PdTNP – 3%.

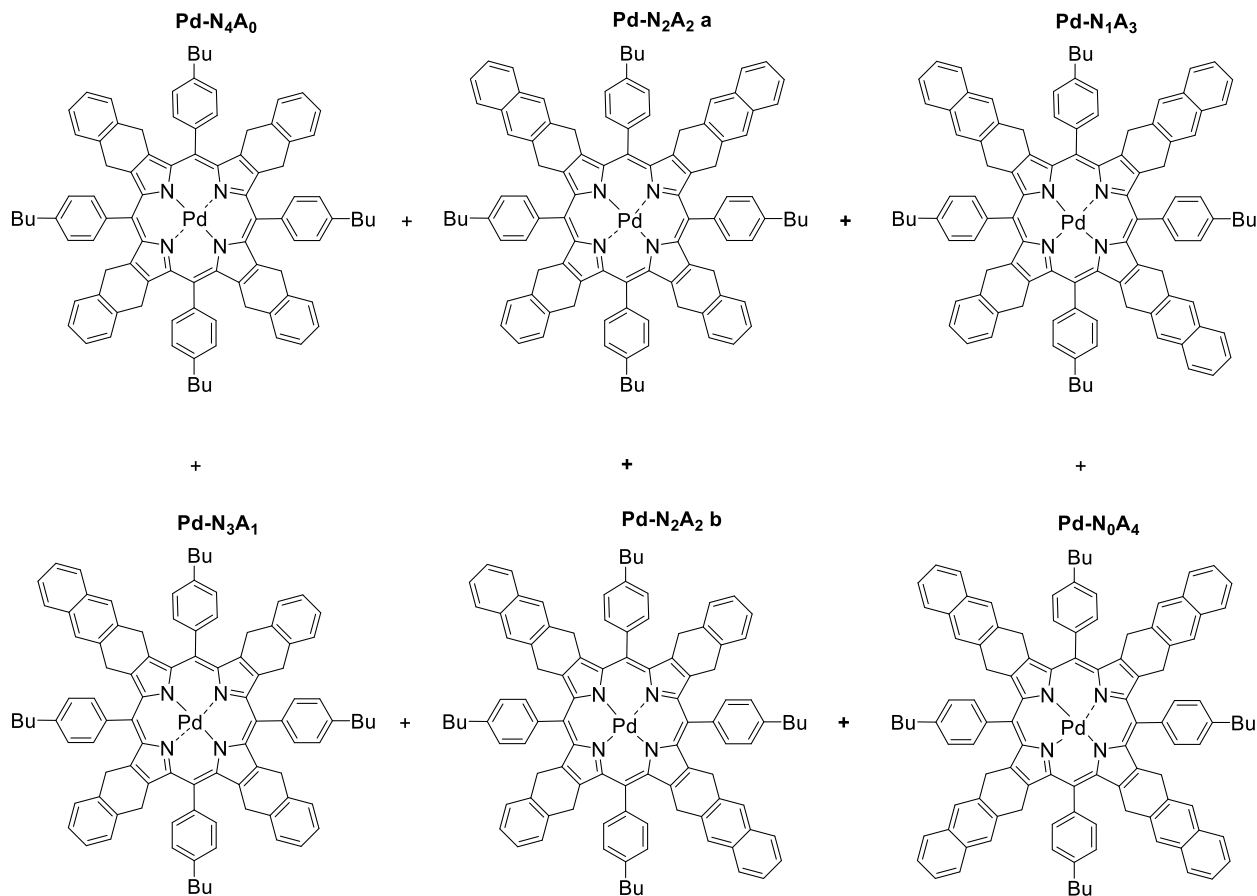
FD-Mass (HABA matrix): *m/z* 1565.3, 1618.6, 1669.2, 1717.7, 1770.8; calculated: 1568.50, 1618.56, 1668.62, 1718.68, 1768.74.

5.4.1.23 Mixed naphtho-antra porphyrin family **27**



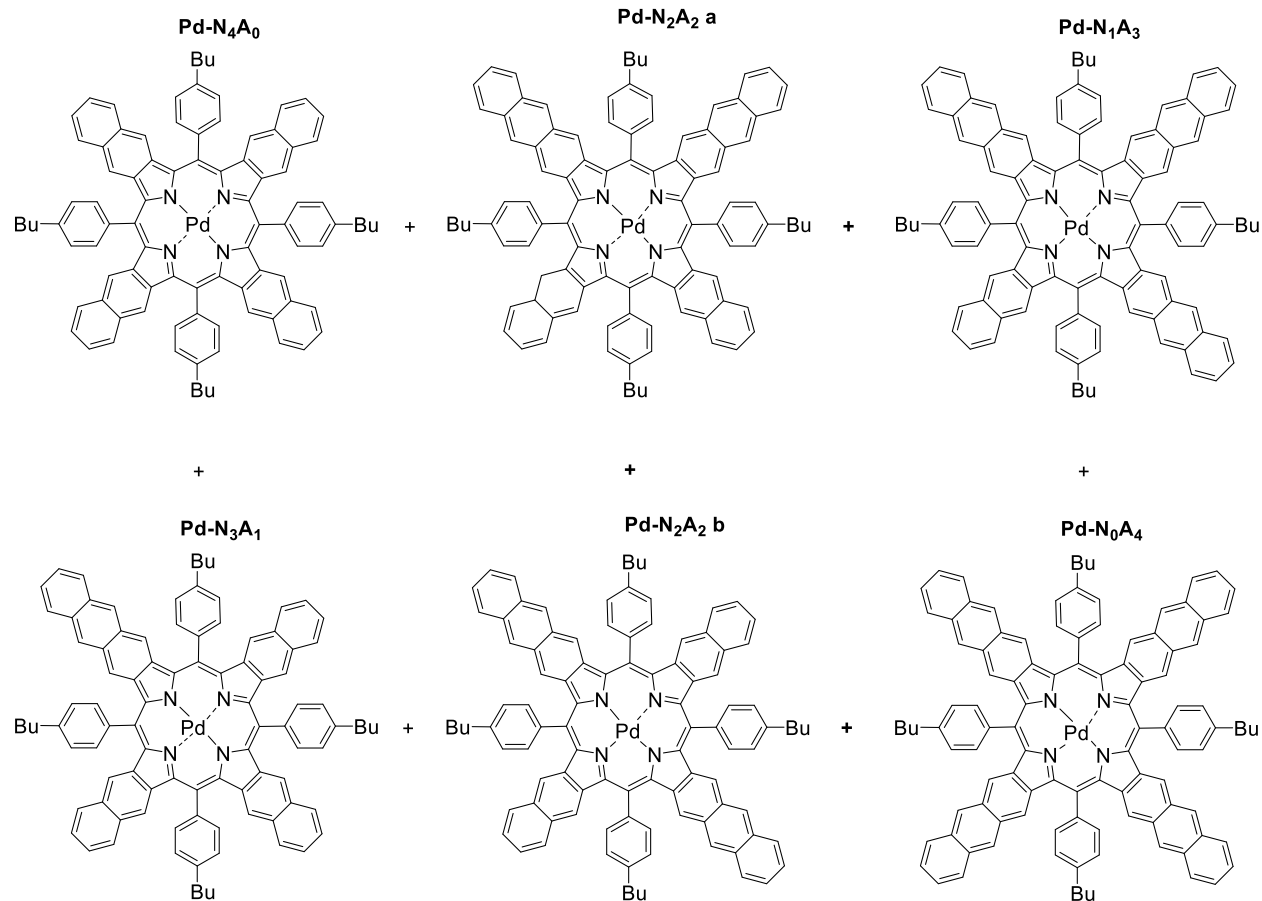
A mixture of 4,9-dihydro-2*H*-benzo[*J*]isoindole **N** (0.210 g, 1.24 mmol), 4,11-dihydro-2*H*-naphtho[2,3-*J*]isoindole **A** (0.271 g, 1.24 mmol) and 3,5-di-*tert*-butylbenzaldehyde **26** (0.541 g, 2.48 mmol) in 250 mL of CH₂Cl₂, which was freshly distilled from CaH₂, was stirred for 10 min at room temperature under nitrogen. After addition of the catalyst BF₃Et₂O (0.035 g, 0.248 mmol) the mixture was stirred for 1 h. Following the addition of DDQ (0.422 g, 1.86 mmol), it was stirred once again for 1 h. Afterwards the mixture was washed with aqueous Na₂SO₃, dried over Na₂SO₄ and the solvent evaporated in vacuum. The crude product was purified on a silica gel column (eluent CH₂Cl₂) resulting in 0.245 g of the mixed naphtho-antra porphyrin family **27**.

5.4.1.24 Metalated mixed naphtho-antra porphyrin family **28**



The mixture of porphyrin **27** (0.2 g), bis(benzonitrile)palladium(II)chloride (0.078 g, 0.204 mmol) and trimethylamine (0.101 g, 1 mmol) in benzonitrile (10 mL) was refluxed for 1 h under nitrogen atmosphere. After completed metal-insertion, the reaction mixture was allowed to cool down to room temperature. The solvent was evaporated in vacuum. The remaining Pd black was separated from the crude product via dissolving in CH₂Cl₂ and filtration through a thin layer of celite. Purification was carried out by chromatography on silica gel using CH₂Cl₂ as an eluent yielding 0.221 g of mixed naphtho-antra porphyrin family **28**.

5.4.1.25 Aromatized mixed naphtho-antra porphyrin family **29**

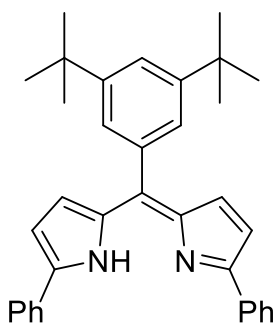


A mixture of the mixed porphyrin family **28** (0.1 g) and DDQ (0.187 g, 0.82 mmol) in THF was refluxed for 20-40 min. After complete aromatization the mixture was allowed to cool down to room temperature. The volume of the solvent was increased and the mixture was washed with a 10% aqueous solution of Na₂SO₃, followed by brine and dried over Na₂SO₄. The solved was evaporated in vacuum and the crude product was purified on a silica gel column (eluent: CH₂Cl₂) yielding 0.94 g of the mixed naphtho-antra porphyrin family **29**.

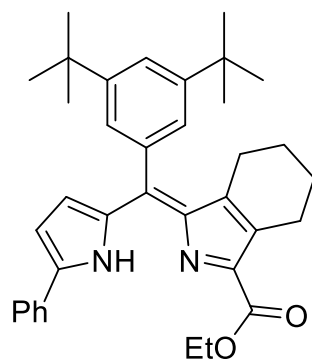
FD-Mass (HABA matrix): *m/z*: 1565.3 (39), 1618.6 (65), 1669.2 (100), 1717.7 (44), 1770.8 (20); calculated: 1568.50, 1618.56, 1668.62, 1718.68, 1768.74.

5.4.2 Mixed emitter

5.4.2.1 Dipyrromethene **31** and **32**



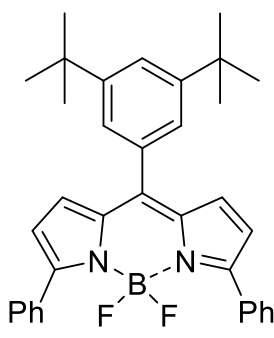
31



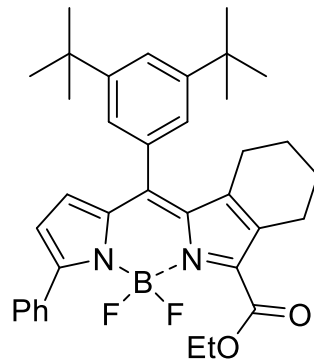
32

3,5-Di(*tert*-butyl)benzaldehyde **26** (218 mg, 1 mmol), ethyl-4,5,6,7-tetrahydro-2H-isoindole-1-carboxylate **4** (193 mg, 1 mmol) and 2-phenylpyrrole **30** (143 mg, 1 mmol) were dissolved in 100 mL of absolute CH₂Cl₂ under Ar atmosphere. Three drops of trifluoroacetic acid (TFA) were added, and the solution was stirred at room temperature overnight in the darkness. Dry 2,3-dichloro-5,6-dicyano-1,4-benzoquinone (DDQ) (250 mg) was added and stirring was continued for 2 h. Triethylamine (2 mL) was added, organic phase was washed with aqueous sodium sulfite (3%, 2x100 mL). Organic layers were separated, dried over anhydrous sodium sulfate, evaporated to dryness and subjected to the following step.

5.4.2.2 DPh-BODIPY **33** and non-aromatized MPh-MB-BODIPY **34**



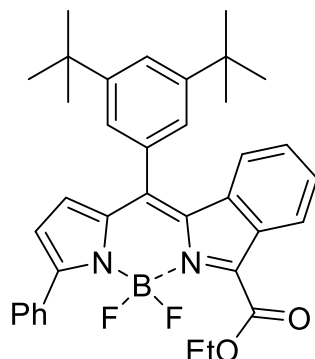
33



34

To the crude dipyrromethene **31** and **32** reaction mixture, *N,N*-diisopropylethylamine (DIEA) (3.0 mL) and 100 mL of absolute CH₂Cl₂ were added under argon atmosphere and the solution was stirred at room temperature for 10 min. BF₃·OEt₂ (3.0 mL) was added, and stirring was continued for 2 h. The reaction mixture was washed with NaHCO₃ solution (5%, 2x100 mL) and water (100 mL). The combined organic extracts were dried over Na₂SO₄, filtered, evaporated to dryness and subjected to the following step.

5.4.2.3 MPh-MB-BODIPY **35**



35

To the crude reaction mixture of DPh-BODIPY **33** and unaromatized MPh-MB-BODIPY **34** toluene (50 mL) and 1,4-dioxane (100 mL) were added, the solution was stirred for 5 min, DDQ (300 mg) was added and the stirring continued at 110 °C for 15 h. The solution was cooled down, washed with aqueous sodium sulfite (3%, 2 x 100 mL). The organic layers were separated, dried over anhydrous sodium sulfate, and evaporated to dryness. Column chromatography with silica gel (eluent - toluene) afforded DPh-BODIPY **33** as a first red fraction with yellow fluorescence, which was evaporated and recrystallized from CH₂Cl₂/methanol to afford dark red crystals after drying under vacuum. The yield was 207 mg (39%). A second violet fraction, possessing red fluorescence, could be isolated, evaporated, dissolved in cyclohexane (20 ml) and freeze-dried for 24 h, to afford MPh-MB-BODIPY **35** as a violet powder (133 mg, 23% yield)

DPh-BODIPY 33:

¹H NMR (250 MHz, C₂D₂Cl₄) δ 7.91-7.87 (m, 4H), 7.63 (s, 1H), 7.49-7.45 (m, 8H), 6.99 (d, *J* = 4.3 Hz, 1H), 6.67 (d, *J* = 4.2 Hz, 1H), 1.42 (s, 18H). ¹³C NMR (126 MHz, C₂D₂Cl₄) δ 158.12, 150.70, 146.04, 136.35, 133.22, 132.65, 125.25, 124.30, 120.91, 74.13, 34.83, 31.39; λ_{max} (toluene)/nm 557 ($\epsilon/\text{dm}^3 \text{ mol}^{-1} \text{ cm}^{-1}$ 30600); fluorescence (toluene): $\lambda_{\text{max}} = 591$ nm ($\Phi=68\%$); MS (FD, 8 kV): m/z (%) 532.5 (100), M⁺;

DPh-BODIPY 35:

¹H NMR (250 MHz, C₂D₂Cl₄) δ 8.05 (d, *J* = 8.1 Hz, 1H), 7.99-7.96 (m, 2H), 7.68 (s, 1H), 7.53-7.51 (m, 3H), 7.38-7.36 (m, 2H), 7.31 (t, *J* = 7.6 Hz, 1H), 7.16 (t, *J* = 7.6 Hz, 1H), 6.84 (d, *J* = 4.3 Hz, 1H), 6.67 (d, *J* = 4.2 Hz, 1H), 6.40 (d, *J* = 8.4 Hz, 1H), 4.56 (q, *J* = 7.1 Hz, 2H), 1.51 (t, *J* = 7.1 Hz, 3H), 1.39 (s, 18H). ¹³C NMR (126 MHz, C₂D₂Cl₄) δ 160.50, 158.10, 151.27, 144.28, 139.99, 137.60, 134.62, 132.53, 132.29, 130.68, 130.46, 129.38, 128.28, 123.84, 123.45, 121.87, 74.04, 62.25, 34.93, 31.31, 29.60, 14.13; λ_{max} (toluene)/nm 597 ($\epsilon/\text{dm}^3 \text{ mol}^{-1} \text{ cm}^{-1}$ 52650); fluorescence (toluene): $\lambda_{\text{max}} = 630$ nm ($\Phi = 74\%$); MS (FD, 8 kV): m/z (%) 578.6 (100), M⁺;

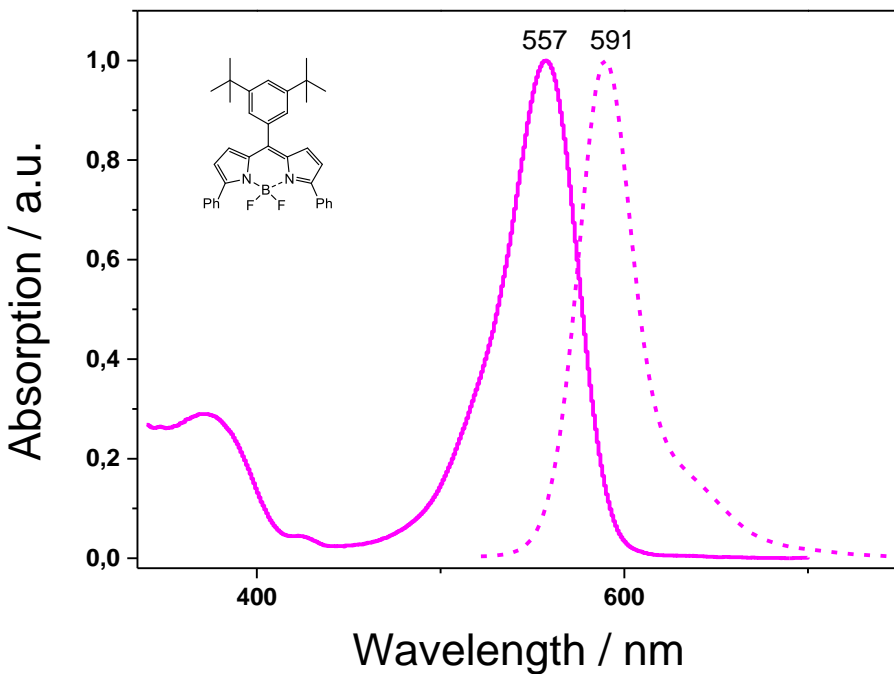
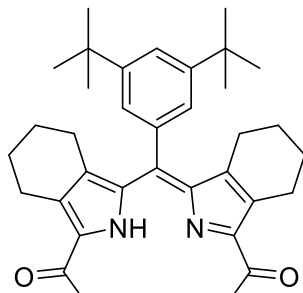


Figure 5.1: Normalized absorption (continuous curve) and fluorescence (dotted curve) of DPh-BODIPY 33 in toluene. The measurements were performed by [REDACTED].

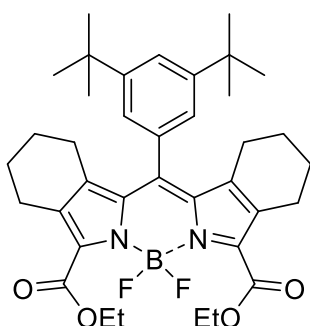
5.4.2.4 Dipyrromethene 36



3,5-Di(*tert*-butyl)benzaldehyde **26** (218 mg, 1 mmol) and ethyl-4,5,6,7-tetrahydro-2*H*-isoindole-1-carboxylate **4** (386 mg, 2 mmol) were dissolved in 100 mL of absolute CH_2Cl_2 under argon atmosphere. Three drops of trifluoroacetic acid (TFA) were added, and the solution was stirred at room temperature overnight in the darkness. Dry 2,3-dichloro-5,6-dicyano-1,4-benzoquinone (DDQ) (250 mg) was added and the stirring was continued for

2 h. Triethylamine (2 mL) was added, the organic phase was washed with aqueous sodium sulfite (3%, 2 x 100 mL). Subsequently the organic layers were separated, dried over anhydrous sodium sulfate, evaporated to dryness and subjected to the following step.

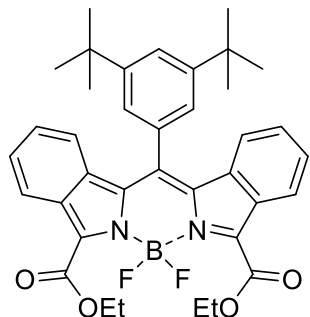
5.4.2.5 Non-aromatized DB-BODIPY 37



37

DIEA (3.0 mL) and 100 mL of absolute CH_2Cl_2 were added to the crude dipyrromethene **36** under argon atmosphere and the solution was stirred at room temperature for 10 min. $\text{BF}_3\cdot\text{OEt}_2$ (3.0 mL) was added and stirring was continued for 4 h. The reaction mixture was washed with NaHCO_3 solution (5%, 2 x 100 mL) and water (100 mL). The combined organic extracts were dried over Na_2SO_4 , filtered, evaporated to dryness and subjected to the following step.

5.4.2.6 DB-BODIPY 38



38

Toluene (50 mL) and 1,4-dioxane (100 mL) were added, stirred for 5 min and then DDQ (500 mg) was added and stirred at 110 °C for 15 h. The solution was cooled down, washed with aqueous sodium sulfite (3%, 2 x 100 mL). The organic layers were separated, dried over anhydrous sodium sulfate, and evaporated to dryness. Column chromatography with silica gel (eluent - toluene) afforded blue fraction, which was evaporated, dissolved in cyclohexane and freeze-dried for 24 h to afford a blue powder of DB-BODIPY **38**. The yield was 230 mg (37%).

¹H NMR (250 MHz, C₂D₂Cl₄) δ 8.09 (d, *J* = 8.2 Hz, 2H), 7.76 (s, 1H), 7.36 (d, *J* = 1.7 Hz, 2H), 7.33 – 7.25 (m, 2H), 7.19 – 7.04 (m, 2H), 6.22 (d, *J* = 8.4 Hz, 2H), 4.61 (q, *J* = 7.1 Hz, 4H), 1.55 (t, *J* = 7.1 Hz, 6H), 1.38 (s, 18H). ¹³C NMR (126 MHz, C₂D₂Cl₄) δ 160.45, 152.68, 142.82, 139.62, 134.58, 132.69, 130.78, 129.62, 129.16, 126.60, 123.76, 123.08, 122.57, 121.85, 74.04, 74.00, 73.78, 73.56, 62.27, 35.12, 31.27, 26.82, 14.18; λ_{max} (toluene)/nm 641 (ϵ / dm³ mol⁻¹ cm⁻¹ 67100); fluorescence (toluene): $\lambda_{\text{max}} = 667$ nm ($\Phi=56\%$); MS (FD, 8 kV): m/z (%) 624.6 (100), M⁺;

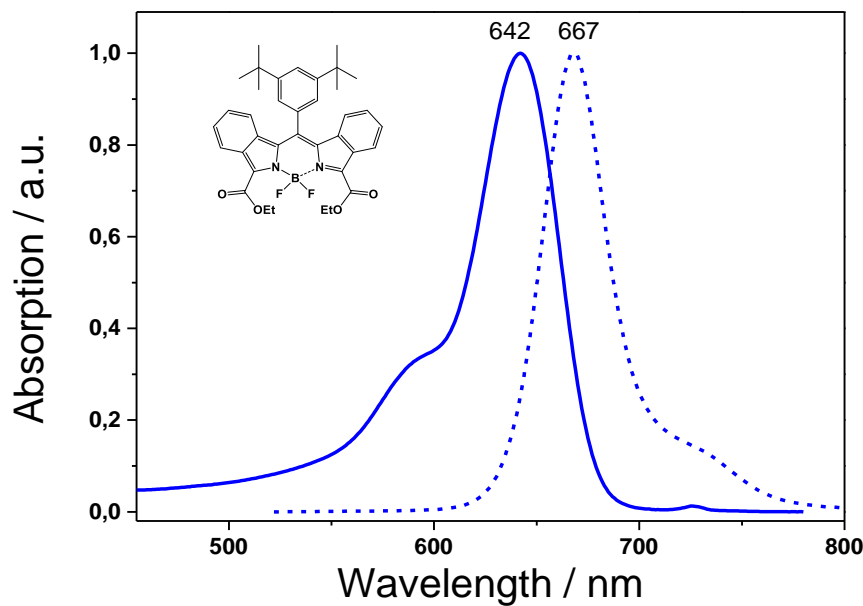
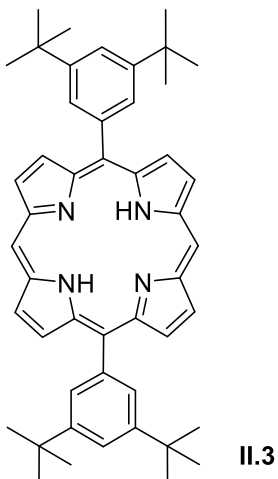


Figure 5.2: Normalized absorption (continuous curve) and fluorescence (dotted curve) of DB-BODIPY **38** in toluene. The measurements were performed by [REDACTED].

5.4.3 Fused porphyrin

5.4.3.1 5,15-Bis(3,5-di-*tert*-butylphenyl)porphyrin II.3



This step was prepared according to a modified literature procedure^{98,116}.

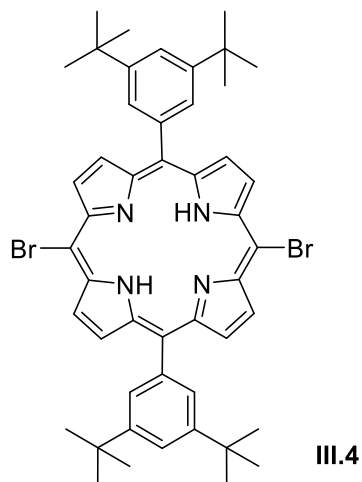
1000.00 mg (6.84 mmol) 2,2'-dipyrromethane **II.1** and 1493.50 mg (6.84 mmol) 3,5-di-*tert*-butyl-benzaldehyde **II.2** were dissolved in 1 L freshly distilled DCM under nitrogen atmosphere. The catalyst boron trifluoride diethyl etherate (43.33 µL, 0.34 mmol) was added and the mixture was stirred for 2 h at room temperature. Subsequently DDQ (573.70 mg, 2.74 mmol) was introduced into the reaction flask and the resulting mixture was stirred overnight. 10 mL of a saturated sodium sulfite solution was added. The layers were separated and the organic phase 3 times washed with water. Chromatography (silica, DCM) and following evaporation in vacuum resulted in raspberry coloured 5,15-bis(3,5-di-*tert*-butylphenyl)porphyrin **II.3** crystals in 56% yield (750.03 mg, 3.83 mmol).

¹H NMR (250 MHz, CD₂Cl₂): δ (ppm) 10.35 (s, 2H, H_{meso}), 9.45 (d, J = 4.7 Hz, 4H, H_d), 9.14 (d, J = 4.6 Hz, 4H, H_c), 8.17 (d, J = 1.8 Hz, 4H, H_a), 7.90 (s, 2H, H_b), 1.59 (s, 36H, H_{t-butyl}), -3.07 (s, 2H). As described in literature.

MALDI TOF: 686.26, calculated: 686.43

UV-Vis: λ_{\max} / nm (THF) (rel. intensity) 406 (100), 501 (3.88), 534 (1.36), 577 (0.96), 634 (0.15)

5.4.3.2 5,15-Dibromo-10,20-bis(3,5-di-*tert*-butylphenyl)-porphyrin III.4



This step was prepared according to a modified literature procedure^{98,116}.

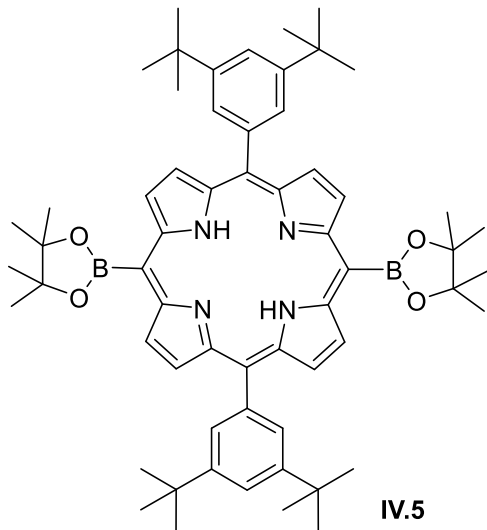
5,15-Bis(3,5-di-*tert*-butylphenyl)porphyrin **II.3** (100.00 mg, 0.15 mmol) was dissolved in 36 mL chloroform. 0.15 mL of pyridine was added and the reaction mixture cooled down to 0 °C. Afterwards NBS (51.98 mg, 0.34 mmol) is added dropwise. The reaction progress was monitored by TLC and at completion the reaction was quenched by addition of 1.5 mL acetone. The solvents were removed under reduced pressure, the crude product washed with methanol and then recrystallized from chloroform-methanol (1:1). Purple crystals of 5,15-dibromo-10,20-bis(3,5-di-*tert*-butylphenyl)porphyrin **III.4** were achieved in 75% yield (92.23 mg, 0.10 mmol).

¹H NMR (250 MHz, CDCl₃). δ (ppm) 9.22 (s, 4H, H_d), 8.89 (s, 4H, H_c), 8.03 (s, 4H, H_a), 7.83 (s, 2H, H_b), 1.55 (s, 36H, H_{t-butyl}), -2.70 (s, 2H). As described in literature.

MALDI TOF: 844.15, calculated: 844.78

UV-Vis: λ_{max} / nm (THF) (rel. intensity) 406 (100), 502 (4.88), 534 (2.30), 576 (1.79), 634 (0.86)

5.4.3.3 5,15-Bis(3,5-di-*tert*-butylphenyl)-10,20-bis(4,4,5,5-tetramethyl-1,3,2-dioxaborolan-2-yl)porphyrin IV.5



This step was prepared according to a modified literature procedure^{98,116}.

To a 50 mL round bottom flask with nitrogen flow 5,15-dibromo-10,20-bis(3,5-di-*tert*-butylphenyl)porphyrin III.4 (200.00 mg, 0.24 mmol) and PdCl₂(PPh₃)₂ (16.60 mg, 0.02 mmol) were added. The flask was evacuated and purged with nitrogen for 3 times. 4,4,5,5-Tetramethyl-1,3,2-dioxaborolane (1.67 g, 13.03 mmol), Et₃N (0.75 mL) and 1,2-dichloroethane (91 mL) were added. The mixture was degassed by bubbling with nitrogen for 45 min and subsequently heated at 90 °C overnight. Once TLC indicated the completion of the reaction, the mixture was allowed to cool down to room temperature. Afterwards it was 3 times washed with water, the organic phase was collected and the solvents were removed under reduced pressure. Chromatography (silica, DCM – petrol ether 2:1 to remove side products, ethyl acetate to elute the product) and following

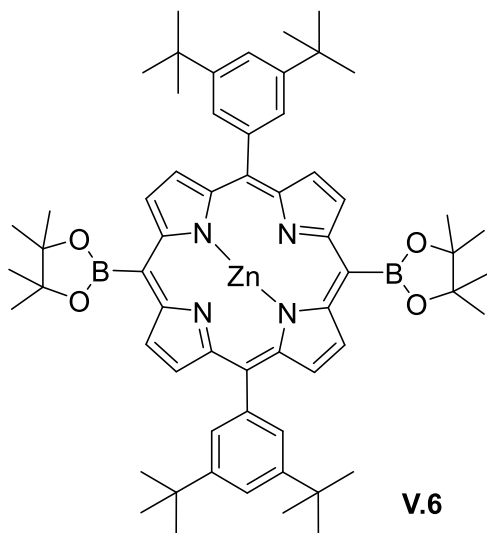
evaporation of the eluent resulted purple crystals of 5,15-bis(3,5-di-*tert*-butylphenyl)-10,20-bis(4,4,5,5-tetramethyl-1,3,2-dioxaborolan-2-yl)porphyrin **IV.5** in 52% yield(117.14 mg, 0.12 mmol).

¹H NMR (250 MHz, CDCl₃): δ (ppm) 9.87 (d, *J* = 4.7 Hz, 4H, H_a), 9.01 (d, *J* = 4.8 Hz, 4H, H_c), 8.08 (d, *J* = 1.9 Hz, 4H, H_a), 7.84 (d, *J* = 1.8 Hz, 2H, H_b), 1.84 (s, 24H, H_{Bpin}), 1.56 (s, 36H, H_{t-butyl}), -2.97 (s, 2H, NH). As described in literature (Maeda, C.; Shinokubo, H.; Osuka, A.; *Org. Lett.*, 2010, 12 (8), pp 1820–1823).

MALDI TOF: 938.47, calculated: 938.61

UV-Vis: λ_{max} / nm (THF) (rel. intensity) 416 (100), 511 (5.36), 546 (1.89), 590 (1.66), 645 (1.24)

5.4.3.4 [5,15-Bis(3,5-di-*tert*-butylphenyl)-10,20-bis(4,4,5,5-tetramethyl-1,3,2-dioxaborolan-2-yl)porphyrinato]zinc(II) **V.6**



This step was prepared according to a modified literature ^{98,116,124}.

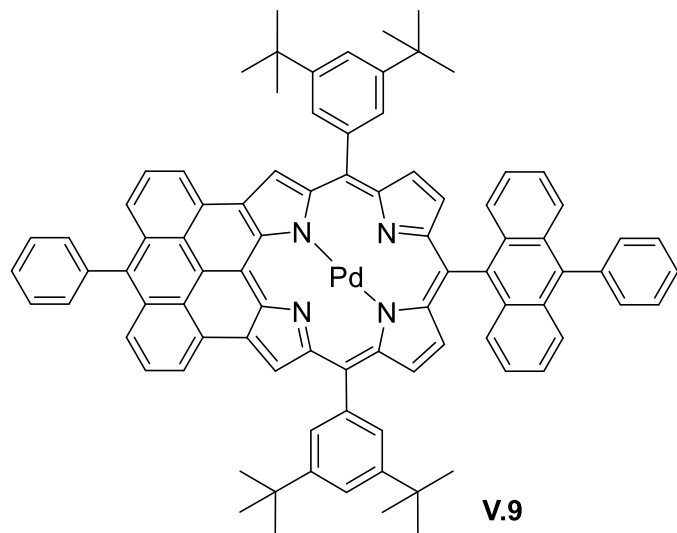
5,15-bis(3,5-di-*tert*-butylphenyl)-10,20-bis(4,4,5,5-tetramethyl-1,3,2-dioxaborolan-2-yl)porphyrin **IV.5** (100.00 mg, 0.11 mmol) and Zn(CH₃COO)₂ (96.93 mg, 0.533 mmol) were dissolved in 30 mL DCM and 5 mL methanol. The mixture was refluxed for 2h. Filtration through a silica gel pad with DCM as solvent and subsequent evaporation thereof in vacuum resulted in a raspberry coloured solid [5,15-bis(3,5-di-*tert*-butylphenyl)-10,20-bis(4,4,5,5-tetramethyl-1,3,2-dioxaborolan-2-yl)porphyrinato]zinc(II) **V.6** in 64% yield (68.52 mg, 0.07 mmol)

¹H NMR (250 MHz, CDCl₃): δ (ppm) 9.93 (d, *J* = 4.6 Hz, 4H, H_d), 9.13 (d, *J* = 4.8 Hz, 4H, H_c), 8.09 (d, *J* = 1.8 Hz, 4H, H_a), 7.82 (s, 2H, H_b), 1.85 (s, 24H, H_{Bpin}) 1.55 (s, 36H, H_{t-butyl}). As described in literature.

MALDI TOF: 1000.41, calculated: 1000.52

UV-Vis: λ_{max} / nm (THF) (rel. intensity) 419 (100), 553 (3.03), 590 (0.86)

5.4.3.5 Porphyrin **V.7**



This step was prepared according to a modified literature procedure^{98,116}.

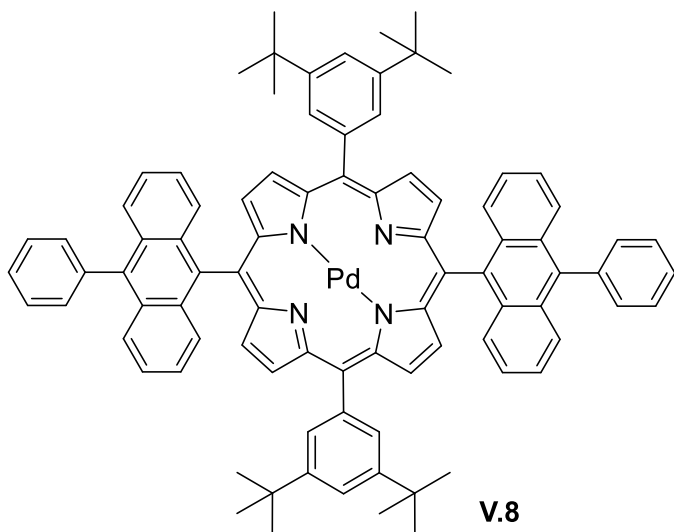
A three-necked flask was charged with [5,15-bis(3,5-di-*tert*-butylphenyl)-10,20-bis(4,4,5,5-tetramethyl-1,3,2-dioxaborolan-2-yl)porphyrinato]zinc(II) **V.6** (50.00 mg, 0.05 mmol), 9-bromo-10-phenylanthracene (36.51 mg, 0.11 mmol), potassium hydroxide (250.68 mg, 4.47 mmol), 2-dicyclohexylphosphino-2',6'-dimethoxybiphenyl (32.83 mg, 0.08 mmol) and tris(dibenzylideneacetone)dipalladium(0) (9.16 mg, 0.01 mmol) and dried under vacuum for 6h. Afterwards 5 mL of dry m-xylol were added by syringe. The reaction mixture was freeze-thaw degassed and subsequently purged with nitrogen. The solution was stirred for 5h at 90 °C and once the reaction was completed, it was allowed to cool down to room temperature. Next the reaction mixture was washed 3 times with water, the organic layers separated and the solvent evaporated under reduced pressure. The crude product was dissolved in DCM and subjected to a silica plug. Washing with methanol eluted the side products. The title product was eluted with THF, the solvent evaporated in vacuum and recrystallized from DCM – methanol (1:1). The product porphyrin **V.7** was a purple-reddish solid in 65% yield (41.02 mg, 0.03 mmol).

¹H NMR (700 MHz, Tetrachloroethane-*d*₂): δ (ppm) 8.37 (d, *J* = 8.5 Hz, 2H), 8.27 (d, *J* = 8.6 Hz, 4H), 7.66 (d, *J* = 7.9 Hz, 4H), 7.61 (t, *J* = 7.5 Hz, 4H), 7.52 (t, *J* = 7.5 Hz, 3H), 7.49 (t, *J* = 7.5 Hz, 4H), 7.40 (d, *J* = 16.1 Hz, 2H), 7.35 (d, *J* = 7.4 Hz, 4H), 7.25 (t, *J* = 7.7 Hz, 4H), 7.18 (d, *J* = 14.6 Hz, 2H), 7.04 (d, *J* = 7.7 Hz, 4H), 6.86 (d, *J* = 7.7 Hz, 2H), 6.66 (d, *J* = 6.9 Hz, 2H), 1.62 (s, 36H).

MALDI TOF: 1253.35, calculated: 1252.54

UV-Vis: λ_{max} / nm (THF) ($\log \epsilon$) 338 (3.52), 356 (3.60), 428 (4.73), 508 (2.85), 551 (3.51), 588 (2.80)

5.4.3.6 Porphyrin V.8



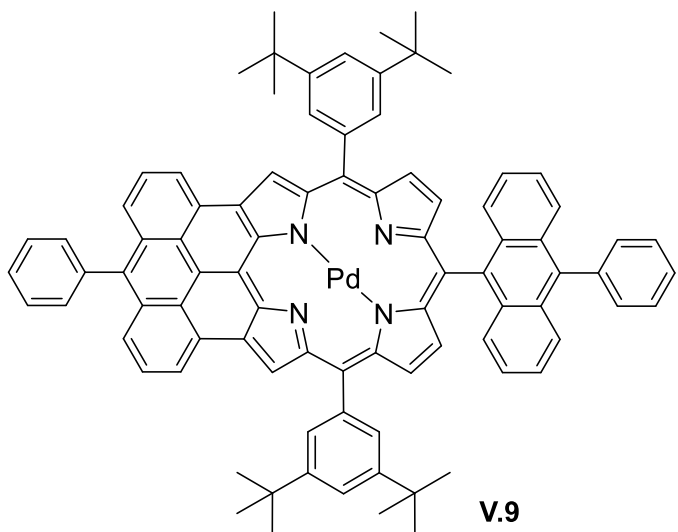
This step was prepared according to a modified literature procedure^{98,116}.

Porphyrin **V.7** (50.00 mg, 0.04 mmol) and $\text{PdCl}_2(\text{PhCN})_2$ (56.00 mg, 0.15 mmol) were dissolved in 30 mL benzonitrile. This mixture was refluxed under nitrogen flow at 140 °C and monitored by TLC. Once the reaction was completed, the mixture was allowed to cool down to room temperature and the solvent was evaporated under reduced pressure. Flash chromatography (silica, chloroform as the eluent) and precipitation by addition of methanol resulted in orange crystals of porphyrin **V.8** in 70% yield (36.17 mg, 0.03 mmol).

MALDI TOF: 1294.34, calculated: 1294.51

UV-Vis: λ_{\max} / nm (THF) ($\log \epsilon$) 340 (3.85), 361 (4.00), 428 (8.21), 526 (4.26), 555 (3.27)

5.4.3.7 One side fused porphyrin **V.9**



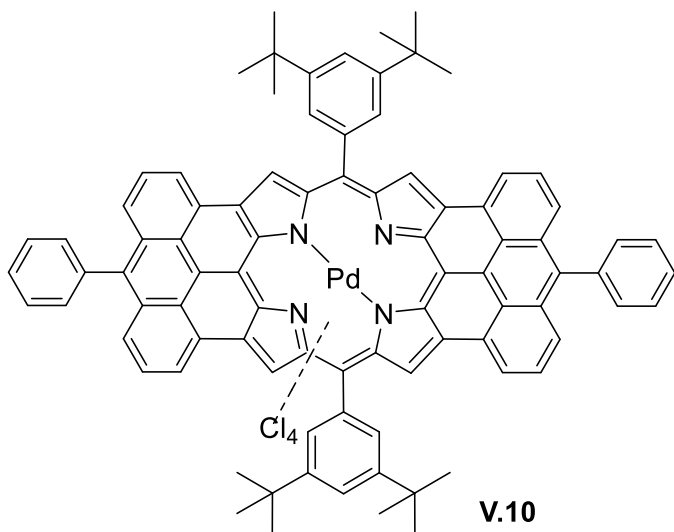
This step was prepared according to a modified literature procedure^{98,116}.

Porphyrin **V.8** (25.00 mg, 0.02 mmol) was dissolved in 15 mL dry DCM. The mixture was bubbled for 30 min by nitrogen. Iron(III) chloride (31.31 mg, 0.20 mmol) dissolved in 5 mL nitromethane was added dropwise. The solution was stirred at room temperature and monitored by TLC. At completion, the solvents were evaporated under reduced pressure. Chromatography through silica with petrol ether – chloroform 2:1 as the solvent and removal of the solvent in vacuum resulted in a reddish brown solid, porphyrin **V.9** in 57% yield (13.98 mg, 0.01 mmol).

MALDI TOF: 1290.25, calculated: 1290.48

UV-Vis: λ_{\max} / nm (THF) ($\log \epsilon$) 332 (4.47), 376 (4.30), 401 (4.41), 485 (4.45), 583 (4.12), 739 (4.19), 818 (4.39)

5.4.3.8 Fully fused porphyrin **V.10**



This step was prepared according to a modified literature procedure^{98,116}.

Porphyrin **V.9** (20.00 mg, 0.02 mmol) and scandium(III) triflate (123.45 mg, 0.48 mmol) were dissolved in 20 mL dry DCM. The mixture was bubbled for 30 min with nitrogen. Iron(III) chloride (25.54 mg, 0.15 mmol) dissolved in 7 mL nitromethane was added dropwise. The solution was stirred at room temperature and monitored by TLC. At completion (10 min), the solvents were evaporated under reduced pressure. Washing with methanol, filtration through a silica plug with chloroform as the eluent and removal of the solvent in vacuum resulted in a purple solid, porphyrin **V.10** in 32% yield (7.05 mg, 0.01 mmol).

MALDI TOF: 1424.29, calculated: 1425.73

UV-Vis: λ_{\max} / nm (THF) ($\log \epsilon$) 429 (3.99), 532 (4.44), 637 (3.96), 801 (3.79), 838 (3.87), 934 (4.23) (Figure 4.17)

6 Summary

The design and syntheses of novel organic dyes with distinct and application optimized photophysical properties and specific characteristics stemming from the field of further application was achieved.

Firstly, the mixed benzo-naphtho porphyrin family and mixed naphtho-antra porphyrin family were prepared. The necessary benzo-, naphtho- and anthra-isoindole building blocks were therefore synthesized from commercially available substances via common techniques. As predicted, different amounts of the building blocks and consequently small changes in size of the conjugated π -system, resulted in small bathochromic shifts in the absorption spectrum. The mixture of the benzo-naphtho porphyrin family displayed a broad Q-band absorption from approximately 600 to 700 nm, with a maximum at 661 nm. The mixture of the naphtho-antra porphyrin family displayed a broad Q-band absorption from approximately 600 to 800 nm, with a maximum at 740 nm. The molecules were well suited for the TTA-UC process, resulting in a broad emitter fluorescence of about 138 nm centring at 560 nm. Hereby a first step to maximize the usable wavelengths for solar harvesting devices was made by simple upconversion of light from the deep-red region to the visible region.

Secondly, an optimal emitter for the mixed benzo-naphtho porphyrin family with possible application in the biomedical field as a part of a subcutaneous oxygen and temperature sensing system needed to be found since *in vivo* straightforward excitation and measuring of the luminescence is hindered due to the absorption and scattering by the surrounding tissue components. Hence all entering and exiting wavelengths need to be within the tissue transparency window, ultimately giving an additional parameter for the design of the emitter dye. Thus, well matching triplet levels of the sensitizer and emitter and the fitting of the complete TTA-UC spectrum into the restricted human skin transparency window were the goals to achieve. Therefore, three BODIPY derived dyes were prepared via statistical acid mediated mixed pyrrole condensation, namely DPh-BODIPY, MPh-MB-BODIPY and DB-BODIPY. The absorption spectra proved the expectation, that every annulation step shifts the Q-band absorption bathochromically by 40-45 nm ranging from absorption peaks at 557, 597 to 641 nm. At the same time molar absorptivity is growing as well, due to the enlargement of the π -system. Overall it could be shown that the parameters were met, the TTA-UC system was successfully optimized towards the tissue transparency window and the registered dF or rPh signals for the UC

dye-couple Pd-BNP/ MPh-MB-BODIPY were more than 8 times higher than using known emitter dyes.

Thirdly, for the application as part of an *in vivo* oxygen and temperature sensing device, the known sensitizer dyes were lacking maximized tissue penetration. A chromophore with absorption in the IR-region was the target. Therefore, a novel palladium-porphyrin-based dye fused with two diphenyl-anthracene moieties was prepared. As these kinds of systems suffer from poor solubility, *tert*-butyl and chlorine-groups were incorporated into the molecular design. The resulting π -system enlarged fused porphyrin displayed a Q-band absorption in the IR-A-region with a maximum at 934 nm. Residual phosphorescence is detectable, giving hope for successful TTA-UC method application. Possible emitters therefore are from the rubrene and TDI family.

7 Appendix

7.1.1 List of tables

Table 1.1: Partial pressure of oxygen for normal tissue and for certain types of tumours. Reprint by permission from British Institute of Radiology: <i>BJR</i> , 2014, 87 (1035), 20130676 – 1-12, Copyright (2019).....	11
Table 4.1: Spectral properties of the different BODIPYs in toluene at room temperature. ^a Fluorescence quantum yields for all BODIPYs ($\lambda_{\text{exc}} = 560$ nm) were calculated using Lumogen Red as a standard ($\Phi_f = 0.96$ in chloroform). The measurements were performed by [REDACTED] [REDACTED].....	65
Table 4.2: TTA – UC parameters for different UC-couples, in toluene at room temperature, glove-box conditions. The measurements were performed by [REDACTED] [REDACTED].....	66

7.1.2 List of figures

Figure 2.1: Transition between energy levels of a molecule demonstrating the Franck-Condon principle. ²²	3
Figure 2.2: Jablonski diagram depicting possible transitions between energy levels of the valence electrons of a molecule in solution. ²³	4
Figure 2.3: Visual representation of red-shifted emission signal (left, broken line) and blue-shifted emission signal (right, broken line). ²⁴	5
Figure 2.4: Simplified energetic scheme of the TTA – UC process in multicomponent organic system. Upper – general structures of the sensitizer ensemble, right – structure of the emitter (rubrene). ¹²	6
Figure 2.5: Molecular orbital of oxygen in its ground level, the triplet state. ³⁹	7
Figure 2.6: Mechanism of quenching of the TTA-UC process due to the presence of oxygen, which competes with the emitter molecules for the energy transfer from the sensitizer, leading to excitation of oxygen from its triplet ground state to its singlet excited state. ⁴¹	8
Figure 2.7: Simplified organic solar cell and possible donor and acceptor materials. ⁶⁰	9
Figure 2.8: Methodology of the European Hyposens project. Formation of nanocapsules with oxygen and temperature sensing molecules and coating with targeting antibodies. Subsequent preclinical testing in tumour cells, animal models and clinical biopsies. Detection of optical signal containing information about temperature and oxygen concentration via photonic imaging detection system. ¹⁵	10

Figure 2.9: Overview of composition of capsules for temperature and oxygen concentration measurement via TTA-UC. ⁶⁴	12
Figure 2.10: Q-band sensitizer absorption: PdTBP (red line); PdPcOPh (light red line); sensitizer phosphorescence: PdTBP (green line); PdPcOPh (brown line). ⁶⁴	14
Figure 2.11: Effective attenuation coefficient of oxygenated whole blood, skin and fat versus the wavelength displaying the ranges of lower attenuation being called first and second (third one not shown) tissue transparency window. Reprinted by permission from Macmillan Publishers Ltd: <i>Nature Natotechnol.</i> 2009, 4, 710-711, Copyright (2019).	15
Figure 2.12: Molar extinction coefficient for different breast tissue components ¹²⁵ as follows: – oxygenated haemoglobin (HbO_2 , red line, in water) and purified white adipose tissue (WAT, grey line) compared with the emission spectral range of the signals of delayed emitter fluorescence (dF) and residual sensitizer phosphorescence (rPh) excited in upconversion regime, using deep-red excitation light with extremely low excitation intensity of 1 mW cm^{-2}	16
Figure 2.13: Experimental setup for measurement of the TTA - UC quantum yield. ¹²	17
Figure 2.14: Ruthenium (II), platinum- and iridium (III) complex derivatives as TTTA-UC sensitizers.	18
Figure 2.15: Porphyrin and phthalocyanine derivatives as TTA-UC sensitizers.	19
Figure 2.16: Absorption spectrum of a porphyrin sensitizer dye (black line) and delayed fluorescence signal of an emitter dye (red) within the transparency window. ⁷⁴	19
Figure 2.17: TTA-UC emitter dyes: perylene, rubrene and BODIPY as unsubstituted core structures (from left to right).	21
Figure 2.18: Rothemund reaction using four equivalents of pyrrole and aldehyde to form <i>meso</i> -substituted porphyrin.	21
Figure 2.19: Lindsey condensation with pyrrole and benzaldehyde reaching equilibrium, where cyclic tetraarylporphyrinogen is thermodynamically favoured over linear polypyrrylmethanes and irreversible oxidation step of cyclic porphyrinogen to porphyrin.....	22
Figure 2.20: Modification of the porphyrin core in β -position in the case of octaethylporphyrin (left) and phenanthroporphyrin (right).	23
Figure 2.21: In β -position modified porphyrin via Lindsey-condensation of predesigned units... ..	24
Figure 2.22: Common distorted 3D shapes of the porphyrin core. Reprinted by permission from Science Direct: <i>Microchemical Journal</i> , 2013, 107, 47-62, Copyright (2019).	25
Figure 2.23: Binding (right) and release (left) of oxygen on the heme group of haemoglobin in the red blood cells designed for oxygen transportation in the mammal body. ⁸⁷	26
Figure 2.24: Relative ionic radii of the elements. ¹²⁶	27
Figure 2.25: Exemplary tetrabenzoporphyrin in H-aggregation (left) and in J-aggregation (right).	29
Figure 2.26: Absorption spectra of palladium-octaethylporphyrin (Pd-OEP, black), palladium-tetrabenzoporphyrin (Pd-TBP, blue) and palladium-tetranaphthoporphyrin (Pd-TNP, red).....	31
Figure 2.27: HOMO and LUMO levels of alkenes with increasing conjugation length. ⁹⁵	32

Figure 2.28: Nickel-porphyrin with one, two or four azulene moieties fused resulting in red-shifted absorption spectrum (modified picture). ⁹⁷	33
Figure 4.1: Benzo- B, naphtho- N and anthra-isoindole A building blocks as precursors for mixed porphyrins.....	36
Figure 4.2: Synthesis of 2-formylcyclohexanone sodium salt 2 from cyclohexanon 1.	37
Figure 4.3: Synthesis of the enamin ethyl-((2-oxocyclohexylidene)methyl)glycinate 3 from 2-formyl-cyclohexanone-sodium salt 2.....	37
Figure 4.4: Synthesis of ethyl-ester-protected 4,5,6,7-tetrahydro-2H-isoindole 4 from ethyl-((2-oxocyclohexylidene)methyl)glycinate 3.	38
Figure 4.5: ¹ H-NMR spectrum of ethyl-4,5,6,7-tetrahydro-2H-isoindole-1-carboxylate 4.	38
Figure 4.6: Decarboxylation of ethyl-4,5,6,7-tetrahydro-2H-isoindole-1-carboxylate 4 yielding 4,5,6,7-tetrahydro-2H-isoindole B.....	39
Figure 4.7: Hydration of naphthalene 4 forming 1,4-dihydroronaphthalene 5.....	39
Figure 4.8: Preparation of phenylsulfenylchloride 8 from thiophenol 7 with NCS.	40
Figure 4.9: Addition of phenylsulfenylchloride 8 to 1,4-dihydroronaphthalene 6 forming (3-chloro-1,2,3,4-tetrahydronaphthalen-2-yl)(phenyl)sulfane 9.	40
Figure 4.10: Oxidation of (3-chloro-1,2,3,4-tetrahydronaphthalen-2-yl)(phenyl)sulfane 9 to 2-chloro-3-(phenylsulfonyl)-1,2,3,4-tetrahydronaphthalene 10.	41
Figure 4.11: Elimination of chlorine from 2-chloro-3-(phenylsulfonyl)-1,2,3,4-tetrahydronaphthalene 10 to form 2-(phenylsulfonyl)-1,2-dihydroronaphthalene 11.....	41
Figure 4.12: Barton-Zard-reaction of 2-(phenylsulfonyl)-1,2-dihydro-naphthalene 11 with t-butyl-cyanoacetate forming t-butyl-4,9-dihydro-2H-benzo[<i>f</i>]isoindole-1-carboxylate 12.	42
Figure 4.13: ¹ H-NMR spectrum of t-butyl 4,9-dihydro-2H-benzo[<i>f</i>]isoindole-1-carboxylate 12....	42
Figure 4.14: Deprotection of t-butyl 4,9-dihydro-2H-benzo[<i>f</i>]isoindole-1-carboxylate 12 forming the naphto- building block 4,9-dihydro-2H-benzo[<i>f</i>]isoindole N.	43
Figure 4.15: Diels-Alder-reaction of 1,2-dibromobenzene 13 and furan 14 forming 1,4-dihydro-1,4-epoxynaphthalene 15.....	43
Figure 4.16: Diels-Alder-reaction of 1,4-dihydro-1,4-epoxynaphthalene 15 and 3-sulfolene 16 forming 1,4,4a,9,9a,10-hexahydro-9-10-epoxyanthracene 17.	44
Figure 4.17: Synthesis of 1,4-dihydroanthracene 18 from 1,4,4a,9,9a,10-hexahydro-9-10-epoxyanthracene 17.....	44
Figure 4.18: Addition of phenylsulfenylchloride 8 to 1,4-dihydroanthracene 18 forming (3-chloro-1,2,3,4-tetrahydroanthracene-2-yl)(phenyl)sulfane 19.....	45
Figure 4.19: Oxidation of (3-chloro-1,2,3,4-tetrahydroanthracene-2-yl)(phenyl)sulfane 19 to 2-chloro-3-(phenylsulfonyl)-1,2,3,4-tetrahydroanthracene 20.....	45
Figure 4.20: Elimination of chlorine from 2-chloro-3-(phenylsulfonyl)-1,2,3,4-tetrahydroanthracene 20 to form 2-(phenylsulfonyl)-1,2-dihydroanthracene 21.....	46
Figure 4.21: Barton-Zard-reaction of 2-(phenylsulfonyl)-1,2-dihydroanthracene 21 with ethyl-2-cyanoacetate forming ethyl 4,11-dihydro-2H-naphtho[2,3- <i>f</i>]isoindole-1-carboxylate 22.....	46

Figure 4.22: ^1H -NMR spectrum of ethyl 4,11-dihydro-2H-naphtho[<i>f</i>]isoindole-1-carboxylate 22..	47
Figure 4.23: Deprotection of ethyl 4,11-dihydro-2H-naphtho[<i>f</i>]isoindole-1-carboxylate 22 forming the anthra- building block 4,11-dihydro-2 <i>H</i> -naphtho[2,3- <i>f</i>]isoindole A	47
Figure 4.24: Synthetic route for obtaining the mixed benzo-naphtho porphyrin family 25.	49
Figure 4.25: Absorption spectra of individual HPLC fractions of the mixed benzo- naphtho porphyrin family 25.....	50
Figure 4.26: Synthetic route for obtaining the mixed naphtho-antra porphyrin family 29.....	52
Figure 4.27: MS spectra of the mixed naphtho-antra porphyrin family 29 in toluene.....	53
Figure 4.28: Normalized absorption spectra of (a) - mixed benzo-naphtho porphyrin family 25 and (b) - mixed naphtho-antra porphyrin family 29, both measured in toluene. These measurements were performed by [REDACTED]	54
Figure 4.29: Excitation spectrum – (a); Transmission spectrum of the broadband notch filter – (b) The measurements were performed by [REDACTED]	55
Figure 4.30: Molar extinction of a sensitizer blend composed of mixed benzo-naphtho porphyrin family 25 and mixed naphtho-antra porphyrin family 29 in molar ratio 1:2, total molar concentration 1×10^{-5} M (the violet line); Sun spectral irradiance (pink line), AM 1.5; Fluorescence spectrum of the emitter – rubrene (orange line); For simplicity, the emitter fluorescence spectrum is normalized regarding the Q-band absorption of the sensitizer ensemble. The measurements were performed by [REDACTED]	56
Figure 4.31: TFA mediated condensation of ethyl-4,5,6,7-tetrahydro-2H-isoindole-1-carboxylate 4, 2-phenylpyrrole 30 and 3,5-di(tert-butyl)benzaldehyde 26 with additional aromatization with DDQ forming dipyrromethenes 31 and 32.....	58
Figure 4.32: Chelation reaction of dipyrromethenes 31 and 32 with $\text{BF}_3\text{-OEt}_2$ yielding DPh-BODIPY 33 and the non-oxidized MPh-MB-BODIPY 34.....	58
Figure 4.33: Aromatization of non-oxidized MPh-MB-BODIPY 34 with DDQ yielding MPh-MB-BODIPY 35.....	59
Figure 4.34: ^1H -NMR spectrum of DPh-BODIPY 33 and MPh-MB-BODIPY 35 in $\text{C}_2\text{D}_2\text{Cl}_4$	60
Figure 4.35: ^{13}C -NMR spectrum of DPh-BODIPY 33 and MPh-MB-BODIPY 35 in $\text{C}_2\text{D}_2\text{Cl}_4$	60
Figure 4.36: ^1H -NMR spectrum of MPh-MB-BODIPY 35 in $\text{C}_2\text{D}_2\text{Cl}_4$	61
Figure 4.37: ^{13}C -NMR spectra of MPh-MB-BODIPY 35 in $\text{C}_2\text{D}_2\text{Cl}_4$	61
Figure 4.38: TFA mediated condensation of ethyl-4,5,6,7-tetrahydro-2H-isoindole-1-carboxylate 4 and 3,5-di(tert-butyl)benzaldehyde 26 and subsequent aromatization with DDQ forming dipyrromethene 36.....	62
Figure 4.39: Chelation reaction of dipyrromethene 36 with $\text{BF}_3\text{-OEt}_2$ yielding non-oxidized DB-BODIPY 37.....	63
Figure 4.40: Aromatization of non-oxidized DB-BODIPY 37 with DDQ yielding DB-BODIPY 38..	63
Figure 4.41: ^1H -NMR spectrum of DB-BODIPY 38 in $\text{C}_2\text{D}_2\text{Cl}_4$	64
Figure 4.42: ^{13}C -NMR spectrum of DB-BODIPY 38 in $\text{C}_2\text{D}_2\text{Cl}_4$	64

Figure 4.43: (a) – Normalized absorption spectrum of the mixed palladium benzo-naphtho porphyrin family (PdBNP) 25; (b) – Normalized absorption (the green curve) and fluorescence (the red curve) of MPh-MB-BODIPY 35 in toluene. The measurements were performed by [REDACTED]

[REDACTED] 66

Figure 4.44: Temporal evolution of the signals of dF and rPh at sample temperature of $T = 22\text{ }^{\circ}\text{C}$. The excitation intensity is kept constant at 1 mW cm^{-2} for all measurements; *cw* – diode laser at $\lambda_{exc} = 658\text{ nm}$; air saturated environment; excitation spot diameter $d = 1.8 \times 10^{-3}\text{ m}$; sample thickness $b = 4 \times 10^{-4}\text{ m}$. Material composition, as follows, $1 \times 10^{-5}\text{ M PdBNP 14/ }2 \times 10^{-4}\text{ M MPh-MB-BODIPY 35/ 40 wt.\% carnauba wax / 30 wt.\% squalene oil / 30 wt.\% peanut oil}$. The black lines are a guide for the eye. The measurements were performed by [REDACTED] 67

Figure 4.45: (a) – Luminescence spectra of the UC-systems for different sample temperatures; (b) – Temperature dependence of the signals of dF (at $\lambda_{max} = 630\text{ nm}$, the blue dots) and rPh (at $\lambda_{max} = 850\text{ nm}$, the red dots) on the sample temperature. Experimental conditions for all measurements: material composition, as follows, $1 \times 10^{-5}\text{ M PdBNP 25/ }2 \times 10^{-4}\text{ M MPh-MB-BODIPY 35/ 40 wt.\% carnauba wax / 30 wt.\% squalene / 30 wt.\% peanut oil}$. The spectra are obtained at the $t = 4\text{ s}$ after starting the optical excitation. The excitation intensity is kept constant, at 1 mW cm^{-2} for all measurements; *cw* – diode laser at $\lambda_{exc} = 658\text{ nm}$; air saturated environment. The measurements were performed by [REDACTED] 68

Figure 4.46: Temperature calibration curve - ratiometric response. Normalized ratio of the signals of dF / rPh as a function of the sample temperature, demonstrated in Figure 4.45 b 69

Figure 4.47: Original synthetic plan 71

Figure 4.48: Lindsey-Condensation of 2,2'-dipyrromethane II.1 with 3,5-di-*tert*-butyl-benzaldehyde II.2 yielding 5,15-bis(3,5-di-*tert*-butylphenyl)porphyrin II.3 72

Figure 4.49: $^1\text{H-NMR}$ spectrum of 5,15-bis(3,5-di-*tert*-butylphenyl)porphyrin II.3 73

Figure 4.50: MALDI-TOF spectrum of 5,15-bis(3,5-di-*tert*-butylphenyl)porphyrin II.3 73

Figure 4.51: Normalized UV-Vis spectrum of 5,15-bis(3,5-di-*tert*-butylphenyl)porphyrin II.3. The inset shows scaled-up Q-bands 74

Figure 4.52: Second synthetic plan, first modification 75

Figure 4.53: Bromination of 5,15-bis(3,5-di-*tert*-butylphenyl)porphyrin II.3 with NBS yielding 5,15-dibromo-10,20-bis(3,5-di-*tert*-butylphenyl)porphyrin III.4 76

Figure 4.54: $^1\text{H-NMR}$ spectrum of 5,15-dibromo-10,20-bis(3,5-di-*tert*-butylphenyl)porphyrin III.4 77

Figure 4.55: MALDI-TOF spectrum of 5,15-dibromo-10,20-bis(3,5-di-*tert*-butylphenyl)porphyrin III.4 77

Figure 4.56: Normalized UV-Vis spectrum of 5,15-dibromo-10,20-bis(3,5-di-*tert*-butylphenyl)porphyrin III.4. The inset shows scaled-up Q-bands 78

Figure 4.57: Third synthetic plan 79

Figure 4.58: Miyaura-borylation of 5,15-dibromo-10,20-bis(3,5-di- <i>tert</i> -butylphenyl)porphyrin III.4 with 4,4,5,5-tetramethyl-1,3,2-dioxaborolane forming 5,15-bis(3,5-di- <i>tert</i> -butylphenyl)-10,20-bis(4,4,5,5-tetramethyl-1,3,2-dioxaborolan-2-yl)porphyrin IV.5.....	80
Figure 4.59: ¹ H-NMR spectrum of 5,15-bis(3,5-di- <i>tert</i> -butylphenyl)-10,20-bis(4,4,5,5-tetramethyl-1,3,2-dioxaborolan-2-yl)porphyrin IV.5.....	81
Figure 4.60: MALDI-TOF spectrum of 5,15-bis(3,5-di- <i>tert</i> -butylphenyl)-10,20-bis(4,4,5,5-tetramethyl-1,3,2-dioxaborolan-2-yl)porphyrin IV.5.....	81
Figure 4.61: Normalized UV-Vis spectrum of 5,15-bis(3,5-di- <i>tert</i> -butylphenyl)-10,20-bis(4,4,5,5-tetramethyl-1,3,2-dioxaborolan-2-yl)porphyrin IV.5. The inset shows scaled-up Q-bands.....	82
Figure 4.62: Fourth synthetic plan.....	83
Figure 4.63: Metalation of 5,15-bis(3,5-di- <i>tert</i> -butylphenyl)-10,20-bis(4,4,5,5-tetramethyl-1,3,2-dioxaborolan-2-yl)porphyrin IV.5 with zinc acetate yielding [5,15-bis(3,5-di- <i>tert</i> -butylphenyl)-10,20-bis(4,4,5,5-tetramethyl-1,3,2-dioxaborolan-2-yl)porphyrinato]zinc(II) V.6	84
Figure 4.64: ¹ H-NMR spectrum of [5,15-bis(3,5-di- <i>tert</i> -butylphenyl)-10,20-bis(4,4,5,5-tetramethyl-1,3,2-dioxaborolan-2-yl)porphyrinato]zinc(II) V.6.....	85
Figure 4.65: MALDI-TOF spectrum of [5,15-bis(3,5-di- <i>tert</i> -butylphenyl)-10,20-bis(4,4,5,5-tetramethyl-1,3,2-dioxaborolan-2-yl)porphyrinato]zinc(II) V.6.....	85
Figure 4.66: Normalized UV-Vis spectrum of [5,15-bis(3,5-di- <i>tert</i> -butylphenyl)-10,20-bis(4,4,5,5-tetramethyl-1,3,2-dioxaborolan-2-yl)porphyrinato]zinc(II) V.6. The inset shows scaled-up Q-bands.....	86
Figure 4.67: Suzuki coupling of [5,15-bis(3,5-di- <i>tert</i> -butylphenyl)-10,20-bis(4,4,5,5-tetramethyl-1,3,2-dioxaborolan-2-yl)porphyrinato]zinc(II) V.6 with 9-Bromo-10-phenylanthracene yielding porphyrin V.7.....	87
Figure 4.68: ¹ H-NMR spectrum of porphyrin V.7	88
Figure 4.69: MALDI-TOF spectrum of porphyrin V.7	88
Figure 4.70: Normalized UV-Vis spectrum of porphyrin V.7. The inset shows scaled-up Q-bands.....	89
Figure 4.71: Fifth synthetic plan, fourth modification.....	90
Figure 4.72: Metal-exchange of the zinc core in porphyrin V.7 with bis(benzonitrile)palladium(II) chloride forming porphyrin V.8, now with a palladium core.....	91
Figure 4.73: MALDI-TOF spectrum of porphyrin V.8	91
Figure 4.74: Normalized UV-Vis spectrum of porphyrin V.8. The inset shows scaled-up Q-bands.....	92
Figure 4.75: Cyclodehydrogenation reaction of porphyrin V.8 with iron(III) chloride yielding on one side fused porphyrin V.9.....	93
Figure 4.76: MALDI-TOF spectrum of porphyrin V.9. One time chlorinated derivative of porphyrin V.9 is also visible at 1326.21. Separation proved impossible due to similar R _f values.....	93
Figure 4.77: Normalized UV-Vis spectrum of porphyrin V.9.....	94

Figure 4.78: Cyclodehydrogenation reaction of porphyrin V.9 with iron(III) chloride yielding fully fused porphyrin V.10.....	95
Figure 4.79: MALDI-TOF spectrum of porphyrin V.10. Derivatives of porphyrin V.10 with 1,2,3 and 5 chlorines are also detected, but impossible to separate due to similar R_f values.	96
Figure 4.80: Normalized UV-Vis spectrum of porphyrin V.10.	96
Figure 4.81: Normalized UV-Vis spectrum of porphyrin II.3 (black line), porphyrin V.8 (orange line) and porphyrin V.10 (purple line).	97
Figure 5.1: Normalized absorption (continuous curve) and fluorescence (dotted curve) of DPh-BODIPY 33 in toluene. The measurements were performed by [REDACTED]	120
Figure 5.2: Normalized absorption (continuous curve) and fluorescence (dotted curve) of DB-BODIPY 38 in toluene. The measurements were performed by [REDACTED]	122

7.1.3 List of publications and other work

Publications before PhD study:

- 1) Filatov, M.A.; **Heinrich**, E.; Busko, D.; Ilieva, I.Z.; Landfester, K.; Baluschev, S., Reversible oxygen addition on a triplet sensitizer molecule: protection from excited state depopulation. *Phys. Chem. Chem. Phys.* 2015, 17(25), 6501-6510.
- 2) Filatov, M.A.; **Heinrich**, E.; Landfester, K.; Baluschev, S., *meso-Tetraphenylporphyrin with pi-system extended by fusion with anthraquinone*. *Org. Biomol. Chem.*, 2015, 13, 6977-6983.

Publications during PhD study:

- 1) **Heinrich**, E.; Avlasevich, Y.; Landfester, K.; Baluschev, S., Annihilation upconversion: Harvesting the entire deep-red spectral range of the sun irradiation. *J. Photonics Energy*, 2017, 022002-1 – 022002-14.
- 2) **Heinrich**, E.; Avlasevich, Y.; Landfester, K.; Baluschev, S., Asymmetrically π -extended BODIPY dyes as efficient emitters for minimally-invasive temperature sensing via annihilation upconversion. - *Submission pending*

Posters:

- 1) Filatov, M.A.; Heinrich, E.; Landfester, K.; Baluschev, S., „**meso-Tetraphenylporphyrin with pi-system extended by fusion with anthraquinone**”, 2nd October 2015, MPIP, Germany, poster presentation.
- 2) E. Heinrich, Y. Avlasevich, S. Baluschev, K. Landfester, „**Mixed benzophenophorphyrins for broadband-excited photon energy annihilation upconversion**“, *ESOC 2017 / 20th European Symposium on Organic Chemistry*, 2-6th July, Cologne, Germany, poster presentation.
- 3) Heinrich, E.; Avlasevich, Y.; Landfester, K.; Baluschev, S., „**Annihilation upconversion: Harvesting the entire deep-red spectral range of the sun irradiation**”, 18th October 2017, MPIP, Germany, poster presentation.

7.1.4 Curriculum vitae

Personal Information

Name, surname Heinrich, Ernesta

Date/place of birth [REDACTED]

[REDACTED]

Nationality [REDACTED]

[REDACTED]

Marital Status [REDACTED]

Address [REDACTED]

Current Position

[REDACTED]

Education**Extracurricular**

7.1.5 Bibliography

- 1 Gratzel, M. Applied physics: Solar cells to dye for. *Nature* **421**, 586-587, doi:10.1038/421586a (2003).
- 2 Schmidt-Mende, L., Kroese, J. E., Durrant, J. R., Nazeeruddin, M. K. & Gratzel, M. Effect of hydrocarbon chain length of amphiphilic ruthenium dyes on solid-state dye-sensitized photovoltaics. *Nano Lett* **5**, 1315-1320 (2005).
- 3 Doyle, R. Oil haves and have-nots. The fossil fuel age will end, but few agree on when. *Sci Am* **291**, 31 (2004).
- 4 Inganás, O. Organic Photovoltaics over Three Decades. *Adv Mater* **30**, e1800388, doi:10.1002/adma.201800388 (2018).
- 5 Dou, L. *et al.* 25th anniversary article: a decade of organic/polymeric photovoltaic research. *Adv Mater* **25**, 6642-6671, doi:10.1002/adma.201302563 (2013).
- 6 Werner, J. *et al.* Efficient Monolithic Perovskite/Silicon Tandem Solar Cell with Cell Area >1 cm(2). *J Phys Chem Lett* **7**, 161-166, doi:10.1021/acs.jpclett.5b02686 (2016).
- 7 Kraemer, D. *et al.* High-performance flat-panel solar thermoelectric generators with high thermal concentration. *Nat Mater* **10**, 532-538, doi:10.1038/nmat3013 (2011).
- 8 Almosni, S. *et al.* Material challenges for solar cells in the twenty-first century: directions in emerging technologies. *Sci Technol Adv Mater* **19**, 336-369, doi:10.1080/14686996.2018.1433439 (2018).
- 9 Baluschev, S. *et al.* Blue-green up-conversion: noncoherent excitation by NIR light. *Angew Chem Int Ed Engl* **46**, 7693-7696, doi:10.1002/anie.200700414 (2007).
- 10 Baluschev, S. *et al.* Metal-enhanced up-conversion fluorescence: effective triplet-triplet annihilation near silver surface. *Nano Lett* **5**, 2482-2484, doi:10.1021/nl0517969 (2005).
- 11 Yakutkin, V. *et al.* Towards the IR limit of the triplet-triplet annihilation-supported up-conversion: tetraanthraporphyrin. *Chemistry* **14**, 9846-9850, doi:10.1002/chem.200801305 (2008).
- 12 Heinrich, E., Avlasevich, Y., Landfester, K. & Baluschev, S. Annihilation upconversion: harvesting the entire deep-red spectral range of the sun irradiation. *Journal of Photonics for Energy* **8** doi:Artn 02200210.1117/1.Jpe.8.022002 (2018)
- 13 Skripka, A. *et al.* Double rare-earth nanothermometer in aqueous media: opening the third optical transparency window to temperature sensing. *Nanoscale* **9**, 3079-3085, doi:10.1039/c6nr08472a (2017).

- 14 Maestro, L. M. *et al.* Deep tissue bio-imaging using two-photon excited CdTe fluorescent quantum dots working within the biological window. *Nanoscale* **4**, 298-302, doi:10.1039/c1nr11285f (2012).
- 15 Hyposens. *Hyposens - Horizon 2020*, <<http://hyposens.eu/overview/>> (2016).
- 16 Singh, A. K., Singh, S. K., Gupta, B. K., Prakash, R. & Rai, S. B. Probing a highly efficient dual mode: down-upconversion luminescence and temperature sensing performance of rare-earth oxide phosphors. *Dalton Trans* **42**, 1065-1072, doi:10.1039/c2dt32054a (2013).
- 17 Dong, B. *et al.* Temperature sensing and in vivo imaging by molybdenum sensitized visible upconversion luminescence of rare-earth oxides. *Adv Mater* **24**, 1987-1993, doi:10.1002/adma.201200431 (2012).
- 18 Presley, K. *et al.* Nanoscale upconversion for oxygen sensing. *Mater Sci Eng C Mater Biol App* **70**, 76-84, doi:10.1016/j.msec.2016.08.056 (2017).
- 19 Carreau, A., El Hafny-Rahbi, B., Matejuk, A., Grillon, C. & Kieda, C. Why is the partial oxygen pressure of human tissues a crucial parameter? Small molecules and hypoxia. *J Cell Mol Med* **15**, 1239-1253, doi:10.1111/j.1582-4934.2011.01258.x (2011).
- 20 Vetrone, F. *et al.* Temperature sensing using fluorescent nanothermometers. *ACS Nano* **4**, 3254-3258, doi:10.1021/nn100244a (2010).
- 21 Heinrich, E. *Functionalization of Macrocycles via Chemical Tuning*, Johannes Gutenberg-Universität Mainz, (2016).
- 22 Smith, K. C. *Basic Photochemistry*, <<http://photobiology.info/Photochem.html>>
- 23 Instruments, E. *Jablonski-diagram*, <<https://www.edinst.com/blog/jablonski-diagram/>>
- 24 McDonald, K. T. Radiative Energy Transfer with Filterrs and Stokes/Anti-Stokes Coatings. (Princeton University, 2017).
- 25 Islangulov, R. R., Lott, J., Weder, C. & Castellano, F. N. Noncoherent low-power upconversion in solid polymer films. *Journal of the American Chemical Society* **129**, 12652-, doi:10.1021/ja075014k (2007).
- 26 Baluschev, S. *et al.* Blue-green up-conversion: Noncoherent excitation by NIR light. *Angewandte Chemie-International Edition* **46**, 7693-7696, doi:10.1002/anie.200700414 (2007).
- 27 Lebedev, A. Y. *et al.* Dendritic Phosphorescent Probes for Oxygen Imaging in Biological Systems. *Acs Applied Materials & Interfaces* **1**, 1292-1304, doi:10.1021/am9001698 (2009).
- 28 Singh-Rachford, T. N., Haefele, A., Ziessel, R. & Castellano, F. N. Boron Dipyrromethene Chromophores: Next Generation Triplet Acceptors/Annihilators for Low Power Upconversion Schemes. *Journal of the American Chemical Society* **130**, 16164-, doi:10.1021/ja807056a (2008).

-
- 29 Keivanidis, P. E., Baluschev, S., Lieser, G. & Wegner, G. Inherent Photon Energy Recycling Effects in the Up-Converted Delayed Luminescence Dynamics of Poly(fluorene)-Pt(II)octaethyl Porphyrin Blends. *Chemphyschem* **10**, 2316-2326, doi:10.1002/cphc.200900290 (2009).
- 30 Cheng, Y. Y. *et al.* Kinetic Analysis of Photochemical Upconversion by Triplet-Triplet Annihilation: Beyond Any Spin Statistical Limit. *Journal of Physical Chemistry Letters* **1**, 1795-1799, doi:10.1021/jz100566u (2010).
- 31 Monguzzi, A. *et al.* Efficient Broadband Triplet-Triplet Annihilation-Assisted Photon Upconversion at Subsolar Irradiance in Fully Organic Systems. *Advanced Functional Materials* **25**, 5617-5624, doi:10.1002/adfm.201502507 (2015).
- 32 Borjesson, K., Dzebo, D., Albinsson, B. & Moth-Poulsen, K. Photon upconversion facilitated molecular solar energy storage. *Journal of Materials Chemistry A* **1**, 8521-8524, doi:10.1039/c3ta12002c (2013).
- 33 Simon, Y. C. *et al.* Low-Power Upconversion in Dye-Doped Polymer Nanoparticles. *Macromolecular Rapid Communications* **33**, 498-502, doi:10.1002/marc.201100708 (2012).
- 34 Askes, S. H. C. *et al.* Imaging the lipid bilayer of giant unilamellar vesicles using red-to-blue light upconversion. *Chemical Communications* **51**, 9137-9140, doi:10.1039/c5cc02197a (2015).
- 35 Filatov, M. A. *et al.* Tetraaryltetraanthra[2,3]porphyrins: Synthesis, Structure, and Optical Properties. *Journal of Organic Chemistry* **77**, 11119-11131, doi:10.1021/jo302135q (2012).
- 36 Jacques, S. L. Optical properties of biological tissues: a review (vol 58, pg R37, 2013). *Physics in Medicine and Biology* **58**, 5007-5008, doi:10.1088/0031-9155/58/14/5007 (2013).
- 37 Monguzzi, A., Tubino, R. & Meinardi, F. Upconversion-induced delayed fluorescence in multicomponent organic systems: Role of Dexter energy transfer. *Physical Review B* **77**, doi:ARTN 15512210.1103/PhysRevB.77.155122 (2008).
- 38 Keivanidis, P. E. *et al.* Electron-Exchange Assisted Photon Energy Up-Conversion in Thin Films of pi-Conjugated Polymeric Composites (vol 2, pg 1893, 2011). *Journal of Physical Chemistry Letters* **2**, 2634-2634, doi:10.1021/jz201334b (2011).
- 39 Chemistry-LibreTexts. *Oxygen*, <chem.libretexts.org>
- 40 Filatov, M. A., Baluschev, S. & Landfester, K. Protection of densely populated excited triplet state ensembles against deactivation by molecular oxygen. *Chemical Society Reviews* **45**, 4668-4689, doi:10.1039/c6cs00092d (2016).

- 41 Baluschev, S., Katta, K., Avlasevich, Y. & Landfester, K. Annihilation upconversion in nanoconfinement: solving the oxygen quenching problem. *Materials Horizons* **3**, 478-486, doi:10.1039/c6mh00289g (2016).
- 42 Liu, Q. *et al.* A General Strategy for Biocompatible, High-Effective Upconversion Nanocapsules Based on Triplet-Triplet Annihilation. *Journal of the American Chemical Society* **135**, 5029-5037, doi:10.1021/ja3104268 (2013).
- 43 O'Riordan, T. C., Soini, A. E. & Papkovsky, D. B. Monofunctional derivatives of coproporphyrins for phosphorescent labeling of proteins and binding assays. *Anal Biochem* **290**, 366-375, doi:10.1006/abio.2001.4989 (2001).
- 44 Ng, K. K. & Zheng, G. Molecular Interactions in Organic Nanoparticles for Phototheranostic Applications. *Chem Rev* **115**, 11012-11042, doi:10.1021/acs.chemrev.5b00140 (2015).
- 45 Huang, J. *et al.* Highly transparent and flexible nanopaper transistors. *ACS Nano* **7**, 2106-2113, doi:10.1021/nn304407r (2013).
- 46 Tang, B., Wang, X., Wang, G., Wang, Y. & Chen, Z. Highly sensitive and selective room-temperature phosphorescence determination of thiabendazole by the supramolecular interaction of thiabendazole/beta-cyclodextrin/triton X-100. *Analyst* **130**, 1038-1045, doi:10.1039/b503217b (2005).
- 47 Vinogradov, S. A. Arylamide dendrimers with flexible linkers via haloacyl halide method. *Org Lett* **7**, 1761-1764, doi:10.1021/o1050341n (2005).
- 48 Dzebo, D., Moth-Poulsen, K. & Albinsson, B. Robust triplet-triplet annihilation photon upconversion by efficient oxygen scavenging. *Photochem Photobiol Sci* **16**, 1327-1334, doi:10.1039/c7pp00201g (2017).
- 49 Marsico, F. *et al.* Hyperbranched unsaturated polyphosphates as a protective matrix for long-term photon upconversion in air. *J Am Chem Soc* **136**, 11057-11064, doi:10.1021/ja5049412 (2014).
- 50 Filatov, M. A. *et al.* Reversible oxygen addition on a triplet sensitizer molecule: protection from excited state depopulation. *Phys Chem Chem Phys* **17**, 6501-6510, doi:10.1039/c4cp05025h (2015).
- 51 Miles, R. W., Zoppi, G. & Forbes, I. Inorganic photovoltaic cells. *Materials Today* **10**, 20-27, doi:Doi 10.1016/S1369-7021(07)70275-4 (2007).
- 52 Chu, S. & Majumdar, A. Opportunities and challenges for a sustainable energy future. *Nature* **488**, 294-303, doi:10.1038/nature11475 (2012).
- 53 Miles, R. W., Hynes, K. M. & Forbes, I. Photovoltaic solar cells: An overview of state-of-the-art cell development and environmental issues. *Progress in Crystal Growth and Characterization of Materials* **51**, 1-42, doi:10.1016/j.pcrysgrow.2005.10.002 (2005).

-
- 54 Mohsen, M., Bagher, A. M., Reza, B. M., Vahid, M. M. A. & Mahdi, T. Comparing the generation of electricity from renewable and non-renewable energy sources in Iran and the world: now and future. *World Journal of Engineering* **12**, 627-638, doi:10.1260/1708-5284.12.6.627 (2015).
- 55 Masuko, K. *et al.* Achievement of More Than 25% Conversion Efficiency With Crystalline Silicon Heterojunction Solar Cell. *Ieee J Photovolt* **4**, 1433-1435, doi:10.1109/Jphotov.2014.2352151 (2014).
- 56 Tiedje, T., Yablonovitch, E., Cody, G. D. & Brooks, B. G. Limiting Efficiency of Silicon Solar-Cells. *Ieee Transactions on Electron Devices* **31**, 711-716, doi:Doi 10.1109/T-Ed.1984.21594 (1984).
- 57 Kosten, E. D., Newman, B. K., Lloyd, J. V., Polman, A. & Atwater, H. A. Limiting Light Escape Angle in Silicon Photovoltaics: Ideal and Realistic Cells. *Ieee Journal of Photovoltaics* **5**, 61-69, doi:10.1109/Jphotov.2014.2360566 (2015).
- 58 Nazeeruddin, M. K., Baranoff, E. & Gratzel, M. Dye-sensitized solar cells: A brief overview. *Solar Energy* **85**, 1172-1178, doi:10.1016/j.solener.2011.01.018 (2011).
- 59 Benanti, T. L. & Venkataraman, D. Organic solar cells: An overview focusing on active layer morphology. *Photosynthesis Research* **87**, 73-81, doi:10.1007/s11120-005-6397-9 (2006).
- 60 tci chemicals. <https://www.tcichemicals.com/eshop/en/gb/category_index/12802/>
- 61 McKeown, S. R. Defining normoxia, physoxia and hypoxia in tumours-implications for treatment response. *British Journal of Radiology* **87**, doi:ARTN 2013067610.1259/bjr.20130676 (2014).
- 62 Nazarova, N. V., Avlasevich, Y. S., Landfester, K. & Baluschev, S. Stimuli-responsive protection of optically excited triplet ensembles against deactivation by molecular oxygen. *Dalton Transactions* **47**, 8605-8610, doi:10.1039/c7dt03698a (2018).
- 63 Iyisan, B. & Landfester, K. Modular Approach for the Design of Smart Polymeric Nanocapsules. *Macromolecular Rapid Communications* **40**, doi:ARTN 180057710.1002/marc.201800577 (2019).
- 64 Baluschev, B. S. (2016).
- 65 Wohlnhaas, C. *et al.* Triplet-Triplet Annihilation Upconversion Based Nanocapsules for Bioimaging Under Excitation by Red and Deep-Red Light. *Macromolecular Bioscience* **13**, 1422-1430, doi:10.1002/mabi.201300149 (2013).
- 66 Hemmer, E. *et al.* Upconverting and NIR emitting rare earth based nanostructures for NIR-bioimaging. *Nanoscale* **5**, 11339-11361, doi:10.1039/c3nr02286b (2013).
- 67 Wan, H. *et al.* A bright organic NIR-II nanofluorophore for three-dimensional imaging into biological tissues. *Nat Commun* **9**, 1171, doi:10.1038/s41467-018-03505-4 (2018).

- 68 Smith, A. M., Mancini, M. C. & Nie, S. Bioimaging: second window for in vivo imaging. *Nat Nanotechnol* **4**, 710-711, doi:10.1038/nnano.2009.326 (2009).
- 69 Baluschev, S. *et al.* Upconversion photoluminescence in poly(ladder-type-pentaphenylene) doped with metal (II)-octaethyl porphyrins. *Applied Physics Letters* **86**, doi:Artn 06190410.1063/1.1857073 (2005).
- 70 Han, J. L. *et al.* The first transition metal phthalocyanines: sensitizing rubrene emission based on triplet-triplet annihilation. *Photochemical & Photobiological Sciences* **16**, 1384-1390, doi:10.1039/c6pp00464d (2017).
- 71 Chen, Z. *et al.* Upconversion Nanocarriers Encapsulated with Photoactivatable Ru Complexes for Near-Infrared Light-Regulated Enzyme Activity. *Small* **13**, doi:10.1002/smll.201700997 (2017).
- 72 Zhong, F. F. & Zhao, J. Z. An Platinum(II) Bis(acetylide) Complex with Naphthalimide and Pyrene Ligands: Synthesis, Photophysical Properties, and Application in Triplet-Triplet Annihilation Upconversion. *European Journal of Inorganic Chemistry*, 5196-5204, doi:10.1002/ejic.201700656 (2017).
- 73 Duan, P., Yanai, N. & Kimizuka, N. A bis-cyclometalated iridium complex as a benchmark sensitizer for efficient visible-to-UV photon upconversion. *Chem Commun (Camb)* **50**, 13111-13113, doi:10.1039/c4cc05718j (2014).
- 74 Busko, D. *Noncoherent Upconversion in Multimolecular Organic Systems* Dr. rer. nat. thesis, (2013).
- 75 Pedrini, J. & Monguzzi, A. Recent advances in the application triplet-triplet annihilation-based photon upconversion systems to solar technologies. *Journal of Photonics for Energy* **8**, doi:Artn 02200510.1117/1.Jpe.8.022005 (2018).
- 76 Moor, K., Kim, J. H., Snow, S. & Kim, J. H. [C-70] Fullerene-sensitized triplet-triplet annihilation upconversion. *Chemical Communications* **49**, 10829-10831, doi:10.1039/c3cc46598e (2013).
- 77 Xu, K. J., Zhao, J. Z., Cui, X. N. & Ma, J. Photoswitching of triplet-triplet annihilation upconversion showing large emission shifts using a photochromic fluorescent dithienylethene-Bodipy triad as a triplet acceptor/emitter. *Chemical Communications* **51**, 1803-1806, doi:10.1039/c4cc09202c (2015).
- 78 Rothemund, P. Formation of porphyrins from pyrrole and aldehydes. *Journal of the American Chemical Society* **57**, 2010-2011, doi:DOI 10.1021/ja01313a510 (1935).
- 79 Adler, A. D., Shergali.W & Longo, F. R. Mechanistic Investigations of Porphyrin Syntheses .I. Preliminary Studies on Ms-Tetraphenylporphin. *Journal of the American Chemical Society* **86**, 3145-&, doi:DOI 10.1021/ja01069a035 (1964).
- 80 Lindsey, J. S., Schreiman, I. C. & Hsu, H. C. Synthesis of Porphyrins under Equilibrium Conditions. *Abstracts of Papers of the American Chemical Society* **192**, 305-Orgn (1986).

-
- 81 Onoe, J., Watanabe, S., Kato, S., Nakaya, M. & Bucher, J. P. Spectroscopic and theoretical studies on the structural, electronic, and optical properties of zinc octaethylporphyrin/C-60 co-deposited films. *Journal of Chemical Physics* **147**, doi:Artn 21470110.1063/1.5005068 (2017).
- 82 Grabowski, E. Y., AbuSalim, D. I. & Lash, T. D. Naphtho[2,3-b]carbaporphyrins. *Journal of Organic Chemistry* **83**, 11825-11838, doi:10.1021/acs.joc.8b01748 (2018).
- 83 Finikova, O. S. *et al.* Synthesis of symmetrical tetraaryltranaphtho[2,3]porphyrins. *J Org Chem* **70**, 4617-4628, doi:10.1021/jo047741t (2005).
- 84 Valicsek, Z. & Horvath, O. Application of the electronic spectra of porphyrins for analytical purposes: The effects of metal ions and structural distortions. *Microchemical Journal* **107**, 47-62, doi:10.1016/j.microc.2012.07.002 (2013).
- 85 Lebedev, A. Y., Filatov, M. A., Cheprakov, A. V. & Vinogradov, S. A. Effects of structural deformations on optical properties of tetrabenzoporphyrins: Free-bases and Pd complexes. *Journal of Physical Chemistry A* **112**, 7723-7733, doi:10.1021/jp8043626 (2008).
- 86 Kanematsu, Y., Kondo, H. X., Imada, Y. & Takano, Y. Statistical and quantum-chemical analysis of the effect of heme porphyrin distortion in heme proteins: Differences between oxidoreductases and oxygen carrier proteins. *Chemical Physics Letters* **710**, 108-112, doi:10.1016/j.cplett.2018.08.071 (2018).
- 87 Chemistry-LibreTexts. *Myoglobin and Hemoglobin*,
<https://chem.libretexts.org/Bookshelves/Organic_Chemistry/Map%3A_Organic_Chemistry>
- 88 Shelnutt, J. A. *et al.* Nonplanar porphyrins and their significance in proteins. *Chemical Society Reviews* **27**, 31-41 (1998).
- 89 Gentemann, S. *et al.* Unusual Picosecond (1)(Pi,Pi-Asterisk) Deactivation of Ruffled Nonplanar Porphyrins. *Chemical Physics Letters* **245**, 441-447, doi:Doi 10.1016/0009-2614(95)01030-D (1995).
- 90 Valiotti, A., Adeyemo, A. & Hambright, P. Iron(II) and Magnesium(II) Porphyrin Acid Solvolysis Reactions. *Inorganic & Nuclear Chemistry Letters* **17**, 213-214, doi:Doi 10.1016/0020-1650(81)80004-9 (1981).
- 91 Kielmann, M. & Senge, M. O. Molecular Engineering of Free-Base Porphyrins as Ligands-The N-H center dot center dot center dot X Binding Motif in Tetrapyrroles. *Angewandte Chemie-International Edition* **58**, 418-441, doi:10.1002/anie.201806281 (2019).
- 92 Bricks, J. L., Slominskii, Y. L., Panas, I. D. & Demchenko, A. P. Fluorescent J-aggregates of cyanine dyes: basic research and applications review. *Methods and Applications in Fluorescence* **6**, doi:ARTN 01200110.1088/2050-6120/aa8d0d (2018).

- 93 Villari, V., Mineo, P., Scamporrino, E. & Micali, N. Role of the hydrogen-bond in porphyrin J-aggregates. *Rsc Advances* **2**, 12989-12998, doi:10.1039/c2ra22260d (2012).
- 94 Vasilopoulou, M. *et al.* Large work function shift of organic semiconductors inducing enhanced interfacial electron transfer in organic optoelectronics enabled by porphyrin aggregated nanostructures. *Nano Research* **7**, 679-693, doi:10.1007/s12274-014-0428-9 (2014).
- 95 Cambridge, U. o. Organic Semiconductors,
<<https://www.oe.phy.cam.ac.uk/research/materials/osemiconductors>>
- 96 Kurotobi, K., Kim, K. S., Noh, S. B., Kim, D. & Osuka, A. A quadruply azulene-fused porphyrin with intense near-IR absorption and a large two-photon absorption cross section. *Angewandte Chemie-International Edition* **45**, 3944-3947, doi:10.1002/anie.200600892 (2006).
- 97 Mori, H., Tanaka, T. & Osuka, A. Fused porphyrinoids as promising near-infrared absorbing dyes. *Journal of Materials Chemistry C* **1**, 2500-2519, doi:10.1039/c3tc00932g (2013).
- 98 Davis, N. K. S., Thompson, A. L. & Anderson, H. L. A Porphyrin Fused to Four Anthracenes. *Journal of the American Chemical Society* **133**, 30-31, doi:10.1021/ja109671f (2011).
- 99 Svagan, A. J. *et al.* Photon Energy Upconverting Nanopaper: A Bioinspired Oxygen Protection Strategy. *Acs Nano* **8**, 8198-8207, doi:10.1021/nn502496a (2014).
- 100 WHO. *Breast Cancer: Prevention and Control*,
<<https://www.who.int/cancer/detection/breastcancer/en/index1.html>>
- 101 Finikova, O., Cheprakov, A., Beletskaya, I. & Vinogradov, S. An expedient synthesis of substituted tetraarylporphyrins. *Chemical Communications*, 261-262, doi:DOI 10.1039/b008816l (2001).
- 102 Brunel, M. *et al.* Reverse saturable absorption in palladium and zinc tetraphenylporphyrin doped xerogels. *Chemical Physics* **218**, 301-307, doi:Doi 10.1016/S0301-0104(97)00084-0 (1997).
- 103 Filatov, M. A. *et al.* Reversible oxygen addition on a triplet sensitizer molecule: protection from excited state depopulation. *Physical Chemistry Chemical Physics* **17**, 6501-6510, doi:10.1039/c4cp05025h (2015).
- 104 Filatov, M. A., Heinrich, E., Landfester, K. & Baluschev, S. meso-Tetraphenylporphyrin with a pi-system extended by fusion with anthraquinone. *Organic & Biomolecular Chemistry* **13**, 6977-6983, doi:10.1039/c5ob00884k (2015).
- 105 Karabasheva, S., Baluschev, S. & Graf, K. Microstructures on soluble polymer surfaces via drop deposition of solvent mixtures. *Applied Physics Letters* **89**, doi:Artn 03111010.1063/1.2227056 (2006).

-
- 106 Kim, J. Y. *et al.* Hybrid polymer microlens arrays with high numerical apertures fabricated using simple ink-jet printing technique. *Optical Materials Express* **1**, 259-269, doi:DOI 10.1364/Ome.1.000259 (2011).
- 107 Zhang, X. Y. *et al.* Control of Polymer Phase Separation by Roughness Transfer Printing for 2D Microlens Arrays. *Small* **12**, 3788-3793, doi:10.1002/smll.201601350 (2016).
- 108 Loudet, A. & Burgess, K. BODIPY dyes and their derivatives: Syntheses and spectroscopic properties. *Chemical Reviews* **107**, 4891-4932, doi:10.1021/cr078381n (2007).
- 109 Thoresen, L. H., Kim, H., Welch, M. B., Burghart, A. & Burgess, K. Synthesis of 3,5-diaryl-4,4-difluoro-4-bora-3a,4a-diaza-s-indacene (BODIPY (R)) dyes (pg 1276, 1998). *Synlett*, 1461-+ (1998).
- 110 Burghart, A. *et al.* 3,5-diaryl-4,4-difluoro-4-bora-3a,4a-diaza-s-indacene (BODIPY) dyes: Synthesis, spectroscopic, electrochemical, and structural properties. *Journal of Organic Chemistry* **64**, 7813-7819, doi:DOI 10.1021/jo990796o (1999).
- 111 Uppal, T. *et al.* Synthesis, Computational Modeling, and Properties of Benzo-Appended BODIPYs. *Chemistry-a European Journal* **18**, 3893-3905, doi:10.1002/chem.201103002 (2012).
- 112 Avlasevich, Y., Li, C. & Mullen, K. Synthesis and applications of core-enlarged perylene dyes. *Journal of Materials Chemistry* **20**, 3814-3826, doi:10.1039/c000137f (2010).
- 113 Eversloh, C. L., Avlasevich, Y., Li, C. & Mullen, K. Palladium-Catalyzed Pentannulation of Polycyclic Aromatic Hydrocarbons. *Chemistry-a European Journal* **17**, 12756-12762, doi:10.1002/chem.201101126 (2011).
- 114 Verbelen, B., Leen, V., Wang, L. N., Boens, N. & Dehaen, W. Direct palladium-catalysed C-H arylation of BODIPY dyes at the 3- and 3,5-positions. *Chemical Communications* **48**, 9129-9131, doi:10.1039/c2cc34549h (2012).
- 115 Turshatov, A. *et al.* Synergetic Effect in Triplet-Triplet Annihilation Upconversion: Highly Efficient Multi-Chromophore Emitter. *Chemphyschem* **13**, 3112-3115, doi:10.1002/cphc.201200306 (2012).
- 116 Davis, N. K. S., Thompson, A. L. & Anderson, H. L. Bis-Anthracene Fused Porphyrins: Synthesis, Crystal Structure, and Near-IR Absorption. *Organic Letters* **12**, 2124-2127, doi:10.1021/ol100619p (2010).
- 117 Davis, N. K., Pawlicki, M. & Anderson, H. L. Expanding the porphyrin pi-system by fusion with anthracene. *Org Lett* **10**, 3945-3947, doi:10.1021/ol801500b (2008).
- 118 Chen, Q. *et al.* Synthesis of Triply Fused Porphyrin-Nanographene Conjugates. *Angewandte Chemie-International Edition* **57**, 11233-11237, doi:10.1002/anie.201805063 (2018).

- 119 Kamo, M. *et al.* Metal-dependent regioselective oxidative coupling of 5,10,15-triarylporphyrins with DDQ-Sc(OTf)3 and formation of an oxo-quinoidal porphyrin. *Org Lett* **5**, 2079-2082, doi:10.1021/o10344826 (2003).
- 120 McKeown, N. B. *et al.* A phthalocyanine clathrate of cubic symmetry containing interconnected solvent-filled voids of nanometer dimensions. *Angew Chem Int Ed Engl* **44**, 7546-7549, doi:10.1002/anie.200502668 (2005).
- 121 Borisov, S. M., Nuss, G. & Klimant, I. Red light-excitable oxygen sensing materials based on platinum(II) and palladium(II) benzoporphyrins. *Anal Chem* **80**, 9435-9442, doi:10.1021/ac801521v (2008).
- 122 Amemori, S., Yanai, N. & Kimizuka, N. Metallonaphthalocyanines as triplet sensitizers for near-infrared photon upconversion beyond 850 nm. *Phys Chem Chem Phys* **17**, 22557-22560, doi:10.1039/c5cp02733k (2015).
- 123 Sommer, J. R. *et al.* Efficient near-infrared polymer and organic light-emitting diodes based on electrophosphorescence from (tetraphenyltetranaphtho[2,3]porphyrin)platinum(II). *ACS Appl Mater Interfaces* **1**, 274-278, doi:10.1021/am800236x (2009).
- 124 Plater, M. J. A., S.; Bourhill, G. Metallated porphyrins containing lead (II), copper (II) or zinc (II). *Tetrahedron* **58(12)**, 2415-2422 (2002).
- 125 Papkovsky, D. B.; Dmitriev, R. I. Biological detection by optical oxygen sensing, *Chem. Soc. Rev.*, **2013**, 42, 8700-8732.
- 126 Schaller,C. Structure & Reactivity in Organic, Biological and Inorganic Chemistry
<<https://employees.csbsju.edu/cschaller/Principles%20Chem/ionics/ionicatoms.htm>>